

UCLA

UCLA Electronic Theses and Dissertations

Title

Magnetic Memory with Topological Insulators and Ferrimagnetic Insulators

Permalink

<https://escholarship.org/uc/item/66p3q5f9>

Author

Shao, Qiming

Publication Date

2019

Peer reviewed|Thesis/dissertation

UNIVERSITY OF CALIFORNIA

Los Angeles

Magnetic Memory with Topological Insulators and Ferrimagnetic Insulators

A dissertation submitted in partial satisfaction of the
requirements for the degree Doctor of Philosophy
in Electrical and Computer Engineering

by

Qiming Shao

2019

© Copyright by

Qiming Shao

2019

ABSTRACT OF THE DISSERTATION

Magnetic Memory with Topological Insulators and Ferrimagnetic Insulators

by

Qiming Shao

Doctor of Philosophy in Electrical and Computer Engineering

University of California, Los Angeles, 2019

Professor Kang Lung Wang, Chair

Ubiquitous smart devices and internet of things create tremendous data every day, shifting computing diagram towards data-driven. Computing and memory units in traditional computers are physically separated, which leads to huge energy cost and time delay. Novel computer architectures bring computing and memory units together for data-intensive applications. These memory units need to be fast, energy efficient, scalable and nonvolatile. This dissertation concerns innovating new types of magnetic memory or spintronic devices to achieve ultrahigh energy efficiency and ultracompact size from a perspective of material and heterostructure design. Especially, we employ quantum materials to enable potentially unprecedented technological advances. The highest energy efficiency of magnetic memory requires the largest charge-to-spin

conversion efficiency that allows the minimum power to manipulate the magnetization. We utilize topological surface states of topological insulators (TIs), which have unique spin-momentum locking and thus are highly spin-polarized. We discover giant spin-orbit torques (SOTs) from TIs at room temperature, which are more than one order of magnitude larger than those of traditional heavy metals. We integrate TIs into room temperature magnetic memories, which promises future ultralow power dissipation. SOT characterization methods and related SOT studies on heavy metals, monolayer two-dimensional materials, and magnetic insulators-based heterostructures are discussed in detail. To have the best scaling performance, we investigate emerging topological skyrmions in magnetic thin films, which are arguably the smallest spin texture in nature. While most of the skyrmions are discovered in metallic systems, insulating skyrmions are desired thanks to their lower damping and thus potentially lower power dissipation. We observe high-temperature electronic signatures of skyrmions in magnetic insulators, topological Hall effect, by engineering heterostructures consisting of heavy metals and magnetic insulators. This new platform is essential for exploring fundamental magnon-skyrmion physics and pursuing practical applications based on insulating skyrmions. To have the highest operation speed, we explore compensated ferrimagnetic insulators, which have THz dynamics due to the strong exchange coupling field. We realize energy efficient switching of the ferrimagnetic insulator in both ferrimagnetic and antiferromagnetic states, promising electrical manipulation of ultrafast dynamics.

The dissertation of Qiming Shao is approved.

Yaroslav Tserkovnyak

Chandra J. Joshi

Chee Wei Wong

Kang Lung Wang, Committee Chair

University of California, Los Angeles

2019

Someday, with my sail piercing the clouds;

I will mount the wind, break the waves, and traverse the vast, rolling sea.

– Bai Li

Table of Contents

Chapter 1 Introduction	1
1.1 Magnetic memory	1
1.2 Spin-orbit torque magneto-resistive random-access memory	5
1.3 Skyrmions for high-density memory.....	8
1.4 Organization of this dissertation	11
Chapter 2 Spin-orbit torque characterization methods	14
2.1 Second harmonic Hall method	16
2.2 Differential MOKE	26
2.3 Spin torque ferromagnetic resonance.....	27
2.3.1 Principle of ST-FMR.....	28
2.3.2 Damping and anisotropy from ST-FMR	31
2.3.3 SOT efficiency in heavy metal/ferromagnet bilayer	38
2.3.4 SOT efficiency in heavy metal/spacer/ferromagnet trilayer.....	39
2.4 Loop shift method	42
Chapter 3 Spin-orbit torques in various material systems	45
3.1 Heavy metal/ferromagnetic metal Pt/Co	45
3.2 Monolayer TMD/CoFeB SOT	47
3.2.1 Materials and methods.....	48
3.2.2 SOT from MoS ₂ /CoFeB	52
3.2.3 SOT from WSe ₂ /CoFeB	57
3.2.4 Discussions on origin of SOT in monolayer TMD/CoFeB	60
3.3 TI/CoFeB SOT	63
3.4 TI/Mo/CoFeB SOT	66
Chapter 4 Ferrimagnetic insulators.....	74
4.1 Motivations for ferrimagnetic insulators with PMA.....	75
4.2 PMA due to strain	75
4.3 SOT in magnetic insulator-based heterostructures.....	77
4.3.1 Materials and methods.....	79
4.3.2 Dimensional crossover of magnetism.....	80
4.3.3 SOT measurement	85

4.3.4 Discussions on MI thickness-dependent SOT efficiency	89
4.4 PMA switching of various magnetic insulators	96
4.4.1 SOT switching of W/TmIG	96
4.4.2 SOT switching of Pt/TmIG.....	100
4.4.3 SOT switching of nearly compensated FMI TbIG	101
Chapter 5 Proximity coupling between magnetic and nonmagnetic materials.....	104
5.1 Anomalous Hall effect	104
5.1.1 Materials and methods.....	108
5.1.2 Onset temperature of magnetic proximity effect.....	109
5.1.3 Magnetization compensation temperature.....	116
5.1.4 Discussions	120
5.2 Spin Hall magnetoresistance effect.....	122
5.2.1 SMR in heavy metal/magnetic insulator	122
5.2.2 SMR in heavy metal/ferromagnetic metal.....	124
5.3 X-ray magnetic circular dichroism.....	125
5.4 Polarized neutron reflectometry	128
Chapter 6 Skyrmions.....	133
6.1 Motivation for high-temperature insulating skyrmions	134
6.2 Theoretical phase diagram	135
6.3 Numerical micromagnetic simulation	137
6.4 Topological Hall effect.....	140
6.4.1 Materials and methods.....	141
6.4.2 Observation of THE.....	142
6.4.3 Self-calibrated determination of topological Hall effect	148
6.4.4 Determination of DMI energy at room temperature.....	151
6.4.5 Temperature dependence of saturation magnetization and anisotropy energy.....	154
6.4.6 MI thickness dependence.....	156
6.4.7 Origins of THE	160
6.5 Spin texture imaging techniques	161
Chapter 7 Device modeling and applications	165
7.1 SOT-MRAM design.....	165
7.1.1 SOT-MRAM with different channel materials.....	165

7.1.2 Light metal spacer insertion for PMA and lower write energy	168
7.2 MRAM scaling: comparison of current- and voltage- approach.....	168
7.3 Memristors with MRAM.....	176
7.4 Microwave applications	178
Chapter 8 Outlook.....	184
Chapter 9 Appendix	187
A. Materials characterization of monolayer TMD/CoFeB	187
B. Atomic model (discrete) to micromagnetic field model (continuum)	189
C. Symmetry analysis of proximity-induced resistance effect	193
D. Symmetry analysis of current-induced spin-orbit torques	200
E. Pulsed laser deposition.....	204
References	207

List of Figures

Figure 1-1 Diagram of a HDD	2
Figure 1-2 Schematic of MRAM arrays.	3
Figure 1-3 Spin-momentum locking for surface state carriers in topological insulators.....	6
Figure 1-4 Summary of damping-like SOT efficiency at different temperatures for different TI-based magnetic heterostructures	8
Figure 1-5 From domain wall to skyrmion racetrack memory	9
Figure 1-6 Schematics of skyrmions and DMIs	10
Figure 1-7 Skyrmions in four categories: skyrmions in bulk metals, bulk insulator, metallic thin films and insulator thin films	11
Figure 2-1 Micromagnetic simulations of multidomain switching process and influence of damping-like SOT efficiency on critical switching current.....	15
Figure 2-2 Schematic of a Hall bar device for transport properties and SOT measurements. Inset show an optical image of a Hall bar device	17
Figure 2-3 Illustrations of the magnetization vector under the current-induced in-plane (a) and out-of-plane (b) spin-orbit effective fields.....	19
Figure 2-4 Second-harmonic Hall resistance as a function of φ with an external magnetic field 100 Oe applied in the MoS ₂ /CoFeB bilayer	20
Figure 2-5 Determination of field-like torque and damping-like torque in the Ta/CoFeB bilayer	21
Figure 2-6 Field-dependent harmonic Hall signal in TmIG(6.4 nm)/Pt(5 nm) bilayer	25
Figure 2-7 MOKE setup and the optical image of the device with laser spot on it	26
Figure 2-8 Schematic of current-induced SOTs in a W/CoFeB bilayer.	28
Figure 2-9 ST-FMR of W/CoFeB.....	33
Figure 2-10 Extraction of damping factor from ST-FMR.	35
Figure 2-11 Extraction of resonant field from ST-FMR	37
Figure 2-12 Current-induced asymmetric domain expansion and out-of-plane field hysteresis loop shift in a HM/FM bilayer	43
Figure 2-13 Determination of damping-like torque efficiency using the current-induced hysteresis loop shift method at room temperature	44
Figure 3-1 ST-FMR for Pt/Co.....	46
Figure 3-2 Second-harmonic method for Pt/Co.....	46
Figure 3-3 Materials characterization and measurement setup.....	50
Figure 3-4 Transport magnetic properties in the MoS ₂ /CoFeB bilayer.....	52
Figure 3-5 Determination of field-like and damping-like torque in the MoS ₂ /CoFeB bilayer.....	54
Figure 3-6 The extracted R_{\parallel} (a) and R_{\perp} (b) as a function of an external magnetic field along the $\pm y$ direction for the WSe ₂ /CoFeB bilayer.	58
Figure 3-7 Temperature dependence of current-induced in-plane spin conductivities for both MoS ₂ /CoFeB and WSe ₂ /CoFeB.....	60
Figure 3-8 Transport properties of pure TIs	64
Figure 3-9 Magnetic properties of the TI/CoFeB bilayer	64

Figure 3-10 Second-harmonic measurements of the $\text{Bi}_2\text{Se}_3(6\text{nm})/\text{CoFeB}(5\text{nm})$ bilayer	65
Figure 3-11 H_D as a function of current density in TI/CoFeB bilayers	66
Figure 3-12 OOP R_H hysteresis loops for $(\text{BiSb})_2\text{Te}_3(6\text{nm})/\text{Mo}(2\text{nm})/\text{CoFeB}(t_{\text{CoFeB}})$	69
Figure 3-13 OOP R_H hysteresis loops at different temperatures for $(\text{BiSb})_2\text{Te}_3(6\text{nm})/\text{Mo}(2\text{nm})/\text{CoFeB}(0.93\text{nm})$	69
Figure 3-14 SOT determination in the $(\text{BiSb})_2\text{Te}_3(6\text{nm})/\text{Mo}(2\text{nm})/\text{CoFeB}(1.02\text{nm})$ sample with PMA.....	70
Figure 3-15 RT SOT-driven magnetization switching in the $(\text{BiSb})_2\text{Te}_3(6\text{nm})/\text{Mo}(2\text{nm})/\text{CoFeB}(1.02\text{nm})$ sample	71
Figure 3-16 Comparison between θ_K and first harmonic Hall resistance (a) and between $\Delta\theta_K$ and second harmonic Hall voltage (b) in the $(\text{BiSb})_2\text{Te}_3(6\text{nm})/\text{Mo}(2\text{nm})/\text{CoFeB}(1.02\text{nm})$	71
Figure 3-17 Progress towards efficient SOT-MRAM with PMA.....	73
Figure 4-1 Dimensional crossover of magnetism in TmIG thin films.....	81
Figure 4-2 ST-FMR characterization of thickness dependent damping factors	82
Figure 4-3 Thickness dependence of magnetic moment per unit area M and magnetic moment per unit volume M_S from different fitting ranges.....	84
Figure 4-4 Spin transport and SOT measurements in the W/TmIG bilayers.....	87
Figure 4-5 Field-like torque efficiency in W/TmIG	88
Figure 4-6 Role of TmIG M_S on the damping-like SOT efficiency	91
Figure 4-7 Temperature dependence of saturation magnetization M_S (a) and damping-like SOT efficiency (c) for different thicknesses.	93
Figure 4-8 Second harmonic Hall resistance as a function of external in-plane magnetic field at different temperatures in the W/TmIG(9.6 nm) (a) and the W/TmIG(3.2 nm) (b), where $\varphi = 45^\circ$	95
Figure 4-9 Current-induced magnetization switching in W/TmIG with different TmIG thicknesses	97
Figure 4-10 Values of T_r estimated from ξ_{DL} and SMR.....	98
Figure 4-11 TmIG thickness dependent PMA effective field (a) and coercive field (b) at room temperature	100
Figure 4-12 Current-induced magnetization switching in a TmIG(3.2 nm)/Pt(4 nm) Hall bar device at room temperature with positive and negative bias fields	101
Figure 4-13 Temperature dependence of out-of-plane hysteresis loops in W/TbIG.	102
Figure 4-14 Heat-assisted SOT switching of TbIG	103
Figure 5-1 Temperature dependent AHE in HM/TmIG.	106
Figure 5-2 Temperature dependence of R_{AHE} in W/TmIG bilayers with different TmIG thickness.	110
Figure 5-3 Temperature dependence of B_C in W/TmIG bilayers with different TmIG thickness.	110
Figure 5-4 Temperature dependence of R_{AHE} in Pt/TmIG bilayers with different TmIG thickness.	111
Figure 5-5 Temperature dependence of B_C in Pt/TmIG bilayers with different TmIG thickness.	111
Figure 5-6 MPE-induced AHE as a function of temperature.	113

Figure 5-7 Schematic of exchange coupling at finite temperature in the HM/MI bilayer.....	115
Figure 5-8 The low temperature AHE sign change temperature (T_1) due to the MPE in the Pt/TmIG and W/TmIG with different TmIG thicknesses	116
Figure 5-9 Emergence of the AHE sign change at the magnetization compensation temperature (T_M) in a W(5 nm)/TmIG(6 nm) bilayer	118
Figure 5-10 AHE resistance as function of temperature in W/TbIG and Pt/TbIG	119
Figure 5-11 Temperature dependence of AHE in the Pt(5nm)/TbIG(30nm) [162] and the Pt(4nm)/TbIG(10nm) [163].	122
Figure 5-12 Longitudinal resistance as a function of an external magnetic field along the $\pm x$ direction for the W (5 nm)/TmIG (9.6 nm), where SMR is observed as the resistance is minimized when magnetization is along the $\pm x$ direction.	123
Figure 5-13 SMR in W/CoFeB.	124
Figure 5-14 Capturing the exchange interactions in the W(5 nm)/TmIG(10 nm) by X-ray techniques	126
Figure 5-15 XMCD across the T_M	127
Figure 5-16 Capturing the spin textures in the W(5 nm)/TmIG(10 nm) by neutron techniques at 200 K.....	130
Figure 5-17 Temperature dependence of in-plane Hall hysteresis loops at 300 K (a), 200 K (b) and 80 K (c). (d) Temperature dependence of B_K	131
Figure 5-18 Capturing the spin textures in the W(5 nm)/TmIG(10 nm) by neutron techniques at 80 K.....	132
Figure 6-1 Analytical model and results for skyrmion lattice.	137
Figure 6-2 Skyrmion phase diagram from full micromagnetic simulations	139
Figure 6-3 Field dependence of skyrmion configurations	140
Figure 6-4 Illustration of topological Hall effect in the TmIG/Pt and transport properties of the TmIG(3.2 nm)/Pt (4 nm) bilayer.....	143
Figure 6-5 Observation of topological Hall effect (THE) in the TmIG(3.2 nm)/Pt (4 nm) bilayer	144
Figure 6-6 Skyrmion phase diagram from the THE as a function of temperature T and external field B_z in the TmIG(3.2 nm)/Pt (4 nm) bilayer.	146
Figure 6-7 Hall resistance as a function of out-of-plane magnetic field for three different TmIG(3.2 nm)/Pt(4 nm) Hall bar devices, D1 (a), D2 (b) and D3 (c).	149
Figure 6-8 Self-consistent determination of THE for the TmIG(3.2 nm)/Pt (4 nm) device D1 .	150
Figure 6-9 Current-induced asymmetric domain expansion and out-of-plane field hysteresis loop shift.	152
Figure 6-10 Temperature-dependent out-of-plane hysteresis loops in the W(5nm)/TmIG(3.2nm)/NGG(substrate).	154
Figure 6-11 Temperature-dependent magnetization for a TmIG.....	155
Figure 6-12 In-plane Hall resistance hysteresis loops at different temperatures for TmIG(3.2 nm)/Pt(4 nm) device D1.....	155
Figure 6-13 Temperature dependent magnetic anisotropy effective field for different TmIG thickness.....	156

Figure 6-14 Experimentally obtained evolution of skyrmion phase diagram as a function of TmIG thickness (t_{TmIG}) in TmIG/Pt (4 nm) bilayers	157
Figure 6-15 Skyrmion phase diagram from the THE in the TmIG (4 nm)/Pt (4 nm) bilayer	158
Figure 6-16 Skyrmion phase diagram from the THE in the TmIG (6 nm)/Pt (4 nm) bilayer	158
Figure 6-17 Out-of-plane Hall hysteresis loops at different temperatures in the TmIG (6.4 nm)/Pt (4 nm) bilayer.....	159
Figure 6-18 Temperature increase due to current-induced Joule heating.....	160
Figure 6-19 XMCD-PEED data for Pt(2nm)/TmIG(~20nm) at room temperature.....	163
Figure 6-20 Detailed magnetization analysis of XMCD-PEED data for Pt(2nm)/TmIG(~20nm) at room temperature.	164
Figure 6-21 XMCD-PEED data for Pt(2nm)/TmIG(~2nm) at 150K	164
Figure 7-1 Schematic of a single SOT-MRAM bit.....	166
Figure 7-2 Write energy as a function of channel material resistivity for different σ_{SH}	166
Figure 7-3 Write voltage as a function of channel material resistivity for different σ_{SH}	167
Figure 7-4 Write energy as a function of MTJ radius for different Δ	167
Figure 7-5 Write energy as a function of spacer thickness for different TI and spacer material resistivities	168
Figure 7-6 Estimated unit cell size (left vertical axis) and scaled feature sizes (right vertical axis) for MeRAM and STT-MRAM for each technology node	171
Figure 7-7 Write energy for MeRAM and STT-MRAM at each technology node for embedded applications..	174
Figure 7-8 Simple neural network.	177
Figure 7-9 Multi-stable resistance state in TI/Mo/CoFeB	178
Figure 7-10 Three types of existing microwave applications based on magnetic tunnel junctions (MTJs).....	182
Figure 9-1 Raman spectra of CVD-grown single-layer WSe ₂ before (black) and after (red) the deposition of the CoFeB layer by grazing-angle sputtering.	188
Figure 9-2 Simple 3D and 2D spin lattice	190
Figure 9-3 Schematic of a nonmagnetic spin-orbit coupled (SOC) layer/magnetic layer bilayer for symmetry analysis of current-induced SOTs	200
Figure 9-4 Picture of a PLD chamber.....	204
Figure 9-5 Inside a PLD chamber.....	205
Figure 9-6 RHEED pattern of NiO growth on TmIG(111)/NGG(111).....	206

List of Tables

Table 3-1 Properties of the investigated films in this work	51
Table 3-2. Current-induced spin-orbit fields in all the devices	59
Table 3-3 Summary of RT resistivity, spin Hall conductivity and SOT efficiency for heavy metals and topological insulators. # This work.	72
Table 4-1. List of magnetostriction constants for (111) and (100) planes at different temperatures and lattice constants for ferrimagnetic garnets and paramagnet substrates.	76
Table 5-1 Sign of AHE in various magnetized heavy metals.....	122
Table 5-2 Exchange coupling configuration in various heavy metal/magnet bilayers	122
Table 7-1 Scaling rules for circuit performance, where $K > 1$ and the single-domain approximation is used. In the table: * for keeping constant voltage and RA such that the ratio of damping factor over spin transfer efficiency has to be scaled.	175

ACKNOWLEDGEMENTS

First of all, I would like to express my deepest appreciation to Prof. Kang L. Wang for bringing me to Device Research Laboratory (DRL) at UCLA and continuous support. The passion, curiosity and diligence of Prof. Wang always inspire me to pursue impactful projects with high standards. I am extremely grateful to Prof. Wang's hands-off style, which allows me to gradually become an independent researcher. Prof. Wang encourages collaborations across disciplines, which influenced me a lot about the style of doing research. Prof. Wang is my role model of how to be a great human being. I also very much appreciate Mrs. Wang for organizing nice annual dinners to make DRL such a wonderful family and unforgettable memory.

I'm deeply indebted to Prof. Yaroslav Tserkovnyak, Prof. Chan Joshi, Prof. Chi Wee Wong, for making effort to serve as my committee members. Special thanks to Prof. Tserkovnyak for all insightful discussions and extremely helpful theoretical support. Prof. Joshi's laser class shows me how to teach a graduate class. Prof. Wong's energetic spirit is always encouragement for me to pursue an academic career.

The completion of my dissertation would not have been possible without the support and nurturing of Dr. Yabin Fan and Dr. Guoqiang Yu. Dr. Fan mentored me doing second-harmonic measurements when I came to DRL. He set a high standard for me since the day one. He does things very slow but very careful. Dr. Yu made my first publication possible, which helped me build up confidence a lot. Many of my works are impossible without back and forth discussions with him. He is always very helpful when one needs him, and he does not afraid to get people credits. His style of mentoring junior students also influenced me a lot.

I would also like to extend my deepest gratitude to many other members in DRL who make this dissertation possible. I would like to thank Xufeng Kou for all the passion and encouragement. He lets me know how to dream big. I really appreciate Lei Pan, Peng Zhang, Koichi Murata for providing excellent topological insulator thin films, Guoqiang Yu and Hao Wu for providing sputtered magnetic multilayers, Xiaoyu Che and Kin Wong for device fabrication, Yann-Wen Lan for providing 2D materials thin films, Qianjun Pan for optical measurements, Yingying Wu for 2D materials fabrication, Congli He for helping with ST-FMR measurements. I'd like to acknowledge the help and assistance from Jianshi Tang, Liang He, Di Wu, Xiang Li, Cheng Zheng, Gen Yin, Pramey Upadhyaya, Chao-Yao Yang, and many other DRL members. I also had great pleasure of working as a teaching assistant for DRL's alumnus Dr. Marko Sokolich, who shows me how to teach an undergraduate class.

Sincere thanks should also go to my collaborators. Prof. Jing Shi from UC Riverside is another important mentor during my graduate study. I cannot perform all the works on magnetic insulators without the excellent thin films provided by his group. Also, I appreciate Prof. Shi's kindness in hosting me doing a summer intern at UC Riverside and fun lunch chat at dining halls. I want to thank Chi Tang and Yawen Liu, who grow all these magnetic insulator thin films. I'd like to acknowledge Yawen Liu, Junxue Li, Mohammed Aldosary and Victor H. Ortiz for teaching me to do PLD growth. I also thank Mark Lohmann for EBL device fabrications.

Collaborations from NIST are always enjoyable experience for me. Especially helpful to me for all the neutron and x-ray measurements is Alex Grutter, who performed all careful analyses and insightful/fun discussions. I also want to thank Dustin Gilbert for helpful discussions.

I also need to acknowledge friendship outside of DRL to make my PhD life enjoyable. The name list includes Shirui Luo, Pengkun Yang, Haojun Zhang, Xiaoqi Sun, Yuxuan Lin, Zhuo Chen,

Jiahao Han, Wei Zhang, and many others. Especially, I want to express my thanks to “uphill eating group” leader, Jinxi Guo, for finding swipes for many years. I also thank him, Linqi Song and Wenlong Jiang for many interesting and insightful discussions.

Last but not least, I cannot leave acknowledgements without mentioning the unconditioned love and support from my family. I was born in Jan. 1993 and lived my childhood in a rural area of a small town in Lu’an City, Anhui Province, Middle East of China. It was my parents who provided me with the best education, always tell me to be independent, and encourage me to take new challenges. I met my wife, Yuan Dai, in the first class when I came to UCLA. We married in Dec. 2014 and had our lovely daughter, Ziqi (Charlotte) Shao, in Dec. 2015. Charlotte brought us a lot of happiness and is our beacon. Yuan is always supporting my pursuit of an academic career. I also want to give special thanks to my mother and mother-in-law for their help on taking care of our daughter. My mother-in-law, Ling Wang, has a very strong character, which encourages my wife and I to pursue our career goals. I cannot express my thanks too much to them, my dear family.

In this dissertation, Session 2.1 and 3.2 (Appendix A) are based on our manuscript titled with “Strong Rashba-Edelstein Effect-Induced Spin–Orbit Torques in Monolayer Transition Metal Dichalcogenide/Ferromagnet Bilayers.” Session 2.3 is based on manuscript titled with “Spin-torque ferromagnetic resonance measurements utilizing spin Hall magnetoresistance in W/Co₄₀Fe₄₀B₂₀/MgO structures.” Session 3.1 and 3.3 are based on manuscript titled with “Large Room Temperature Charge-to-Spin Conversion Efficiency in Topological Insulator/CoFeB bilayers.” Session 3.4 and 7.1 are based on manuscript titled with “Room Temperature Highly Efficient Topological Insulator/Mo/CoFeB Spin-Orbit Torque Memory with Perpendicular Magnetic Anisotropy.” Session 4.3 and 4.4.1 are based on manuscript title with “Role of dimensional crossover on spin-orbit torque efficiency in magnetic insulator thin films.” Session

5.1, 5.3, and 5.4 are based on manuscript titled with “Exploring interfacial exchange coupling and sublattice effect in heavy metal/ferrimagnetic insulator heterostructures using Hall measurements, x-ray magnetic circular dichroism, and neutron reflectometry.” Session 7.2 is based on manuscript titled with “Electric-field control of spin-orbit interaction for low-power spintronics.” Session 7.4 is based on manuscript titled with “Heat-assisted microwave amplifier.”

VITA

Education

2015-2019 **Ph.D. candidate** in Electrical and Computer Engineering

University of California, Los Angeles, USA

2013-2015 **M.S.** in Electrical Engineering

University of California, Los Angeles, USA

2009-2013 **B.S.** in Microelectronics and Nanoelectronics

Tsinghua University, Beijing, China

Selected Journal Publications (*Equal contribution)

9. **Qiming Shao***, Alexander Grutter*, Yawen Liu, Guoqiang Yu, Chao-Yao Yang, Dustin A. Gilbert, Elke Arenholz, Padraic Shafer, Xiaoyu Che, Chi Tang, Aryan Navabi, Qing Lin He, Brian J. Kirby, Jing Shi, Kang L. Wang, Exploring interfacial exchange coupling and sublattice effect in heavy metal/ferrimagnetic insulator heterostructures using Hall measurements, x-ray magnetic circular dichroism, and neutron reflectometry, *Physical Review B* 00, 004400 (2019)

8. Yabin Fan*, **Qiming Shao***, Lei Pan, Xiaoyu Che, Qinglin He, Gen Yin, Cheng Zheng, Guoqiang Yu, Tianxiao Nie, Massoud R. Masir, Allan H. MacDonald, Kang L. Wang, Unidirectional Spin-dependent Magneto-Resistance in Modulation-doped Magnetic Topological Insulators, *Nano Letters* 19, 692 (2019)

7. **Qiming Shao**, Kang L. Wang, Heat-assisted microwave amplifier, *Nature Nanotechnology* 14, 9 (2019)

6. **Qiming Shao***, Chi Tang*, Guoqiang Yu, Aryan Navabi, Hao Wu, Congli He, Junxue Li, Pramey Upadhyaya, Peng Zhang, Seyed Armin Razavi, Qing Lin He, Yawen Liu, Pei Yang, Se Kwon Kim, Cheng Zheng, Yizhou Liu, Lei Pan, Roger Lake, Xiufeng Han, Yaroslav Tserkovnyak, Jing Shi, Kang L. Wang, Role of dimensional crossover on spin-orbit torque efficiency in magnetic insulator thin films, *Nature Communications* 9, 3612 (2018)

5. **Qiming Shao***, Guoqiang Yu*, Yann-Wen Lan*, Yumeng Shi, Ming-Yang Li, Cheng Zheng, Xiaodan Zhu, Lain-Jong Li, Pedram Khalili Amiri, Kang L. Wang, Strong Rashba-Edelstein Effect-Induced Spin-Orbit Torques in Monolayer Transition Metal Dichalcogenide/Ferromagnet Bilayers, *Nano Letters* 16 (12), 7514-7520 (2016)

4. Congli He, Aryan Navabi, **Qiming Shao**, Guoqiang Yu, Di Wu, Weihua Zhu, Cheng Zheng, Xiang Li, Qing Lin He, Seyed Armin Razavi, Kin L Wong, Zongzhi Zhang, Pedram Khalili Amiri, Kang L Wang, Spin-torque ferromagnetic resonance measurements utilizing spin Hall magnetoresistance in W/Co₄₀Fe₄₀B₂₀/MgO structures, *Applied Physics Letters* 109 (20), 202404 (2016)

3. Di Wu, Guoqiang Yu, **Qiming Shao**, Xiang Li, Hao Wu, Kin L Wong, Zongzhi Zhang, Xiufeng Han, Pedram Khalili Amiri, Kang L Wang, In-plane current-driven spin-orbit torque switching in

perpendicularly magnetized films with enhanced thermal tolerance, *Applied Physics Letters* 108 (21), 212406 (2016)

2. Yabin Fan*, Xufeng Kou*, Pramey Upadhyaya*, **Qiming Shao**, Lei Pan, Murong Lang, Xiaoyu Che, Jianshi Tang, Mohammad Montazeri, Koichi Murata, Li-Te Chang, Mustafa Akyol, Guoqiang Yu, Tianxiao Nie, Kin L. Wong, Jun Liu, Yong Wang, Yaroslav Tserkovnyak, Kang L. Wang, Electric-field control of spin-orbit torque in a magnetically doped topological insulator, *Nature Nanotechnology* 11 (4), 352 (2016)

1. Xufeng Kou*, Shih-Ting Guo*, Yabin Fan*, Lei Pan, Murong Lang, Ying Jiang, **Qiming Shao**, Tianxiao Nie, Koichi Murata, Jianshi Tang, Yong Wang, Liang He, Ting-Kuo Lee, Wei-Li Lee, Kang L Wang, Scale-invariant quantum anomalous Hall effect in magnetic topological insulators beyond the two-dimensional limit, *Physical Review Letters* 113, 137201 (2014)

Review Articles and Book Chapters

3. Kang L Wang, Xufeng Kou, Pramey Upadhyaya, Yabin Fan, **Qiming Shao**, Guoqiang Yu, and Pedram Khalili Amiri, Electric-field control of spin-orbit interaction for low-power spintronics, *Proceedings of the IEEE* 104 (10), 1974-2008 (2016)

2. Pedram Khalili Amiri, Juan G Alzate, Xue Qing Cai, Farbod Ebrahimi, Qi Hu, Kin Wong, Cécile Grèzes, Hochul Lee, Guoqiang Yu, Xiang Li, Mustafa Akyol, **Qiming Shao**, Jordan A Katine, Jürgen Langer, Berthold Ocker, and Kang L Wang, Electric-field-controlled magnetoelectric RAM: progress, challenges, and scaling, *IEEE Transactions on Magnetics* 51 (11), 1-7 (2015)

1. Kang L Wang, Jianshi Tang, **Qiming Shao**, Pramey Upadhyaya, and Pedram Khalili Amiri, Electric Control of Magnetic Devices for Spintronic Computing, book chapter in *Spintronics-based computing*, Springer, 53-112 (2015)

Conference Proceedings

4. **Qiming Shao**, Hao Wu, Quanjun Pan, Peng Zhang, Lei Pan, Kin Wong, Xiaoyu Che and Kang L. Wang, Room Temperature Highly Efficient Topological Insulator/Mo/CoFeB Spin-Orbit Torque Memory with Perpendicular Magnetic Anisotropy, *IEEE International Electron Devices Meeting* (Dec. 2018)

3. Kang L. Wang, Hao Wu, Seyed Armin Razavi, **Qiming Shao**, Spintronic devices for low energy dissipation (invited), *IEEE International Electron Devices Meeting* (Dec. 2018)

2. **Qiming Shao**, Guoqiang Yu, Lei Pan, Xiaoyu Che, Yabin Fan, Koichi Murata, Qing-Lin He, Tianxiao Nie, Xufeng Kou and Kang L. Wang, Large Room Temperature Charge-to-Spin Conversion Efficiency in Topological Insulator/CoFeB bilayers, *Device Research Conference* (Jun. 2018)

1. **Qiming Shao**, Can Zhao, Can Wu, Jinyu Zhang, Li Zhang, and Zhiping Yu, Compact model and projection of silicon nanowire tunneling transistors (NW-tFETs), *IEEE International Conference of Electron Devices and Solid-State Circuits* (Jun. 2013)

Chapter 1 Introduction

Spintronics is a subject of using spin degree of freedom to process information [1]. It is very different from the traditional charge or electron-based information processing from two perspectives. First, collective phenomena of spins or magnetism is nonvolatile, which could keep its state for a period depending on the energy barrier and the strength of thermal fluctuation. For example, a 10-year retention time requires an energy barrier $40k_B T$, where k_B is the Boltzmann constant and T is the operation temperature. Therefore, spintronic devices have naturally low-power dissipation. Second, spin state itself could be dissipationless and thus is possible to enable quantum information processing [2]. Examples include quantum spin Hall effect [3-5], quantum anomalous Hall effect [6, 7] and many coherent single spin systems [8]. In this dissertation, we focus on the collective phenomena or magnetism, where the information is encoded by the direction of magnetic moment or magnetization. Along this direction, people are investigating how to manipulate the magnetization and read the magnetization state without least energy and time.

1.1 Magnetic memory

Most magnetic memories can be found in hard disk drives (HDDs), where the platter is magnetic disk filled with patterns to store the information. The magnetization patterns can be read through a read/write head equipped with a giant magnetoresistance (GMR) [9, 10] or tunnel magnetoresistance (TMR) [11, 12] sensor. The reading mechanism is explained later in this session. The capacity of a HDD is determined by how much one can pack domains on a platter. So, it is fundamentally limited by the domain size. Nowadays, a 3.5-inch HDD could store information up to several Terabytes. However, the speed is a major issue for a HDD since it requires mechanical

motion of the platter to locate the read/write head (Figure 1-1). So, the typical speed of write and read is at the order of millisecond (ms).

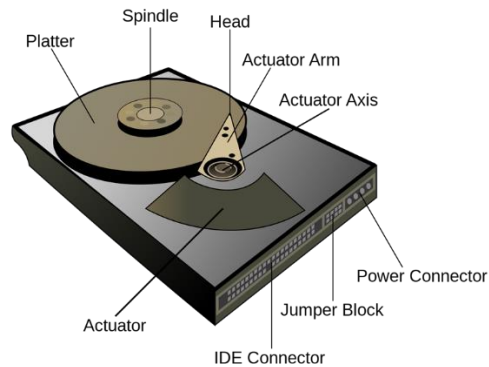


Figure 1-1 Diagram of a HDD (credit: https://en.wikipedia.org/wiki/Hard_disk_drive)

Another major type of magnetic memory is magneto-resistive random-access memory (MRAM). The key difference from a HDD is that the read/write process does not involve any mechanical motion. Instead, the choice of the magnetic bit for read/write is done through a selector (Figure 1-2), which is a transistor in the simplest case. MRAM has several advantages compared with other emerging nonvolatile memory technologies, including resistive random-access memory (RRAM) and phase-change memory (PCM) [13]. First, MRAM has almost unlimited endurance since its operations do not involve ionic motion in the RRAM case and structural change in the PCM case. Second, MRAM is the fastest memory among all nonvolatile memories, which is operating at GHz speed. At this stage, the drawback of MRAM is the relatively low density.

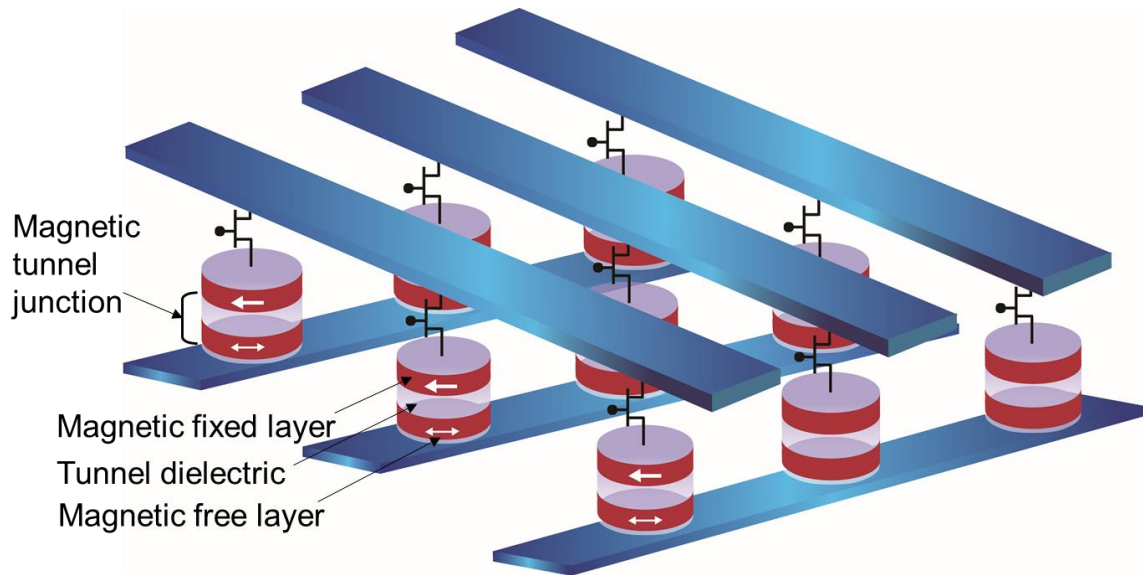


Figure 1-2 Schematic of MRAM arrays

The key component of MRAM is the magnetic tunnel junction (MTJ). It is a sandwich structure, including a magnetic fixed layer, tunnel dielectric, and magnetic free layer. The free layer magnetization can be manipulated. The most commonly one is CoFeB/MgO/CoFeB MTJ, which is used in industry. We consider four important parameters for MRAM. First thing is how to read the magnetization state. The magnetoresistance (MR) plays a role as the magnetic information to electrical information converter. When the magnetizations of fixed layer and free layer are parallel, MTJ has a low resistance. When they are antiparallel, MTJ has a high resistance. The resistance difference between these two states is the MR, which determines the read margin. The second thing is write energy. We need to reduce write energy for single MTJ to reduce the overall energy consumption. The third thing is speed. It is GHz for most of MRAMs when the ferromagnetic materials are used. The last thing is the thermal stability or the thermal energy barrier. It determines the retention time, how long you can keep the information. We always need to have a sufficient thermal stability.

Here, I discuss the history of how people improve MRAM from four perspectives: energy efficiency, scalability, write and read. Regarding the energy efficiency, we have gone through stages of field-MRAM, spin-transfer torque MRAM (STT-MRAM), and spin-orbit torque MRAM (SOT-MRAM). This part has been extensively discussed in Chapter 1 of my master thesis [14]. In Session 1.2, I will briefly recap the key point and state the motivation for highly efficient spin-orbit torque generation.

Regarding the scalability, we have transitioned from in-plane magnet to magnet with perpendicular magnetic anisotropy (PMA), which greatly improved scalability. This is because the PMA MTJ has a lower switching current and simpler structure as explained in Chapter 1 of my master thesis [14]. In Session 1.3, I will talk about the potential information carrier, topological skyrmion, which promises a very high-density memory.

The write speed is limited by the intrinsic ferromagnetic characteristic frequency, which is several GHz [15]. People are thinking about using antiferromagnet (AFM) to replace ferromagnet, which can boost the intrinsic speed limit from GHz to THz due to strong internal exchange field [16].

Regarding reading, we have transitioned from GMR to TMR. Despite the name GMR has giant, it is only tens of percent. TMR can be as large as 600% in some special cases, like CoFeB/MgO/CoFeB annealed at a temperature 525 °C [17]. Note that this temperature has been higher than standard 400 °C back-end-of-line process. Commonly available MTJs have a TMR ratio around 200%, which is much smaller than that of RRAM, PCM, which is 10^5 to 10^7 percent. How to improve this number remains a fundamental challenge. Recently, studies on two-dimensional van der Waals magnet suggest that the spin-filter TMR may provide an extraordinarily large TMR ratio up to 19,000 % [18, 19]. However, this effect is only observed at low temperature

so far and the reproducibility remains to be checked. Nevertheless, these studies encourage further investigations on achieving large MR ratio at room temperature.

In this dissertation, I will focus on energy efficiency and scalability, especially topological SOT-MRAM and topological skyrmions. Regarding write speed, I will briefly discuss the possibility of realizing AFM spintronics using ferrimagnetic insulator systems.

1.2 Spin-orbit torque magneto-resistive random-access memory

Spin current can be generated in nonmagnetic materials with strong spin-orbit coupling. This spin current can exert on the adjacent magnetic layer and generate SOTs. SOTs are very different from STTs, where the spin angular momentum is transferred from one magnet to another magnet. The STT efficiency is fundamentally limited by the spin polarization at the Fermi level of the magnetic materials, which cannot be larger than one. Also, in the STT case, the spin current and charge current are collinear. In the SOT case, the spin current and charge current are orthogonal. And the SOT efficiency is quantified by the ratio of the spin current to the charge current. There is no fundamental limit of this SOT efficiency, which could be larger than one.

In 2014, topological insulators (TIs) are discovered to have extraordinarily large SOT efficiencies both at low temperature [20] and room temperature [21]. Three-dimensional (3D) TIs are a class of materials that have an inverted band gap due to strong spin-orbit coupling [22, 23]. Inside the gap, there is a gapless helical mode (see Figure 1-3a). As a result, the bulk is insulating, and surface is conducting. These surface states have a unique property, spin momentum locking (see Figure 1-3b). The spin direction is naturally locked to the momentum direction. So, the surface current is

highly spin-polarized. In reality, in molecular beam epitaxy (MBE)-grown TIs, like Bi_2Se_3 , Bi_2Te_3 and Sb_2Te_3 , there are finite bulk carriers because of impurity and thermal excitations.

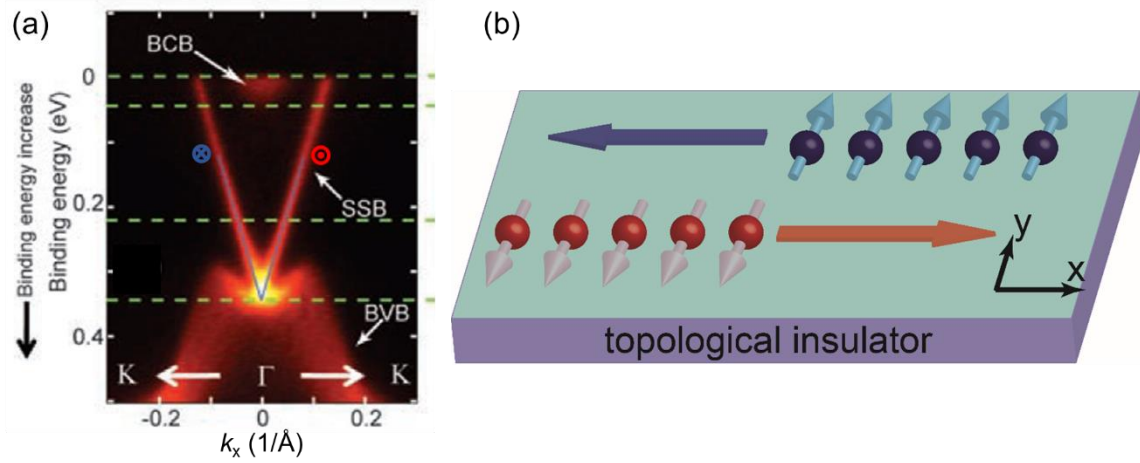


Figure 1-3 Spin-momentum locking for surface state carriers in topological insulators. (a) Angle-resolved photoemission spectrum (ARPES) of intrinsic 3D Bi_2Te_3 . Intrinsic Bi_2Te_3 is n-type due to growth defect. The Fermi level is in the bulk conduction band (BCB). Between BCB and bulk valence band (BVB), there are two surface state bands (SSBs) with linear energy dispersion. In addition, the carriers in SSBs are spin-polarized: electrons at SSB with positive crystal momentum are spin-up polarized, and electrons at SSB with negative crystal momentum are spin-down polarized. (b) Spin-momentum locking on the surface of TIs. When electrons are moving with a positive k_x , their spins are pointing to $-y$ direction; when electrons are moving with a negative k_x , their spins are pointing to $+y$ direction. (a) is reprinted with permission from [24], Copyright (2009) AAAS

In 2014, our group demonstrated a giant SOT efficiency, larger than 100, in a magnetic TI heterostructure at ultra-low temperature, where the surface current is dominant [20]. In this work, ternary compound $(\text{BiSb})_2\text{Te}_3$ is used to minimize the bulk carriers by putting the Fermi level into the middle of the bulk band gap. Slightly later, another group from Cornell university reported a large SOT efficiency, larger than 1, in TI-based heterostructures at room temperature [21]. Our

group have also studied the electric field control of SOT in magnetic TI heterostructures [25]. The results show that when the surface current contribution is maximized, the SOT strength is also maximized. This suggests dominant role of topological surface states in generating SOTs.

Now, people are intensively studying TI SOT using three methods, spin-torque ferromagnetic resonance, loop shift method, and second harmonic Hall method. We will introduce these methods in Chapter 2. Interestingly, several works reveal that bulk insulating TI $(\text{BiSb})_2\text{Te}_3$ has a larger SOT efficiency than relatively metallic Bi_2Se_3 . Here, the $(\text{BiSb})_2\text{Te}_3$ is insulating because the Fermi level is tuned inside bulk band gap through band structure. This is another evidence that the topological surface states are the major source for the SOT.

However, before one could use TI for real SOT-MRAM applications, several important issues need to be addressed. First, there is a large discrepancy in reported SOT efficiency in literatures even at same temperature, room temperature (Figure 1-4) [20, 21, 25-35]. For most of works, only one method was used to determine SOT efficiency. As the important part of this dissertation, we have utilized two methods to determine the SOT efficiency in a single Hall bar device [35]. Consistent results are obtained, which concludes that the difference is probably not from the technique. Instead, TI materials in different reports have different quality, probably resulting in different percentages of surface current contribution in total current and thus different SOT efficiencies.

Second, there is no interfacial PMA at the TI/ferromagnet interface, like TI/CoFeB interface. Many groups, including us, have extensively investigated the SOT efficiency in TI/in-plane magnet at room temperature. But the highly efficient SOT in room temperature TI/PMA magnet remains elusive until our recent work (see Session 3.4). We demonstrate a highly efficient, room temperature PMA, thermally stable and industry-compatible material stack, TI/Mo/CoFeB/MgO.

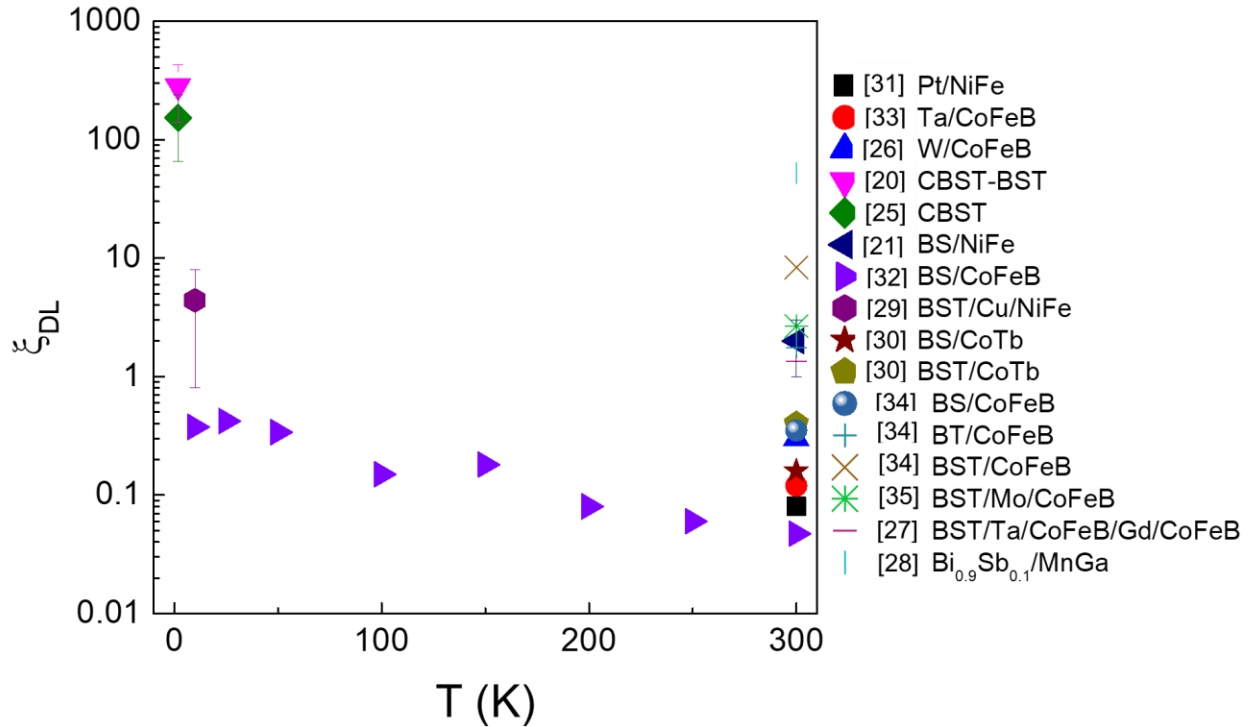


Figure 1-4 Summary of damping-like SOT efficiency at different temperatures for different TI-based magnetic heterostructures

In this dissertation, I have been focusing on room temperature SOT determination using different techniques for different material systems. The motivation for each work will be introduced when the work is presented.

1.3 Skyrmions for high-density memory

As discussed before, the density of HDDs is determined the domain size (Figure 1-5a). 200 gigabits (Gb) per square inch corresponds to data-bit size of 150 nm in width (radial direction) and 25 nm in length (circumferential direction) [36]. To further reduce the domain size, a significant challenge is that the magnetic domain meets paramagnetic limit, which means that the magnetic bit is not

stable at room temperature. While having stronger PMA materials could help with thermal stability, it also causes the magnetic domain harder to flip. Heat-assisted magnetic recording was utilized to achieve advanced writing, where localized heat is used to temporarily reduce the PMA and thus enable easier writing.

While HDDs have very high density, write and read speeds are slow. To have a faster writing and reading, using electrical method instead of mechanical motion to position domain is required. Domain wall racetrack memory is then proposed [37], where the domain wall between domains is pushed using electric current. Again, the domain wall racetrack memory faces the same issue of density as the HDDs do.

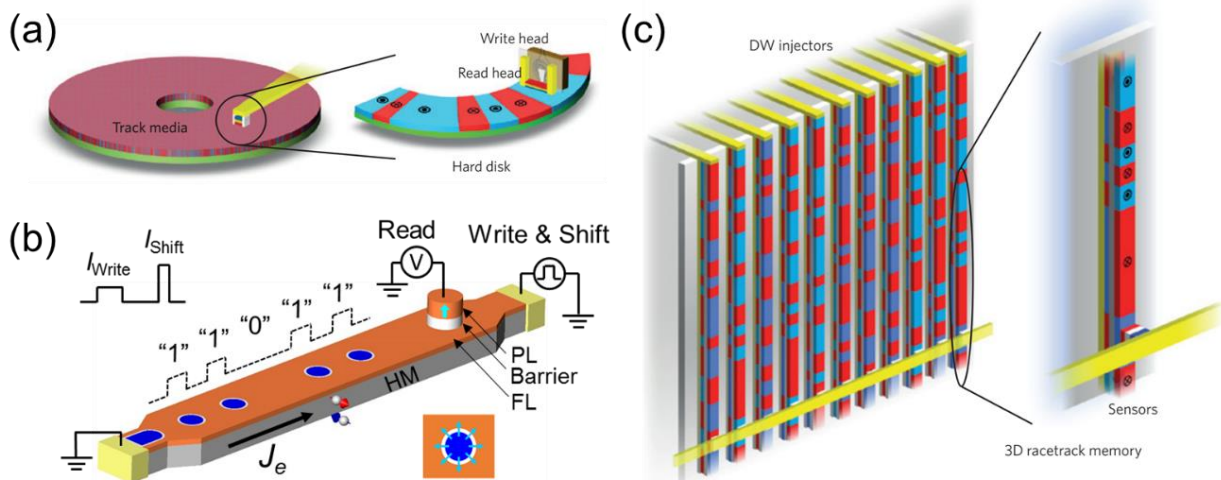


Figure 1-5 From domain wall to skyrmion racetrack memory. (a) Schematic of a HDD. (b) Schematic of a skyrmion racetrack. The special current pulses are designed to achieve skyrmion write and shift functions. (c) Schematic of 3D racetrack memory. (a) and (c) are reprinted with permission by permission from [38], Copyright (2015) Springer Nature and (b) is reprinted with permission from [39], Copyright (2017) American Chemical Society

Skyrmions are arguably the smallest spin texture in nature and thus promising for high-speed and high-density racetrack memory. There are two major types of skyrmions, Bloch-type (Figure 1-6a) and Néel-type (Figure 1-6b), which are usually stabilized by bulk Dzyaloshinskii–Moriya interaction (DMI) (Figure 1-6c) and interfacial DMI (Figure 1-6d). The detailed introduction of skyrmions will be given in Chapter 6. The topological number of skyrmions or the center magnetization direction encodes the information, which can be potentially read out through MTJ structure. The simple skyrmion racetrack structure is shown in Figure 1-5b, where the current-induced skyrmion and shift have been demonstrated by our group [39].

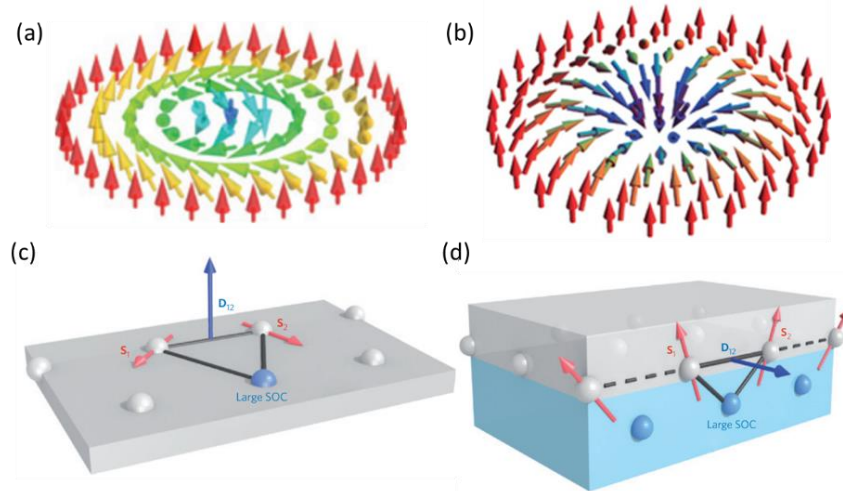


Figure 1-6 Schematics of skyrmions and DMIs. (a) Bloch-type skyrmion and (b) Néel-type skyrmion in 2D magnets with uniaxial magnetic anisotropy. (c) Bulk DMI. (d) Interfacial DMI. Figures are reprinted with permission from Ref. [40], Copyright (2013) Springer Nature

To further improve density of domain wall or skyrmion racetrack memory and domain wall velocity, 3D racetrack memory with antiferromagnetic domain wall or skyrmion has been proposed [38] (Figure 1-5c). Here, antiferromagnetic domain wall or skyrmion could exhibit much higher speed because of eliminated Walker breakdown and skyrmion Hall effect.

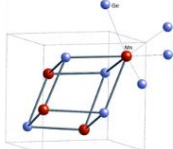
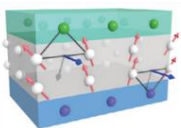
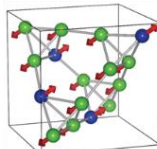
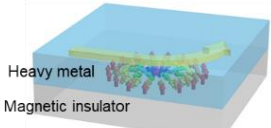
<p style="text-align: center;">Skyrmions in bulk metals</p>  <p>(B20) MnSi, MnGe, FeGe, Fe_{1-x}Co_xSi, etc.</p>	<p style="text-align: center;">Skyrmions in metallic thin films</p>  <p>Ir/Fe, Ta/CoFeB/TaO_x, Pt/Co/Ta, etc.</p>
<p style="text-align: center;">Skyrmions in bulk insulator</p>  <p>Cu₂OSeO₃ (60K)</p>	<p style="text-align: center;">Skyrmions in insulator thin films</p>  <p>Pt/Tm₃Fe₅O₁₂ (≥ 300K)</p>

Figure 1-7 Skyrmions in four categories: skyrmions in bulk metals, bulk insulator, metallic thin films and insulator thin films. Top left inset is reprinted with permission from [241], Copyright (2014) American Physical Society. Top right is reprinted with permission from [177], Copyright (2016) Springer Nature. Bottom left is reprinted with permission from [180], Copyright (2012) AAAS

The skyrmions exist in various material systems as I will introduce further in Chapter 6. While most of them have been observed, high temperature insulating skyrmion systems have not been reported. I have observed the signatures of skyrmions in magnetic insulator thin films, which complete the paradigm of the skyrmions (Figure 1-7).

1.4 Organization of this dissertation

In Chapter 2, I will introduce SOT characterization techniques: second harmonic Hall method (or second harmonic method), differential MOKE, spin-torque ferromagnetic resonance (ST-FMR) and loop shift method in sequence.

In Chapter 3, I will discuss several important SOT material systems. First, I measure SOT in Pt/Co, a traditional heavy metal/ferromagnetic metal bilayer system, as a reference. I used two methods, second harmonic method and ST-FMR, and obtained consistent SOT efficiencies. Second, I discuss SOT generation from another interesting system, monolayer transition metal dichalcogenides (TMDs). The band spin texture of TMDs can be referred from the SOT measurement. Third, I measured SOT for TI/CoFeB systems with different TIs, where the CoFeB has in-plane anisotropy. Fourth, I achieved PMA in TI/Mo/CoFeB at room temperature and measured the SOT efficiency using two methods, second harmonic method and differential MOKE. I also realized current-induced magnetization switching in this TI/Mo/CoFeB heterostructures.

In Chapter 4, I further discuss SOT and switching in magnetic insulator-based heterostructures. First, I discuss the motivation for studying magnetic insulators. Then, we discuss magnetic insulator growth and the strain-induced PMA. Then, I discuss the SOT in magnetic insulator-based heterostructures. The interesting thing is that the spin current cannot be injected into magnetic insulators since insulators do not have free electrons. Instead, the interfacial exchange coupling can transfer spin angular momentum carried by electron to magnon spin angular momentum. The significant dependence of SOT efficiency on the saturation magnetization is reported in W/Tm₃Fe₅O₁₂ (TmIG), where TmIG is a ferrimagnetic insulator with PMA. At last, I show current-induced switching in several heterostructures.

In Chapter 5, I discuss how to investigate proximity effect between magnetic and nonmagnetic materials. I will introduce four methods, anomalous Hall effect, spin Hall magnetoresistance, polarized neutron reflectometry and X-ray magnetic circular dichroism in sequence.

In Chapter 6, I will discuss skyrmion-related works. First, I will discuss the motivation for finding room temperature magnetic insulator thin films that host skyrmions. Second, I will analytically

calculate the appropriate condition for the existence of skyrmions. Third, I will numerically simulate the skyrmion phase diagram by using the micromagnetic simulations, which includes the magnetostatic energy that was ignored by analytical calculations in analytical calculations. Fourth, I will discuss the experimental observation of transport signatures of skyrmions, topological Hall effect, in a heavy metal/magnetic insulator bilayer, Pt/TmIG. At last, I will show the progress towards direct imaging of skyrmions in magnetic insulators. Meanwhile, several important techniques for spin texture imaging will be introduced.

In Chapter 7, I will mention device applications based on spintronic heterostructures. First, I will discuss the design principle of a unit SOT-MRAM cell. Second, I will compare the scaling performance of the current- and voltage-based MRAMs. Third, I will discuss the potential of using MRAM as a memristor for neuromorphic computing. At last, I will briefly mention other possible applications of using magnetic devices. Special focus will be given on microwave applications.

In the last Chapter 8, conclusions will be made. In addition, challenges and future directions will be discussed.

Chapter 2 Spin-orbit torque characterization methods

Characterization of SOT efficiency (ξ_{SOT}) is very important for spintronic applications since it determines how efficient one can generate spin current using a specific nonmagnetic material. For a magnet in the single domain state, this SOT efficiency directly determines how efficiently one can switch the magnet since the switching current is inversely proportional to the ξ_{SOT} . For switching a PMA magnet, the damping-like SOT efficiency (ξ_{DL}) is critical and thus in this dissertation, I will focus on this ξ_{DL} . Since the most of SOT-driven magnetization switching experiments are done in devices with relatively large size ($> 1 \times 1 \mu\text{m}^2$), the switching is achieved through domain nucleation and domain wall motion (Figure 2-1a). In this case, the domain nucleation and domain wall depinning energy are important, which are device-dependent. In other words, even one device has a higher SOT efficiency, it may have a higher switching current because of extrinsic factors that lead to a large domain nucleation and domain wall depinning energy. Nevertheless, if everything keeps the same, a larger ξ_{SOT} still provides a lower switching current in a large device (Figure 2-1b).

The measurements of SOT are usually done in the single domain scenario or assuming a simple domain wall structure. The achievement of the single domain state is realized by either applying a large magnetic field to align the magnetization or relying on the PMA to align the magnetization out-of-plane. The SOT efficiency quantification based on domain wall motion assumes a simple Néel domain wall structure, which normally requires interfacial Dzyaloshinskii–Moriya interaction (DMI) to be stable. The details will be explained in Session 2.4.

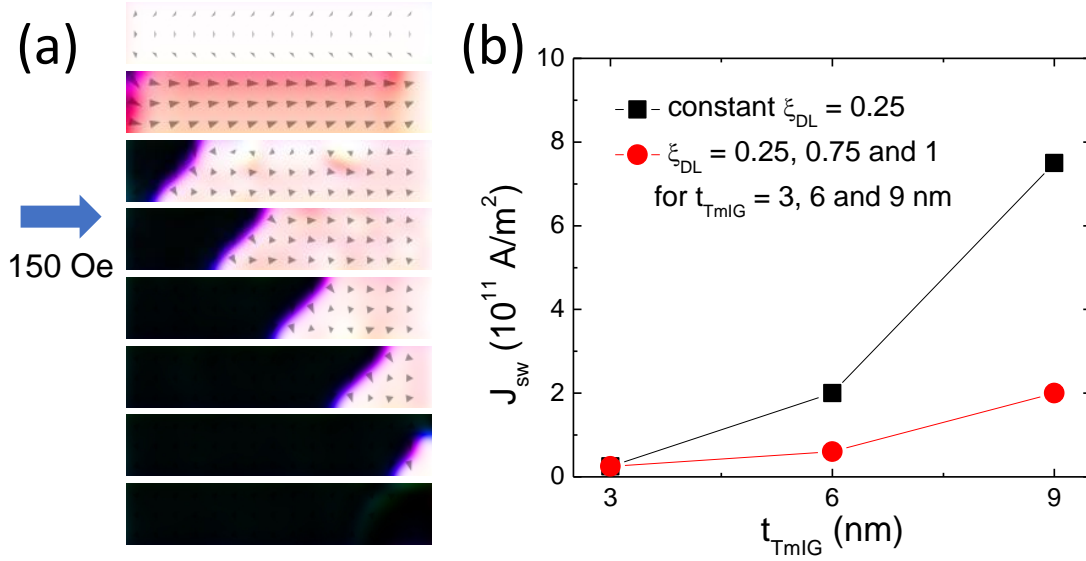


Figure 2-1 Micromagnetic simulations of multidomain switching process and influence of damping-like SOT efficiency ξ_{DL} on critical switching current. (a) Typical snapshots of multidomain switching through current-driven domain nucleation and domain wall propagation with a small in-plane external field 150 Oe. The simulated area is $1000 \times 200 \text{ nm}^2$. The top snapshot is the initial state ($m_z = +1$) and the bottom one is the final state ($m_z = -1$). The simulation is done using the mumax³ package [41]. (b) t_{TmIG} dependent critical switching current without and with enhancement of ξ_{DL} . The black curve is simulated with a constant $\xi_{DL}=0.25$ for different t_{TmIG} , and the red curve is with an increase of ξ_{DL} from 0.25 to 1 when t_{TmIG} increases from 3 nm to 9 nm. Here, ξ_{DL} is the spin polarization parameter in the mumax³ package [41]. Note that we are not trying to reproduce the experimental switching current here. Instead, using this plot, we show that regardless of single domain or multidomain switching mechanism, the increase of ξ_{DL} will always help reduce switching current density.

Of fundamental interest, SOT characterization methods are directly related to the charge-spin interconversion in a nonmagnetic material, which is very important for understanding the symmetry and band spin texture of the nonmagnetic material. Here, I provide several important examples from literatures.

First, 1T' phase WTe₂ has broken rotational symmetry, where the ac plane mirror symmetry is broken. When the current is applied along the low-symmetry a axis, the symmetry breaking generates additional out-of-plane damping-like SOT [42].

Second, the surface states of TIs Bi₂Se₃ and Bi₂Te₃ have hexagonal warping effect when the Fermi level is far above the Dirac point [43]. This effect has been detected electrically by using unidirectional magnetoresistance (UMR) in these thin films, which exhibit a crystal angle dependence with a period $\frac{2}{3}\pi$ [44]. Bulk crystal can also exhibit UMR effect as long as the inversion symmetry is broken such as in a polar semiconductor like BiTeBr without inversion symmetry [45]. UMR can also be observed in nonmagnetic/magnetic heterostructures, where the relative directions of current-induced spin polarization at the interface and the magnetization determines the resistance [46]. TI/magnetic TI heterostructure have been shown to an extraordinarily large UMR [47, 48], where the surface state is suggested to play a dominant role.

In this Chapter, I will introduce several important techniques to characterize SOTs.

2.1 Second harmonic Hall method

Second harmonic (Hall) method has been extensively used for SOT characterizations. During the development of this method, important references include [49-54].

The basic measurement setup is applying a low-frequency a.c. current and measuring second harmonic Hall voltage response (Figure 2-2). The applied current is $I(t) = \sqrt{2}I_{\text{RMS}} \sin(\omega t)$, where ω is the frequency. The typical used a.c. current frequency is 15.85 Hz or 195.85Hz in this dissertation. When the higher a.c. frequency is used, the better signal to noise ratio is achieved. However, one needs to be careful about potential parasitic effects due to higher frequency since

the second harmonic method is supposed to be a d.c. measurement. The general expression of a voltage is given by

$$V(t) = V^0 + \sqrt{2}V^{1\omega} \sin(\omega t) + \sqrt{2}V^{2\omega} \sin(2\omega t) + \text{high order terms},$$

where V^0 , $V^{1\omega}$ and $V^{2\omega}$ are the d.c., first-harmonic and second-harmonic voltage (root mean square r.m.s. values read by SR830 lock-in amplifiers, independent of time). The first-harmonic resistance and the second-harmonic resistance are given as $R^{1\omega} = V^{1\omega}/I_{\text{RMS}}$ and $R^{2\omega} = V^{2\omega}/I_{\text{RMS}}$ (independent of time). The first-harmonic resistance here is the same as the d.c. measurement case (apply d.c. current and measure the d.c. voltage).

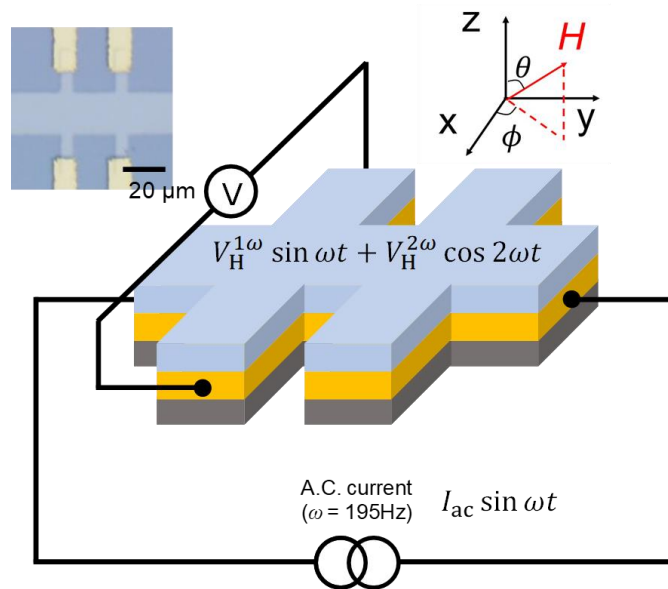


Figure 2-2 Schematic of a Hall bar device for transport properties and SOT measurements. Inset show an optical image of a Hall bar device

To understand the effect of current-induced spin torques, we introduce the equation that govern the magnetization dynamics. The general equation of motion for the magnetization under an effective magnetic field is given by the Landau–Lifshitz–Gilbert equation

$$\frac{d\mathbf{m}}{dt} = -\gamma\mathbf{m} \times \mathbf{H}_{\text{eff}} + \alpha\mathbf{m} \times \frac{d\mathbf{m}}{dt}, \quad (2-1)$$

where γ is the gyromagnetic ratio, \mathbf{m} is the magnetization vector, α is the Gilbert damping constant, and \mathbf{H}_{eff} is the sum of the external magnetic field, the demagnetization field and the crystalline anisotropy field. The first term on the right side of Eq. (2-1) is a field (or precessional) term, and the \mathbf{m} precesses around the \mathbf{H}_{eff} . The second term on the right side of Eq. (2-1) is a damping term, and forces the \mathbf{m} gradually towards the \mathbf{H}_{eff} . When a charge current passes through the heavy metal layer with strong spin-orbit coupling, a nonequilibrium spin accumulation is generated at the heavy metal/magnet interface, giving rise to SOTs on the magnet. The general form including the current-induced SOTs can be written as

$$\frac{d\mathbf{m}}{dt} = -\gamma\mathbf{m} \times \mathbf{H}_{\text{eff}} + \alpha\mathbf{m} \times \frac{d\mathbf{m}}{dt} - I_c\beta_D\mathbf{m} \times (\mathbf{m} \times \boldsymbol{\sigma}) - I_c\beta_F\mathbf{m} \times \boldsymbol{\sigma}, \quad (2-2)$$

where I_c is the current amplitude and $\boldsymbol{\sigma}$ is the current-induced spin polarization vector. β_D (β_F) is the damping-like (field-like) torque coefficient, because $I_c\beta_D\mathbf{m} \times (\mathbf{m} \times \boldsymbol{\sigma})$ ($I_c\beta_F\mathbf{m} \times \boldsymbol{\sigma}$) has the same form as the damping term (field term). In the magnetic multilayers, the inversion symmetry is broken along the z direction and thus the induced spin polarization $\boldsymbol{\sigma} \propto \mathbf{J} \times \mathbf{z}$, which is in the film plane. When we perform the second-harmonic measurements in the film plane by applying a large field to pull the magnetization in the film plane, we have effective out-of-plane damping-like SOT field $H_{\perp} = I_c\beta_D$ and in-plane field-like SOT field $H_{\parallel} = I_c\beta_F$, because the \mathbf{m} and $\boldsymbol{\sigma}$ are both in the film plane. After we understand the response of magnetization to the current, we calculate what is the voltage (or resistance) response.

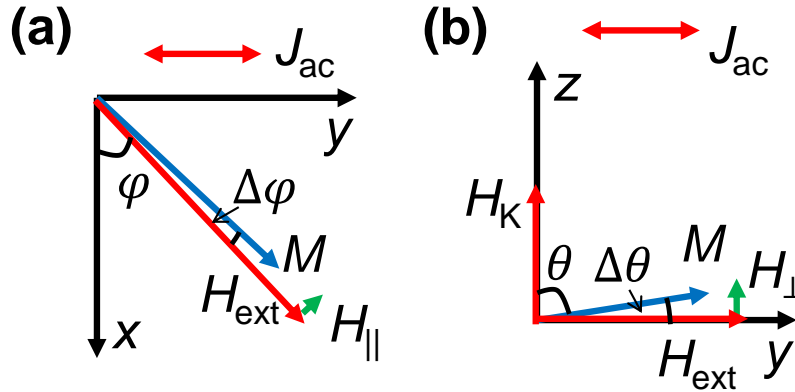


Figure 2-3 Illustrations of the magnetization vector under the current-induced in-plane (a) and out-of-plane (b) spin-orbit effective fields.

The Hall resistance without ordinary Hall effect is given by

$$R_{\text{Hall}} = R_A \cos \theta + R_P \sin^2 \theta \sin 2\varphi, \quad (2-3)$$

where θ and φ are the polar and azimuthal angles for the \mathbf{m} , R_A and R_P are the saturation anomalous Hall coefficient and planar Hall coefficient. When the magnetization is in the film plane and a small d.c. current is applied, the \mathbf{m} will deviate from its equilibrium position by $\Delta\varphi$ under the (field-like) in-plane spin-orbit field and $\Delta\theta$ under the (damping-like) out-of-plane spin-orbit field as shown in Figure 2-3. The current is along the +y direction, and thus $\boldsymbol{\sigma}$ is along the -x direction.

$\Delta\varphi = \frac{H_{\parallel} \sin \varphi}{|H_{\text{ext}}|}$, where H_{ext} is the external magnetic field and $H_{\parallel} \sin \varphi$ represents the component of the H_{\parallel} that is perpendicular to the \mathbf{m} . Similarly, by taking the anisotropy field into account, $\Delta\theta = \frac{H_{\perp} \sin \varphi}{|H_{\text{ext}}| - H_K}$ [20], where H_K is the out-of-plane anisotropy field and $\sin \varphi$ originates from the $\mathbf{m} \times \boldsymbol{\sigma}$.

When the magnetization is in the film plane and a small a.c. current (peak amplitude I_{ac_peak} and frequency ω) is applied, the \mathbf{m} will oscillate around the equilibrium position and the Hall voltage can be calculated by

$$V_{Hall} \left(\theta = \frac{\pi}{2}, \varphi \right) = \left[R_A \cos \left(\frac{\pi}{2} + \Delta\theta(t) \right) + R_P \sin^2 \left(\frac{\pi}{2} + \Delta\theta(t) \right) \sin 2(\varphi + \Delta\varphi(t)) \right] \cdot I_{ac_peak} \sin \omega t,$$

where $\Delta\theta(t) = \frac{H_{\perp} \sin \varphi \sin \omega t}{H_{ext} - H_K}$ and $\Delta\varphi(t) = \frac{H_{\parallel} \sin \varphi \sin \omega t}{H_{ext}}$. By using Taylor expansion to the first order of $\Delta\theta$ and $\Delta\varphi$, we are able to obtain the second-harmonic Hall resistance as

$$R_{Hall}^{2\omega} = \frac{R_A}{2} \cdot \frac{H_{\perp}}{|H_{ext}| - H_K} \sin \varphi + R_P \frac{H_{\parallel}}{|H_{ext}|} \cos 2\varphi \sin \varphi. \quad (2-4)$$

Here, as an example, I show the second-harmonic Hall resistance (in a MoS₂/CoFeB bilayer) in Figure 2-4, where both $\sin \varphi$ and $\cos 2\varphi \sin \varphi$ terms are observed. In addition, the coefficients of the $\cos 2\varphi \sin \varphi$ and $\sin \varphi$ terms follow $\frac{1}{|H_{ext}|}$ and $\frac{1}{|H_{ext}| - H_K}$, respectively, as shown in Figure 2-5.

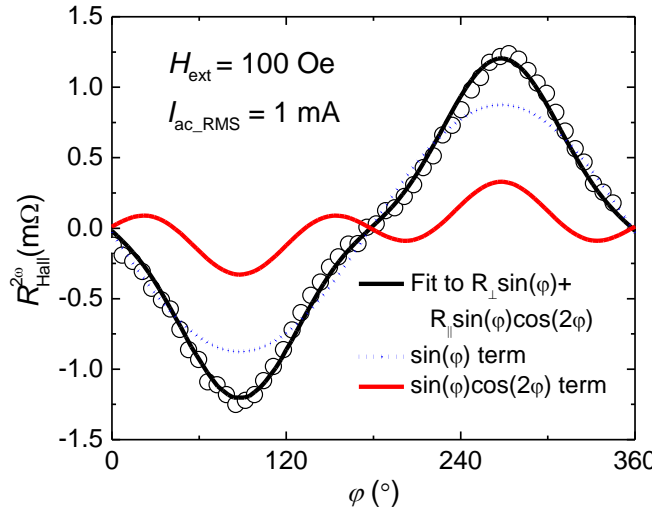


Figure 2-4 Second-harmonic Hall resistance as a function of φ with an external magnetic field 100 Oe applied in the MoS₂/CoFeB bilayer. The black solid curve is fitted curve using $R_{\perp} \sin \varphi +$

$R_{\parallel} \cos 2\varphi \sin \varphi$, where the first and second term are plotted in blue dotted and red solid curves, respectively. Reprinted with permission from [55], Copyright (2016) American Chemical Society

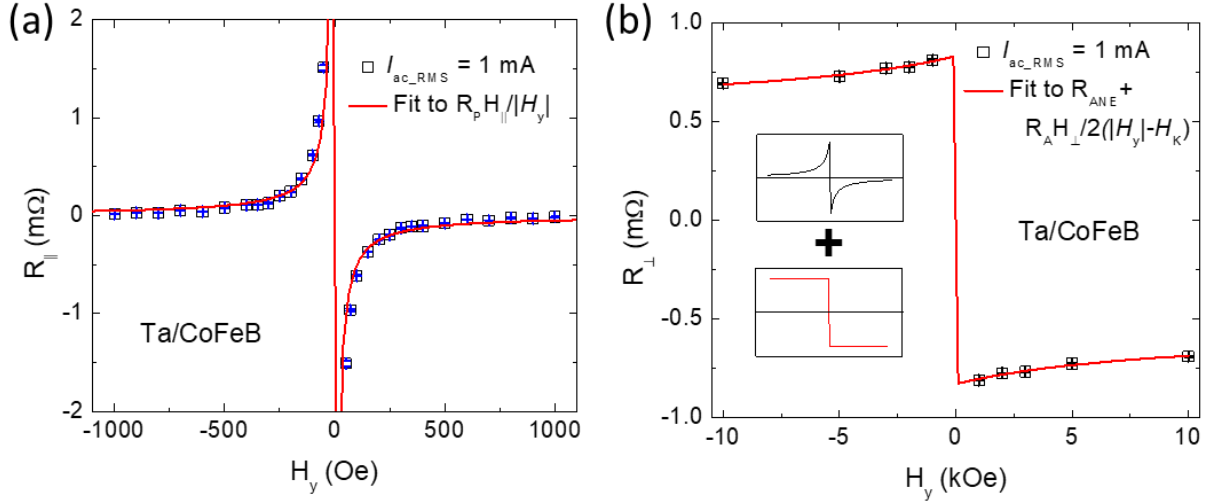


Figure 2-5 Determination of field-like torque and damping-like torque in the Ta/CoFeB bilayer. (a) The extracted R_{\parallel} as a function of the external magnetic field along the $\pm y$ direction in the Ta/CoFeB. The red solid curve is fitted curve using $R_P \frac{H_{\parallel}}{|H_y|}$, where the (field-like) in-plane spin-orbit field H_{\parallel} is determined to be 0.21 Oe. (b) The extracted R_{\perp} as a function of an external magnetic field along the $\pm y$ direction for Ta/CoFeB. The red solid curves are fitted curves using $\frac{R_A}{2} \frac{H_{\perp}}{|H_y| - H_K} + R_{ANE}$, where the (damping-like) out-of-plane spin-orbit field H_{\perp} are determined to 0.50 Oe for the Ta/CoFeB. In the inset of (b), field dependencies of damping-like torque term ($\frac{R_A}{2} \frac{H_{\perp}}{|H_y| - H_K}$) and anomalous Nernst Effect term (R_{ANE}) term are plotted on the top and bottom, respectively. Reprinted with permission from [55], Copyright (2016) American Chemical Society

If there is additional mirror symmetry breaking with respect to the yz plane, additional torques besides $\mathbf{m} \times (\mathbf{m} \times \boldsymbol{\sigma})$ and $\mathbf{m} \times \boldsymbol{\sigma}$ are allowed (see Appendix D for detailed discussion on symmetry analysis of current-induced spin torques):

$$\tau_{\parallel}(\varphi, E) = E(S_0 + S_2 \sin \varphi + S_4 \cos 2\varphi + S_6 \sin 3\varphi + \dots)$$

$$\tau_{\perp}(\varphi, E) = E(A_0 + A_2 \sin \varphi + A_4 \cos 2\varphi + A_6 \sin 3\varphi + \dots)$$

Therefore, if we find additional $\cos 2\varphi$ dependence, it suggests an additional damping-like torque with effective spin polarization pointing out-of-plane (along z direction). If we find additional offset in the $R_{\text{Hall}}^{2\omega}$ that depends on the current magnitude, it suggests an additional field-like torque with effective field pointing out-of-plane (along z direction) [42].

After we obtain the SOT effective field (like damping-like SOT field H_{DL}), we calculate ξ_{DL} using

$$\xi_{\text{DL}} = \frac{2eM_s t_{\text{FM}} H_{\text{DL}}}{\hbar J_c} \text{ [33]},$$

where e is the electron charge, \hbar is the reduced Planck constant, t_{FM} is the ferromagnetic layer thickness, and J_c is the applied current density. Let's give an example and

calculate this equation in SI units. If $t_{\text{FM}} = 1\text{nm}$, $M_s = 0.64\text{MA/m}$, $B_{\text{DL}} = \mu_0 H_{\text{DL}} = 0.1\text{T}$, $e \approx$

$$1.6 \times 10^{-19}\text{C}, \quad \hbar \approx 1.055 \times 10^{-34}\text{J} \cdot \text{s}, \quad J_c = 10^{12}\text{A/m}^2, \quad \text{we have } \xi_{\text{DL}} = \frac{J_s}{J_c} = \frac{2eM_s t_{\text{FM}} B_{\text{DL}}}{\hbar J_c} \approx$$

0.194.

Normally, in addition to SOT effects, we also have thermoelectric contribution in the $R_{\text{Hall}}^{2\omega}$. As an

example, we consider Si/SiO₂/Ta/CoFeB/TaO_x, where Ta is a heavy metal with a large ξ_{DL} and

CoFeB is a ferromagnetic metal. In addition to the field-dependent second-harmonic anomalous

Hall resistance in the Ta/CoFeB device, there is a step function in the measured second-harmonic

Hall resistance (Figure 2-5b); the second-harmonic Hall resistance changes sign as we change the

magnetization direction, while the magnitude does not change with that of the external magnetic

field. This is attributed to the anomalous Nernst effect, a thermoelectric effect [53]. There is a

vertical thermal gradient that originates from the asymmetric heat conduction in the vertical

direction. The top layer above the Ta/CoFeB is the TaO_x(3nm)/Air (<20 Torr), which has a very

low thermal conductivity (<0.025 W/mK). In contrast, the substrate below the Ta/CoFeB is the

SiO₂, which has a relatively large thermal conductivity (~1.4 W/mK). So, the positive thermal

gradient direction is the +z direction. The thermo-voltage is given by $\mathbf{V}_{\text{ANE}} \propto \nabla T \times \mathbf{m}$, which also gives rise to a $\sin \varphi$ angle dependence of second-harmonic Hall voltage response. So, we can only differentiate the thermo-voltage and the SOT-induced second-harmonic anomalous Hall resistance by the field dependence. Note that due to a large effective anisotropy field ($H_K \approx -1$ T), even if there is a damping-like spin-orbit field, the field dependence of R_{\perp} will not be as clear as the field dependence of R_{\parallel} , which is diverging at the zero field.

Also, for PMA systems, we have another popular second-harmonic method to quantify the SOT. We first apply a large +z direction magnetic field to align the magnetic moments along +z direction, and the anomalous Hall resistance is given by $R_{\text{AHE}}(t) = R_A \cos \theta$. When we apply a small magnetic field along the $\pm y$ direction, the magnetization will be slightly tilted by a tilting angle θ due to the current-induced longitudinal spin-orbit field ΔH_L . The ΔH_L is along the $\pm y$ direction, and it is a damping-like field. Here, we define the +y direction is the positive direction of longitudinal spin-orbit fields for a positive current (along the +y direction). The tilting angle is given by $\theta(I) = \frac{H_y + \Delta H_L \sin \omega t}{H_k}$, where H_y is the external magnetic field along the y direction and H_k is the effective magnetic anisotropy field along the z direction (a constant depending only on the magnetic property of Ta/CoFeB/MgO). So, the Hall resistance is given by $V(t) =$

$$R_{\text{AHE}}(t) \sqrt{2} I_{\text{RMS}} \sin(\omega t) = \sqrt{2} I_{\text{RMS}} R_A \cos \theta \sin(\omega t) \approx \sqrt{2} I_{\text{RMS}} R_A \left(1 - \frac{\theta^2}{2}\right) \sin(\omega t) =$$

$$\sqrt{2} I_{\text{RMS}} R_A \left(1 - \frac{H_y^2 + 2H_y \Delta H_L \sin \omega t}{2H_k^2}\right) \sin(\omega t) = V^0 + \sqrt{2} I_{\text{RMS}} R_A \left(1 - \frac{H_y^2}{2H_k^2}\right) \sin(\omega t) -$$

$$\sqrt{2} I_{\text{RMS}} R_A \frac{H_y \Delta H_L}{2H_k^2} \cos 2\omega t. \text{ So, } V^{1\omega} = I_{\text{RMS}} R_A \left(1 - \frac{H_y^2}{2H_k^2}\right) \text{ and } V^{2\omega} = I_{\text{RMS}} R_A \frac{H_y \Delta H_L}{2H_k^2} \text{ (imaginary}$$

part). Here, the planar Hall resistance (PHR) is assumed to be much smaller than the anomalous

Hall resistance (AHR). To calculate the current-induced longitudinal (damping-like) spin-orbit field, we just use the formula:

$$\Delta H_L = -2 \frac{\partial V^{2\omega} / \partial H_y}{\partial^2 V^{1\omega} / \partial^2 H_y}$$

Similarly, to measure the current-induced transverse (field-like) spin-orbit field, we apply the magnetic field along the $\pm x$ direction. The formula is

$$\Delta H_T = -2 \frac{\partial V^{2\omega} / \partial H_x}{\partial^2 V^{1\omega} / \partial^2 H_x}$$

These equations are the same as Eq. (1) in Ref. [51].

If the PHR is comparable or larger than the AHR, we need to consider the PHE. If one defines the ratio $\delta = \frac{R_P}{R_A}$, the damping-like and field-like effective SOT fields are described by [54]

$$\Delta H_{L,adjusted} = \frac{\Delta H_L \pm 2\delta \Delta H_T}{1 - 4\delta^2}$$

$$\Delta H_{T,adjusted} = \frac{\Delta H_T \pm 2\delta \Delta H_L}{1 - 4\delta^2}$$

where the \pm sign corresponds to magnetization pointing along the $\pm z$ direction. When the δ is small, these equations are the same as the previous two.

In addition to the SOT effects, there is also thermoelectric contribution in this measurement scheme. When the field is applied along the $\pm y$ direction, there is also quasi-linear contribution in longitudinal $R_{AHE}^{2\omega}$ (ΔH_L) from the ANE in the heavy metal/ferromagnetic metal and spin Seebeck effect (SSE) in the heavy metal/magnetic insulator cases. The SSE contribution can be very large and thus these two equations can be inapplicable. Luckily, in some special cases, δ is very large

and thus $\Delta H_{L,adjusted}$ is mainly determined by the transverse $R_{AHE}^{2\omega}$ (ΔH_T) [50]. We have determined the SOT in the Pt/TmIG layer [56] and we can see that longitudinal field sweeping is completely dominated by the SSE.

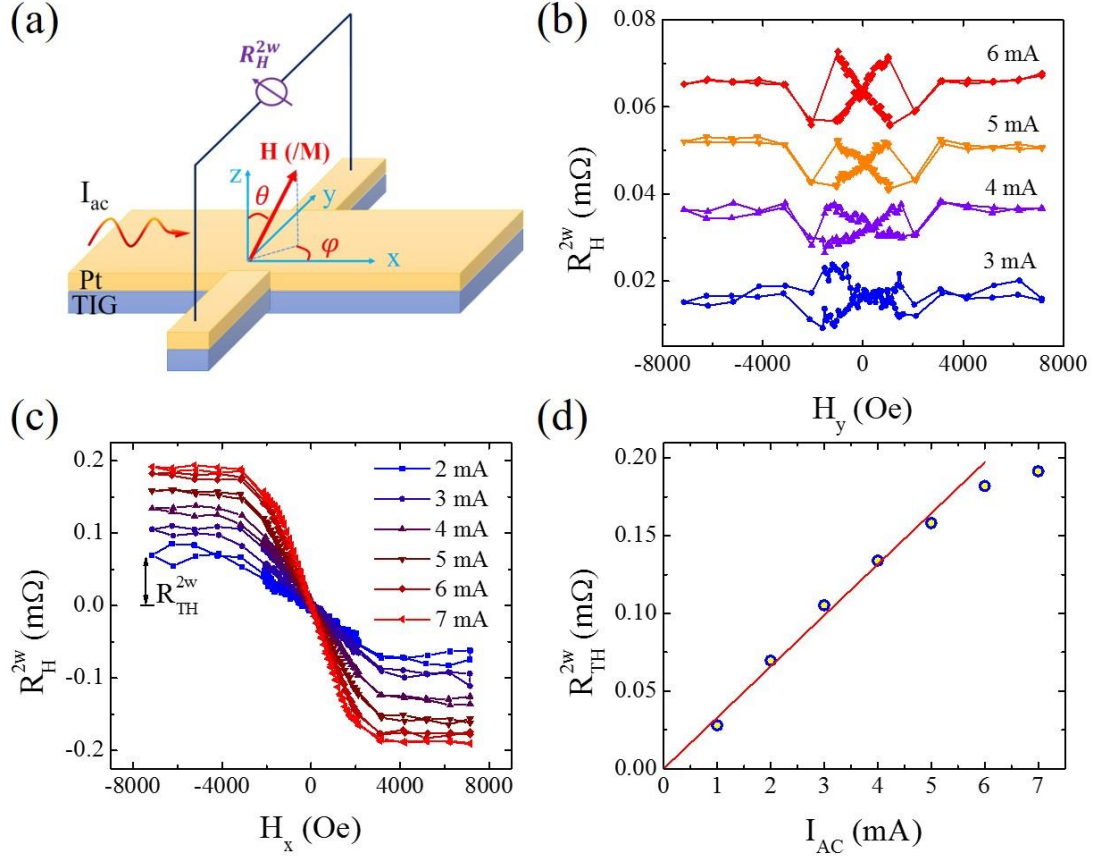


Figure 2-6 Field-dependent harmonic Hall signal in TmIG(6.4 nm)/Pt(5 nm) bilayer. (a) Schematic illustration of measurement geometry for field-dependent harmonic Hall measurement; (b) (c) Typical second harmonic Hall resistance as a function of in-plane transverse magnetic field H_y . (c) Prototypical second harmonic Hall resistance as a function of in-plane longitudinal magnetic field H_x . The arrow indicates the second harmonic Hall resistance from thermal effect R_{TH}^{2w} . (d) Current dependence of R_{TH}^{2w} , the red line is linear fitting curve. Reprinted with permission from [56], Copyright (2017) American Physical Society

In conclusion, we see that the second-harmonic Hall method is a very versatile, which can be used for many situations. One needs to choose the appropriate version to accurately determine the SOT.

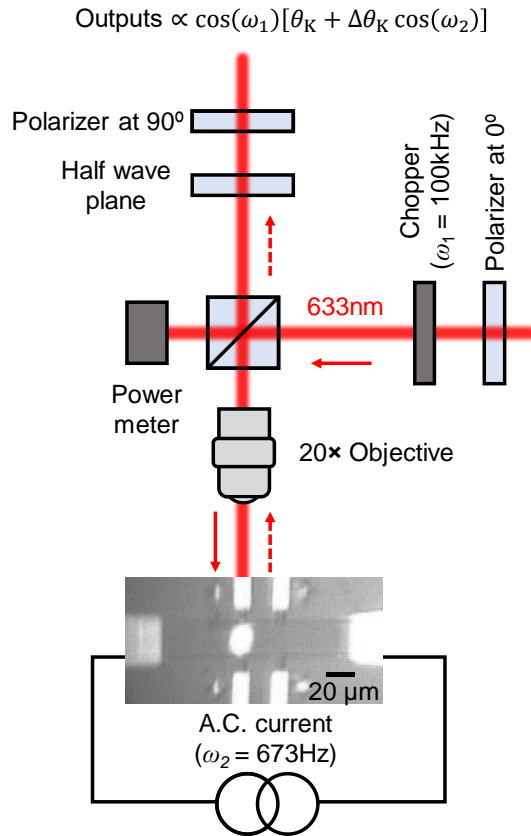


Figure 2-7 MOKE setup and the optical image of the device with laser spot on it. Since the current and MOKE laser are modulated at different frequencies, the $\Delta\theta_K$ is free of any thermal contributions

2.2 Differential MOKE

The differential MOKE is utilizing magneto-optical Kerr effect. The polar Kerr rotation is directly proportional to the m_z . To my knowledge, this method was first discussed in [57] and later

expanded in [58]. Since there is no thermal contribution in MOKE measurements, it is a direct measurement of the B_{DL} . The differential Kerr ($\Delta\theta_K$) is given by [58]

$$\Delta\theta_K = \theta_{\parallel} \frac{B_{FL}}{|B_{ext}|} \cos 2\varphi_P + \theta_{\perp} \frac{B_{DL}}{|B_{ext}| - B_K}, \quad (2-5)$$

where φ_P is the angle between the current and the polarization of the laser, θ_{\perp} and θ_{\parallel} are the first- and second-order MO coefficients that parameterize the strength of the coupling of the light to the out-of-plane (OOP) and the in-plane (IP) magnetization. Figure 2-7 shows the measurement schematic and device image during the measurement.

2.3 Spin torque ferromagnetic resonance

The effect of spin-transfer torque on ferromagnetic resonance in magnetic spin valves and tunnel junctions have been studied for a long time. In 2007-2008, two group reported spin-transfer torque measurements using ferromagnetic resonance in MTJs [59, 60]. Later, in 2011, L. Liu et al. used spin-torque ferromagnetic resonance (ST-FMR) to characterize the SOT in heavy metal/ferromagnetic metal bilayers [31]. Here, we discuss the principle of ST-FMR using the W/CoFeB and W/Cu/CoFeB bilayers, where W is a heavy metal with a large ξ_{DL} .

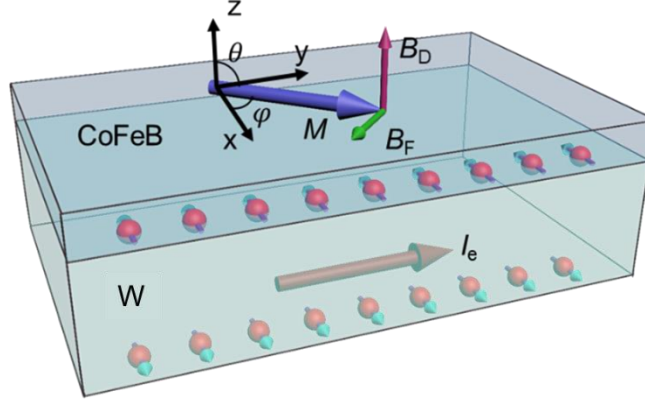


Figure 2-8 Schematic of current-induced SOTs in a W/CoFeB bilayer.

2.3.1 Principle of ST-FMR

The LLG equations with out-of-plane torques and in-plane torques are written as

$$\frac{d\mathbf{m}}{dt} = -\gamma\mathbf{m} \times (\mathbf{B} - H_k m_z \hat{z}) + \alpha\mathbf{m} \times \frac{d\mathbf{m}}{dt} + \boldsymbol{\tau}_{\parallel} + \boldsymbol{\tau}_{\perp},$$

where \mathbf{B} is the external field, H_k is the effective anisotropy field, γ is gyromagnetic ratio and α is the Gilbert damping. Note that $H_k = H_{\perp} - 4\pi M_S$, where H_{\perp} is the uniaxial perpendicular magnetic anisotropy field and M_S is the saturation magnetization. Now, let's derive the ferromagnetic resonance voltage signals in a heavy metal/ferromagnetic metal bilayer in the presence of out-of-plane and in-plane torques. To simplify the calculation, we assume the magnetization along the +y direction because the external field is along the +y direction (Figure 2-8). The magnetization can be written as $\mathbf{m} = (m_x e^{i\omega t}, m_y, m_z e^{i\omega t})$, where ω is the ferromagnetic resonance frequency. Assuming a small precession cone angle, it is approximately $\mathbf{m} = (m_x e^{i\omega t}, 1, m_z e^{i\omega t})$. We first analyze the effect of out-of-plane torque:

$$i\omega m_z = -\gamma m_x B - i\omega \alpha m_x + \gamma \tau_{\perp},$$

$$i\omega m_x = \gamma(m_z B + H_k m_z) + i\omega \alpha m_z,$$

where we can get m_z from the first equation: $m_z = \frac{-m_x(\gamma B + i\omega \alpha) + \gamma \tau_{\perp}}{i\omega}$. Then we replace m_z in the second equation with this expression and get:

$$i\omega m_x = m_z[\gamma(B + H_k) + i\omega \alpha] = \frac{-m_x(\gamma B + i\omega \alpha) + \gamma \tau_{\perp}}{i\omega} [\gamma(B + H_k) + i\omega \alpha]$$

$$\Rightarrow -\omega^2 m_x = [-m_x(\gamma B + i\omega \alpha) + \gamma \tau_{\perp}][\gamma(B + H_k) + i\omega \alpha]$$

$$\Rightarrow m_x[\gamma(B + H_k)(\gamma B + i\omega \alpha) + i\omega \alpha(\gamma B + i\omega \alpha) - \omega^2] = \gamma \tau_{\perp}[\gamma(B + H_k) + i\omega \alpha]$$

$$\Rightarrow \approx m_x[\gamma^2 B(B + H_k) + i\omega \alpha \gamma(2B + H_k) - \omega^2] = \gamma \tau_{\perp}[\gamma(B + H_k) + i\omega \alpha]$$

$$\Rightarrow m_x = \frac{\gamma \tau_{\perp}[\gamma(B + H_k) + i\omega \alpha]}{\gamma^2 B(B + H_k) + i\omega \alpha \gamma(2B + H_k) - \omega^2}$$

We define $\omega_0 = \gamma \sqrt{B(B + H_k)}$ and $\Delta = \alpha \gamma(2B + H_k)$. Therefore,

$$m_x = \frac{\gamma \tau_{\perp}[\gamma(B + H_k) + i\omega \alpha]}{\omega_0^2 + i\Delta \omega - \omega^2}$$

$$\Rightarrow m_x = \frac{\tau_{\perp}[\gamma^2(B + H_k) + i\omega \alpha \gamma][\omega_0^2 - \omega^2 - i\Delta \omega]}{(\omega_0^2 - \omega^2)^2 + \Delta^2 \omega^2}$$

$$\Rightarrow \text{Re} m_x \approx \frac{\tau_{\perp} \gamma^2 (B + H_k) (\omega_0^2 - \omega^2)}{(\omega_0^2 - \omega^2)^2 + \Delta^2 \omega^2} = \gamma \frac{\tau_{\perp}}{\Delta} \frac{\Delta \omega (\omega_0^2 - \omega^2) \frac{B + H_k}{\sqrt{B(B + H_k)}}}{(\omega_0^2 - \omega^2)^2 + \Delta^2 \omega^2} = \gamma \frac{\tau_{\perp}}{\Delta} \sqrt{1 + \frac{H_k}{B}} \frac{\Delta \omega (\omega_0^2 - \omega^2)}{(\omega_0^2 - \omega^2)^2 + \Delta^2 \omega^2}.$$

So, the effect of this out-of-plane torque is to produce an antisymmetric Lorentzian shape. Also, we get the Kittel formula at the same time by understanding ω_0 .

Similarly, we analyze the effect of in-plane torque:

$$i\omega m_z = -\gamma m_x B - i\omega\alpha m_x,$$

$$i\omega m_x = \gamma(m_z B + H_k m_z) + i\omega\alpha m_z + \gamma\tau_{\parallel},$$

where we can get m_z from the first equation: $m_z = \frac{-m_x(\gamma B + i\omega\alpha)}{i\omega}$. Then we replace m_z in the second equation by using this expression and get:

$$i\omega m_x = m_z[\gamma(B + H_k) + i\omega\alpha] + \gamma\tau_{\parallel} = \frac{-m_x(\gamma B + i\omega\alpha)}{i\omega}[\gamma(B + H_k) + i\omega\alpha] + \gamma\tau_{\parallel}$$

$$\Rightarrow -\omega^2 m_x = [-m_x(\gamma B + i\omega\alpha)][\gamma(B + H_k) + i\omega\alpha] + i\omega\gamma\tau_{\parallel}$$

$$\Rightarrow m_x\{[(\gamma B + i\omega\alpha)][\gamma(B + H_k) + i\omega\alpha] - \omega^2\} = i\omega\gamma\tau_{\parallel}$$

$$\Rightarrow m_x = \frac{i\omega\gamma\tau_{\parallel}}{[(\gamma B + i\omega\alpha)][\gamma(B + H_k) + i\omega\alpha] - \omega^2} \approx \frac{i\omega\gamma\tau_{\parallel}}{\gamma^2 B(B + H_k) + i\omega\alpha\gamma(2B + H_k) - \omega^2}$$

$$\Rightarrow m_x = \frac{i\omega\gamma\tau_{\parallel}}{\omega_0^2 + i\Delta\omega - \omega^2} = \frac{i\omega\gamma\tau_{\parallel}[\omega_0^2 - \omega^2 - i\Delta\omega]}{(\omega_0^2 - \omega^2)^2 + \Delta^2\omega^2}$$

$$\Rightarrow \text{Re}m_x = \gamma \frac{\tau_{\parallel}}{\Delta} \frac{\Delta^2\omega^2}{(\omega_0^2 - \omega^2)^2 + \Delta^2\omega^2}$$

So, the effect of the in-plane torque is to produce a symmetric Lorentzian shape. The overall ST-FMR voltage should be proportional to the product of derivative of resistance (with respect to the azimuthal angle) and this $\text{Re}m_x$:

$$V_{\text{mix}} \propto \frac{dR}{d\varphi} \left[\gamma \frac{\tau_{\perp}}{\Delta} \sqrt{1 + \frac{H_k}{B}} \frac{\Delta\omega(\omega_0^2 - \omega^2)}{(\omega_0^2 - \omega^2)^2 + \Delta^2\omega^2} + \gamma \frac{\tau_{\parallel}}{\Delta} \frac{\Delta^2\omega^2}{(\omega_0^2 - \omega^2)^2 + \Delta^2\omega^2} \right]. \quad (2-6)$$

This is because if the derivative of resistance with respect to the azimuthal angle is zero, the induced magnetization oscillation cannot generate a resistance change and thus the ST-FMR

voltage signals would be zero. Normally, ST-FMR utilizes anisotropic magnetoresistance (AMR) and the derivative of resistance is given by

$$\frac{dR}{d\varphi} = \frac{-d(R_0 \cos 2\varphi)}{d\varphi} = 2R_1 \sin 2\varphi,$$

where R_1 is the maximum resistance due to AMR effect. In typically heavy metal/ferromagnet bilayers with only inversion symmetry breaking, the torques are proportional to $\sin \varphi$, the overall ST-FMR voltage is $V_{\text{mix}} \propto \sin 2\varphi \sin \varphi$. If there is additional mirror symmetry breaking with respect to the yz plane (see Appendix D for detailed discussion on symmetry analysis of current-induced spin torques), additional torques are allowed:

$$\tau_{\parallel}(\varphi, E) = E(S_0 + S_2 \sin \varphi + S_4 \cos 2\varphi + S_6 \sin 3\varphi + \dots)$$

$$\tau_{\perp}(\varphi, E) = E(A_0 + A_2 \sin \varphi + A_4 \cos 2\varphi + A_6 \sin 3\varphi + \dots)$$

Therefore, if we find additional $\sin 2\varphi$ dependence in the antisymmetric peak, it suggests an additional field-like torque with effective field pointing out-of-plane (along z direction). If we find additional $\sin 2\varphi$ dependence in the symmetric peak, it suggests an additional damping-like torque with effective spin polarization pointing out-of-plane (along z direction) [42].

2.3.2 Damping and anisotropy from ST-FMR

The schematic diagram of the ST-FMR measurement setup is shown in Figure 2-9a. An I_{rf} with a power of 4 dBm was applied in the device. The rectified voltage was detected by using a lock-in amplifier. An in-plane magnetic field with a fixed angle θ_{H} of 45° was swept between -0.5 T and $+0.5$ T. Figure 2-9b shows the ST-FMR spectra for the as-grown sample with 1.1 nm thick CoFeB

layer. The results can be well fitted to a Lorentzian function consisting of symmetric and antisymmetric Lorentzian components[61],

$$V_{mix} = S \frac{\Delta^2}{\Delta^2 + (H_{ext} - H_0)} + A \frac{\Delta(H_{ext} - H_0)}{\Delta^2 + (H_{ext} - H_0)}, \quad (2-7)$$

where Δ is the linewidth (full width at half maximum), H_0 is the resonant magnetic field, S is the symmetric Lorentzian coefficient, which is proportional to the oscillating spin current $J_{s,rf}$ and A is the antisymmetric Lorentzian coefficient, which is proportional to the Oersted field H_{rf} generated by the I_{rf} . The inset in Figure 2-9b shows the spectrum of 6 GHz for both positive and negative magnetic fields. Figure 2-9c shows the resonance frequency f as a function of the resonant field H_0 for different thickness. The results are fitted to the Kittel equation[61-63],

$$f = (\gamma/2\pi)[\mu_0 H_0(\mu_0 H_0 + 4\pi M_{eff})]^{1/2}, \quad (2-8)$$

where γ is the gyromagnetic ratio. The extracted effective magnetization fields $4\pi M_{eff}$ are shown in Figure 2-9d. The $4\pi M_{eff}$ decreases dramatically from 1.282 ± 0.006 T to 0.010 ± 0.003 T as the thickness of CoFeB layer reduces from 3 nm to 0.8 nm. The decreasing $4\pi M_{eff}$ reflects the gradual increasing contribution of the interfacial anisotropy with decreasing thickness, as expected from the formula $4\pi M_{eff} = 4\pi M_s - 2K_i/M_s t_{CoFeB}$.

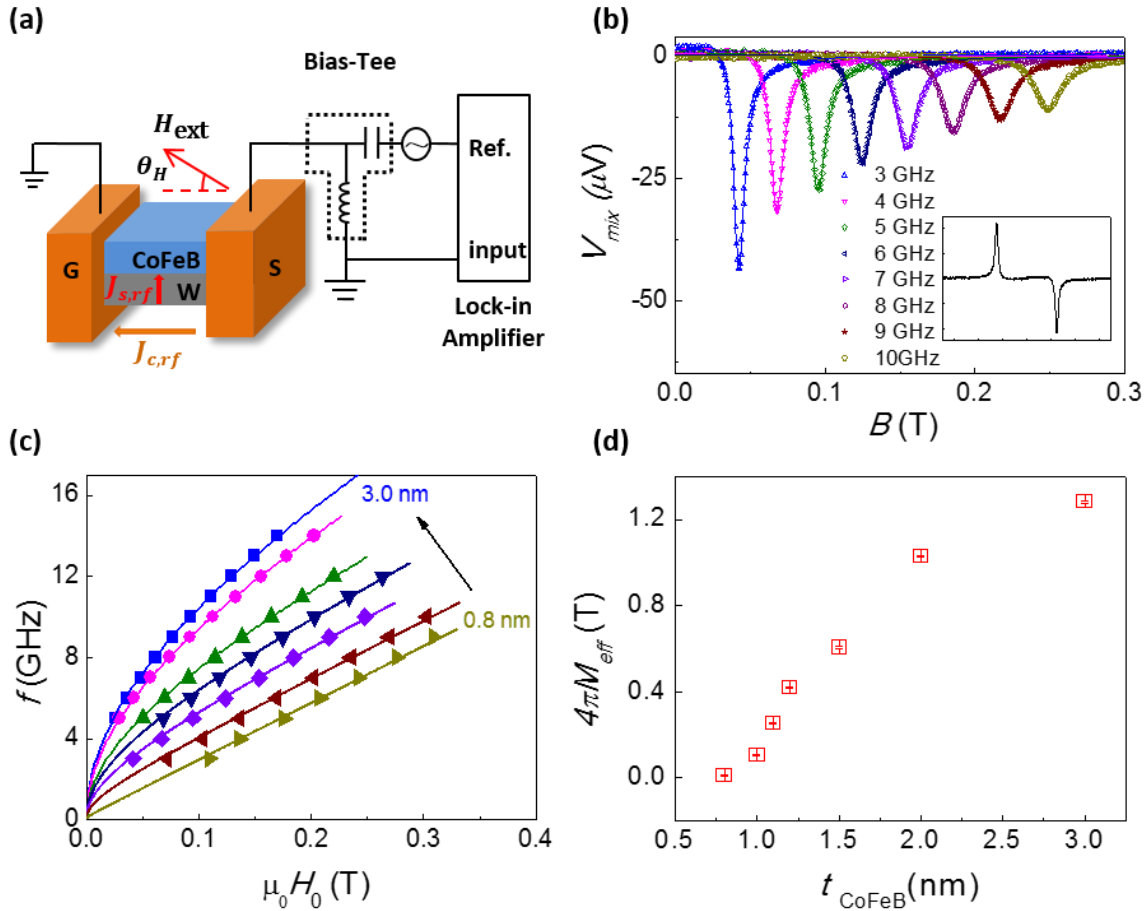


Figure 2-9 ST-FMR of W/CoFeB. (a) Schematic diagram of the setup for ST-FMR measurements. The $J_{c,rf}$ indicates the charge current (orange arrow) and the $J_{s,rf}$ indicates the spin current (yellow arrow). H_{ext} is the applied external magnetic field. θ_H is the angle between H_{ext} and device channel. (b) The ST-FMR spectra for sample with $t_{CoFeB} = 1.1$ nm. The solid curves are the fits to a sum of symmetric and antisymmetric Lorentzian functions. The inset shows the spectrum of 6 GHz for both positive and negative magnetic fields. (c) Resonance frequency f as a function of the resonant field H_0 for W(5)/CoFeB(t)/MgO devices with thickness of 0.8, 1.0, 1.1, 1.2, 1.5, 2.0, and 3.0 nm. The solid curves are fitting of the Kittel formula. (d) The effective magnetization field $4\pi M_{eff}$ for W(5)/CoFeB(t)/MgO were determined by the Kittel equation fitting as a function of CoFeB thickness. Reprinted with permission from [64], Copyright (2016) AIP Publishing

We have also studied the magnetic damping based on the frequency dependence of resonance linewidth, as shown in Figure 2-10a. The resonance linewidth usually includes intrinsic and extrinsic origins, which is given by [62, 63]:

$$\Delta = \Delta_0 + (2\pi\alpha/\gamma)f.$$

The Δ_0 is the extrinsic contribution (*e.g.*, inhomogeneous broadening) to the linewidth, which is usually independent of frequency. The second term is the intrinsic contribution (*e.g.*, Gilbert damping), which is linearly proportional to frequency. The α values for studied samples are obtained by fitting the data, as shown in Figure 2-10b. The α value increases from 0.0097 ± 0.0001 to 0.0400 ± 0.0005 when the thickness decreased from 3.0 nm to 1.0 nm. The thickness dependence of α was attributed to two-magnon scattering[65, 66] and spin pumping effect[66-68]. The α values in our structure are comparable to the results in W/CoFeB bilayer structure reported by Pai et al.[63], but a little larger than that reported in Ta/CoFeB/MgO[69], which is likely due to different interfacial morphology and different spin mixing conductance in spin pumping[66, 68]. The inset of Figure 2-10a shows the results for the sample with 0.8 nm CoFeB layer, which cannot be fitted linearly. This nonlinearity probably comes from the fact that the 0.8 nm thick CoFeB film becomes discontinuous and the magnetization is not saturated in the film plane, *i.e.*, there is a distribution of magnetization angles in the film relative to the applied field direction [70].

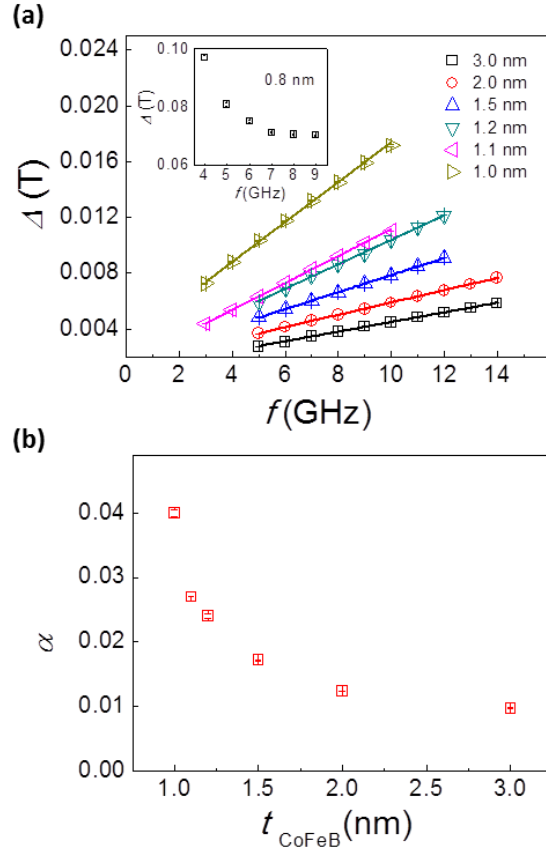


Figure 2-10 Extraction of damping factor from ST-FMR. (a) The linewidth Δ extracted from the fitting of ST-FMR signal versus the resonance frequency f for different CoFeB thicknesses. The solid lines are the linear fitting. The inset is the linewidth Δ versus resonance frequency f for the sample with 0.8 nm CoFeB layer, which cannot be linearly fitted. (b) The Gilbert damping constant α as a function of CoFeB thickness. Reprinted with permission from [64], Copyright (2016) AIP Publishing

We next show the results for the samples, which were annealed at 250 °C for 0.5 hr in a vacuum environment. After annealing, the samples of $t_{\text{CoFeB}} \geq 1.2$ nm show an in-plane magnetic anisotropy and the samples ($t_{\text{CoFeB}} = 1.0$ and 1.1 nm) show a perpendicular magnetic anisotropy, which were determined by anomalous Hall measurement (not shown here). For the samples with in-plane magnetic anisotropy, the spectra are similar to the as-grown samples. However, the spectra of the

perpendicularly magnetized samples are significantly different from those of the in-plane samples, where additional peaks are observed, as shown in Figure 2-11a. Therefore, the resonance frequency dependence on the resonant field exhibits an additional low field branch, which cannot be simply fitted by the Kittel equation. The emergence of this additional branch in the perpendicularly magnetized samples is because the magnetization is not aligned with external magnetic field as the fields are below the alignment field (H_a^{FMR}). For $H_0 < H_a^{FMR}$, the left branch can be described by the following equation,

$$f = (\gamma/2\pi)[(\mu_0 H_k)^2 - (\mu_0 H_0)^2]^{1/2} \quad (0 < H_0 < H_k), \quad (2-9)$$

which was derived from the previous work. Here, $\mu_0 H_k = \mu_0 H_\perp - 4\pi M_S = -4\pi M_{eff}$. For $H > H_a^{FMR}$, the \mathbf{M} is tilted to in-plane by the external field, and the ST-FMR signal, in this case, is similar with that in the sample with in-plane anisotropy. The fits to the resonant field using Eqs. (2-8) and (2-9) are shown in Figure 2-11b. The $4\pi M_{eff}$ for both as-grown and annealed samples are shown in Figure 2-11c. For thicker CoFeB film, the values of $4\pi M_{eff}$ are a little bit smaller than before annealing, revealing interfacial PMA becomes stronger after annealing. For thinner CoFeB layer, the sign of $4\pi M_{eff}$ changes, indicating that the anisotropy field of the system changes from in-plane to out-of-plane.

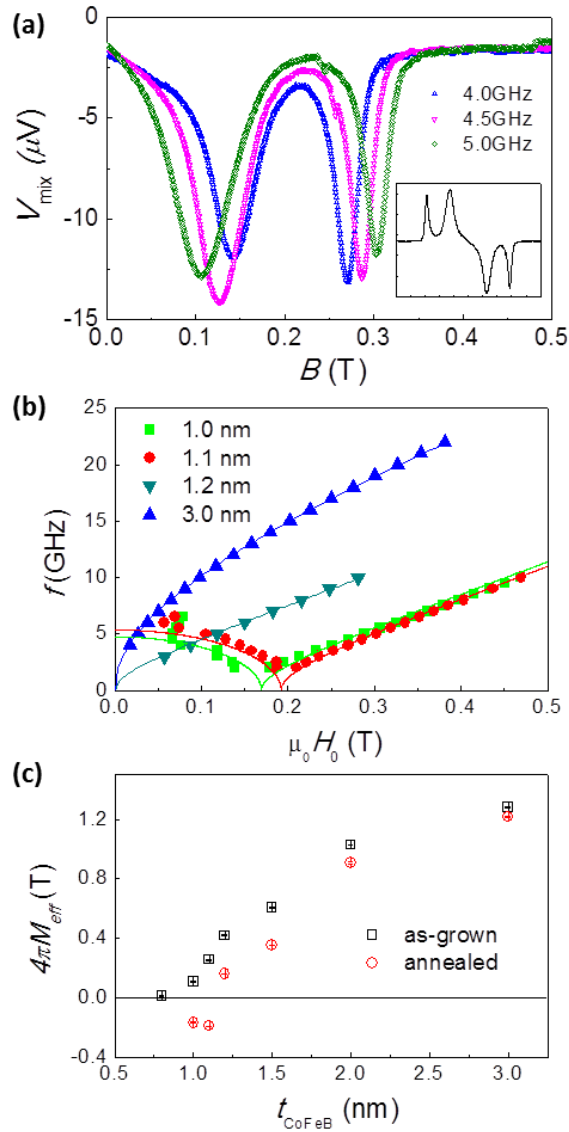


Figure 2-11 Extraction of resonant field from ST-FMR. (a) The ST-FMR spectra for the annealed sample with 1.1 nm CoFeB layer under the frequency of 4.0, 4.5, and 5.0 GHz. The inset shows the spectrum of 4.5 GHz for both positive and negative magnetic fields. (b) Resonance frequency f versus the resonant field H_0 for W(5)/CoFeB(t)/MgO devices after 250 °C annealing. The solid curves are fitting curves. (c) The effective magnetization field $4\pi M_{\text{eff}}$ for both as-grown and annealed samples. Reprinted with permission from [64], Copyright (2016) AIP Publishing

2.3.3 SOT efficiency in heavy metal/ferromagnet bilayer

In addition to the damping and anisotropy, we can also use ST-FMR in W/CoFeB to quantify the damping-like spin-orbit torque efficiency (or charge-to-spin conversion efficiency) ξ_{DL} , which is given by $\xi_{DL} = \frac{J_{s,rf}}{J_{c,rf}}$. While both S and A are related to many parameters, the dimensionless ratio

S/A is only related to the τ_{\parallel} and τ_{\perp} :

$$\frac{S}{A} = \frac{\tau_{\parallel}}{\tau_{\perp} \sqrt{1 + \frac{B_k}{B}}}$$

Here, the τ_{\parallel} is in-plane damping-like torque ($\tau_{\parallel} = \frac{\hbar J_{s,rf}}{2e\mu_0 M_s t_{CoFeB}}$), where t_{CoFeB} is the ferromagnet layer thickness. The τ_{\perp} is the out-of-plane field-like torque. In the case where there is no current-induced field-like spin-orbit torque, the τ_{\perp} is only related to current-induced Oersted field. In the simple bilayer structure, like W/CoFeB, $\tau_{\perp} = \frac{J_{c,rf} d_W}{2}$. Therefore, the S/A can be written as

$$\begin{aligned} \frac{S}{A} &= \frac{\frac{\hbar J_{s,rf}}{2e\mu_0 M_s t_{CoFeB}}}{\frac{J_{c,rf} d_W}{2} \sqrt{1 + \frac{B_k}{B}}} = \frac{J_{s,rf}}{J_{c,rf}} \frac{\hbar}{e\mu_0 M_s t_{CoFeB} d_W \sqrt{1 + \frac{B_k}{B}}} \\ \Rightarrow \xi_{DL} &= \frac{J_{s,rf}}{J_{c,rf}} = \frac{S}{A} \frac{e\mu_0 M_s t_{CoFeB} d_W}{\hbar} \sqrt{1 + \frac{B_k}{B}}. \quad (2-10) \end{aligned}$$

Let's give use data from ref.[31] as an example and calculate this equation in SI units. If $\frac{S}{A} = 0.63$,

$t_{CoFeB} = 4nm$, $d_W = 6nm$, $M_s = 0.64MA/m$, $B_k = 0.8T$, $B = 0.08T$, $e \approx 1.6 \times 10^{-19}C$,

$\mu_0 = 4\pi \times 10^{-7}H/m$, $\hbar \approx 1.055 \times 10^{-34}J \cdot s$, we have $\xi_{DL} = \frac{J_{s,rf}}{J_{c,rf}} \approx 0.06$.

2.3.4 SOT efficiency in heavy metal/spacer/ferromagnet trilayer

In most of cases, in the symmetric peak, there is spin pumping (+ inverse spin Hall effect) contribution in addition to the damping-like SOT contribution. In the antisymmetric peak, there is field-like SOT contribution in addition to the Oersted field torque contribution. As shown in ref. [71], the spin pumping contribution can be very significant. Here, we follow the basic idea of this paper and show how spin pumping affects the ξ_{DL} determination.

$$V_{ST-FMR}^{Sym} = \frac{1}{4} \frac{dR}{d\varphi} \frac{\gamma I_c}{2\pi\Delta(df/dH)_{H=H_{res}}} \left(\frac{\hbar \xi_{DL} J_{c,W}}{2e\mu_0 M_s t_{CoFeB}} \right) = \frac{1}{4} \frac{dR}{d\varphi} \frac{\gamma J_{c,W} W d_W \left(1 + \frac{\sigma_{CoFeB} t_{CoFeB}}{\sigma_W d_W} \right)}{2\pi\Delta(df/dH)_{H=H_{res}}} \left(\frac{\hbar \xi_{DL} J_{c,W}}{2e\mu_0 M_s t_{CoFeB}} \right)$$

$$V_{SP} = \frac{L\xi_{DL}\lambda_W \tanh(d_W/2\lambda_W)}{\sigma_W d_W + \sigma_{CoFeB} t_{CoFeB}} J_s^{SP} = \frac{L\xi_{DL}\lambda_W \tanh(d_W/2\lambda_W)}{\sigma_W d_W + \sigma_{CoFeB} t_{CoFeB}} e f g_{eff} P \left(\frac{\gamma H_{rf}}{2\alpha\omega} \right)^2 =$$

$$\frac{L\xi_{DL}\lambda_W \tanh(d_W/2\lambda_W)}{\sigma_W d_W + \sigma_{CoFeB} t_{CoFeB}} e \frac{\omega}{2\pi} g_{eff} P \left(\frac{H_{rf}}{\Delta} \right)^2 = \frac{L\xi_{DL}\lambda_W \tanh(d_W/2\lambda_W)}{\sigma_W d_W + \sigma_{CoFeB} t_{CoFeB}} e \frac{\omega}{2\pi} g_{eff} P \left(\frac{J_{c,W} d_W}{2\Delta} \right)^2$$

Note that $\sin \frac{H_{rf}}{\Delta}$ is the effective cone angle excited by the current-induced Oersted field (assuming no inhomogeneous linewidth). When it is small, it is approximately $\frac{H_{rf}}{\Delta}$. Importantly, the J_s^{SP} also depends on the azimuthal angle of the external field φ . The cone angle is proportional to $\sin \varphi$ since the out-of-plane torque due to H_{rf} follows $\sin \varphi$. The factor P originates from the ellipticity of magnetization precession [72]. Therefore, the magnitude of J_s^{SP} should be proportional to $\sin^2 \varphi$. Since the longitudinal voltage (along y direction) is generated by the inverse spin Hall effect $\vec{J}_c = \xi_{DL} \vec{J}_s^{SP} \times \vec{\sigma}$, where the spin polarization $\vec{\sigma}$ of the pumped spin current is along the external field (magnetization direction). As a result, the V_{SP} has an additional $\cos \varphi$. Overall, $V_{SP} \propto \cos \varphi \sin^2 \varphi \propto \sin \varphi \sin 2\varphi$, which has the same relation as the symmetric peak.

Therefore,

$$\frac{V_{SP}}{V_{ST-FMR}^{Sym}} = \frac{\frac{L\xi_{DL}\lambda_W \tanh(d_W/2\lambda_W)}{\sigma_W d_W + \sigma_{CoFeB} t_{CoFeB}} e^{\frac{\omega}{2\pi}} g_{eff} P\left(\frac{J_{c,W} d_W}{2\Delta}\right)^2}{\frac{1}{2} R_1 \frac{\gamma J_{c,W} d_W \left(1 + \frac{\sigma_{CoFeB} t_{CoFeB}}{\sigma_W d_W}\right)}{2\pi \Delta (df/dH)_{H=H_{res}}} \left(\frac{\hbar \xi_{DL} J_{c,W}}{2e\mu_0 M_s t_{CoFeB}}\right)} =$$

$$\frac{L\lambda_W \tanh(d_W/2\lambda_W) e^2 \mu_0 M_s \omega g_{eff} (df/dH)_{H=H_{res}} d_W^2 t_{CoFeB} \sigma_W}{R_0 \gamma W \hbar \Delta (\sigma_W d_W + \sigma_{CoFeB} t_{CoFeB})^2}$$

$$f = (\gamma/2\pi) [H_0(H_0 + H_k)]^{\frac{1}{2}} \Rightarrow \left(\frac{df}{dH}\right)_{H_0=H_{res}} = \frac{\gamma}{4\pi} \frac{2H_{res} + H_k}{[H_{res}(H_{res} + H_k)]^{\frac{1}{2}}}$$

$$\frac{V_{SP}}{V_{ST-FMR}^{Sym}} = \frac{L\lambda_W \tanh(d_W/2\lambda_W) e^2 \mu_0 M_s f g_{eff} d_W^2 t_{CoFeB} \sigma_W}{2R_1 W \hbar \Delta (\sigma_W d_W + \sigma_{CoFeB} t_{CoFeB})^2} \frac{2H_{res} + H_k}{[H_{res}(H_{res} + H_k)]^{\frac{1}{2}}}$$

Let's give use data from ref. [71] as an example and calculate this equation in SI units. If $H_{res} = 1 \text{ kOe}$, $H_k = 10 \text{ kOe}$, $t_{CoFeB} = 4 \text{ nm}$, $d_W = 6 \text{ nm}$, $M_s = 0.64 \text{ MA/m}$, $\lambda_W = 1 \text{ nm}$, $L/W=1$, $R_1 = 1 \Omega$, $f = 8 \text{ GHz}$, $e \approx 1.6 \times 10^{-19} \text{ C}$, $\mu_0 = 4\pi \times 10^{-7} \text{ H/m}$, $\hbar \approx 1.055 \times 10^{-34} \text{ J} \cdot \text{s}$, $\sigma_{CoFeB} = \sigma_W = 2 \times 10^6 \Omega^{-1} \cdot \text{m}^{-1}$, $\Delta = 500e = 50 \times \frac{10^3}{4\pi} \text{ A/m}$, $g_{eff} = 4 \times 10^{18} \text{ m}^{-2}$, $\frac{V_{SP}}{V_{ST-FMR}^{Sym}} = 2 \times 10^{-3}$.

In ref. [71], the authors defined a coefficient to quantify the contribution of V_{ST-FMR}^{Sym} in total symmetric peak,

$$\eta = \frac{V_{ST-FMR}^{Sym}}{V_{ST-FMR}^{Sym} + V_{SP}} = \frac{1}{1 + \frac{V_{SP}}{V_{ST-FMR}^{Sym}}}$$

For this case, $\eta \cong 1$. So, the spin pumping contribution is negligible, and the symmetric peak is dominated by the damping-like torque ferromagnetic resonance.

If $H_{res} = 1.8 \text{ kOe}$, $H_k = 13 \text{ kOe}$, $t_{CoFeB} = 3 \text{ nm}$, $d_W = 5 \text{ nm}$, $M_s = 1 \text{ MA/m}$, $\lambda_W = 1 \text{ nm}$, $L/W=1$, $R_1 = 0.85 \Omega$, $f = 8 \text{ GHz}$, $e \approx 1.6 \times 10^{-19} \text{ C}$, $\mu_0 = 4\pi \times 10^{-7} \text{ H/m}$, $\hbar \approx 1.055 \times$

$$10^{-34} J \cdot s, \sigma_W = 6 \times 10^5 \Omega^{-1} \cdot m^{-1}, \sigma_{CoFeB} = 5 \times 10^5 \Omega^{-1} \cdot m^{-1}, \Delta = 400e = 40 \times \frac{10^3}{4\pi} A/m,$$

$$g_{eff} = 10^{19} m^{-2}, \frac{V_{SP}}{V_{ST-FMR}^{Sym}} \approx 0.03206. \text{ In this case, } \eta \approx 0.969.$$

Sometimes, to match the device resistance and avoid magnetic proximity effect between nonmagnetic material and ferromagnetic metal, one can insert a light metal with relatively high conductivity. For example, if we have a Cu insertion layer, then

$$\frac{S}{A} = \frac{\frac{\hbar J_{s,rf}}{2e\mu_0 M_s t_{CoFeB}}}{\frac{J_{c,rf}}{2} \left(d_W + \frac{\sigma_{Cu} t_{Cu}}{\sigma_W} \right) \sqrt{1 + \frac{B_k}{B}}} = \frac{J_{s,rf}}{J_{c,rf}} \frac{\hbar}{e\mu_0 M_s t_{CoFeB} \left(d_W + \frac{\sigma_{Cu} t_{Cu}}{\sigma_W} \right) \sqrt{1 + \frac{B_k}{B}}} \Rightarrow$$

$$\xi_{DL} = \frac{J_{s,rf}}{J_{c,rf}} = \frac{S}{A} \frac{e\mu_0 M_s t_{CoFeB}}{\hbar} \left(d_W + \frac{\sigma_{Cu} t_{Cu}}{\sigma_W} \right) \sqrt{1 + \frac{B_k}{B}}$$

$$V_{ST-FMR}^{Sym} = \frac{1}{4} \frac{dR}{d\phi} \frac{\gamma I_c}{2\pi \Delta (df/dH)_{H=H_{res}}} \left(\frac{\hbar \xi_{DL} J_{c,W}}{2e\mu_0 M_s t_{CoFeB}} \right) =$$

$$\frac{1}{4} \frac{dR}{d\phi} \frac{\gamma J_{c,W} W d_W \left(\frac{\sigma_W d_W + \sigma_{CoFeB} t_{CoFeB} + \sigma_{Cu} t_{Cu}}{\sigma_W d_W} \right)}{2\pi \Delta (df/dH)_{H=H_{res}}} \left(\frac{\hbar \xi_{DL} J_{c,W}}{2e\mu_0 M_s t_{CoFeB}} \right)$$

$$V_{SP} = \frac{L \xi_{DL} \lambda_W \tanh(d_W/2\lambda_W)}{\sigma_W d_W + \sigma_{CoFeB} t_{CoFeB} + \sigma_{Cu} t_{Cu}} J_S^{SP} = \frac{L \xi_{DL} \lambda_W \tanh(d_W/2\lambda_W)}{\sigma_W d_W + \sigma_{CoFeB} t_{CoFeB} + \sigma_{Cu} t_{Cu}} e f g_{eff} P \left(\frac{\gamma H_{rf}}{2\alpha\omega} \right)^2 =$$

$$\frac{L \xi_{DL} \lambda_W \tanh(d_W/2\lambda_W)}{\sigma_W d_W + \sigma_{CoFeB} t_{CoFeB} + \sigma_{Cu} t_{Cu}} e \frac{\omega}{2\pi} g_{eff} P \left(J_{c,W} \frac{\sigma_W d_W + \sigma_{Cu} t_{Cu}}{2\Delta \sigma_W} \right)^2$$

$$\frac{V_{SP}}{V_{ST-FMR}^{Sym}} = \frac{L \lambda_W \tanh(d_W/2\lambda_W) e^2 \mu_0 M_s f g_{eff} \sigma_W t_{CoFeB} \left(\frac{\sigma_W d_W + \sigma_{Cu} t_{Cu}}{\sigma_W} \right)^2}{2 R_{1,Cu} W \hbar \Delta (\sigma_W d_W + \sigma_{CoFeB} t_{CoFeB} + \sigma_{Cu} t_{Cu})^2} \frac{2 H_{res} + H_k}{[H_{res} (H_{res} + H_k)]^{\frac{1}{2}}}$$

So, it changes from $\frac{d_W^2 t_{CoFeB} \sigma_W}{R_{1,Cu} (\sigma_W d_W + \sigma_{CoFeB} t_{CoFeB})^2}$ to $\frac{t_{CoFeB} \sigma_W \left(\frac{\sigma_W d_W + \sigma_{Cu} t_{Cu}}{\sigma_W} \right)^2}{R_{1,Cu} (\sigma_W d_W + \sigma_{CoFeB} t_{CoFeB} + \sigma_{Cu} t_{Cu})^2}$ with a ratio

$$\left(\frac{\sigma_W d_W + \sigma_{Cu} t_{Cu}}{\sigma_W d_W} \right)^2 \left(\frac{\sigma_W d_W + \sigma_{CoFeB} t_{CoFeB}}{\sigma_W d_W + \sigma_{CoFeB} t_{CoFeB} + \sigma_{Cu} t_{Cu}} \right)^2 \frac{R_{1,Cu}}{R_{1,Cu}}.$$

If $t_{Cu} = 1.2nm$, $R_{1,Cu} = 0.2 \Omega$, $\sigma_{Cu} = 5 \times 10^6 \Omega^{-1} \cdot m^{-1}$, the ratio is around 6.109 and thus

$$\frac{V_{SP}}{V_{ST-FMR}^{Sym}} \approx 0.196 . \text{ In this case, } \eta \approx 0.836 .$$

2.4 Loop shift method

The loop shift method detects the effect of current-induced SOTs on the out-of-plane hysteresis loops and specifically the coercive field. The SOT can act as an effective field and shift the hysteresis loop towards positive or negative field (out-of-plane direction) depending on the current polarity. In heterostructures with lateral structure broken symmetry, the current can generate out-of-plane effective field, which naturally shifts the hysteresis loop [73]. In normal heterostructures with rotational symmetry, in-plane field is required to break symmetry and induce out-of-plane effective field and the principles of measurements are developed in refs. [74, 75].

In a heavy metal/ferromagnet (HM/FM) bilayer nanowire system with perpendicular magnetic anisotropy (PMA), the current-induced switching is achieved through domain nucleation and domain wall motion. If the initial magnetization is up, we consider the case of applying current along the +y direction in the absence of in-plane external magnetic field. The current generates damping-like torque with an effective field following $H_{DL} \propto \hat{m} \times (\vec{j} \times \hat{z}) = \hat{m} \times \hat{\sigma}$, where the induced spin polarization $\hat{\sigma}$ along the x direction. If a down domain is nucleated through the spin-orbit torque (SOT), in the presence of Dzyaloshinskii–Moriya interaction (DMI), the magnetization directions in the domain walls would be opposite in the up to down domain wall and down to up domain wall. Since from the left to right, the magnetizations follow clockwise rotation, and thus this domain wall has right-handed chirality. We then calculate the damping-like effective field to be opposite on the up to down and down to up domain walls and thus move the

down domain (Figure 2-12a). There is no switching. If we apply enough in-plane field to break the chirality and align the magnetizations in domain walls along the same directions. Then the damping-like effective field will be the same on the up to down and down to up domain walls and thus shrink/expand the down domain depending on the external field direction.

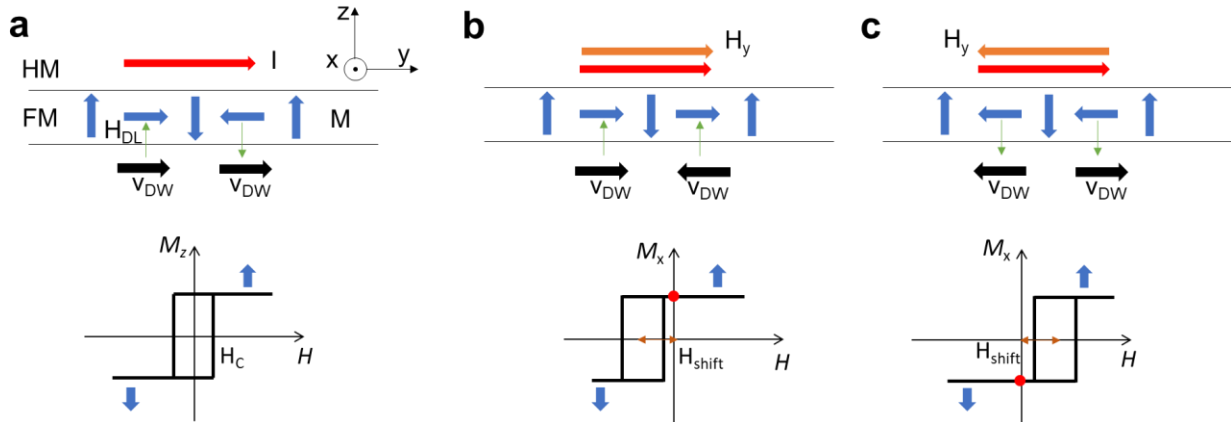


Figure 2-12 Current-induced asymmetric domain expansion and out-of-plane field hysteresis loop shift in a HM/FM bilayer. **a**, In the absence of the external field and the presence of DMI (assuming right-handed chirality), the magnetization direction in the domain wall is always pointing from up to down. Due to the current-induced damping-like spin-orbit torque (effective field, H_{DL}), the velocities of both up to down and down to up domain walls are along the same direction and there is no domain expansion. Therefore, the presence of current will not favor one particular magnetization direction and thus there is no shift of out-of-plane hysteresis loop. **b**, When the external field along the $+y$ direction is able to overcome the DMI effective field (H_{DMI}) and pull the magnetization in all domain walls along the $+y$ direction, the velocities of up to down and down to domain walls in the presence of current along the $+y$ direction are opposite and there is an up domain expansion. Therefore, the current along the $+y$ direction will favor up magnetization and thus shift the out-of-plane hysteresis towards the negative field. **c**, When the external field along the $-y$ direction is able to overcome the H_{DMI} , the current along the $+y$ direction will shift the out-of-plane hysteresis towards the positive field

As an example, we determine the damping-like SOT effective field in the W(5nm)/TmIG(3.2nm) bilayer. The measurement setup and results are shown in Figure 2-13. The obtained efficiency is around 4×10^{-3} , which is consistent with the result from the second harmonic method (see Session 4.3).

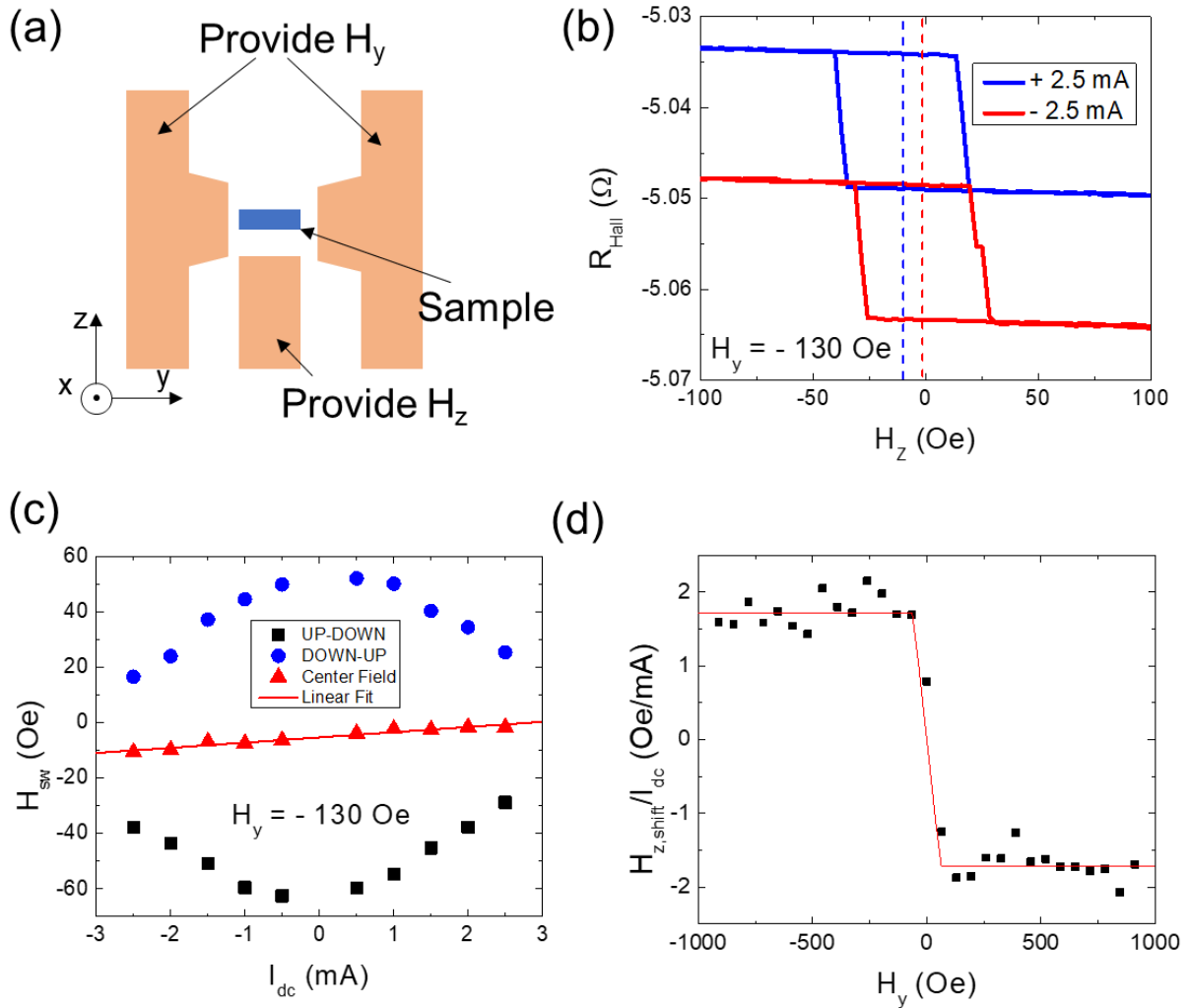


Figure 2-13 Determination of damping-like torque efficiency using the current-induced hysteresis loop shift method at room temperature. (a) Schematic of measurement setup. (b) Out-of-plane Hall hysteresis loops at $I_{\text{dc}} = +2.5 \text{ mA}$ and -2.5 mA with an in-plane external field $H_y = -130 \text{ Oe}$ applied. (c) Switching fields as a function of I_{dc} with $H_y = -130 \text{ Oe}$. (d) Out-of-plane hysteresis loop shift per mA as a function of the in-plane external magnetic field along the $\pm y$ direction

Chapter 3 Spin-orbit torques in various material systems

History and origins of spin-orbit torque have been extensively discussed in Chapter 1 of my master thesis. Here, we present several material systems that have not been discussed in the master thesis.

3.1 Heavy metal/ferromagnetic metal Pt/Co

ST-FMR [31] and second-harmonic method [55] are extensively used to characterize the SOT efficiency in various materials with strong spin-orbit coupling. However, their equivalence has rarely been established in one work. We use magnetron sputtering to prepare Pt(6nm)/Co(2.5nm)/Ta(1nm) on SiO₂ substrate and then measure the SOT efficiency using both ST-FMR (Figure 3-1) and second harmonic method (Figure 3-2). Here, 1 nm-thick Ta is for better adhesion, which does not contribute to the SOT much due to much higher resistivity of this 1 nm-thick Ta. ST-FMR results are shown in Fig. 1b and analyzed using Eq. (1) in Figure 3-1 to get S and A, which are attributed to damping-like SOT and Oersted field contributions, respectively. We use Eq. (2) in Figure 3-1 to determine the SOT efficiency [31] and obtain a value 0.039 ± 0.015 . Second harmonic method results are shown in Figure 3-2 and analyzed using Eq. (3) in Figure 3-2 to get damping-like SOT effective field H_D . We use Eq. (4) in Figure 3-2 to determine the SOT efficiency [55] and obtain a value 0.05, which is consistent with the value from ST-FMR.

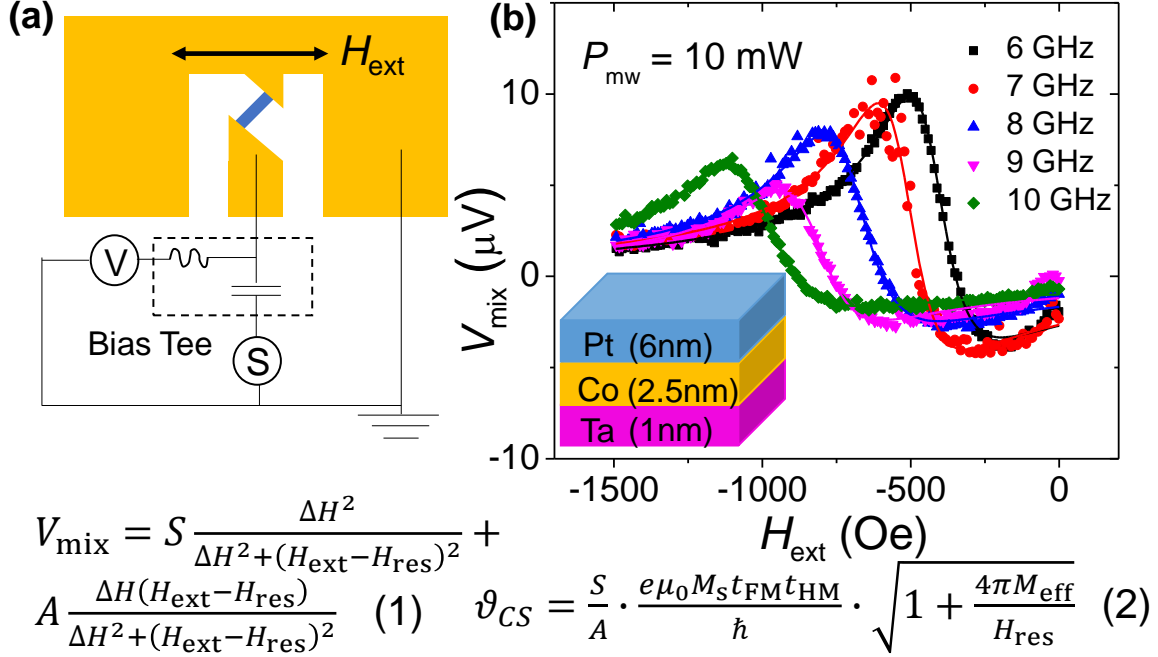


Figure 3-1 ST-FMR for Pt/Co. (a) Schematic of ST-FMR circuits. (b) ST-FMR signals at different frequencies for Pt/Co. Reprinted with permission from [34], Copyright (2018) IEEE

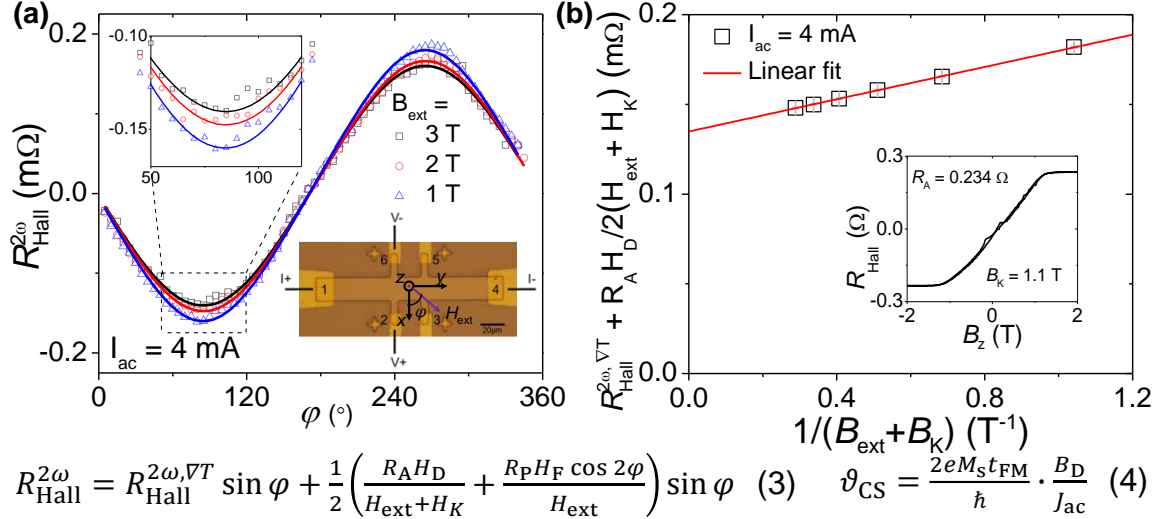


Figure 3-2 Second-harmonic method for Pt/Co. (a) $R_{\text{Hall}}^{2\omega}$ as a function of azimuthal angle φ at different external fields. Inset shows the optical image of a Hall bar device. (b) Sine component of $R_{\text{Hall}}^{2\omega}$ as a function of the inverse of summation of external field and effective anisotropy field. Inset shows the out-of-plane hysteresis loop for Pt/Co. Reprinted with permission from [34], Copyright (2018) IEEE

3.2 Monolayer TMD/CoFeB SOT

The efficient generation of spin current is crucial for improving the energy efficiency of spintronics. The spin current can be used to exert SOTs on a magnetic layer, enabling the manipulation and even switching of magnetization in an energy efficient way [76, 77]. In the past decade, heavy metals, such as Pt[31, 78] and Ta[33, 73, 79, 80], or bulk semiconductors, such as GaAs[81, 82] have been extensively studied due to the presence of a strong spin-orbit coupling, allowing the spin Hall effect or the Rashba-Edelstein effect (REE) to generate a spin accumulation. Compared with these three-dimensional materials, the conversion between spin and charge in two-dimensional materials, *i.e.*, van der Waals materials, has not been studied until recently [83].

Monolayer graphene has been extensively studied as a spin channel due to its weak spin-orbit coupling[84]. A modified graphene with an enhanced spin-orbit coupling strength or increased extrinsic spin-dependent scattering rates could give rise to a significant spin Hall effect. However, it requires specific treatments, such as hydrogen bonding[85] or Cu (Au) adatoms[86], which are hard to control. A giant SOT was demonstrated in heterostructures based on three-dimensional topological insulators, *i.e.*, the Bi₂Se₃ family, which are also van der Waals materials[20, 21, 32]. The colossal SOT originates from the topological surface states. However, a thickness larger than the hybridization length of two surface states, six quintuple layers (~ 6 nm), is needed for topological insulators[87]. So far, it remains elusive whether or not we can have a large spin torque from an ultrathin atomically monolayer film (< 1 nm). Monolayer transition metal dichalcogenides (TMDs), such as MX₂ (M = Mo, W, X = S, Se, Te), provide a unique platform for studying the generation of SOTs at the two-dimensional limit because monolayer TMDs have both strong spin-orbit coupling and inversion symmetry breaking[88-91]. Very recently, signatures of current-induced SOTs were found in the composite of monolayer MoS₂/ferromagnet bilayer[92], but the

SOTs have not been quantitatively characterized and the origin of the SOTs has not been interpreted.

In this Session, we report the observation of current-induced SOTs in MX_2/CoFeB bilayers, where the MX_2 is monolayer MoS_2 or WSe_2 . The monolayer MX_2 is grown by chemical vapor deposition (CVD) and has a size up to mm scale. Using a second-harmonic method, we succeeded in determining both field-like torque per unit moment (or in-plane spin-orbit effective field) and damping-like torque per unit moment (or out-of-plane spin-orbit effective field). The field-like torque is large in MX_2/CoFeB bilayers despite most of the current are going through the CoFeB layer. The damping-like torque is negligible within measurement uncertainty, which is consistent with the REE dominated SOT generation in the MX_2/CoFeB bilayers. Moreover, the current-induced in-plane spin conductivity due to the REE is almost independent of temperature.

3.2.1 Materials and methods

High-quality large-area monolayer MoS_2 and WSe_2 were grown on sapphire using CVD method, where the transition metal trioxides were vaporized and reacted with the S or Se vapor in a chamber under a controlled temperature and gas environment (see Appendix A) [93, 94]. The insets of Figure 3-3a and b are the optical images of MoS_2 and WSe_2 , which show the uniformity of the thin film sample. Raman spectra further confirm that the films are monolayers. The Raman spectrum of MoS_2 (Figure 3-3a) exhibits two characteristic bands: the in-plane phonon mode, E_{2g}^1 , centered near 385 cm^{-1} and the out-of-plane phonon mode, A_{1g} , centered near 405 cm^{-1} , with a peak frequency difference of 20 cm^{-1} , which is a clear signature of monolayer MoS_2 . Similarly, a high-intensity peak (E_{2g}^1) shows near 250 cm^{-1} for WSe_2 (Figure 3-3b), which indicates that the WSe_2 film is a monolayer as well. The sheet resistances of monolayer MoS_2 and WSe_2 are larger than

$10^6 \Omega/\text{sq}$ as shown in the current-voltage curve (Figure 3-3c). To study the current-induced SOTs on the magnetic moment, we deposited 3 nm CoFeB on top of the monolayer MoS₂ and WSe₂ using a magnetron sputtering system. The deposition rates were 0.03 nm/s for CoFeB in an argon pressure of 3 mTorr. The CoFeB layer was capped by TaO_x (~ 3 nm). For details of the deposition process and Raman characterization of MX₂/CoFeB bilayers after the deposition, see Appendix A. The MX₂/CoFeB bilayers were patterned into Hall bars (channel width is 20 μm) using standard photolithography as shown in Figure 3-3d. We used a second-harmonic analysis of both anomalous Hall resistance and planar Hall resistance ($R_{\text{Hall}}^{2\omega} = V_{\text{Hall}}^{2\omega}/I_{\text{ac_peak}} = R_{\text{AHE}}^{2\omega} + R_{\text{PHE}}^{2\omega}$) to determine the current-induced spin-orbit effective fields in the MX₂/CoFeB bilayers as in refs. [53, 95]. The applied a.c. current frequency is $\frac{\omega}{2\pi} = 35.85$ Hz. Since the magnitudes of second-harmonic signals are proportional to the a.c. current amplitude, here we only present the results using an a.c. current amplitude 1 mA (*r.m.s.* value).

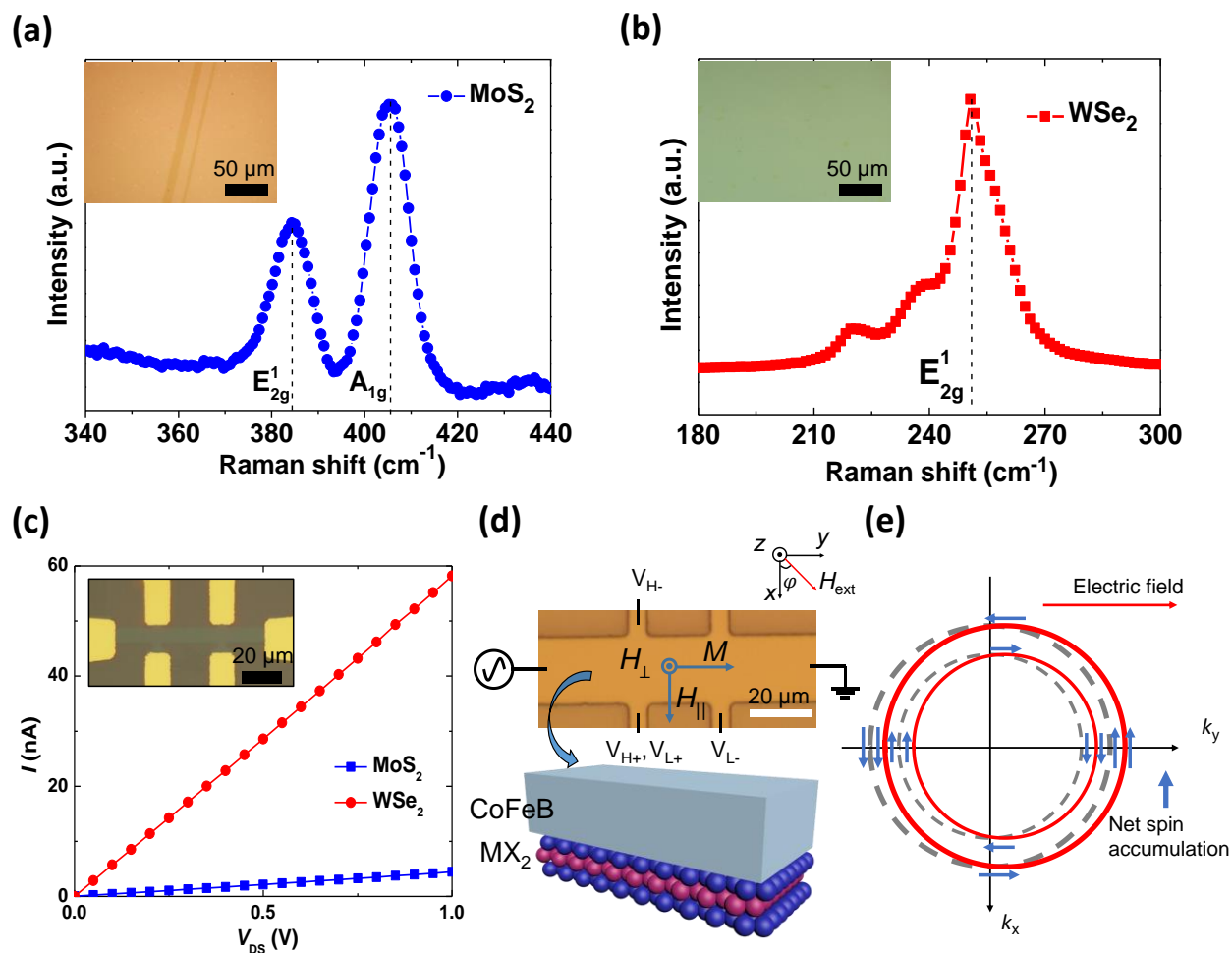


Figure 3-3 Materials characterization and measurement setup. Raman spectra of monolayer MoS₂ (a) and WSe₂ (b). The inset is a large scale optical image of monolayer MoS₂ (a) and WSe₂ (b) on sapphire. The scratches in (a) reveal the color contrast between the monolayer MoS₂ and the substrate. (c) Current-voltage characteristics of monolayer MoS₂ and WSe₂. The inset is an optical image of Hall bar structure used for the measurement. (d) Measurement setup of spin-orbit torque measurements for the MX₂/CoFeB bilayer. The MX₂ is a single layer, and the thickness of the CoFeB layer is 3 nm. (e) Illustration of induced spin accumulation by the Rashba-Edelstein effect at the interface of MX₂/CoFeB under an external electric field. The dashed gray circles are Rashba spin-split Fermi surfaces in the equilibrium, and the solid red circles are for under an applied electric field. The blue arrows represent the spin angular momenta. Reprinted with permission from [55], Copyright (2016) American Chemical Society

Table 3-1 Properties of the investigated films in this work. Adapted with permission from [55], Copyright (2016) American Chemical Society

Devices (nm)	Monolayer MoS₂/CoFeB (3)	Monolayer WSe₂/CoFeB (3)	CoFeB (3)	Ta (0.8)/CoFeB (3)
R_A (300K, Ω)	14.4	14.2	14.3	11.3
R_P (300K, Ω)	0.18	0.20	0.20	0.24
$-H_K$ (300K, T)	1.01	1.18	1.00	1.16
Sheet resistance (Ω /sq)	642	489	649	402
Effective sheet resistance of MX ₂ (k Ω /sq)	59.5	1.98		
Effective sheet resistance of CoFeB (k Ω /sq)			0.649	
Effective sheet resistance of Ta (k Ω /sq)				1.06
Resistivity of MX ₂ ($\mu\Omega\cdot\text{cm}$)	4760	159		
Resistivity of CoFeB ($\mu\Omega\cdot\text{cm}$)			195	
Resistivity of Ta ($\mu\Omega\cdot\text{cm}$)				84.5

We examine the magneto-transport properties of the MX₂/CoFeB bilayers using a physical properties measurement system at T = 300 K unless otherwise stated. In the following, we will first present the results for the MoS₂/CoFeB bilayer, and subsequently the WSe₂/CoFeB bilayer when we discuss the results. The MoS₂/CoFeB bilayer shows an in-plane easy plane, and the effective anisotropy field (H_K) is -1 T (see Figure 3-4a). Here, we define the PMA by a positive value of the anisotropy field. There is no easy axis in the film plane because the planar Hall resistance as a function of in-plane azimuthal angle (φ) in the presence of in-plane external magnetic field ($H_{\text{ext}} = 1000$ Oe) follows the $\sin 2\varphi$ relation well as shown in Figure 3-4b. The presence of monolayer MoS₂ layer does not affect the magnetic properties of the 3nm CoFeB layer

since the MoS₂/CoFeB bilayer has similar saturation anomalous Hall resistance (R_A), planar Hall resistance (R_P), and effective anisotropy field as the 3 nm CoFeB directly deposited on the SiO₂ (see Table 3-1).

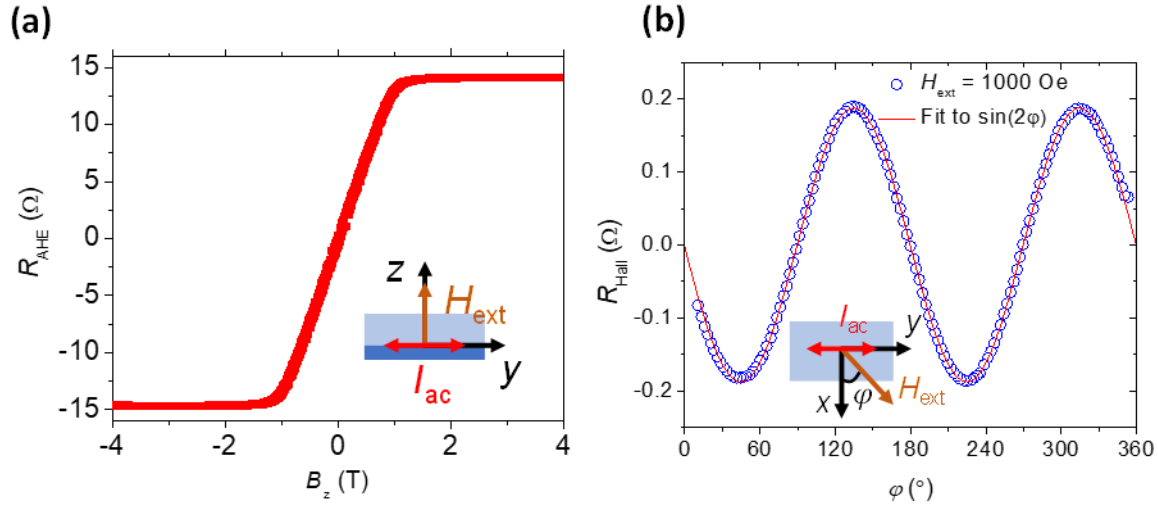


Figure 3-4 Transport magnetic properties in the MoS₂/CoFeB bilayer. (a) Anomalous Hall resistance as a function of out-of-plane magnetic field. (b) Hall resistance as a function of in-plane azimuthal angle (φ) with an external magnetic field 1000 Oe applied. (c) Second-harmonic Hall resistance as a function of φ with an external magnetic field 100 Oe applied. The black solid curve is fitted curve using $R_{\perp} \sin \varphi + R_{\parallel} \cos 2\varphi \sin \varphi$, where the first and second term are plotted in blue dotted and red solid curves, respectively. Reprinted with permission from [55], Copyright (2016) American Chemical Society

3.2.2 SOT from MoS₂/CoFeB

The idea of SOT measurement is described as following. When the injection charge current passes through the MoS₂/CoFeB bilayer, a net spin accumulation could develop in a direction transverse to the current direction in the film plane due to the inversion symmetry breaking and spin-orbit coupling in the monolayer MoS₂ and/or the MoS₂/CoFeB bilayer. In other words, the nonequilibrium spin accumulation $\sigma \propto \mathbf{z} \times \mathbf{j}$, where the mirror symmetry with respect to the xy

plane is broken, and \mathbf{j} is the current direction (along $\pm y$ direction). This current-induced spin polarization, in general, could give rise to two types of SOTs, the field-like torque ($\boldsymbol{\tau}_F = \mathbf{m} \times \boldsymbol{\sigma}$) and the damping-like torque ($\boldsymbol{\tau}_D = \mathbf{m} \times (\mathbf{m} \times \boldsymbol{\sigma})$). Therefore, the in-plane azimuthal angle dependence of $R_{\text{Hall}}^{2\omega}$ (Figure 2-4) can be divided into two major components depending on the symmetry of current-induced SOTs:

$$R_{\text{Hall}}^{2\omega} = R_{\parallel} \cos 2\varphi \sin \varphi + R_{\perp} \sin \varphi = R_P \frac{H_{\parallel}}{|H_{\text{ext}}|} \cos 2\varphi \sin \varphi + \frac{R_A}{2} \frac{H_{\perp}}{|H_{\text{ext}}| - H_K} \sin \varphi, \quad (3-1)$$

where the first term originates from the current-induced in-plane spin-orbit effective field (\mathbf{H}_{\parallel}) and the second term comes from the current-induced out-of-plane spin-orbit effective field (\mathbf{H}_{\perp}). The magnitudes of both in-plane and out-of-plane spin-orbit fields are proportional to the magnitude of current. When the current is along the $+y$ axis, the \mathbf{H}_{\parallel} is along the $-x$ axis and is independent with the magnetization. Therefore, the \mathbf{H}_{\parallel} gives rise to a field-like torque $\boldsymbol{\tau}_F = \mathbf{m} \times \mathbf{H}_{\parallel}$. This oscillating \mathbf{H}_{\parallel} induced by the a.c. current causes the magnetization to oscillate in the film plane, and thus gives rise to a $R_{\text{PHE}}^{2\omega} \propto \cos 2\varphi \sin \varphi$ since $\frac{dR_{\text{PHE}}}{d\varphi} \propto \cos 2\varphi$ and $H_{\parallel} \propto \sin \varphi$. As shown in Figure 2-4, $R_{\text{PHE}}^{2\omega}$ reaches minimum $-R_{\parallel}$ when the \mathbf{H}_{ext} is along the $+y$ direction, and maximum R_{\parallel} when the \mathbf{H}_{ext} is along the $-y$ direction. The field dependence of R_{\parallel} follows $1/|H_{\text{ext}}|$, which is consistent with the picture of an in-plane spin-orbit field; the larger the external field is, the smaller angle the current-induced field-like torque can induce. By fitting the field dependence of the extracted R_{\parallel} with $R_P \frac{H_{\parallel}}{|H_y|}$, where H_y is the magnetic field along the $\pm y$ direction, we obtain the magnitude of $H_{\parallel, \text{MoS}_2} / I_{\text{ac-peak}} \approx 0.13 \text{ Oe/mA}$ (Figure 3-5). To get a more intrinsic property for the SOT generation, we convert the H_{\parallel} into the effective spin conductivity (σ_{\parallel}) using $\sigma_{\parallel} = \frac{J_s}{\varepsilon} = \frac{H_{\parallel} M_s t_{\text{FM}}}{\varepsilon}$ [21], where $M_s t_{\text{FM}}$ is the saturation magnetization per unit area for the 3 nm CoFeB layer,

and \mathcal{E} is the applied electric field inside the MoS₂/CoFeB bilayer. We independently determine $M_s t_{\text{FM}} = 2.34$ mA using superconducting quantum interference device and $\mathcal{E} = 3.21 \times 10^4$ V/m for $I_{\text{ac_peak}} = 1$ mA. Therefore, the corresponding effective in-plane spin conductivities for MoS₂/CoFeB is $\sigma_{\parallel, \text{MoS}_2} \approx 2.88 \times 10^3 \hbar/2e$ ($\Omega^{-1} \text{m}^{-1}$). If we consider that the electronic conductivity of the monolayer MoS₂ is very low, the intrinsic ratio of generated spin current density over charge current density, or the so-called “spin torque ratio,” will be relatively high, and comparable with traditional heavy metals, such Pt and Ta (will be discussed below).

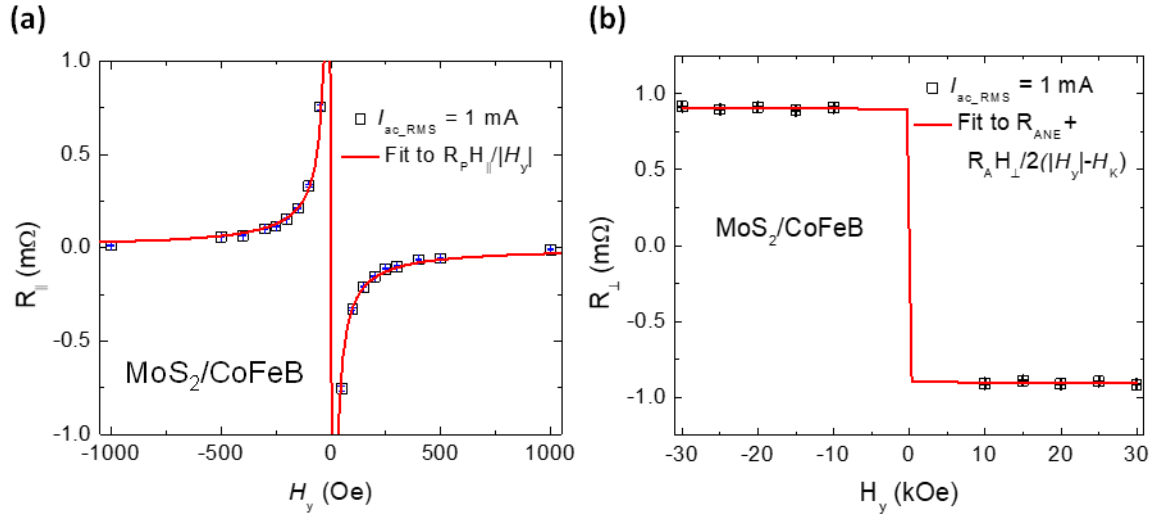


Figure 3-5 Determination of field-like and damping-like torque in the MoS₂/CoFeB bilayer. (a) The extracted R_{\parallel} as a function of the external magnetic field along the $\pm y$ direction. The red solid curve is fitted curve using $R_p \frac{H_{\parallel}}{|H_y|}$, where the (field-like) in-plane spin-orbit field H_{\parallel} is determined to be 0.18 Oe. (b) The extracted R_{\perp} as a function of an external magnetic field along the $\pm y$ direction. The red solid curves are fitted curves using $\frac{R_A}{2} \frac{H_{\perp}}{|H_y| - H_K} + R_{\text{ANE}}$, where the (damping-like) out-of-plane spin-orbit fields H_{\perp} is determined to be negligible for the MoS₂/CoFeB, respectively. Reprinted with permission from [55], Copyright (2016) American Chemical Society

The current-induced \mathbf{H}_\perp changes its direction when the direction of magnetization is reversed, and thus it gives rise to a damping-like torque $\boldsymbol{\tau}_D = \mathbf{m} \times \mathbf{H}_\perp$. The \mathbf{H}_\perp induced by the a.c. current causes the magnetization to oscillate out of the film plane and thus gives rise to a $R_{\text{AHE}}^{2\omega} \propto \sin \varphi$ since $\left. \frac{dR_{\text{AHE}}}{d\theta} \right|_{\theta=90^\circ} = R_A \left. \frac{d \cos \theta}{d\theta} \right|_{\theta=90^\circ} = R_A$ and $H_\perp \propto \mathbf{m} \times \boldsymbol{\sigma} \propto \sin \varphi$. The R_\perp decreases as the external magnetic field increases according to Eq. (1). As shown in Figure 2-5, we do see a distinct field dependence of the extracted R_\perp for the Ta(0.8 nm)/CoFeB bilayer (as the control sample), and the estimated $H_{\perp, \text{Ta}}/J_{\text{ac_peak}}$ is around 2.71 Oe per 10^{11} A/m². This value is consistent with the previously reported values on the ultrathin Ta film with the same thickness[51]. In addition to the field-dependent $R_{\text{AHE}}^{2\omega}$, there is an additional step function $R_{\text{Hall,VT}}^{2\omega}$ as illustrated in the inset of Fig. 3a; the $R_{\text{Hall,VT}}^{2\omega}$ changes sign as the magnetization direction reverses, while the magnitude does not vary with that of the external magnetic field. This step function is due to the anomalous Nernst effect (ANE), a thermoelectric effect [53]. Nevertheless, we can differentiate the thermovoltage ($V_{\text{Hall,VT}}^{2\omega}$) and the SOT-induced second-harmonic anomalous Hall resistance ($R_{\text{Hall}}^{2\omega}$) by their field dependencies. For the MoS₂/CoFeB bilayer, as shown in Figure 3-5b, within measurement uncertainty, we do not observe a clear trend that the R_\perp decreases as field increases. The observed negative $V_{\text{Hall}}^{2\omega}$ when the magnetization is along the +y direction is consistent with the ANE picture. When the magnetization reverses, the $V_{\text{Hall}}^{2\omega}$ becomes positive as expected from the ANE. So, the ANE dominates in the observed $V_{\text{Hall}}^{2\omega}$, and the damping-like torque or H_\perp is not observed within measurement uncertainty.

Here, we interpret that the REE is the mechanism for the observations of a large H_\parallel and a negligible H_\perp in the sapphire/MoS₂/CoFeB/TaO_x heterostructure (see Session 3.2.4 for details). The REE appears in the presence of a electric potential gradient and strong spin-orbit coupling,

i.e., typically at the interface between a material with strong spin-orbit coupling and a different material, such as the Bi/Ag interface[96]. In our MoS₂/CoFeB bilayer, the strong spin-orbit coupling and the broken vertical symmetry (together with the intrinsic inversion symmetry breaking in the monolayer MoS₂) could give rise to a large Rashba-type spin splitting[97]. The Rashba Hamiltonian can be expressed by $H_R = \alpha_R(\mathbf{k} \times \mathbf{z}) \cdot \boldsymbol{\sigma}$, where α_R is the Rashba coefficient, \mathbf{k} is the electron momentum, and $\boldsymbol{\sigma}$ is the spin Pauli matrices. As shown in Fig. 1e, at the equilibrium state, there is no net spin accumulation due to an equal number of electrons moving in two directions. Under an external electric field along the +y direction, the Rashba spin-split Fermi surfaces shift, causing a net spin accumulation along the -x direction, which is consistent with the direction of the observed in-plane spin-orbit field. Moreover, theoretical calculation shows that to the first order, the Rashba spin-splitting can only give rise to a field-like torque[98] or the Rashba effect gives a much larger field-like torque compared with the damping-like torque[99] as we observed in the MoS₂/CoFeB bilayer. If the spin Hall effect plays an important role in the MoS₂/CoFeB, we should have seen a sizeable damping-like torque like the Ta/CoFeB (see Table 3-2). However, we didn't observe any significant damping-like torque in the MoS₂/CoFeB. Regarding the charge-spin conversion efficiency, it has been shown that the inverse REE can convert the spin current into the charge current, and the efficiency is quantified as $\lambda_{\text{IREE}} = \alpha_R \tau_s / \hbar$ [96], where τ_s is the effective spin relaxation time and \hbar is the reduced Planck constant. Since the valley and spin are coupled in monolayer MoS₂, the relaxation time of spin polarization could be longer than 1 ns due to the considerable energy required for flipping the valley index[100]. So, the charge-spin conversion efficiency could be very high in the MoS₂/CoFeB bilayer.

From the harmonic measurement, we learn that the in-plane effective spin conductivity is $\sigma_{\parallel, \text{MoS}_2} \approx 2.88 \times 10^3 \hbar / 2e$ ($\Omega^{-1} \text{m}^{-1}$), even when most of the current does not flow through the

MoS₂ layer. The conductivity of MoS₂ in the MoS₂/CoFeB bilayer is around $\sigma_{\text{MoS}_2} \approx 2.1 \times 10^4 \text{ } (\Omega^{-1}\text{m}^{-1})$ (assuming that the thickness of monolayer MoS₂ with van der Waals gaps is 0.8 nm) and thus the spin torque ratio, *i.e.*, the ratio of spin current density over charge current density, is given by $\vartheta_{\parallel, \text{MoS}_2} = \frac{2e}{\hbar} \sigma_{\parallel, \text{MoS}_2} / \sigma_{\text{MoS}_2} \approx 0.14$. If we can find an intrinsic MoS₂ with a much higher resistivity ($>10^6 \text{ } \Omega/\text{sq}$), for example, by putting a monolayer MoS₂ on top of a magnetic insulator, and assume that the $\sigma_{\parallel, \text{MoS}_2}$ remains the same, an even larger spin torque ratio (>2.3) could be obtained. A recent experiment on the spin-charge conversion, the Onsager reciprocal process of the charge-spin conversion, in the Co/Al/MoS₂ heterostructure shows that the efficiency of the spin-charge conversion is very high, and the estimated λ_{IREE} can be as large as 4.3 nm, which corresponds to a spin torque ratio as large as 12.7 [101]. More recently, spin-torque ferromagnetic resonance in the MoS₂/Permalloy bilayer reveals a large symmetric Lorentzian peak compared with the antisymmetric Lorentzian peak[92], which could be ascribed to either a large damping-like torque or a highly efficient spin pumping-driven inverse REE. Combining the results given by the spin-torque ferromagnetic resonance measurement[92] and the present work, we can claim that the large symmetric Lorentzian peak is mainly due to the inverse REE induced by the spin pumping, rather than the damping-like torque generated by the rf current.

3.2.3 SOT from WSe₂/CoFeB

To see if other TMDs can produce such a large in-plane spin-orbit field, we carry out the SOT measurement on another TMD material, WSe₂. The extracted R_{\parallel} and R_{\perp} as a function of an external magnetic field along $\pm y$ direction are plotted in Figure 3-6a and b, respectively. Similar to the MoS₂/CoFeB bilayer, the in-plane spin-orbit field $H_{\parallel, \text{WSe}_2} / I_{\text{ac_peak}} \approx 0.19 \text{ Oe/mA}$, and we

do not observe the damping-like out-of-plane spin-orbit field within measurement uncertainty. Using the same conversion method, we determine the effective in-plane spin conductivity $\sigma_{\parallel, \text{WSe}_2} \approx 5.52 \times 10^3 \hbar/2e$ ($\Omega^{-1} \text{m}^{-1}$), which is larger than the $\sigma_{\parallel, \text{MoS}_2}$ and is consistent with the stronger spin-orbit coupling in the monolayer WSe_2 compared with the MoS_2 [90]. However, we should notice that although the monolayer MoS_2 and WSe_2 have very different conductivity (the monolayer MoS_2 has much higher resistivity than the monolayer WSe_2 in our study), they have similar spin conductivity. This result indicates that spin torques in these bilayers share the same origin, *i.e.*, REE[102].

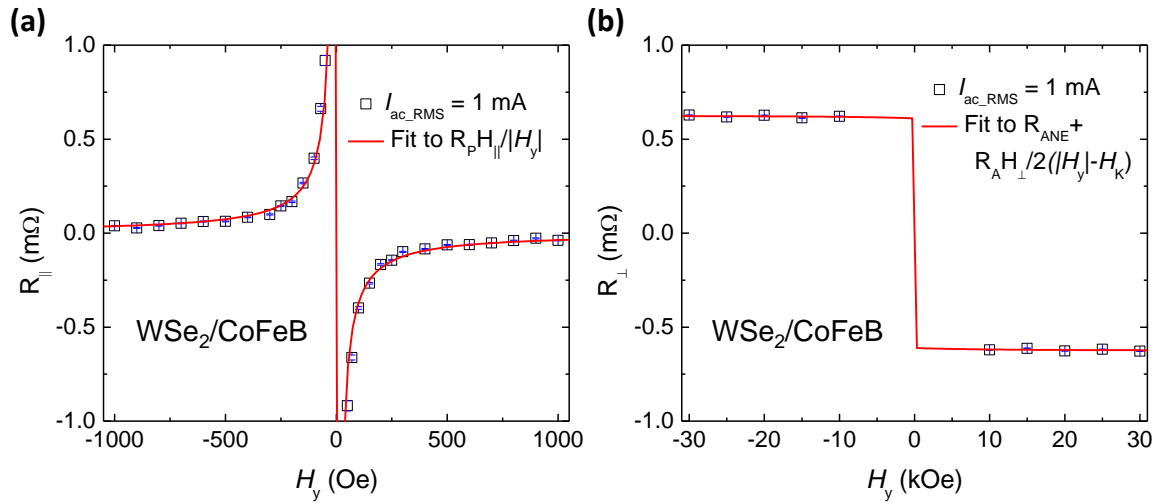


Figure 3-6 The extracted R_{\parallel} (a) and R_{\perp} (b) as a function of an external magnetic field along the $\pm y$ direction for the $\text{WSe}_2/\text{CoFeB}$ bilayer. Reprinted with permission from [55], Copyright (2016) American Chemical Society

Table 3-2. Current-induced spin-orbit fields in all the devices. Adapted with permission from [55], Copyright (2016) American Chemical Society

Devices (nm)	MoS ₂ /CoFeB (3)	WSe ₂ /CoFeB (3)	Ta (0.8)/CoFeB (3)
In-plane (field-like) spin-orbit field, H_{\parallel} (Oe/mA)	0.13	0.19	0.15
Out-of-plane (damping-like) spin-orbit field, H_{\perp} (Oe/mA)	~ 0	~ 0	0.35

We also study the temperature dependence of the current-induced in-plane spin conductivity. We do not identify the damping-like torque within the investigated temperature range. We observed that the current-induced in-plane spin conductivity is almost temperature independent (slightly increases as the temperature decreases) as shown in Figure 3-7, which is similar to the report on the inverse REE in the Ag/Bi interface[103]. A possible explanation for the temperature-independent charge-spin conversion due to REE is the temperature-insensitive strength of Rashba spin-splitting and the Fermi level position. The Rashba spin-splitting developed at the MX₂/CoFeB interface relies on the band structure or wave function hybridization between the MX₂ and CoFeB[97, 103]. The band structure and the Fermi level position of MX₂/CoFeB could be temperature independent as reflected in the temperature independence of resistance (slight increase as the temperature decreases) of MX₂/CoFeB bilayers (see the inset of Figure 3-7). However, detailed theories and more experiments are still required to fully understand the results.

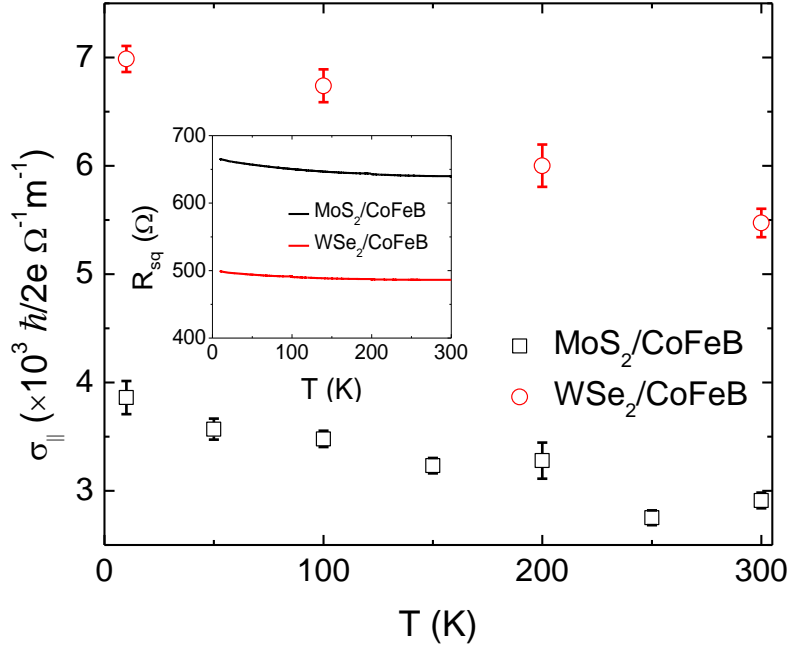


Figure 3-7 Temperature dependence of current-induced in-plane spin conductivities for both MoS₂/CoFeB and WSe₂/CoFeB. The inset shows the temperature dependence of sheet resistance for both MoS₂/CoFeB and WSe₂/CoFeB. Reprinted with permission from [55], Copyright (2016) American Chemical Society

3.2.4 Discussions on origin of SOT in monolayer TMD/CoFeB

In the sapphire/MoS₂/CoFeB/TaO_x heterostructure, in principle, there are two possible reasons for the observation of the in-plane spin-orbit field beyond the Rashba-Edelstein effect as we discussed in the main text. The first one is the current-induced Oersted field caused by the finite current going through the MoS₂ layer. Although the resistance of the as-grown MoS₂ monolayer on Sapphire is very high, we do observe that the resistance of MoS₂/CoFeB bilayers is smaller than that of the single CoFeB layer. This is not predicted by a parallel resistor model since the resistance of monolayer MoS₂ is more than three orders of magnitude larger than that of the 3 nm CoFeB layer. We believe that the growth of the CoFeB layer induces dopants into the monolayer MoS₂

and increases the conductance of the monolayer MoS₂. This is possible during the sputtering process, which involves high energy particles. The sheet resistance of the CoFeB layer and the MoS₂/CoFeB bilayer are $R_{\text{CoFeB}} \approx 649 \text{ } \Omega/\text{sq}$ and $R_{\text{MoS}_2/\text{CoFeB}} \approx 642 \text{ } \Omega/\text{sq}$, respectively. So, the effective resistance of MoS₂ is estimated to be 60 k Ω/sq . Based on this estimation, the maximum Oersted field is $3.4 \times 10^{-3} \text{ Oe}$ per mA for the MoS₂/CoFeB bilayer by using $H_{\text{Oe}} = \frac{I}{2W} \frac{R_{\text{CoFeB}}}{R_{\text{MX}_2} + R_{\text{CoFeB}}}$, where W is the Hall bar width (20 μm) and we assume the film is an infinitely wide conducting plate ($W \gg$ thickness of both CoFeB and MX₂ layer, 3.8 nm). We should notice that this estimation should give an upper bound of the Oersted field, since the direct growth of CoFeB on SiO₂ does not produce good-quality CoFeB and thus the CoFeB itself could have a low resistance in the MoS₂/CoFeB bilayer. The unambiguous evidence is that the Oersted field for the MoS₂/CoFeB bilayer is along the $+x$ direction when the current is along the $+y$ direction. In contrast, the observed in-plane spin-orbit field is along the $-x$ direction when the current is along the $+y$ direction. Therefore, the current-induced Oersted field cannot explain the observed in-plane spin-orbit field.

The second possible reason for the in-plane spin-orbit field is the spin Hall Effect. In principle, the spin Hall Effect can also give rise to an in-plane spin-orbit field (*i.e.*, a field-like torque). We argue that the spin Hall Effect cannot be the reason for the observation of in-plane spin-orbit field here for two reasons. First, it has been shown that the spin Hall effect will give rise to a large damping-like torque along with a field-like torque and the magnitude of the damping-like torque is typically larger than that of field-like torque[99]. For our Ta/CoFeB bilayer, the field-like field is 0.15 Oe/mA, which is more than two times of magnitudes smaller than the damping-like field (0.35 Oe/mA). So, spin Hall effect dominates the spin-orbit torque generation process in the Ta/CoFeB bilayer. In contrast, we do not observe a clear damping-like torque in the MoS₂/CoFeB bilayer.

Second, the theory only predicts a spin Hall effect that generates an edge spin current at the boundary of monolayer MoS₂, but not at the top surface of MoS₂. And this anisotropic spin Hall effect is believed to be due to the intrinsic band berry curvature[91]. For these reasons, the spin Hall Effect is not likely to be the main reason for the observed in-plane spin-orbit field.

In conclusion, we have shown that a current can generate a large in-plane spin-orbit effective field in a bilayer consisting of CVD-grown large-scale monolayer TMDs and a ferromagnetic layer and this effective field is temperature-insensitive. Our findings could be beneficial for future design of spintronic devices exclusively based on two-dimensional materials, where monolayer TMDs are coupled with magnetic van der Waals materials to form heterostructures that provide novel functionalities beyond electronics and optoelectronics[83, 104]. For future studies of two-dimensional semiconducting TMDs, on the one hand, systematic measurements on various TMDs need to be carried out to clarify the relation between the spin-orbit coupling strength and the spin torque efficiency. On the other hand, if the ferromagnetic metal we used in this study can be replaced by a magnetic insulator, such as yttrium iron garnet, there will be no shunting problem and the spin-charge conversion efficiency may be significantly improved[21]. Alternatively, metallic TMDs, such as 1T' phase WTe₂, have also been shown to give rise to a unique out-of-plane damping-like torque due to breaking of the in-plane mirror symmetry[105], which is preserved in our 1H phase TMDs. At last, we would like to mention that the REE-induced spin polarization at the atomically thin interface is expected to have a broad tunability with an external gate voltage[25], thus allowing for further improvement of energy efficiency for spintronic devices based on two-dimensional materials.

3.3 TI/CoFeB SOT

We grow TIs, Bi₂Se₃(6nm), Bi₂Te₃(10nm) and (BiSb)₂Te₃(10nm), on sapphire or semi-insulating GaAs using MBE [20]. The Bi₂Se₃ and Bi₂Te₃ show a metallic resistance vs temperature behavior (Figure 3-8a), indicating that the Fermi level is near or in the conduction band. In contrast, the (BiSb)₂Te₃ thin film shows a semi-insulating resistance vs temperature behavior (Figure 3-8a), suggesting that the Fermi level is in the band gap. All TI thin films show a weak anti-localization behavior (Figure 3-8b), demonstrating their nontrivial π Berry phase [106]. The TI thin films are transferred to the sputtering chamber for the deposition of CoFeB(5nm)/MgO(2nm)/Ta(2nm). The Ta(2nm) will be oxidized into roughly TaO_x(3nm). The TI/CoFeB thin films have an effective in-plane anisotropy field B_K around 1.3 T as shown from magnetization hysteresis loops (Figure 3-9a). The out-of-plane Hall hysteresis loop provides the value of anomalous Hall (AHE) resistance R_A and B_K (Figure 3-9b). Since the planar Hall resistance R_P is much smaller than R_A (Figure 3-9b inset) and we measure second harmonic Hall resistance ($R_{\text{Hall}}^{2\omega}$) at fields larger than 1 T, the field-like SOT contribution is negligible (see Eq. (3-1)). The thermoelectric contribution must be carefully considered using field-dependence of $R_{\text{Hall}}^{2\omega}$. Note that the differential resistance method used in [27] cannot rule out this contribution without considering field-dependence of $R_{\text{Hall}}^{2\omega}$. First, we measure the azimuthal angle (φ)-dependence of $R_{\text{Hall}}^{2\omega}$ at different fields (Figure 3-10a) and then extract the maximum H_D along the current direction from the field-dependence (Figure 3-10b). Second, we measure field-dependence of $R_{\text{Hall}}^{2\omega}$ at different φ 's (Figure 3-10c) and then extract the H_D for different φ 's (Figure 3-10d), which satisfies the sin(φ) relation and thus is consistent with the damping-like SOT physics. The average current density-dependence of H_D are shown in Figure 3-11, which show a linear behavior for all TI/CoFeB bilayers. We obtain an overall effective SOT efficiency 0.07, 0.53, 0.75±0.06 using $\xi_{\text{DL}} = \frac{2eM_{\text{S}}t_{\text{FM}}H_{\text{DL}}}{\hbar J_{\text{c}}}$ for Bi₂Se₃/, Bi₂Te₃/ and

(BiSb)₂Te₃/CoFeB, respectively. After independently calibrating resistance for CoFeB (5nm) and TI thin films, we obtain current density in TI layers and thus obtain CS efficiency 0.35, 1.76 and 8.33±0.65 for Bi₂Se₃, Bi₂Te₃ and (BiSb)₂Te₃, respectively.

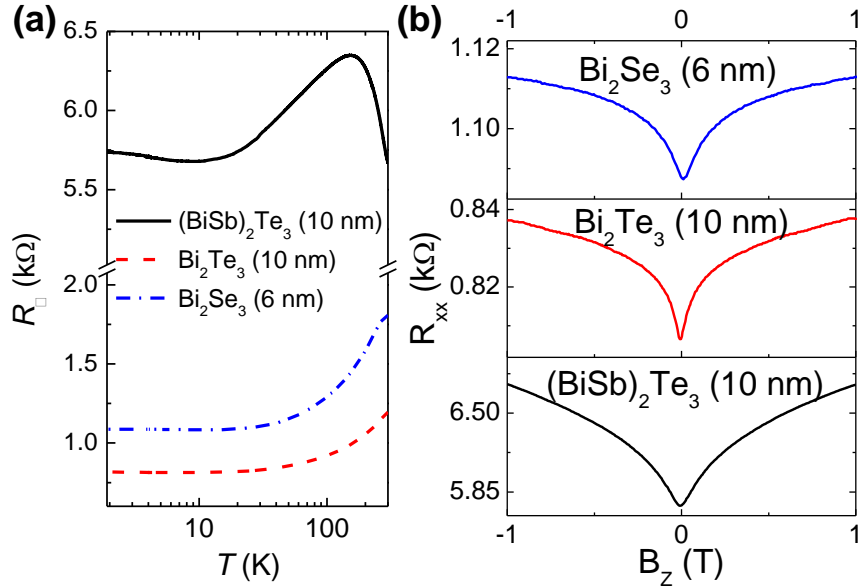


Figure 3-8 Transport properties of pure TIs. (a) Resistance vs temperature curves for TIs. (b) Resistance as a function of out-of-plane field for TIs. Reprinted with permission from [34], Copyright (2018) IEEE

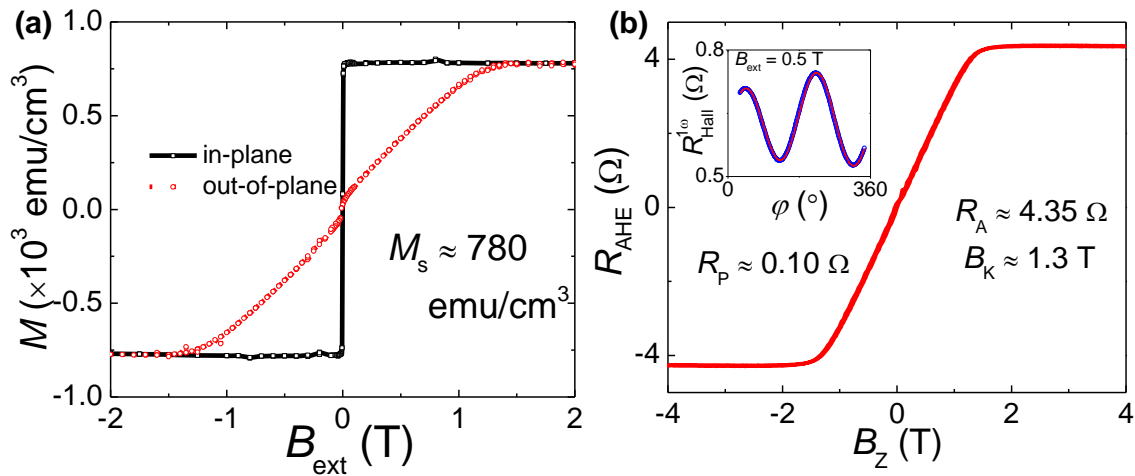


Figure 3-9 Magnetic properties of the TI/CoFeB bilayer. (a) Typical magnetization hysteresis loops for TI/CoFeB(5nm). (b) AHE resistance as a function of out-of-plane field for TI/CoFeB(5nm).

Bi₂Se₃(6nm)/CoFeB(5nm). Inset shows the planar Hall resistance as a function of ϕ . Reprinted with permission from [34], Copyright (2018) IEEE

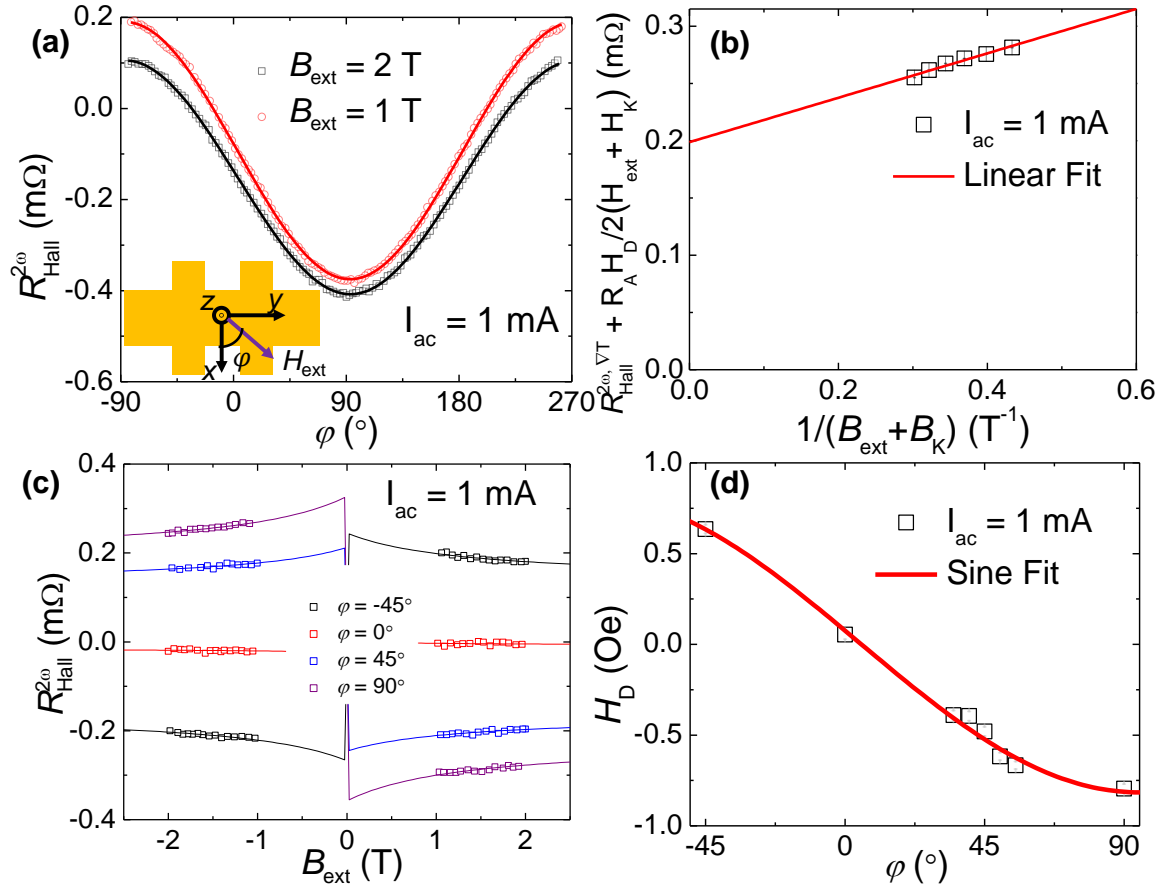


Figure 3-10 Second-harmonic measurements of the Bi₂Se₃(6nm)/CoFeB(5nm) bilayer. (a) $R_{Hall}^{2\omega}$ as a function of azimuthal angle ϕ at different external fields. Inset shows the optical image of a Hall bar device. (b) Sine component of $R_{Hall}^{2\omega}$ as a function of the inverse of summation of external field and effective anisotropy field. (c) $R_{Hall}^{2\omega}$ as a function of external field at different ϕ 's. (d) Extracted H_D from (c) as a function of ϕ . Reprinted with permission from [34], Copyright (2018) IEEE

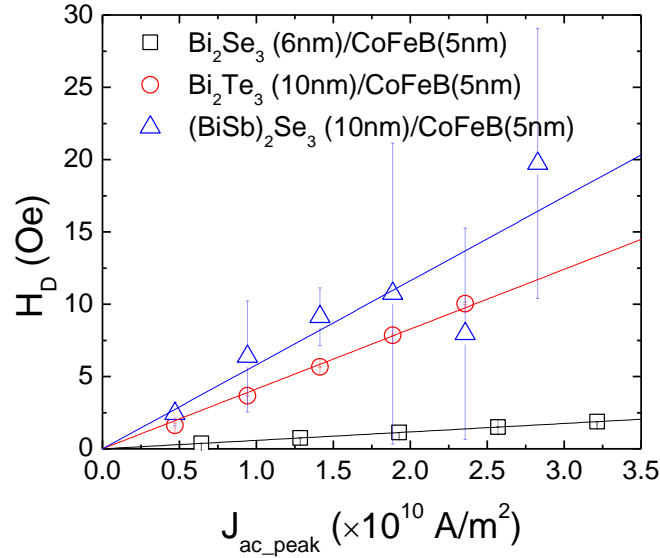


Figure 3-11 H_D as a function of current density in TI/CoFeB bilayers. Reprinted with permission from [34], Copyright (2018) IEEE

3.4 TI/Mo/CoFeB SOT

SOT-MRAM is a promising candidate for future nonvolatile memory technology. Finding materials that have large SOT efficiency (ζ_{DL}) is critical for developing the SOT-MRAM. TIs have been shown to exhibit giant ζ_{DL} (>1) at room temperature. However, integration of high ζ_{DL} TIs with CoFeB with PMA at room temperature (RT) has not been achieved. In this Session, we demonstrate a record-high ζ_{DL} (~ 2.66) in the $(\text{BiSb})_2\text{Te}_3$ with PMA CoFeB and achieve magnetization switching with TI current density as low as $3 \times 10^9 \text{ A/m}^2$ at RT. For the first time, we propose to insert a light metal spacer between TI and CoFeB to achieve resistance matching and thus reduce write energy. The discussion on the role of spacer is presented in Session 7.1. We show that without insertion, TI/CoFeB show in-plane magnetic anisotropy but TIs show high ζ_{DL} , consistent with previous reports. We then insert a Mo spacer to achieve PMA at RT. We accurately determine the ζ_{DL} using both second harmonic method and differential MOKE for the first time.

We investigate the SOT-driven switching and discover a memristor-like behavior in the TI/Mo/CoFeB. This memristor-like behavior will be investigated in Session 7.3.

Ever-present data require large and fast data processing capability. Traditional von Neumann architecture separates the computing and storage units, which cause significant delay and energy consumption over the data bus. STT-MRAM and SOT-MRAM are promising for embedded memory technology thanks to their fast write and read (several ns) [76]. STT-MRAM single bit is a two-terminal device whereas SOT-MRAM single bit is three-terminal, where the write and read paths are separate. Since there is no charge current directly going through the magnetic tunnel junction (MTJ), the endurance and reliability of SOT-MRAM could be much higher. The switching current density (J_{sw}) of a SOT-MRAM device is given by $J_{sw} = 4ekT\Delta/(\hbar\zeta_{DL}A_{MTJ})$, where Δ is the thermal stability factor and ζ_{DL} is the (anti-damping-like) SOT efficiency. Heavy metals (HMs), such as β -Ta [33], Pt [78, 102], and β -W [26], are common channel materials used in SOT-MRAM for generating SOTs, whose ζ_{DL} range from 0.08 to 0.3 (see Table 3-3). Recently, TIs, like Bi_2Se_3 [21] and $(\text{BiSb})_2\text{Te}_3$ [20], have emerged as potential channel materials thanks to their extraordinary large ζ_{DL} (>1). However, questions about the energy efficiency have been raised since TIs usually have a resistivity (ρ_{TI}) at the order of $10^3 - 10^4 \mu\Omega\cdot\text{cm}$ and thus during switching, most of current flows in the CoFeB layer, which is the most common MTJ ferromagnet and has a $\rho_{\text{CoFeB}} \sim 170 \mu\Omega\cdot\text{cm}$. Also, PMA MTJ is essential for MRAM scaling. But TIs with bulk PMA CoTb show a $\zeta_{DL} < 1$ [30]. RT high ζ_{DL} TIs with PMA CoFeB has remain elusive.

In this work, we demonstrate a large $\zeta_{DL} \sim 2.66$ in the TI/Mo/CoFeB/MgO structure with RT PMA using the second harmonic method and the differential MOKE. Moreover, we show the SOT-driven magnetization switching with TI current density as low as $3 \times 10^9 \text{ A/m}^2$.

The advantages of molybdenum (Mo) are threefold. First, Mo has very small ζ_{DL} and relatively long spin diffusion length. Thus, it does not affect the spin current generated from the HM layer [107]. Second, Mo/CoFeB/MgO has strong PMA. Third, Mo/CoFeB/MgO can survive high temperature (> 400 °C) without losing PMA. This thermal stability is required for industry back-end-of-line process. Motivated by the SOT-MRAM energy modeling (Session 7.1) and advantages of Mo, we insert 2 nm-thick Mo between $(\text{BiSb})_2\text{Te}_3$ and CoFeB. Figure 3-12 shows the OOP R_H hysteresis loops for different CoFeB thickness (t_{CoFeB}). The PMA exists in a narrower t_{CoFeB} window in $(\text{BiSb})_2\text{Te}_3/\text{Mo}/\text{CoFeB}$, compared with the Ta/CoFeB and W/CoFeB cases. Nevertheless, we achieve RT PMA in the $(\text{BiSb})_2\text{Te}_3(6\text{nm})/\text{Mo}(2\text{nm})/\text{CoFeB}(1.02\text{nm})$. Figure 3-13 shows that the $(\text{BiSb})_2\text{Te}_3(6\text{nm})/\text{Mo}(2\text{nm})/\text{CoFeB}(0.93\text{nm})$ exhibits strong PMA with a sizeable coercive field when the sample is cooled down to 200 K. This suggests that the 0.93 nm-thick CoFeB on TI is superparamagnetic (multi-domain state) at RT. Figure 3-14 show the SOT determination in the TI/Mo/CoFeB using second-harmonic method. Note that the R_{th} is negligible in PMA systems, which allows accurate determination of B_{DL} . The B_{DL} is linearly dependent on the current and the result of ζ_{DL} is summarized in Table 3-3.

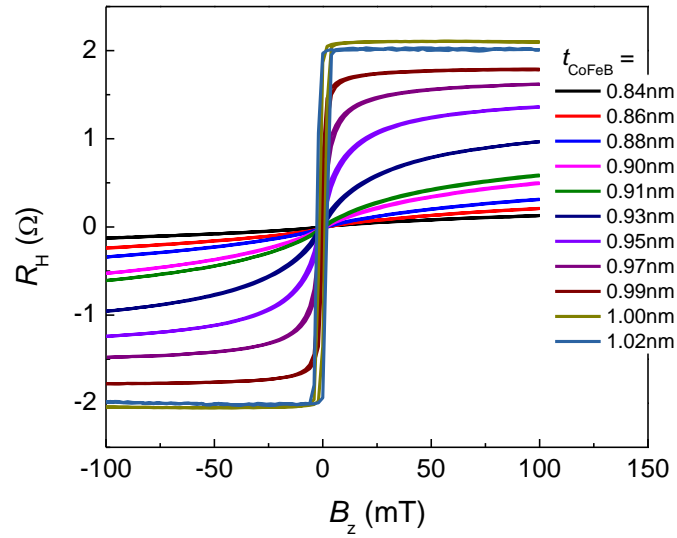


Figure 3-12 OOP R_H hysteresis loops for $(\text{BiSb})_2\text{Te}_3$ (6nm)/Mo(2nm)/CoFeB(t_{CoFeB}). Reprinted with permission from [35], Copyright (2018) IEEE

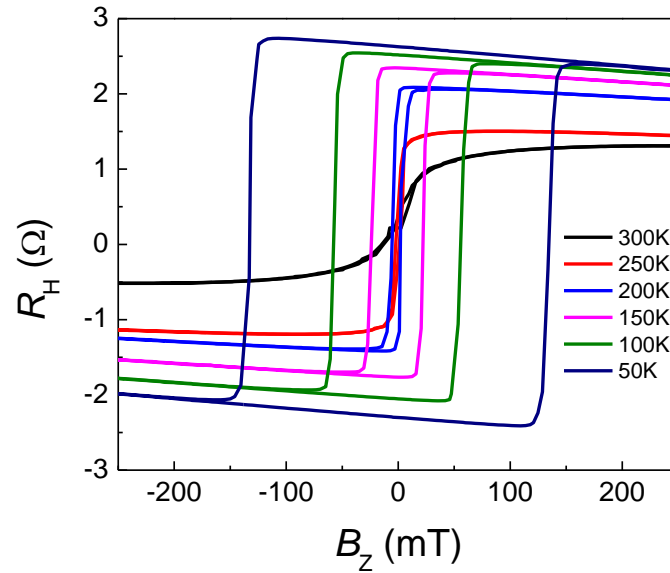


Figure 3-13 OOP R_H hysteresis loops at different temperatures for $(\text{BiSb})_2\text{Te}_3$ (6nm)/Mo(2nm)/CoFeB(0.93nm). Reprinted with permission from [35], Copyright (2018) IEEE

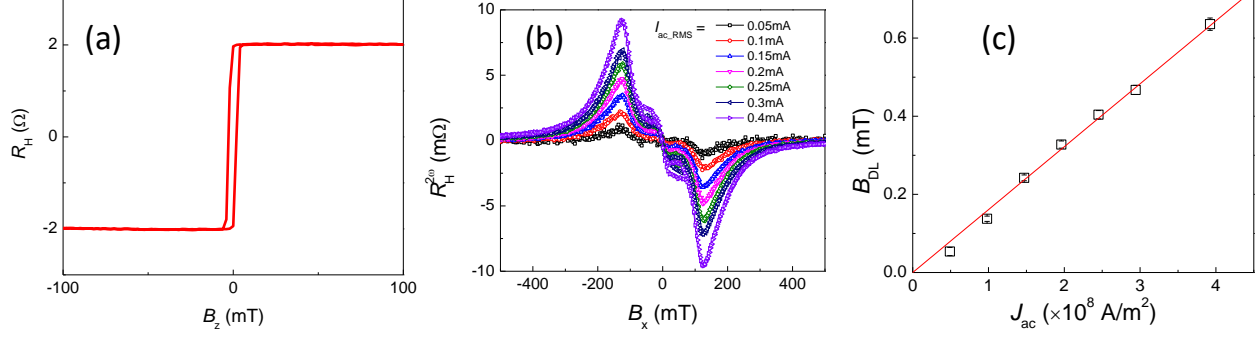


Figure 3-14 SOT determination in the $(\text{BiSb})_2\text{Te}_3(6\text{nm})/\text{Mo}(2\text{nm})/\text{CoFeB}(1.02\text{nm})$ sample with PMA. (a) OOP R_H hysteresis. (b) $R_H^{2\omega}$ as a function of external field at different currents. (c) B_{DL} as a function of TI current density. Reprinted with permission from [35], Copyright (2018) IEEE

We realize current-driven magnetization switching in the $(\text{BiSb})_2\text{Te}_3(6\text{nm})/\text{Mo}(2\text{nm})/\text{CoFeB}(1.02\text{nm})$ Hall bar device as shown in Figure 3-15. The channel width is $20\ \mu\text{m}$. The switching direction is opposite with opposite bias fields, agreeing with the nature of anti-damping-like SOT. We notice that the I_{sw} is around $4.5\ \text{mA}$ and the J_{sw} in $(\text{BiSb})_2\text{Te}_3$ is around $3 \times 10^9\ \text{A}/\text{m}^2$. This low J_{sw} is consistent with large ζ_{DL} .

We also carried out the different MOKE to quantify the SOT efficiency in TI/Mo/CoFeB. Consistent results are obtained for both the $R_H^{2\omega}$ and $\Delta\theta_K$. Note that this is happening only when $R_p \ll R_A$, the R_{th} is very small compared with the $R_A B_{DL}/(|B_{ext}| - B_K)$, and $\theta_{\parallel} \ll \theta_{\perp}$ [58].

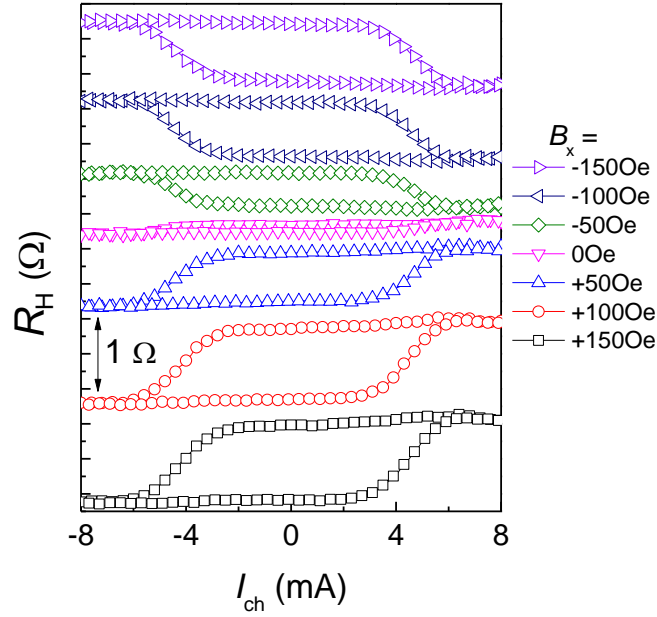


Figure 3-15 RT SOT-driven magnetization switching in the $(\text{BiSb})_2\text{Te}_3(6\text{nm})/\text{Mo}(2\text{nm})/\text{CoFeB}(1.02\text{nm})$ sample. Reprinted with permission from [35], Copyright (2018) IEEE

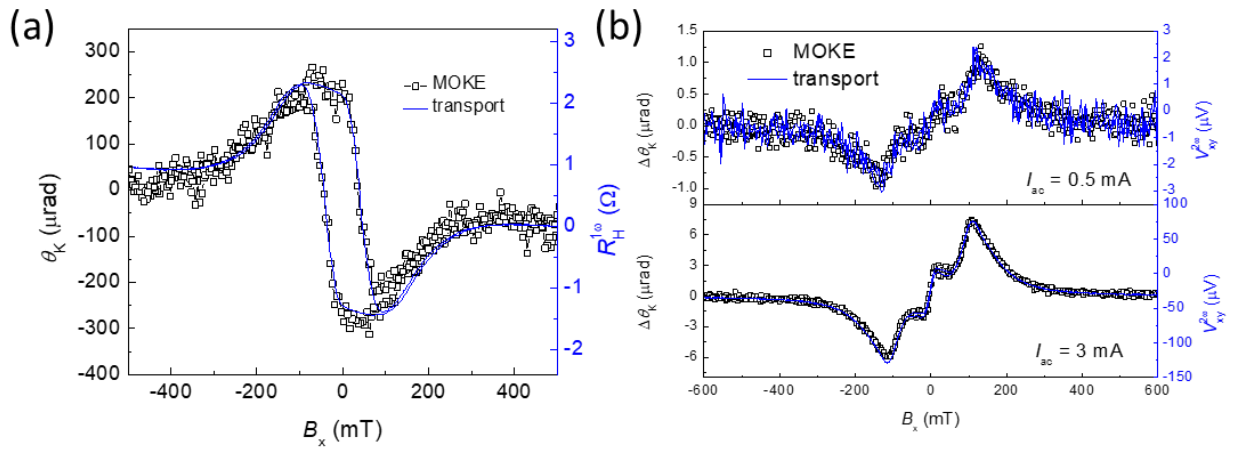


Figure 3-16 Comparison between θ_K and first harmonic Hall resistance ($R_H^{1\omega}$) (a) and between $\Delta\theta_K$ and second harmonic Hall voltage ($V_H^{2\omega}$) (b) in the $(\text{BiSb})_2\text{Te}_3(6\text{nm})/\text{Mo}(2\text{nm})/\text{CoFeB}(1.02\text{nm})$. Reprinted with permission from [35], Copyright (2018) IEEE

Table 3-3 Summary of RT resistivity, spin Hall conductivity and SOT efficiency for heavy metals and topological insulators. # This work. S1 and S2 are TI samples from two different batches. Adapted with permission from [35], Copyright (2018) IEEE

Materials	Magnetic anisotropy	Resistivity $\rho_{\text{HM, TI}}$ ($\mu\text{m}\cdot\text{cm}$)	Spin Hall conductivity σ_{SH} ($\times 10^5 \Omega^{-1}\text{m}^{-1}$)	Spin-orbit torque efficiency (ξ_{DL})
β -Ta [33]	PMA	190	0.63	0.12
Pt [102]	PMA	50	2.4	0.12
β -W [26]	PMA	170	1.76	0.3
Bi_2Se_3 [21]	IP	1770	1.55	2.75
$\text{Bi}_x\text{Se}_{1-x}$ [27]	PMA	1250	1.08	1.35
Bi_2Se_3 [#]	IP	1080	0.32	0.35
Bi_2Te_3 [#]	IP	1200	1.47	1.76
$(\text{BiSb})_2\text{Te}_3$ (S1) [#]	IP	5700	1.46(± 0.11)	8.33(± 0.65)
$(\text{BiSb})_2\text{Te}_3$ (S2) [#]	PMA	2500	1.06	2.66

Figure 3-17 summarizes the research progress on channel materials towards an energy efficient SOT-MRAM with PMA. This work is among the first to demonstrate the combination of TIs and interfacial PMA CoFeB, which is industry-compatible. Moreover, we achieve a record-high ξ_{DL} .

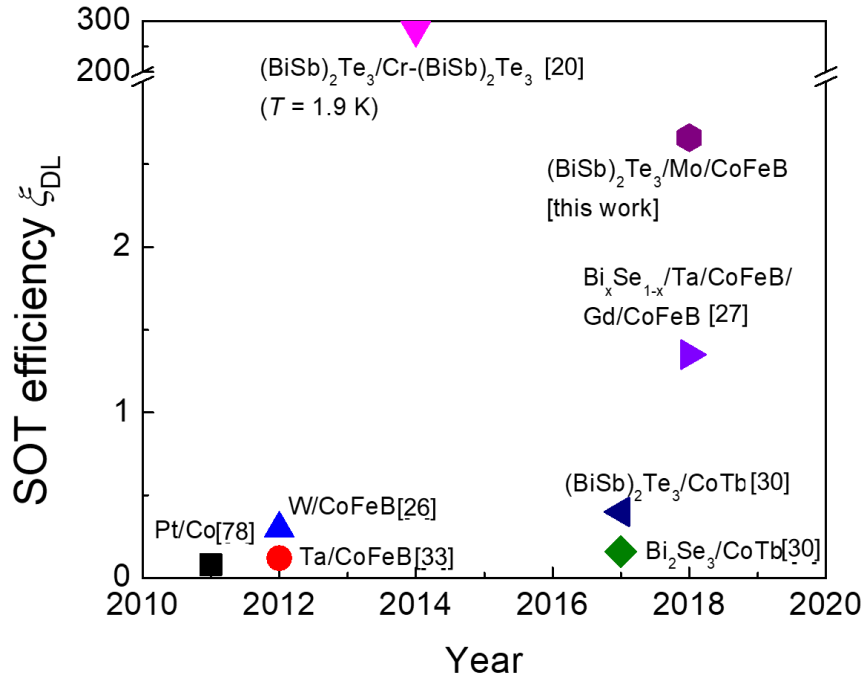


Figure 3-17 Progress towards efficient SOT-MRAM with PMA. All references are from RT unless specifically mentioned. Reprinted with permission from [35], Copyright (2018) IEEE

Chapter 4 Ferrimagnetic insulators

Commonly available magnetic insulators (MIs) at room temperature include magnetic garnets and ferrites. They have been used for many applications, including radiofrequency passive devices, magnonic circuits and introducing magnetic proximity effect (MPE) to the adjacent nonmagnetic materials [108].

Metallic magnetic metals typically have relatively high damping because of free electron scattering. In contrast, MIs are believed to have much lower damping due to the absence of free electrons. So far, the magnetic material with lowest damping is $\text{Y}_3\text{Fe}_5\text{O}_{12}$ (YIG), the damping constant of which can be as low as 10^{-5} . This low damping could enable much longer propagation distance of magnetic information, which is usually carried by the magnons, the quanta of the spin wave excitations [109, 110]. The propagation length is usually at tens of micrometers for YIG, which is almost two to three orders of magnitude larger than common magnetic metals. This long propagation length is critically for developing magnon-based logic devices and circuits [111, 112].

Due to the absence of free charge carrier, the MI could provide MPE to the adjacent nonmagnetic material without introducing disorders. This MPE is suggested to be able to make functional time-reversal broken quantum systems working at higher temperatures. For example, magnetic topological insulators (MTIs) exhibit quantum anomalous Hall effect (QAHE) at ultralow temperature ($< 1\text{K}$) even though the Curie temperature of MTIs is at the order of 30 K [6, 7]. The reason is believed to be the scenario that the magnetic dopants introduce impurity bands and destroy the QAHE at higher temperature. The MPE in the MI/TI/MI sandwich structure may provide a solution for high temperature QAHE.

Ferrimagnetic insulators (FMIs) have additional advantage of high characteristic frequency due to the antiferromagnetic exchange coupling between magnetic sublattices. Recent studies have shown the ferrimagnetic material near the angular momentum compensation temperature (T_A) could provide ultrafast dynamics and near the magnetization compensation temperature (T_M) could provide stability of AFM [113, 114]. The FMI could potentially bring advantages of both low damping and high speed at the same time, which motivates our works on FMIs.

4.1 Motivations for ferrimagnetic insulators with PMA

PMA magnet is critical for developing magnetic memory technology and introducing MPE. First, PMA magnet is better in terms of scalability and thus could allow higher density for memory applications. Second, PMA magnet could induce finite magnetization in the out-of-film-plane of the adjacent nonmagnetic material in the absence of external magnetic field, which is important for realizing quantum dissipationless transport.

4.2 PMA due to strain

Some MIs have strong uniaxial crystalline magnetic anisotropy and thus have PMA. Examples include barium hexagonal ferrite ($\text{BaFe}_{12}\text{O}_{19}$, BaM) [115]. In most of MI thin films, the magnetic anisotropy tends to be in the film plane because of the demagnetization field. However, by introducing appropriate strain through the lattice mismatch between the grown material and substrate, the PMA can be achieved with the strain-induced magnetoelastic effect. Here, I discuss major effort on achieving PMA using strain in magnetic garnet thin films, which have cubic lattice. The method I use to grow MI thin films is pulsed laser deposition (PLD, see Appendix E).

Table 4-1. List of magnetostriction constants for (111) and (100) planes at different temperatures and lattice constants for ferrimagnetic garnets and paramagnet substrates. The magnetostriction constant values are taken from ref. [116]

	λ_{111} ($\times 10^{-6}$) 300K	λ_{100} ($\times 10^{-6}$) 300K	λ_{111} ($\times 10^{-6}$) 78K	λ_{100} ($\times 10^{-6}$) 78K	Lattice constant (\AA)
Y ₃ Fe ₅ O ₁₂ (YIG)	-2.4	-1.4	-3.6	-1.0	12.376
Tm ₃ Fe ₅ O ₁₂ (TmIG)	-5.2	1.4	-31.2	25	12.324
Tb ₃ Fe ₅ O ₁₂ (TbIG)	12	-3.3	560	67	12.435
Eu ₃ Fe ₅ O ₁₂ (EuIG)	1.8	21	9.7	86	12.498
Gd ₃ Fe ₅ O ₁₂ (GdIG)	-3.1	0	-5.1	4.0	12.47
Gd ₃ Ga ₅ O ₁₂ (GGG)					12.383
Substituted GGG (SGGG)					12.497
Nd ₃ Ga ₅ O ₁₂ (NGG)					12.509

The magnetic anisotropy induced by strain is determined by the magnetostriction constant of a magnetic garnet, which depends on crystal plane and temperature. Table 4-1 provides a list of materials that could show PMA due to strain effect and their substrates. To achieve PMA in a specific magnetic garnet, we need to choose appropriate substrate. We define the lattice constants of magnetic garnets and substrates as c_{FMI} and c_{sub} . So the induced magnetoelastic anisotropy is proportional to $\lambda_{FMI}(c_{FMI} - c_{sub})$, where λ_{FMI} is the magnetostriction of the magnetic garnet. If $\lambda_{FMI}(c_{FMI} - c_{sub}) > 0$, it means that induced magnetoelastic anisotropy is out-of-film-plane. So, if one wants to have PMA TmIG at room temperature, one may choose SGGG(111) and

NGGG(111). While $c_{TmIG} - c_{GGG} < 0$, the absolute magnitude of the number is small so that the induced magnetoelastic anisotropy in TmIG(111)/GGG(111) is also small, which may not be sufficient to overcome the demagnetization energy.

So far, we have achieved PMA in TmIG(111)/SGGG(111) [117, 118], TmIG(111)/NGG(111) [56, 119, 120], TbIG(110)/GGG(110) [120], TbIG(111)/GGG(111) [121], EuIG(100)/GGG(100) [121].

4.3 SOT in magnetic insulator-based heterostructures

MIIs attract tremendous interest for spintronic applications due to low Gilbert damping and absence of Ohmic loss. SOTs on MIIs are more intriguing than magnetic metals since SOTs cannot be transferred to MIIs through direct injection of electron spins. Understanding of SOTs on MIIs remains elusive, especially how SOTs scale with the MI film thickness. In this Session, we report the critical role of dimensionality on the SOT efficiency by studying the MI layer thickness dependent SOT efficiency in tungsten/thulium iron garnet (W/TmIG) bilayers. We show that the TmIG thin film evolves from two-dimensional to three-dimensional magnetic phase transitions as the thickness increases. We report the significant enhancement of the measured SOT efficiency as the TmIG thickness increases, which is attributed to the increase of the magnetic moment density. We demonstrate the current-induced SOT switching in the W/TmIG bilayers with a TmIG thickness up to 15 nm.

The interplay between heavy metals (HMs) and magnetic insulators (MIIs) in heavy metal/magnetic insulator (HM/MI) bilayer systems has attracted tremendous attention from both fundamental research and practical applications [108, 109, 122, 123]. First, the HM/MI bilayer benefits from the low Gilbert damping in the MI. In contrast to magnetic metal, MIIs only allow spin information

to propagate through magnons, instead of itinerant electrons, due to their large electronic bandgaps. The absence of Ohmic loss from the magnetic layer makes HM/MI bilayers more energy efficient than HM/magnetic metal bilayers.

The second advantage of the HM/MI bilayer is that the spin-orbit coupling in the HM or at the HM/MI interface allows the efficient generation of spin-orbit torques (SOTs) on the MI layer through the spin Hall effect (SHE) or Rashba-Edelstein effect [33, 73, 78, 124, 125]. These SOTs enable efficient manipulation of magnetization dynamics in the MI layer. Although the MI layer is electrically insulating, SOT-driven magnetization dynamics of magnetic insulators can be detected through anomalous Hall resistance (AHR) and spin Hall magnetoresistance (SMR) in the HM layer [117, 126-128]. By probing the AHR, current-induced magnetization switching (CIMS) was observed in both Pt/BaM [115] and Pt/Tm₃Fe₅O₁₂ (TmIG) bilayers [50, 56]. However, whether SOTs in Pt/MI bilayers are from SHE remains ambiguous due to the potential existence of the Rashba-Edelstein effect [56]. It remains unclear whether the switching direction will be opposite when we utilize HMs with opposite spin Hall angles. Moreover, the observed damping-like SOT efficiency (ξ_{DL}) in the Pt/TmIG that is responsible for switching is still much lower than those in the Pt/ferromagnetic metals (FMs) [50, 129, 130]. To understand the origin of SOTs and to increase the value of ξ_{DL} in HM/MI bilayers, we utilize a HM with a large spin Hall angle opposite to that of Pt in a HM/MI bilayer, demonstrate magnetization switching, and analyze the contributions to the SOT.

In this Session, we study the ξ_{DL} and CIMS in tungsten (W)/TmIG heterostructures with different TmIG layer thicknesses (t_{TmIG}). The thickness dependence of the damping-like SOT allows us to understand the interplay between spin current and magnetism in TmIG. Here, W is chosen since it is reported to give the largest spin Hall angle among elemental heavy metals and its sign is opposite

to that of Pt [26]. When the TmIG film thickness is reduced from 15 nm to 3.2 nm, the effective exchange coupling is strongly reduced due to long-wavelength thermal fluctuations, resulting in a dimensional crossover from three-dimension-like to two-dimension-like magnetic phase transitions. We quantify ξ_{DL} by using second-harmonic Hall measurements [52, 53]. The ξ_{DL} increases with the t_{TmIG} in W/TmIG bilayers; this is attributed to the enhanced magnetic moment density due to suppression of thermal fluctuations. We then demonstrate the CIMS in W/TmIG bilayers up to $t_{TmIG} = 15$ nm; for $t_{TmIG} = 15$ nm, the switching current density is as low as 8×10^{10} A/m². The estimated current switching efficiency enhances as t_{TmIG} increases, which is consistent with the increase of ξ_{DL} with t_{TmIG} . Importantly, the switching direction of our W/TmIG devices is indeed opposite to that of the Pt/TmIG device [50]; this contrast confirms the important role of SHE in CIMS of MIs.

4.3.1 Materials and methods

All TmIG(111) films were grown on Nd₃Ga₅O₁₂(111) by pulsed laser deposition [117] before transferring to a magnetron sputtering chamber in the ambient condition. At room temperature, we deposited a 5 nm-thick W layer on top of TmIG followed by subsequent deposition of MgO(2 nm)/TaO_x(3 nm) layers to protect W from oxidization. Magnetization hysteresis loops as a function of an out-of-plane magnetic field were measured by a vibrating sample magnetometer and a superconducting quantum interference device. The nominal thin film area is 5×5 mm².

The films were patterned into Hall bar devices (Fig. 2a) by using standard photolithography and dry etching for the resistance, SOT, and switching measurements. The channel width is 20 μ m, and the distance between two neighboring Hall contacts is 26 μ m. We measured the second

harmonic Hall resistance by applying a $I_{ac,r.m.s} = 1$ mA ($J_{ac,r.m.s} = 10^{10}$ A/m²) with a frequency $\omega/2\pi = 195.85$ Hz. The magnetic field and angle controls were done in a physical properties measurement system. The CIMS experiments were performed in the ambient environment by applying a pulse current with 5 ms pulse width and reading Hall voltage subsequently.

4.3.2 Dimensional crossover of magnetism

To access SOT and realize CIMS, we prepare high-quality TmIG thin films with different t_{TmIG} and characterize their magnetic properties. These TmIG(111) thin films were grown on substrate Nd₃Ga₅O₁₂(111) by pulsed laser deposition [117]. All TmIG thin films show an atomically flat surface with mean roughness as low as 0.1 nm (Figure 4-1a), providing a sharp interface for efficient spin momentum transfer.

We use ST-FMR to determine the damping constant of another series of TmIG thin films (Figure 4-2). We see that the damping factor increases when the TmIG film thickness decreases, which is typical for magnetic thin films.

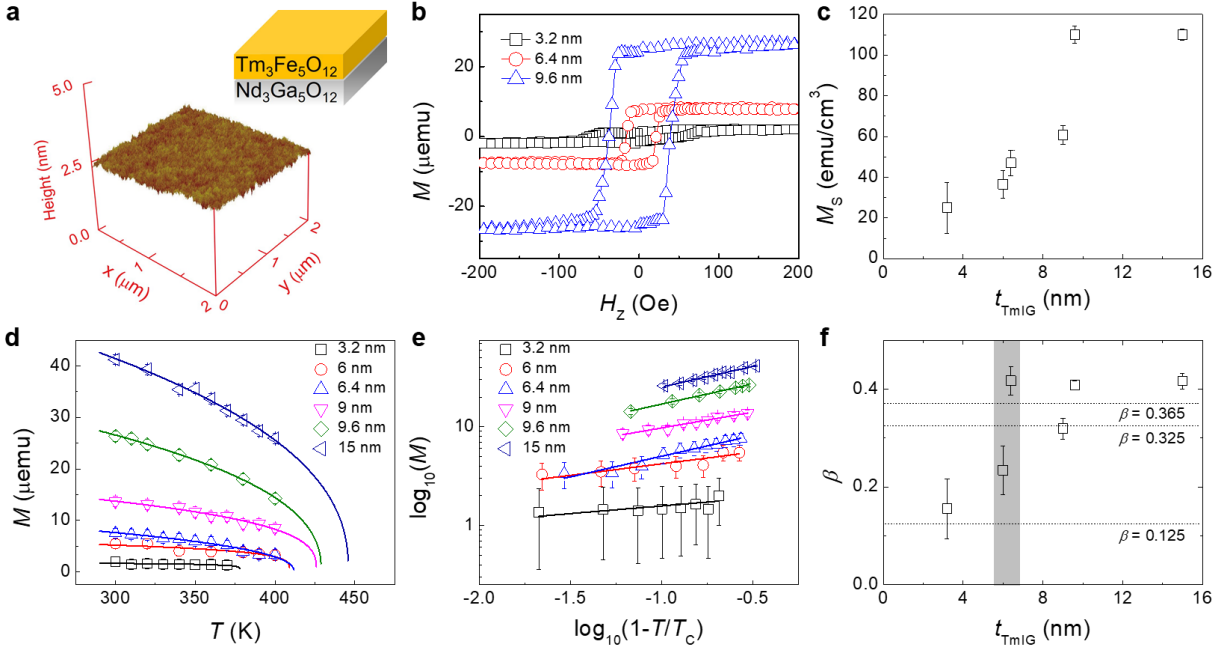


Figure 4-1 Dimensional crossover of magnetism in TmIG thin films. (a) Atomic force microscopy image of a 10 nm-thick TmIG film. (b) Magnetic moment as a function of out-of-plane magnetic field for TmIG thin films with different thicknesses at room temperature. (c) Saturation magnetization as a function of TmIG thickness at room temperature. (d) Total magnetic moment as a function of temperature for different TmIG thicknesses. The solid lines are power-law fits to $M = M_0(1 - T/T_C)^\beta$. (e) $\log_{10}(M)$ vs $\log_{10}(1-T/T_C)$ plots from (d) showing the thickness dependence of the β values. (f) Critical exponent vs TmIG thickness showing a dimensional crossover from 2D to 3D. The dashed lines are theoretical values for 2D Ising ($\beta = 0.125$), 3D Ising ($\beta = 0.325$) and 3D Heisenberg ($\beta = 0.365$) models. The error bars in (c-e) stand for the measurement uncertainty, and the error bar in (f) stands for the fitting uncertainty. Reprinted with permission from [119]

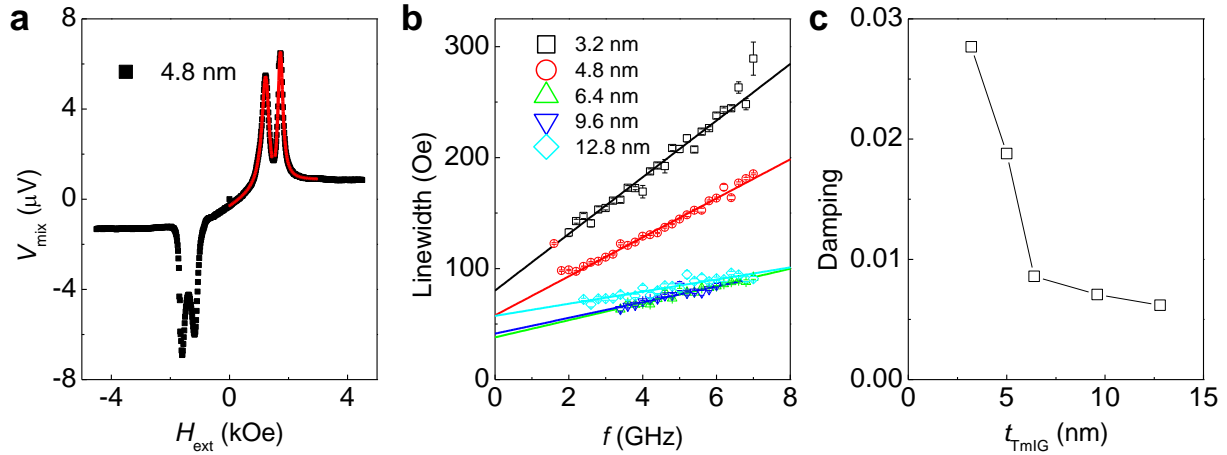


Figure 4-2 ST-FMR characterization of thickness dependent damping factors. (a) Spectra of a 4.8 nm-thick TmIG. Red curves are fits to the resonant peaks [64]. (b) Extracted linewidth of in-plane resonance peaks for different thicknesses. Solid curves are linear fits. The error bars originate from the fitting uncertainty. (c) Extracted damping factor as a function of the TmIG thickness. Reprinted with permission from [119]

The large lattice mismatch between the TmIG and the $\text{Nd}_3\text{Ga}_5\text{O}_{12}$ provides the tensile strain to generate perpendicular magnetic anisotropy in all TmIG thin films. The nature of perpendicular magnetic anisotropy is confirmed using magnetization hysteresis loops of TmIG thin films as a function of an out-of-plane magnetic field (Figure 4-1b), from which we can determine saturation magnetization (M_S). We observe a strong t_{TmIG} dependence of the M_S at room temperature (Figure 4-1c); the M_S reduces significantly from the bulk M_S (110 emu/cm^3) [131] with decreasing film thickness.

Note that the estimated dead layer thickness is less than 1 nm (see Figure 4-3), which also suggests a sharp interface between TmIG and substrate [118]. If we do a linear fit to thickness dependent magnetic moment per unit area M for thickness from 9.6 nm to 50 nm, we obtain a negligible MDL

thickness (t_{MDL}) around 0 nm (Figure 4-3a). We can calculate M_S by using $M_S = M/(t - t_{\text{MDL}})$ and the results are shown in Figure 4-3c, where the saturated value of M_S is around the bulk value 110 emu/cc from the literature. Alternatively, if we do a linear fit for thickness from 9 nm to 50 nm, we obtain a t_{MDL} around 1 nm (Figure 4-3b). Correspondingly, the obtained thickness dependent M_S is shown in Figure 4-3d, where values of M_S larger than 110 emu/cc are observed. This suggests that this 1 nm t_{MDL} is overestimated. Nevertheless, we still observe that the M_S increases dramatically as the TmIG thickness increases before the thickness reaches 10 nm. More importantly, the exact value of t_{MDL} will not affect our observations as follows. The dimensional crossover is observed using $M = M_0(1 - T/T_C)^\beta$, which describes the temperature dependence of magnetic moment and is irrelevant to the effective thickness ($t - t_{\text{MDL}}$). The SOT efficiency ($\xi_{\text{DL}} = \frac{2eMH_{\text{DL}}}{\hbar J_{\text{ac}}}$) and switching efficiency ($\eta = \frac{2eMH_{\text{P}}}{\hbar J_{\text{sw}}}$) only depend on the M , which is the measured areal magnetization, independent of the effective thickness ($t - t_{\text{MDL}}$).

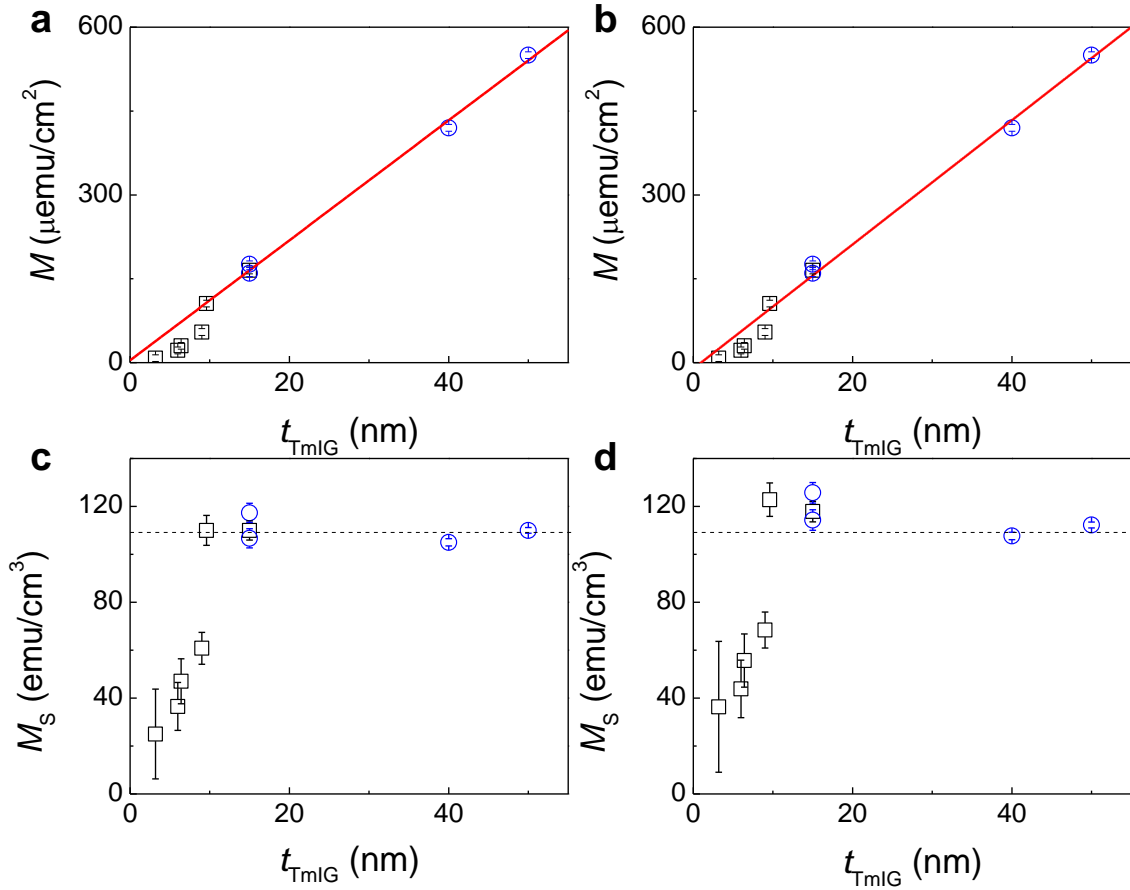


Figure 4-3 Thickness dependence of magnetic moment per unit area M and magnetic moment per unit volume M_S from different fitting ranges. Red curve is a linear fit to thickness ranging from 9.6 nm to 50 nm (a) and 9 nm to 50 nm (b). Black square symbols are films being used for SOT and switching studies. Blue circle symbols are additional films for determining magnetic dead layer. The estimated magnetic dead layer thickness is 0 nm for (a) and 1 nm for (b). (c) The calculated M_S a function of thickness for 0 nm magnetic dead layer. (d) The calculated M_S a function of thickness for 1 nm magnetic dead layer. The black dashed line in (c) and (d) is bulk magnetization value 110 emu/cc from literature [131]. The error bars stand for the measurement uncertainty. Reprinted with permission from [119]

The reduction of the M_S at room temperature is attributed to finite size effect, strong thermal fluctuation and strong surface modification effect in ultrathin magnetic films [132-134]. Following

ref. [133], we extract the critical exponents β for magnetic phase transitions in these TmIG thin films using temperature dependence of magnetic moment (M - T). The M - T curves follow the $M = M_0(1 - T/T_C)^\beta$ (Figure 4-1d), where zero-temperature magnetic moment (M_0) and Curie temperature (T_C) are fitting parameters. The t_{TmIG} dependent β is better illustrated using log-log plots as shown in Figure 4-1e and the results are summarized in Figure 4-1f. We see a clear increase of β from 0.16 ± 0.06 to 0.42 ± 0.02 when the t_{TmIG} increases from 3.2 nm to 15 nm, where the uncertainty is coming from the fitting. This increase of β suggests a dimensional crossover from two-dimension-like to three-dimension-like magnetism since 2D Ising model and 3D Heisenberg model predict β to be 0.125 and 0.365, respectively [134, 135]. The dimensional crossover happens at around 6 nm, which is one order of magnitude larger than the typical transition thickness around 1 nm for magnetic metals [133-135]. In the following Sessions, we point out that the reduction of M_s due to dimensional crossover has a major influence on the magnitude of the SOT and switching efficiency, which has been neglected in the previous experiments.

4.3.3 SOT measurement

To perform resistance, SOT and CIMS measurements, we fabricate W(5nm)/TmIG(t_{TmIG}) thin films into Hall bar devices (Figure 4-4a). By using four-probe resistance measurements in different Hall bar devices, we determine the W resistivity to be $155 \pm 15 \mu\Omega \cdot \text{cm}$, where the uncertainty is estimated from the multiple (> 20) device measurements. According to ref. [26], pure α -W has resistivity around $20 \mu\Omega \cdot \text{cm}$, and 6 nm-thick W with mixed α - and β -phases has a resistivity as high as $170 \mu\Omega \cdot \text{cm}$. So, most likely, our 5 nm-thick W thin films have mixed α - and β -phases. The AHR in the W/TmIG is accurately determined by the sharp anomalous Hall hysteresis at low fields

(Figure 4-4b). The transverse planar Hall resistance (PHR) accompanying the longitudinal SMR is measured by rotating the magnetization in the xy -plane (Figure 4-4c). The observation of sizeable AHR and PHR (SMR) indicates that there is a significant spin current being transmitted across the W/TmIG interface or a sizable spin mixing conductance [127] (see Session 5.2).

We quantify ξ_{DL} by using the second-harmonic analysis of both AHR and PHR (R_{AHE} and R_{PHE}) [52, 53]. The second-harmonic Hall resistance ($R_{\text{H}}^{2\omega}$) in a single domain subjected to an in-plane magnetic field can be written as [53, 55]

$$R_{\text{H}}^{2\omega} = R_{\text{FL}}^{2\omega} \cos 2\varphi \sin \varphi + R_{\text{DL}}^{2\omega} \sin \varphi = R_{\text{PHE}} \frac{H_{\text{FL}}}{|H_{\text{ext}}|} \cos 2\varphi \sin \varphi + \left(\frac{R_{\text{AHE}}}{2} \frac{H_{\text{DL}}}{|H_{\text{ext}}| - H_{\text{K}}} + R_{\text{SSE}} \right) \sin \varphi, \quad (4-1)$$

where H_{K} and H_{ext} are perpendicular magnetic anisotropy effective field and in-plane external field. In Eq. (4-1), $R_{\text{FL}}^{2\omega}$ and $R_{\text{DL}}^{2\omega}$ are the peak values of $\cos 2\varphi \sin \varphi$ and $\sin \varphi$ components in $R_{\text{H}}^{2\omega}$, which are field-like SOT and damping-like SOT contributions, respectively. H_{FL} and H_{DL} are the current-induced field-like and damping-like effective fields, respectively. For example, when the $H_{\text{ext}} = 2500$ Oe, we observe significant contributions from both damping-like and field-like SOTs, as reflected by the $\cos 2\varphi \sin \varphi$ and $\sin \varphi$ angle dependencies (see Figure 4-4d). According to Eq. (4-1), slopes of linear fits to the $R_{\text{DL}}^{2\omega}$ as a function of $1/(H_{\text{ext}} - H_{\text{K}})$ (Figure 4-4e) give the information about H_{DL} , and the intercepts are the spin Seebeck resistances (or voltages), which is field-independent in the single domain case (see Eq. (4-1)) [53, 136].

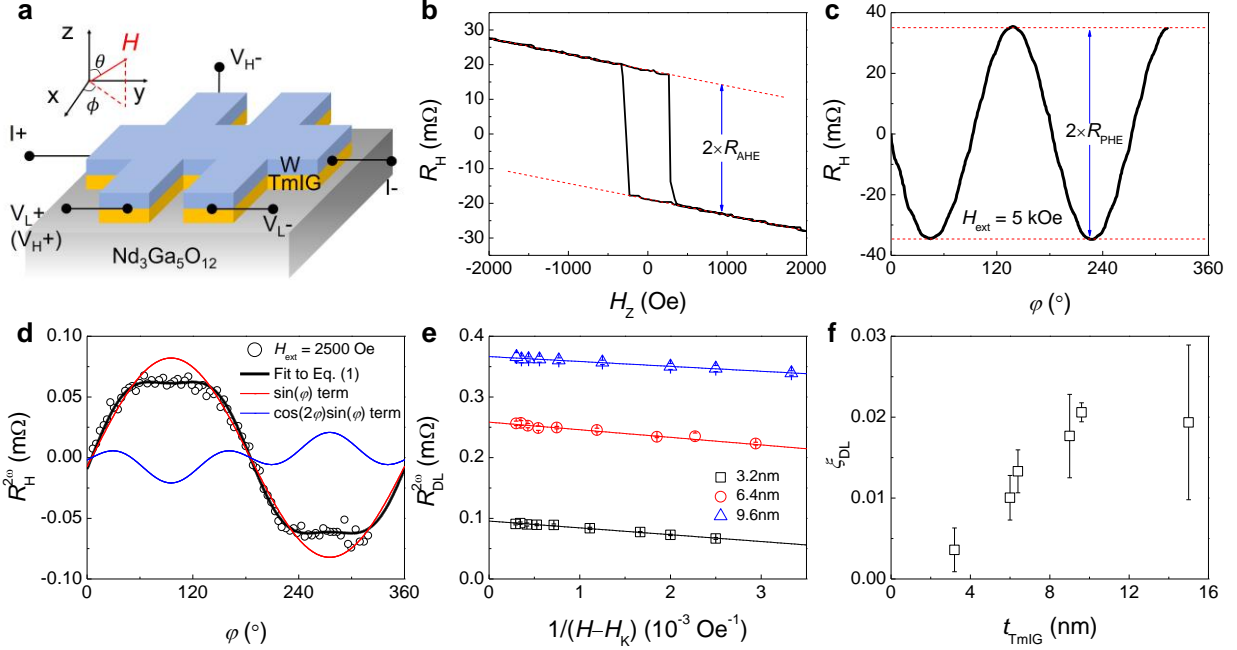


Figure 4-4 Spin transport and SOT measurements in the W/TmIG bilayers. (a) Experimental setup for measuring resistance, SOT and current-induced magnetization switching. (b) Hall resistance as a function of an out-of-plane magnetic field for the W (5 nm)/TmIG (9.6 nm), where AHE is observed as the sharp square hysteresis loop. (c) Hall resistance as a function of a rotating in-plane constant magnetic field (5 kOe) for the W (5 nm)/TmIG(9.6 nm), where SMR-induced PHE is observed. (d) Second-harmonic Hall resistance as a function of in-plane azimuthal angle for the external magnetic field 2500 Oe for the W (5 nm)/TmIG (3.2 nm), where the black curve is the fit to Eq. (1). Both $\cos 2\phi \sin \phi$ (blue curve) and $\sin \phi$ (red curve) angle dependencies are revealed. (e) Extracted damping-like torque contribution as a function of the inverse of external magnetic field subtracting the anisotropy field. The large intercepts are the spin Seebeck resistance. (f) Damping-like spin-orbit torque efficiency as a function of TmIG thickness. The error bar stands for the fitting uncertainty. Reprinted with permission from [119]

In principle, we can determine the field-like SOT effective field H_{FL} using Eq. (4-1). According to Eq. (4-1), slopes of linear fits to the field-like SOT contribution $R_{FL}^{2\omega}$ as a function of $1/H_K$ (Figure 4-5a) give the information of H_{FL} . Ideally, the intercepts should be close to zero. However, we do

observe large intercepts that accompany the large error bars in the $R_{\text{FL}}^{2\omega}$ of thicker TmIG devices (Figure 4-5a). The reason for the nonzero intercepts could be as follows. As the $R_{\text{FL}}^{2\omega}$ is divergent near zero field according to Eq. (4-1), the $R_{\text{FL}}^{2\omega}$ decreases significantly and becomes very small in the range 1500 – 5000 Oe that we use to pull magnetization to the in-plane single domain state for determining SOT efficiency. As a result, the dominant $\sin \varphi$ contribution $R_{\text{DL}}^{2\omega}$ will mix into the $\cos 2\varphi \sin \varphi$ part, resulting into a large error bar and sizeable intercept of $R_{\text{FL}}^{2\omega}$. Therefore, the quantitative determination of H_{FL} becomes difficult. Nevertheless, we can still estimate the field-like SOT efficiency by using $\xi_{\text{FL}} = \frac{2eM_{\text{st}}t_{\text{TmIG}}(H_{\text{FL}}+H_{\text{Oersted}})}{\hbar J_{\text{ac}}}$ (Figure 4-5b). Note that the current-induced Oersted field has been considered since it has the same symmetry as the field-like SOT effective field.

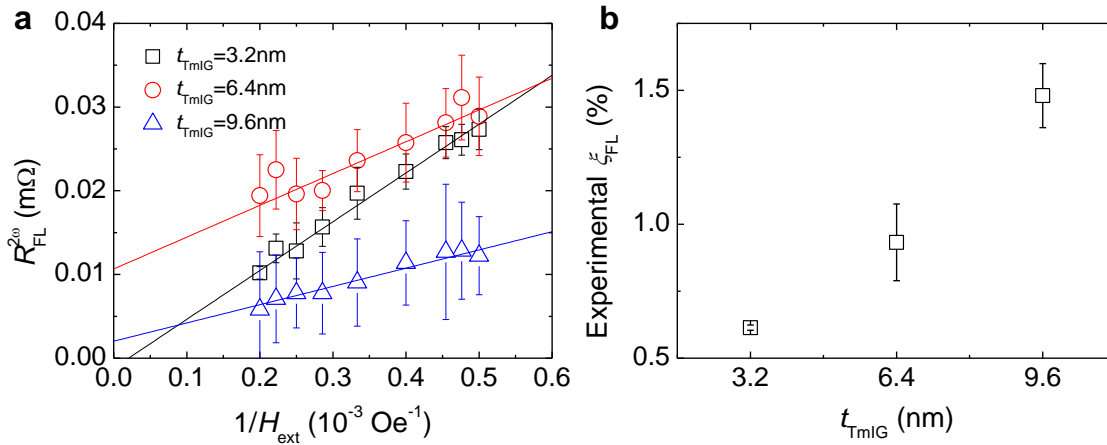


Figure 4-5 Field-like torque efficiency in W/TmIG. (a) Extracted field-like torque contribution ($R_{\text{FL}}^{2\omega}$) as a function of the inverse of external magnetic field. The intercepts are due to the uncertainty during the extraction of $R_{\text{FL}}^{2\omega}$, where the large signals with $\sin \varphi$ angle dependence come in [55]. (b) Field-like SOT efficiency as a function of TmIG thickness. The error bars originate from the fitting uncertainty. Reprinted with permission from [119]

We calculate ξ_{DL} using $\xi_{\text{DL}} = \frac{2eM_S t_{\text{TmIG}} H_{\text{DL}}}{\hbar J_{\text{ac}}}$ [33], where e is the electron charge, \hbar is the reduced Planck constant and J_{ac} is the applied current density. We observe a characteristic increase of ξ_{DL} as t_{TmIG} increases with a saturation length 10 nm (see Figure 4-4f). Similarly, previous experiments have revealed a saturation length around 1 nm in ferromagnetic metal heterostructures [51, 75, 130]. This saturation length is very close to the measured penetration depth of transverse spin current for ferromagnetic metals using spin pumping technique [137-139]. Thus, the saturation length has been interpreted as an indicator of penetration depth [138, 139]. However, for our MI TmIG thin films, the scenario becomes complex since the electron spin cannot directly tunnel into the MI and the magnetism of MI thin films is strongly dependent on the MI thickness (Figure 4-1). Note that the SOT efficiency ($\xi_{\text{DL}} \sim 0.02$) in our W/TmIG (≥ 9 nm) devices is smaller than that in β -W/CoFeB ($\xi_{\text{DL}} \sim 0.3$) [26]. There are two possible reasons. First, our W thin films are in mixed phases, which have a smaller spin Hall angle. Second, the material interfaces in W/magnetic metal and W/magnetic insulator bilayers could be very different [129], which requires further investigations.

4.3.4 Discussions on MI thickness-dependent SOT efficiency

Here, we discuss the mechanism for the MI thickness dependence of ξ_{DL} . We propose that ξ_{DL} depends on M_S when M_S of the thin films is well below the corresponding bulk value. The Landau–Lifshitz–Gilbert equation in the presence of damping-like SOT can be written as

$$M_S t_M \frac{d\hat{m}}{dt} = -\gamma M_S t_M \hat{m} \times \vec{H}_{\text{eff}} + \alpha M_S t_M \hat{m} \times \frac{d\hat{m}}{dt} + \gamma J_C \xi_{\text{DL}} \frac{\hbar}{2e} (\hat{m} \times \hat{\sigma} \times \hat{m}), \quad (4-2)$$

where \hat{m} is the unit vector of magnetization, $\hat{\sigma}$ is the unit vector of current-induced spin polarization, γ is the gyromagnetic ratio, α is the Gilbert damping, t_M is the thickness of the

magnetic layer, J_C is the charge current density, and $\vec{H}_{\text{eff}} (= \vec{H}_K + \vec{H}_{\text{ext}})$ is the total effective magnetic field acting on the magnetization. The last term on the right-hand side of Eq.(4-2) arises due to the absorption of transverse spin current by the magnet, which is referred to as the current-induced damping-like (dissipative) SOT. Its strength is parameterized by dimensionless efficiency parameters ξ_{DL} . The origin of the SOT can be understood in a simple microscopic picture as follows. A charge current at the heavy metal and ferromagnet interface induces an accumulation of spin density, $\rho\hat{\sigma}$, due to the finite spin-orbit interaction (for example, by SHE or Rashba-Edelstein effect). Here ρ is the magnitude of the spin density, which is proportional to the strength of the spin-orbit interaction. This spin density interacts with the ferromagnet via exchange interaction, of the form $U_{\text{ex}} \sim \rho M_S \hat{m} \cdot \hat{\sigma}$, enabling the absorption of the spin current by the ferromagnet. In the perturbative treatment, the spin current absorbed by the ferromagnet can be obtained up to second order in the exchange interaction to yield the damping-like spin-orbit torque with $\xi_{\text{DL}} \sim M_S^2$ [140]. The positive correlation between ξ_{DL} and M_S is referred as the M_S -effect; it has also been theoretically studied in the frame of spin pumping effect (in Appendix B of ref. [141]), which is the Onsager reciprocal process of the spin torque effect. The increase of spin mixing conductance with M_S is consistent with the calculation from first principles [142] when the surface modification effect presents in the ultrathin regime [143].

Our experiments are the demonstrations of the M_S -effect; we show that as the thickness increases, the SOT efficiency significantly increases with M_S in the low M_S -regime (see Figure 4-6), which is in qualitative agreement with the M_S -effect. Intuitively, as the magnetic moment density (M_S) increases, the interfacial exchange interaction is enhanced, which allows more spin current to pass through the interface. As the thickness increases, the SOT efficiency saturates earlier than M_S , around half of the bulk magnetization (60 emu/cm^3), which suggests that the SOT is determined

by the local magnetization that is saturated at a smaller thickness than the global magnetization M_S . Our experiments show the need for further investigation of the interaction between ultrathin magnetic films and heavy metals, which would include the spin physics of dimensional crossover.

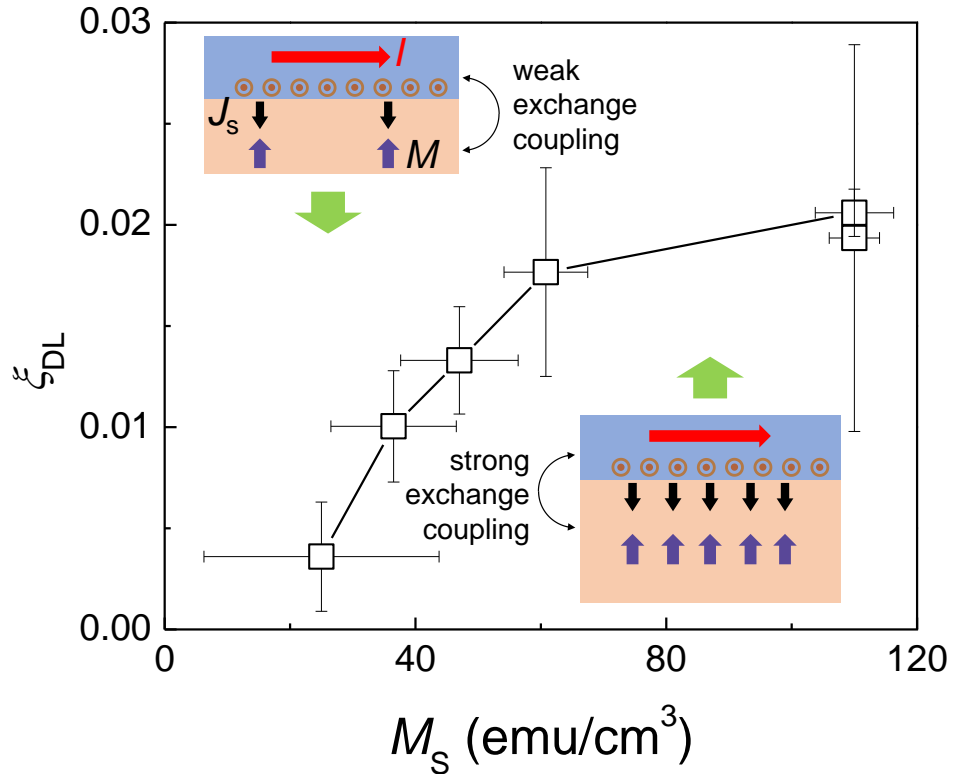


Figure 4-6 Role of TmIG M_S on the ξ_{DL} . ξ_{DL} is proportional to the M_S squared as shown in the text when the M_S is small due to strong thermal fluctuation and surface modification effect. Insets show two cases: in the left inset, the magnetic moment density is small and thus the interfacial exchange interaction is weak, resulting in a small spin current injection; in the right inset, the magnetic moment density is large due to suppressed thermal fluctuation and thus the interfacial exchange interaction is strong, resulting in a large spin current injection. Definitions of the error bars for M_S and ξ_{DL} are given in Figure 4-1 and Figure 4-4. Reprinted with permission from [119]

Also, we show that as the temperature decreases, the SOT efficiency increases with M_S , due to suppression of thermal fluctuations. We show the temperature dependence of M_S for three samples,

3.2 nm-, 6.4 nm- and 9.6 nm-thick TmIG thin films (Figure 4-7a), which were measured before the Hall bar device fabrication. Indeed, the difference between M_S 's of these three samples at low temperature (250 K) is slightly smaller than those at high temperatures (300 – 350 K).

We also performed second harmonic measurements at different temperatures to determine the temperature dependence of damping-like SOT efficiency $R_{FL}^{2\omega}$. We apply external field along the $\varphi = 45^\circ$ direction while we measure the second harmonic Hall resistance. Now, Eq. (4-1) becomes

$$R_H^{2\omega} = \frac{\sqrt{2}}{2} \left(\frac{R_{AHE}}{2} \frac{H_{DL}}{|H_{ext}| - H_K} + R_{SSE} \right),$$

which can be used to extract relevant damping-like SOT effective field H_{DL} . Figure 4-7b shows the thickness dependent second harmonic Hall resistance together with fitting curves. From Figure 4-7c, we observed that the difference between $R_{DL}^{2\omega}$'s in these three samples is significantly smaller than those at high temperatures (300 - 350 K). Our observations of temperature dependence of M_S and $R_{DL}^{2\omega}$ are qualitatively in agreement with the conclusion that the thermal fluctuations suppress the SOT efficiency.

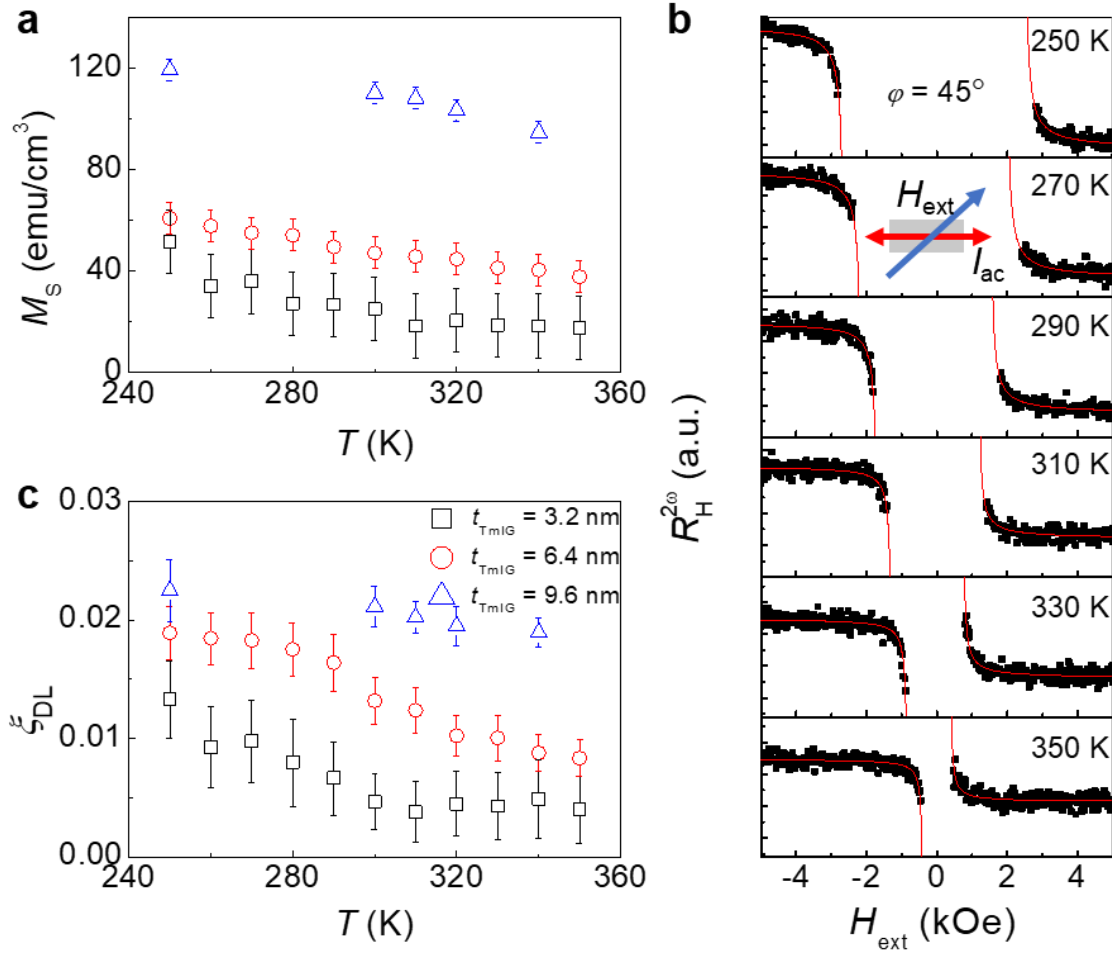


Figure 4-7 Temperature dependence of saturation magnetization M_S (a) and damping-like SOT efficiency $R_{\text{DL}}^{2\omega}$ (c) for different thicknesses. The error bars in (a) and (c) stand for the measurement uncertainty and fitting uncertainty, respectively. (b) Temperature dependence of second harmonic Hall resistance at different temperatures. The external field direction is $\varphi = 45^\circ$ as shown in the inset of top second panel. Reprinted with permission from [119]

We would like to emphasize that any mechanism that affects the M_S would in principle affect the SOT efficiency. Our data about thickness and temperature dependence of M_S and SOT efficiency strongly suggest that the role of thermal fluctuations is important. However, we cannot fully exclude other effects, such as the surface modification effect mentioned in ref. [134], which shows

that the surface modification effect in the ultrathin magnetic films could play an important role in determining the M_S .

There is a technical challenge to get an accurate damping-like spin-orbit torque (SOT) efficiency ξ_{DL} at lower temperatures (below 250 K) for thick TmIG samples. As described by Eq. (4-1), the second-harmonic Hall resistance $R_H^{2\omega}$ is divergent at the anisotropy field (H_K) since $R_H^{2\omega} = \frac{\sqrt{2}}{2} \left(\frac{R_{AHE}}{2} \frac{H_{DL}}{|H_{ext}| - H_K} + R_{SSE} \right)$ when $\varphi = 45^\circ$ and the external field is along the defined positive direction (Figure 4-8). When $\varphi = 45^\circ$ and the external field is along the defined negative direction, $R_H^{2\omega} = -\frac{\sqrt{2}}{2} \left(\frac{R_{AHE}}{2} \frac{H_{DL}}{|H_{ext}| - H_K} + R_{SSE} \right)$. Note that the contribution of spin Seebeck effect R_{SSE} is proportional to the in-plane magnetization (m_{ip}), which is a smooth (non-divergent) function from $+M_S$ to $-M_S$ that saturates at the $\pm H_K$ when the external field is swept from the large positive field to the large negative field. Therefore, the existence of the peaks due to damping-like SOT facilitates the accurate determination of the damping-like SOT effective field (H_{DL}) by fitting the region where the external field is larger than the H_K . In this work, we determine the temperature dependence of ξ_{DL} between 250 K and 350 K for TmIG samples with thickness 3.2 nm, 6.4 nm and 9.6 nm, where the peaks due to the damping-like SOT are well observed (Figure 4-8). As temperature decreases, the peaks become less clear (Figure 4-8). This problem is more apparent when the TmIG thickness increases since given the same ξ_{DL} , the larger TmIG thickness gives rise to a smaller H_{DL} according to $H_{DL} = \frac{\xi_{DL} \hbar J_{ac}}{2eM_S t_{TmIG}}$. By comparing the $R_H^{2\omega}$ for the W/TmIG(9.6 nm) and the W/TmIG (3.2 nm), we observe that the peaks due to the damping-like SOT are less clear in the W/TmIG(9.6 nm) at 250 K (Figure 4-8a), but very clear in the W/TmIG(3.2 nm) at 250 K (Figure 4-8b). Therefore, we cannot simply use the field-dependence of $R_H^{2\omega}$ to determine the H_{DL} in thicker TmIG films at lower temperatures, such as temperatures below 250 K.

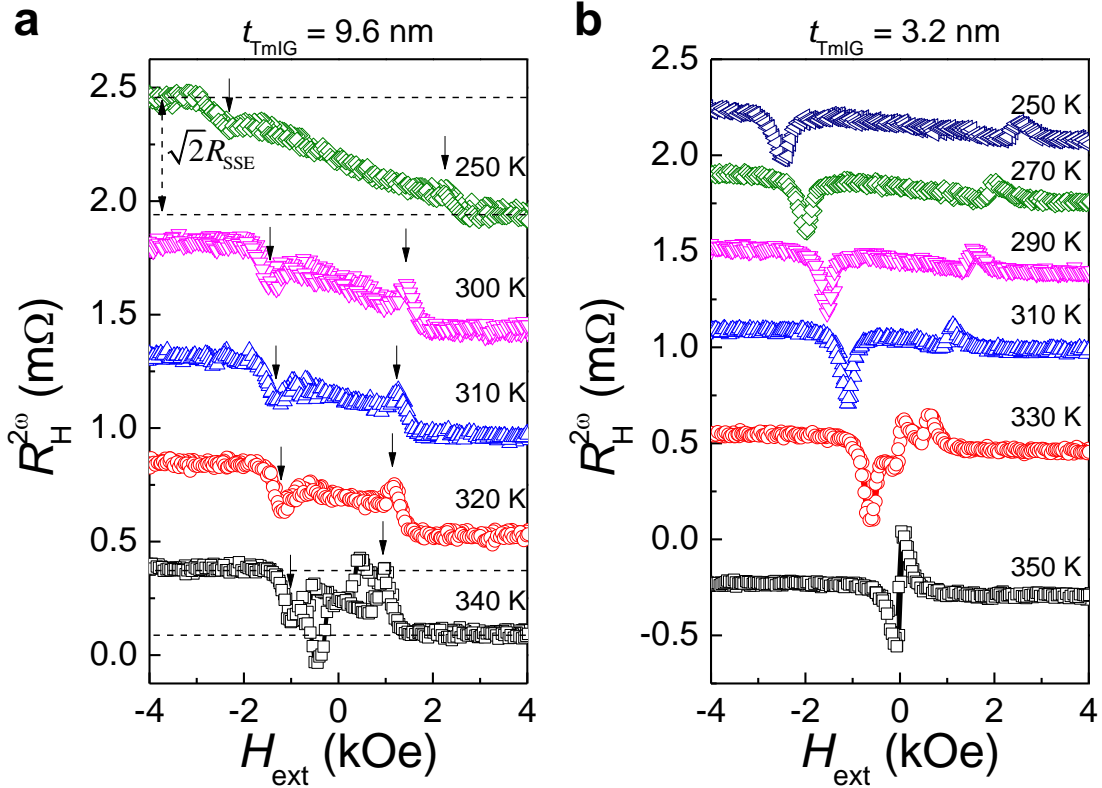


Figure 4-8 Second harmonic Hall resistance ($R_H^{2\omega}$) as a function of external in-plane magnetic field at different temperatures in the W/TmIG(9.6 nm) (a) and the W/TmIG(3.2 nm) (b), where $\varphi = 45^\circ$. The difference in the saturated $R_H^{2\omega}$ under large positive and negative fields is due to the spin Seebeck effect (R_{SSE}). The black arrows in (a) highlight the peaks due to damping-like spin-orbit torque. Reprinted with permission from [119]

In summary, we have systematically studied the dimensional crossover of magnetism and its effect on SOTs in ultrathin MI films with perpendicular magnetic anisotropy. The characteristic increase of SOT efficiency with the MI thickness can be understood from the enhancement of magnetic moment density and the suppression of thermal fluctuations. In addition, we have realized CIMS in W/TmIG devices with t_{TmIG} up to 15 nm. The switching current density for W/TmIG devices is lower or comparable with these for HM/ferromagnetic metals despite the fact that the saturated

ξ_{DL} is estimated to be only around 0.02 at this stage, which is much less than the 0.3 that is estimated for W in W/CoFeB bilayers [26]. Further improvement of the ξ_{DL} could be done by spin mixing conductance matching [144] and surface treatment [145]. Our results presented here show the great potential of ultrathin MI-based spintronics.

4.4 PMA switching of various magnetic insulators

In this Session, we demonstrate CIMS in several MIs to show the usefulness of SOTs.

4.4.1 SOT switching of W/TmIG

After quantifying the SOT efficiency, we perform the CIMS experiments for W/TmIGs with different t_{TmIG} . The switching is achieved in all devices with t_{TmIG} up to 15 nm and the switching phase diagrams are summarized in Figure 4-9a. In the presence of an external field along the +y direction, a sufficiently large charge current along the +y direction will cause magnetization (AHR) switching from the +z direction to the -z direction (negative to positive). The required amount of charge current to flip the magnetization decreases as the external field increases. When we apply a sufficiently large charge current along the -y direction while keeping the external field along the +y direction, the magnetization (AHR) is switched from the -z direction to the +z direction (positive to negative) (upper panels in Figure 4-9b and Figure 4-9c). For the same current direction, the switching direction is opposite when we reverse the external field direction (lower panels in Figure 4-9b and Figure 4-9c). All of the above facts agree with the picture of SOT-driven magnetization switching. Note that the switching current density is as low as 6×10^{10} A/m² for the W(5 nm)/TmIG (9.6 nm) (Figure 4-9b), which is three times smaller than the Pt(5 nm)/TmIG(8 nm) case [50]. This suggests that W enables more energy efficient magnetization switching.

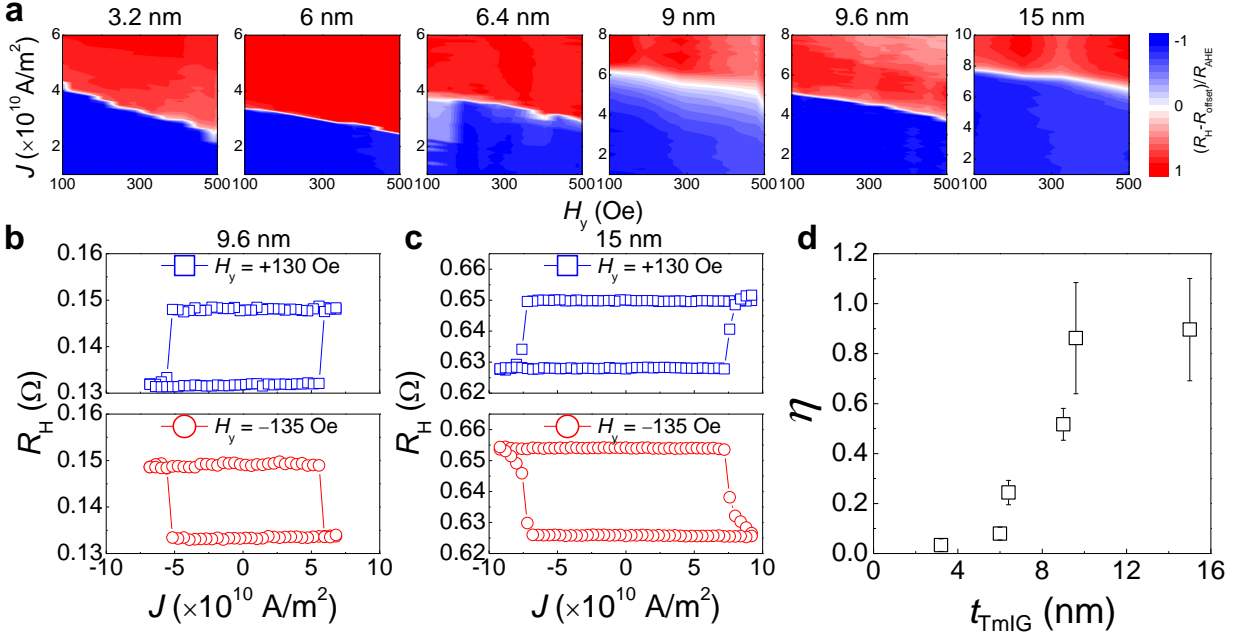


Figure 4-9 Current-induced magnetization switching in W/TmIG with different TmIG thicknesses. (a) Switching phase diagram for TmIG with thicknesses from 3.2 nm to 15 nm, where the external field is along the current direction. R_{offset} is device-dependent Hall resistance offset. For instances, (b) and (c) show the current-induced switching for TmIG with thickness 9.6 nm and 15 nm, respectively, in the presence of a magnetic field along and against the current direction. The switching is done by applying a 5 ms pulse with varying current amplitude. (d) TmIG thickness dependent current switching efficiency, which is estimated from the depinning (coercive) field over switching current density in the zero-external field limit. The error bar originates from the multiple (> 3) device measurements. Reprinted with permission from [119]

The switching direction driven by current-induced SOTs is consistent with the sign of the spin Hall angle of W, and it is opposite to that in the Pt/TmIG bilayer [50]. Therefore, our work strongly suggests the dominant role of the SHE in the generation of SOTs and CIMS in HM/MI bilayers. However, we do notice that there could be an interfacial Rashba-Edelstein effect at the W/TmIG

interface contributing to the SOTs by comparative analyses of SOTs and SMR(AHR) as explained below.

Here, we present the inconsistency of determined spin transparency T_r between SMR and ξ_{DL} .

After we obtaining $G_{\uparrow\downarrow}$ using SMR as done in see Session 5.2, we can calculate the spin

transparency following $T_r = \text{Re} \frac{2G_{\uparrow\downarrow} \tanh \frac{d}{2\lambda}}{\frac{1}{\rho\lambda} + 2G_{\uparrow\downarrow} \coth \frac{d}{\lambda}}$ [127]. On the other hand, the T_r can also be directly

determined using $T_r = \frac{\xi_{DL}}{\theta_{SH}}$ [75, 127]. In Figure 4-10, we plot the TmIG thickness dependent T_r

estimated from ξ_{DL} and SMR with different λ 's. The quantitative difference suggests the complex

relation between spin current effect and interfacial spin transparency. A good match with

extremely small (and unrealistic) λ highlights the importance of interfacial effects, such as Rashba-

Edelstein effect. Note that another interfacial effect, magnetic proximity effect, is not considered

since the W is far away from the Stoner instability.

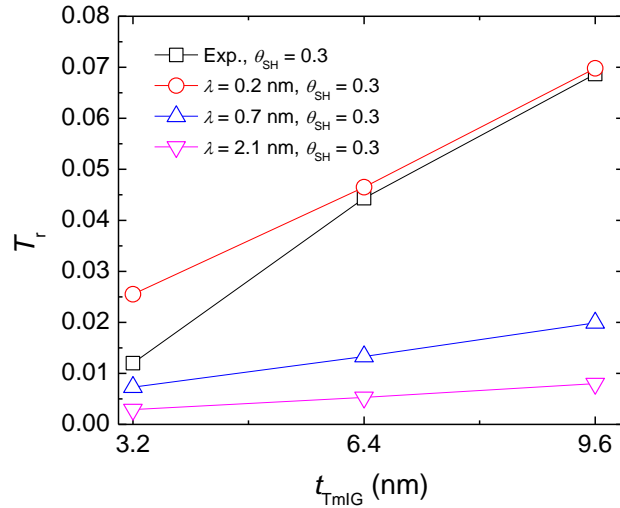


Figure 4-10 Values of T_r estimated from ξ_{DL} and SMR. We assume the spin Hall angle is 0.3 [26] and the spin diffusion length varies from 0.2 nm to 2.1 nm [72, 146]. Reprinted with permission from [119]

To quantitatively compare the switching efficiency of W/TmIG devices with different t_{TmIG} , we define an effective switching efficiency as $\eta = \frac{2eM_S t_{\text{TmIG}} H_P}{\hbar J_{\text{sw}}(H_y \rightarrow 0)}$ [147], where H_P is the domain wall depinning field estimated from the coercive field (Figure 4-11) and $J_{\text{sw}}(H_y \rightarrow 0)$ is the zero-field limit of current density in the switching phase diagram. This formula is chosen because the CIMS is achieved through domain nucleation and domain wall motion in the Hall bar devices due to the large scale of our Hall bar devices, of which the channel width is 20 μm [80]. We observe a dramatic increase of η with t_{TmIG} (Figure 4-9d), for which we consider two reasons. First, the ξ_{DL} increases with t_{TmIG} , which means that the same amount of charge current in the W layer generates stronger damping-like SOT on the TmIG layer. Thus, the increase of ξ_{DL} contributes to a lower J_{sw} and thus a larger η . Second, the Joule heating effect becomes much more significant when a larger charge current is applied, which is the case for switching a thicker TmIG. Joule heating causes reduction of thermal stability through decreasing the M_S and H_P ; these two values will be smaller than those measured at the low current limit. Therefore, the M_S and H_P used to calculate η are overestimated, leading to a larger η .

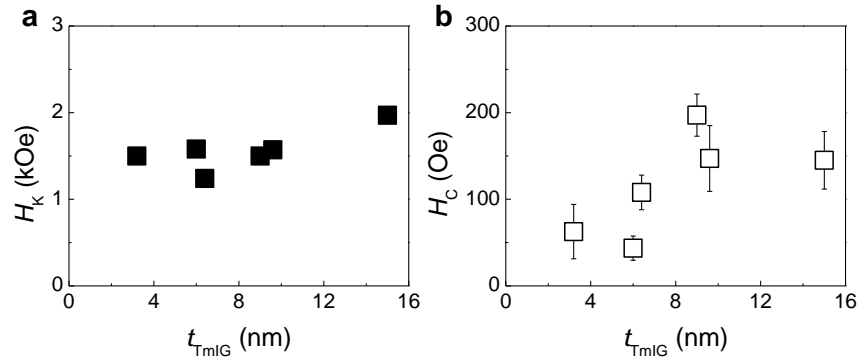


Figure 4-11 TmIG thickness dependent PMA effective field (a) and coercive field (b) at room temperature. The error bar in (b) is from the variation of coercive fields in different Hall bar devices. The error bars are estimated from the multiple (> 6) device measurements. Reprinted with permission from [119]

4.4.2 SOT switching of Pt/TmIG

We have also studied CIMS in Pt/TmIG [56] and SOT-switching results of TmIG(3.2nm)/Pt(4nm) are shown in Figure 4-12. The switching polarity is opposite with the W/TmIG case, which is consistent with the sign of spin Hall angle. During switching experiments, we apply 5 ms-long

pulse currents with varying amplitude (between -8 and $+8$ mA) and then use 0.1 mA to read out the Hall resistance subsequently.

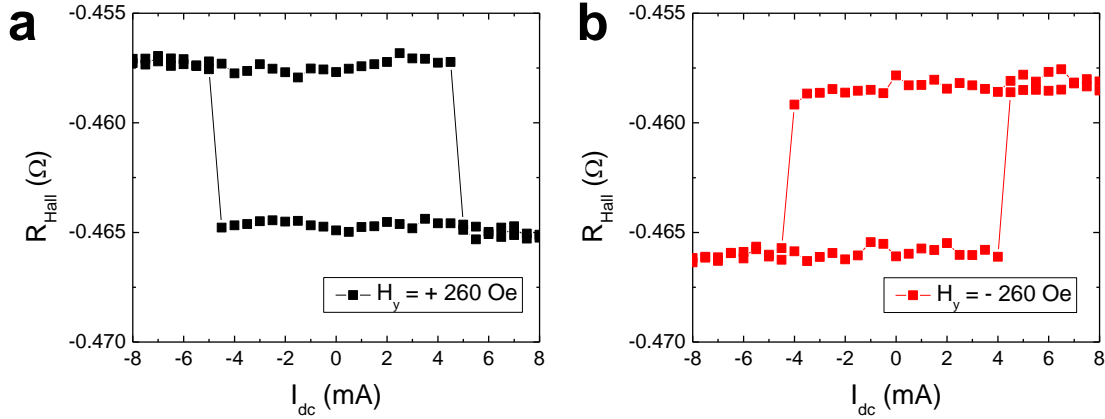


Figure 4-12 Current-induced magnetization switching in a TmIG(3.2 nm)/Pt(4 nm) Hall bar device at room temperature with positive and negative bias fields. **a**, The applied bias field is 260 Oe along the $+y$ direction. **b**, The applied bias field is 260 Oe along the $-y$ direction

4.4.3 SOT switching of nearly compensated FMI TbIG

To achieve ultrafast switching of FMI at room temperature, we need to design the material to have a T_A close to room temperature. Here, we show that across the T_M of 6 nm-thick TbIG, CIMS can always be observed, which suggests that the SOT can efficiently drive antiferromagnetic switching. To characterize the T_M , we study the temperature dependence of the out-of-plane hysteresis loops. From the temperature dependence of anomalous Hall resistance, we can obtain the T_M , at which the anomalous Hall sign suddenly flips (Session 5.1). From Figure 4-13, we can tell that the for this TbIG thin film, the T_M is around 353 K.

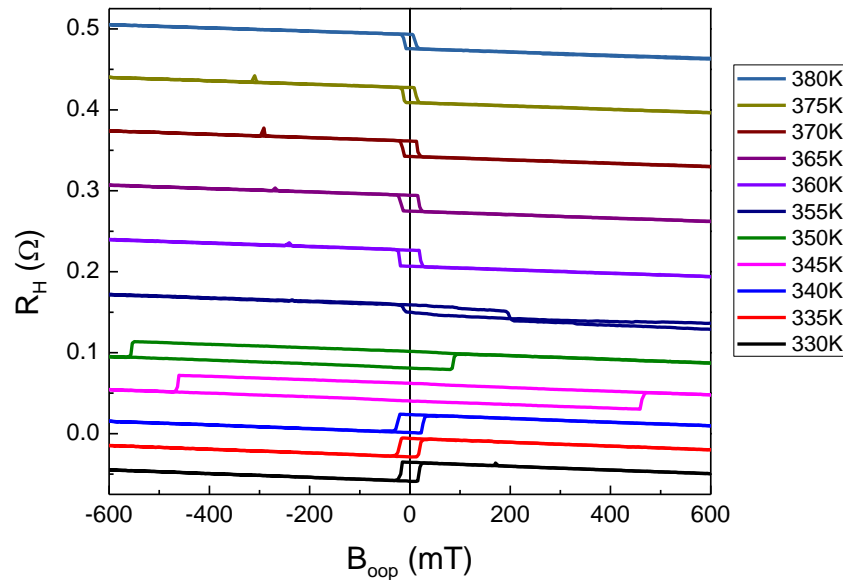


Figure 4-13 Temperature dependence of out-of-plane hysteresis loops in W/TbIG

I observed CIMS in the W/TbIG both below T_M (Figure 4-14a) and above T_M (Figure 4-14b). Note that the external field definition for the W/TbIG is opposite to previous two cases: W/TmIG and Pt/TmIG. Since the anomalous Hall resistance changes sign and the spin Hall effect does not change sign (SOT always acts on the net magnetization) across the T_M , we expect to see an opposite switching polarity for these cases as shown in ref. [105]. I didn't observe an opposite switching polarity in the CIMS experiment. To understand the reason, I first studied the temperature dependence of switching current, where I found an increasing switching current as the temperature reduces (Figure 4-14c). This is reasonable since the anisotropy energy gets larger as the temperature decreases, which makes the switching harder. More importantly, I measured the resistance vs temperature curve and resistance under the applied small d.c. current (up to 4 mA), from which I estimated the temperature increase due to the applied d.c. current (Figure 4-14d). I conclude that no matter what temperature the device was measured, the device temperature during the switching is always above the T_M . Therefore, there is no switching polarity switch.

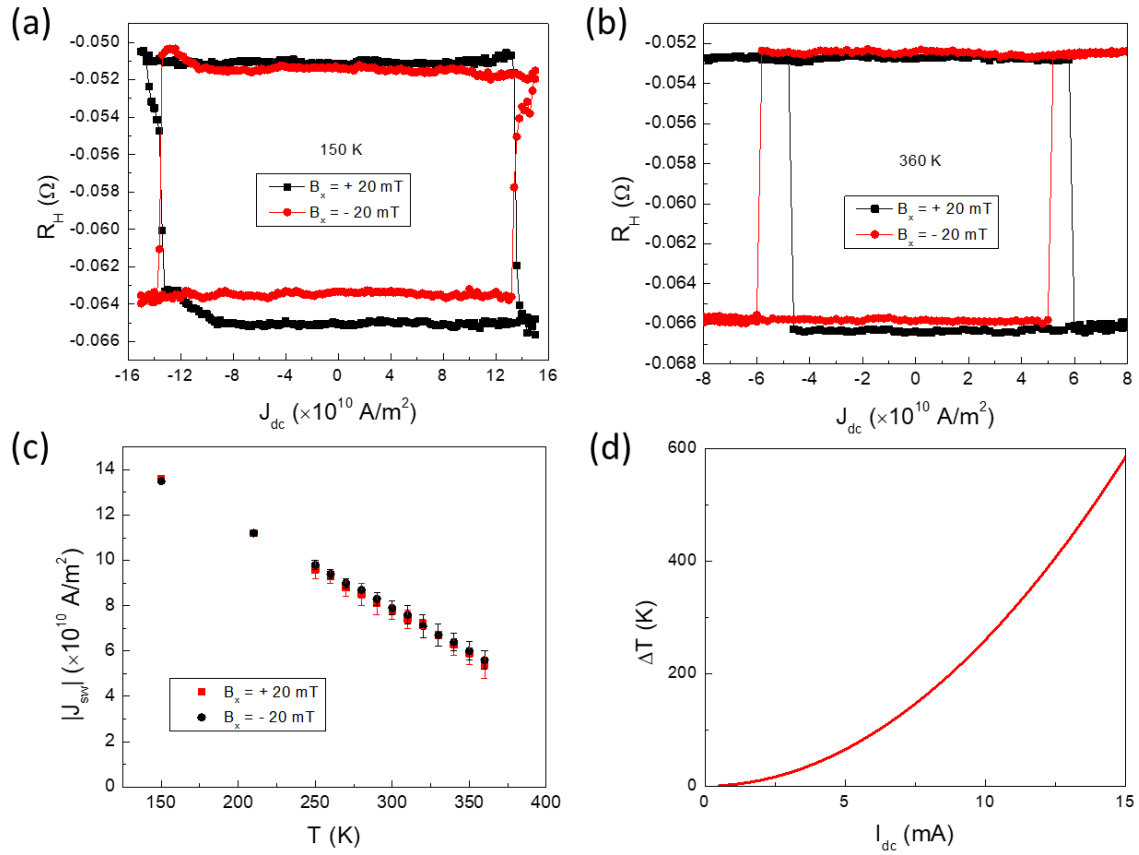


Figure 4-14 Heat-assisted SOT switching of TbIG. CIMS in W/TbIG at 150 K (a) and 360 K (b), which are below T_M and above T_M , respectively. (c) Switching current density as a function of temperature. (d) Estimated temperature increase due to applied d.c. current

Chapter 5 Proximity coupling between magnetic and nonmagnetic materials

Probably, the most well-known proximity effect in solid-state systems could be the Josephson effect, which describes the tunneling supercurrent across a superconducting/non-superconducting/superconducting junction [148]. In a Josephson junction, the superconductor could induce superconducting state in an adjacent non-superconducting material. Similarly, people are thinking about the magnetic proximity effect, where the magnetic material can induce magnetic state in an adjacent nonmagnetic material. This effect has been well observed in metallic systems using X-ray magnetic circular dichroism (XMCD). For example, while Pt has zero magnetic moment (zero spin splitting at the Fermi level), the Pt in the Pt/Fe bilayer develop a spontaneous magnetic moment (finite spin splitting at the Fermi level), which has been resolved by XMCD [149]. Recently, people start to investigate the proximity effect between nonmagnetic materials and magnetic insulators because the magnetic insulators could provide the magnetic proximity effect without introducing free electrons. In this case, the transport properties of the nonmagnetic materials can be well analyzed.

5.1 Anomalous Hall effect

We use temperature dependent Hall measurements to identify contributions of spin Hall, magnetic proximity, and sublattice effects to the anomalous Hall signal in heavy metal/ferrimagnetic insulator heterostructures with perpendicular magnetic anisotropy. This approach enables detection of both the magnetic proximity effect onset temperature and magnetization compensation temperature and provides essential information regarding the interfacial exchange coupling. Onset of a magnetic proximity effect yields a local extremum in the temperature dependent anomalous

Hall signal, which occurs at higher temperature as magnetic insulator thickness increases. This magnetic proximity effect onset occurs at much higher temperature in Pt than W. The magnetization compensation point is identified by a sharp anomalous Hall sign change and divergent coercive field. We directly probe the magnetic proximity effect using X-ray magnetic circular dichroism and polarized neutron reflectometry, which reveal an antiferromagnetic coupling between W and magnetic insulator. At last, we summarize the exchange coupling configurations and the anomalous Hall effect sign of the magnetized heavy metal in various heavy metal/magnetic insulator heterostructures.

Like magnetic metals, ferrimagnetic insulators (FMIs) enable information storage and propagation through magnetization direction and spin wave transport, respectively. Unlike metallic systems, however, spin currents in FMIs do not require a commensurate charge transport component and thus are free of current-induced Joule heating, a beneficial feature for low power spintronic applications [108]. However, the electrical readout of magnetization and spin waves in FMIs have been challenging until the recent discovery of the inverse spin Hall effect (SHE) [109]. The inverse SHE in a heavy metal (HM) layer allows conversion from magnon spin current to charge current at the HM-FMI interface. In addition, the combined action of SHE and inverse SHE can give rise to a spin Hall magnetoresistance and anomalous Hall effect (AHE) [126, 127] (Figure 5-1a). Interestingly, the sign of AHE in some HM/FMI systems can be tuned by varying the temperature [150-153]. Studies on the temperature dependence of magnetoresistance [154] and the AHE [152] have suggested the important role of the magnetic proximity effect (MPE), which appears below an onset temperature ($T_{\text{on,MPE}}$) and induces a spontaneous magnetization in the interfacial HM layer. The magnetized HM produces an AHE (Figure 5-1b), the sign of which may be different from that due to the SHE. Currently, a great deal of important information about the MPE, such as

the onset temperature and whether ferromagnetic or antiferromagnetic exchange coupling is preferred, must be investigated by using spectroscopic or scattering techniques, such as X-ray magnetic circular dichroism (XMCD) and polarized neutron reflectometry (PNR), which require large facilities to implement.

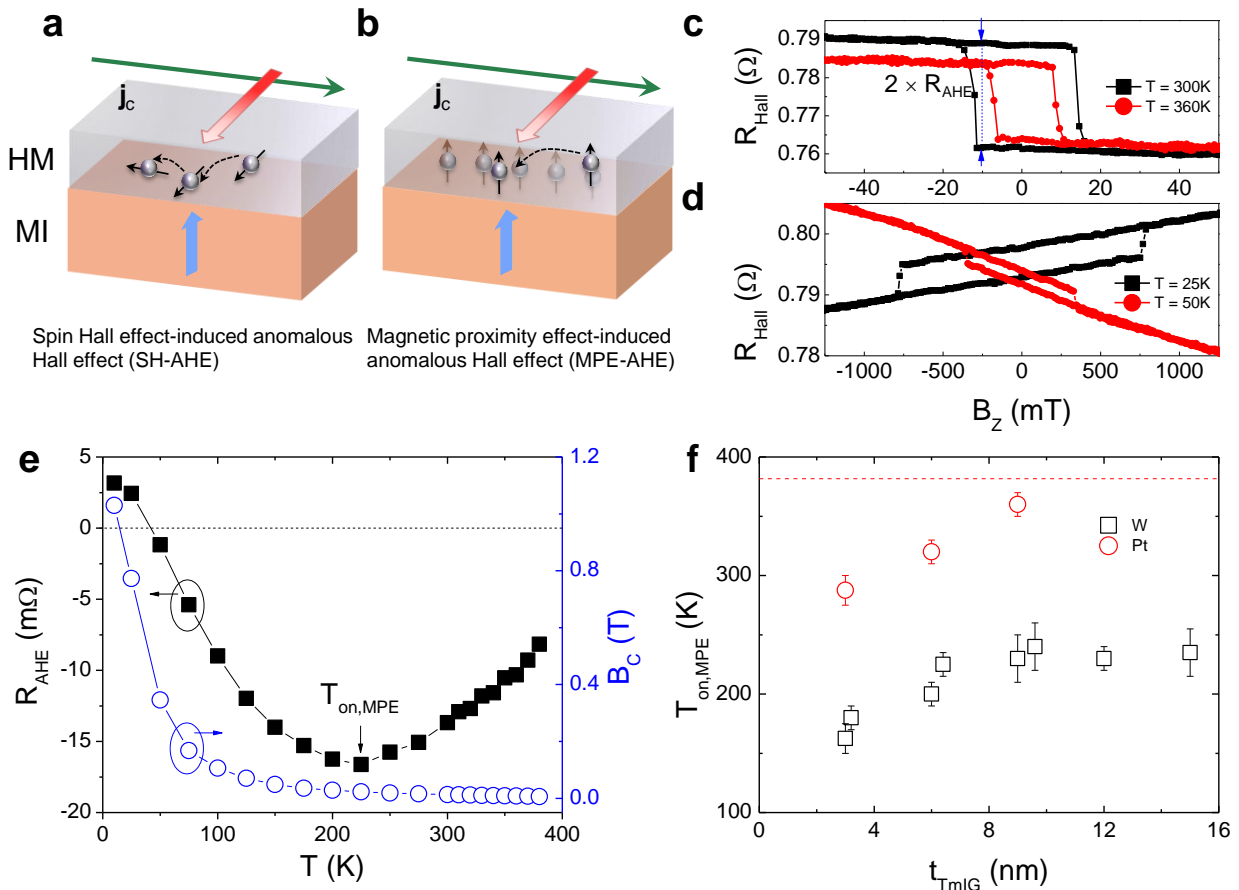


Figure 5-1 Temperature dependent AHE in HM/TmIG. (a-b) Schematics of SH-AHE and MPE-AHE, respectively, in HM/magnetic insulator heterostructures. For the SH-AHE, the reflected spin angular momenta are rotated by 90 degrees compared with the incident spin angular momenta due to spin-dependent scattering at the interface. This rotated spin angular momenta create a transverse charge current due to inverse SHE, resulting in an AHE. For the MPE-AHE, the AHE is from the interfacial magnetized HM layer due to the MPE. (c-d) Hall resistance as a function of out-of-plane magnetic field for $T = 300$ K and 360 K (c) and $T = 25$ K and 50 K (d) for a W(5 nm)/TmIG(15 nm) bilayer. (e) AHE resistance and coercive field of out-of-plane hysteresis loops

as a function of temperature for a W(5 nm)/TmIG(15 nm) bilayer. MPE onset temperature is indicated by the arrow $T_{\text{on,MPE}}$. (f) Onset temperature as a function of TmIG thickness in both the W/TmIG and Pt/TmIG. The error bars reflect standard deviations from multiple measurements. Reprinted with permission from [155], Copyright (2019) American Physical Society

Another important feature of FMIs is that they consist of multiple antiferromagnetically coupled magnetic sublattices, leading to a high characteristic frequency which is essential for high-speed spintronic applications [108]. In some cases, the different temperature dependencies of the sublattice magnetizations cause a magnetization compensation temperature (T_M), at which the net magnetization is zero. The T_M is typically characterized using a bulk volume sensitive magnetometer, such as superconducting quantum interference devices. To probe local T_M in ultrathin FMI films, an alternative method is required. Although the AHE has been used as a local probe to detect T_M in ferrimagnetic metals [105, 113], it cannot directly probe an insulating system. As described above, by combining a HM with a FMI, the magnon spin current from the FMI, spin Hall magnetoresistance and AHE can be measured through inverse SHE. While the magnon spin current excited by the spin Seebeck effect [156] and spin Hall magnetoresistance [157] have been used to probe the T_M , the AHE remains an unexplored avenue.

In this Session, we demonstrate that the AHE provides an electrical desktop microprobe for detecting and separating AHE contributions, SHE, MPE, and sublattice orientation, in thin film bilayers consisting of tungsten (W) or platinum (Pt) and FMI thulium iron garnet ($\text{Tm}_3\text{Fe}_5\text{O}_{12}$, TmIG) or terbium iron garnet ($\text{Tb}_3\text{Fe}_5\text{O}_{12}$, TbIG). The observation of a local extremum in the AHE temperature dependence allows us to identify $T_{\text{on,MPE}}$, which increases with TmIG thickness and is much higher in Pt than W. The T_M is identified by a sudden AHE sign change commensurate with a divergent coercive field (B_C). To confirm this interpretation, we directly probe the MPE using

XMCD (Session 5.3) and PNR (Session 5.4), which indicate antiferromagnetic exchange coupling between the W and the TmIG. Our data suggest that the Fe sublattice dominates the interfacial exchange coupling. These results provide a comprehensive picture of interfacial exchange coupling and sublattice effects in HM/FMI bilayers, which can be utilized in applications based on spintronics[50, 118, 119, 158], magnonics[109], and spin caloritronics [122].

5.1.1 Materials and methods

All TmIG(111) films were grown on $\text{Nd}_3\text{Ga}_5\text{O}_{12}$ (111) by pulsed laser deposition [117]. The TmIG films were grown at a moderate temperature of $\sim 200^\circ\text{C}$ by KrF excimer laser pulses of 248 nm in wavelength with a power of 150 mJ at a repetition of 1 Hz under 1.5-mtorr oxygen pressure with 12 wt% ozone. Rapid thermal annealing processes were performed at 800°C for 5 min to magnetize the TmIG films. Each film has a nominal area $5\text{ mm} \times 5\text{ mm}$. We deposited W(5 nm)/MgO(2 nm)/TaO_x(3 nm) and Pt(5 nm) layers on top of TmIG using magnetron sputtering. For TmIG thicknesses 3 nm, 6 nm, 9 nm, 12 nm and 15 nm, W and Pt thin films each cover $2.5\text{ mm} \times 5\text{ mm}$. For other TmIG thicknesses, only W thin films are deposited on the TmIG. We also prepare the W/TbIG and Pt/TbIG thin films with detailed structures: GGG(111)/TbIG(6 nm)/W(5 nm)/MgO(2 nm)/ TaO_x(3 nm) and GGG(110)/TbIG(6 nm)/Pt(5 nm). The growth recipe for TmIG and TbIG thin films are the same.

The HM/FMI thin films were patterned into Hall bar devices by using standard photolithography and dry etching for the four-probe lock-in resistance measurements. The magnetic field and temperature control were performed with a physical property measurement system.

5.1.2 Onset temperature of magnetic proximity effect

We first discuss contributions to the AHE and their temperature dependence, which allows detection of $T_{\text{on,MPE}}$. The MPE becomes pronounced when interfacial exchange coupling between the W and the TmIG is strong enough to suppress thermal fluctuations and induce a spontaneous magnetic moment in the interfacial HM layer. Magnetization induced by the MPE will give rise to an AHE, which we refer to as MPE-AHE (Figure 5-1b). At higher temperature, thermal fluctuations dominate, disrupting the spontaneous W magnetization and eliminating the MPE-AHE. Even in the absence of the MPE, however, spin current transmitted across and reflected at the W/TmIG interface through the SHE and inverse SHE can give rise to an anomalous Hall signal [126], which we refer to as SH-AHE (Figure 5-1a). A sign change or local extremum of the AHE may occur when a low-temperature MPE-AHE has the opposite sign of the SH-AHE which dominates at elevated temperatures.

To probe these contributions through transport measurements, we use $\text{Nd}_3\text{Ga}_5\text{O}_{12}$ (111)/TmIG (t_{TmIG})/(W, Pt)(5 nm)/MgO(2 nm)/TaO_x(3 nm), where t_{TmIG} is the TmIG thickness. We observe a clear AHE with a square hysteresis loop in the W/TmIG (Fig. 1c) due to the perpendicular magnetic anisotropy of TmIG thin films. In W/TmIG, the observed SH-AHE sign at room temperature is negative and the magnitude increases as temperature decreases from 360 K to 300 K due to increased spin mixing conductance [126, 141, 159]. As temperature is reduced further, we observe signatures of a MPE-AHE-related sign change in the W/TmIG (Figure 5-1d). This behavior cannot be explained by a T_M since the B_C does not exhibit a divergent behavior (Figure 5-1e). This suggests an emergent low-temperature MPE with an induced MPE-AHE with a positive sign. To understand how the MPE varies with temperature, we analyze the temperature dependence of the AHE resistance (Figure 5-1e). Additional AHE and B_C data in W/TmIG are

shown in Figure 5-2 and Figure 5-3, respectively. Additional AHE and B_C data in Pt/TmIG are shown in Figure 5-4 and Figure 5-5, respectively.

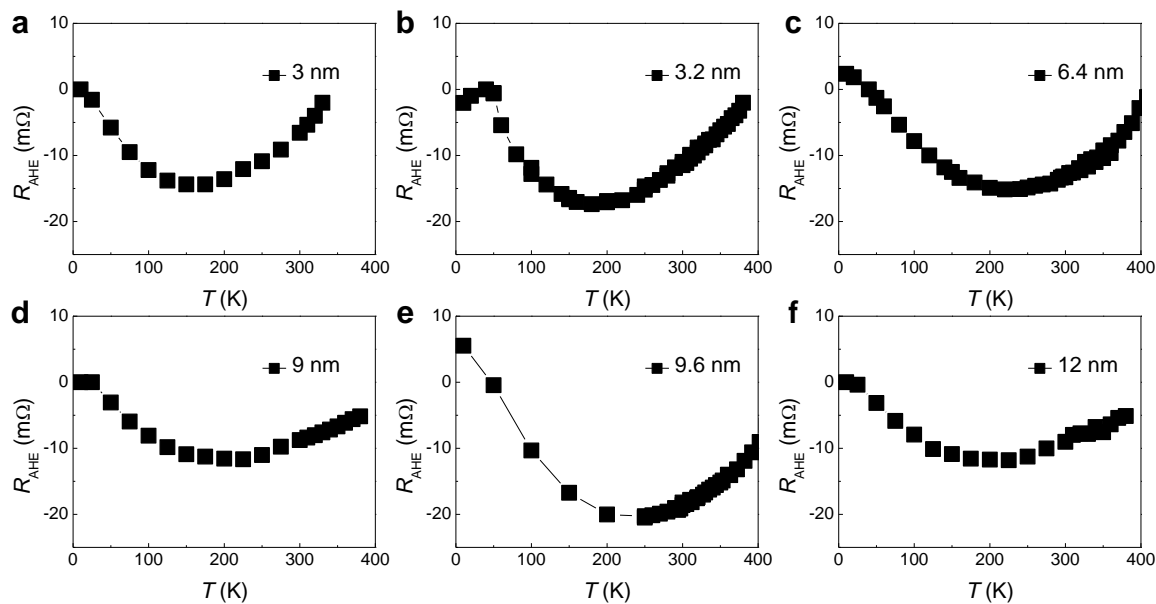


Figure 5-2 Temperature dependence of R_{AHE} in W/TmIG bilayers with different TmIG thickness. Reprinted with permission from [155], Copyright (2019) American Physical Society

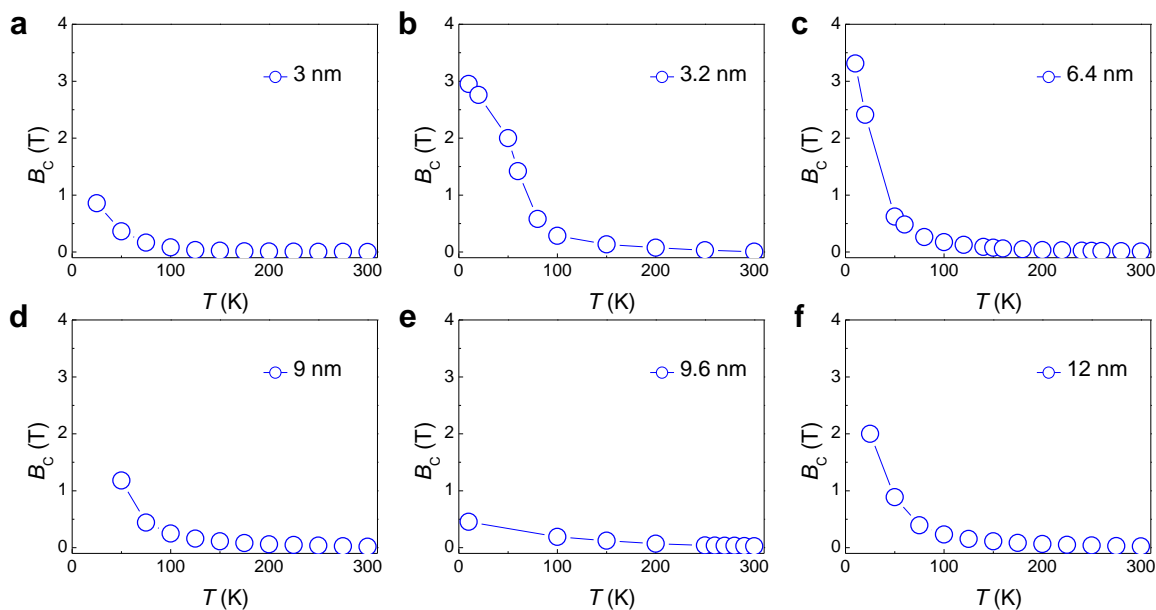


Figure 5-3 Temperature dependence of B_C in W/TmIG bilayers with different TmIG thickness. Reprinted with permission from [155], Copyright (2019) American Physical Society

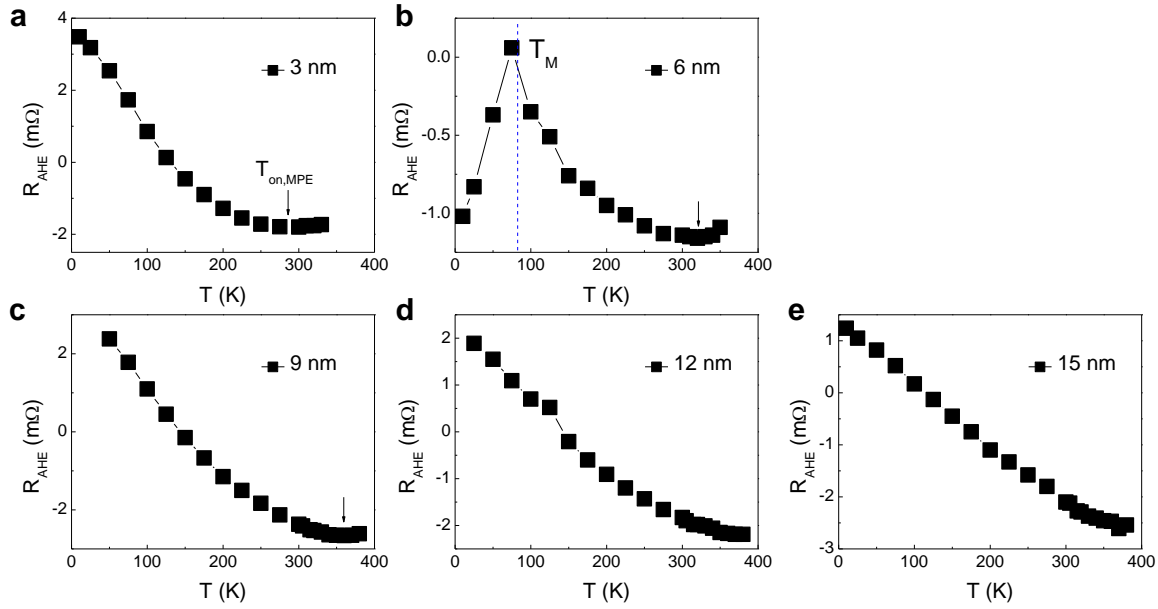


Figure 5-4 Temperature dependence of R_{AHE} in Pt/TmIG bilayers with different TmIG thickness. Reprinted with permission from [155], Copyright (2019) American Physical Society

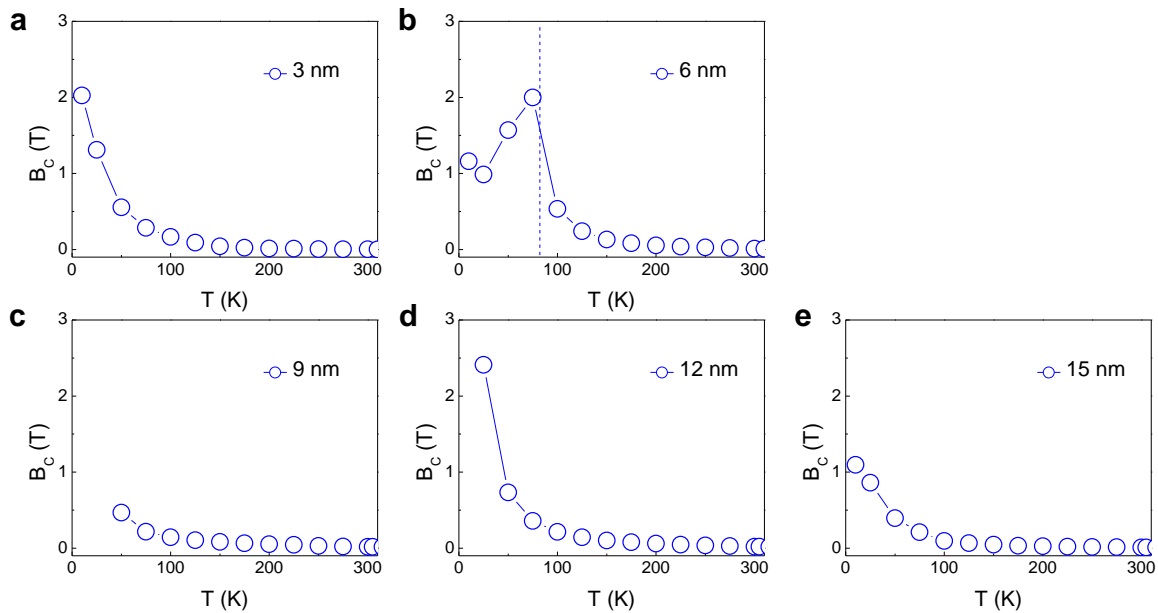


Figure 5-5 Temperature dependence of B_C in Pt/TmIG bilayers with different TmIG thickness. Reprinted with permission from [155], Copyright (2019) American Physical Society

As the temperature is reduced from above room temperature to low temperature (10 K), the anomalous Hall signal first increases in magnitude then decreases, with the extremum identified as T_{ex} , before reversing sign. As the temperature is reduced, interfacial exchange dominates over the thermal fluctuations, stabilizing a MPE and contributing a positive AHE signal opposing the negative SH-AHE. Further, we note that MPEs are known to suppress the SHE and may reduce the spin mixing conductance [160]. Therefore, we expect an extremum near but somewhat below $T_{\text{on,MPE}}$, which may then be used to indicate of $T_{\text{on,MPE}}$ (Figure 5-1e). There are four primary reasons to draw this conclusion.

First, it has been predicted that in the absence of a MPE, the spin Hall effect (SHE)-induced AHE (SH-AHE) resistance is proportional to the magnetization M [141]. We assume that, as suggested by room-temperature W XMCD, the MPE onset in our tungsten/thulium iron garnet (W/TmIG) samples is significantly below the Curie temperature of the MI (T_{MI}). This is unsurprising given that W is far from a Stoner instability and therefore difficult to magnetize. At the $T_{\text{on,MPE}}$, the M of the TmIG is nearly saturated since $M = M_0(1 - T/T_{\text{MI}})^{\frac{1}{2}}$ and $T_{\text{MI}} \gg T_{\text{on,MPE}}$. Thus, the SH-AHE is relatively insensitive to the temperature near the $T_{\text{on,MPE}}$. In contrast, the MPE-induced AHE (MPE-AHE) should increase rapidly immediately below $T_{\text{on,MPE}}$. Note that the exact temperature dependence of MPE-AHE may be very complex. In Figure 5-6a, we summarize the temperature dependence of MPE-AHE resistance in graphene/YIG [158] and topological insulator (TI)/TmIG [118] from literature. We can see that they are very different from $(1 - T/T_{\text{on,MPE}})^{\frac{1}{2}}$ behavior. Empirically, the TI/TmIG data can be fit using a parabolic function. We obtain the theoretical curve in Figure 5-6b, where we find that the parabolic temperature dependence assumption gives the most similar curve to the experimental data. Nevertheless, the T_{ex} is close to the $T_{\text{on,MPE}}$.

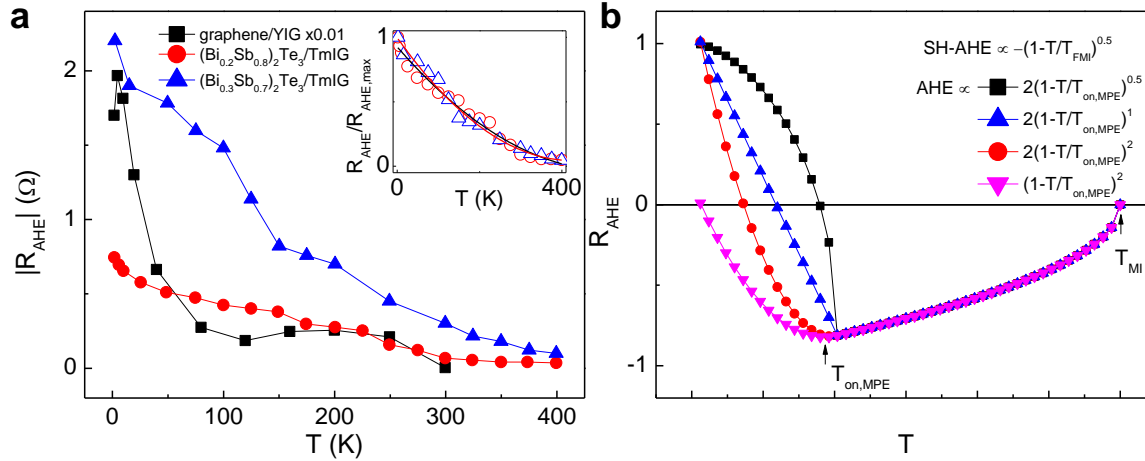


Figure 5-6 MPE-induced AHE as a function of temperature. (a) Temperature dependence of AHE resistance in graphene/YIG [158] and TI/TmIG [118] systems. The inset shows parabolic fitting to the normalized AHE resistance data of TI/TmIG. (b) Schematic of AHE resistance due to competition between MPE-AHE and SH-AHE. Temperature dependences of MPE-AHE with different scaling exponents and coefficients are shown. Reprinted with permission from [155], Copyright (2019) American Physical Society

Second, the presence of the MPE will suppress the SHE, as shown experimentally in ref. [160]. Therefore, the SH-AHE will be decreasing as the MPE-AHE develops. As the MPE becomes stronger with decreasing temperature, the SH-AHE will be suppressed further rather than increasing with the MI Magnetization, so that the SHE-AHE may even decrease. This makes the MPE-AHE more likely to dominate the SHE-AHE at low temperature, resulting in T_{ex} .

Third, the T_{ex} increases as the TmIG thickness increases. This enhanced T_{ex} is consistent with the enhanced $T_{on,MPE}$ as the TmIG saturation magnetization increases with the t_{TmIG} [119]. The reason is explained later.

Fourth, the T_{ex} is much higher in the Pt/TmIG than that in the W/TmIG at the same t_{TmIG} . This is consistent with the fact that the Pt is much easier to magnetize as compared with the W since the

Pt is closer to the Stoner instability.

With the relationship between the T_{ex} and $T_{\text{on,MPE}}$ in mind, we can examine the tunability of $T_{\text{on,MPE}}$ by investigating its dependence on t_{TmIG} and choice of HM. Both W and Pt films exhibit increasing $T_{\text{on,MPE}}$ with t_{TmIG} . In the W/TmIG, $T_{\text{on,MPE}}$ saturates at 7 nm (Figure 5-1f), which is very long considering the interfacial nature of the exchange coupling. This t_{TmIG} -dependent $T_{\text{on,MPE}}$ is likely related to the TmIG saturation magnetization as explained later. In the Pt/TmIG case, both 12 nm- and 15 nm-thick TmIG films yield $T_{\text{on,MPE}}$ above 380 K (Figure 5-4). The higher $T_{\text{on,MPE}}$ in Pt for the same t_{TmIG} is consistent with the fact that the Pt is closer to the Stoner instability and thus much easier to magnetize through proximity effect.

Here, we explore possible mechanism for achieving a MI thickness-dependent $T_{\text{on,MPE}}$. The strength of the MPE in the HM/MI depends on both the magnetic susceptibility of the HM and surface (saturation) magnetization of the MI. (Typically, if the temperature is above the MI Curie temperature, there is no MPE since there is no magnetization.) We observe a much higher $T_{\text{on,MPE}}$ for Pt than W at the same MI thickness, which is consistent with the fact that Pt has a much stronger susceptibility than W. We also observe that the $T_{\text{on,MPE}}$ increases with the MI thickness with a characteristic length around 7 nm in W/TmIG, which is surprisingly large considering that the HM electrons cannot penetrate the MI over such long ranges. This could be explained by the thickness-dependent MI saturation magnetization, which saturates over a longer range. As shown in our TmIG thin films, the MI saturation magnetization and Curie temperature increases with the thickness and saturates around 10 nm (see Figure 1c and Figure 1d of ref. [119]) at room temperature. This contrasts with the saturation length around 1-2 nm for ferromagnetic metals (Co, CoFeB, etc.) at room temperature. Since the thicker MI film has a larger saturation magnetization at a given temperature, it provides a stronger exchange interaction (**Error! Reference source not f**

ound.) and thus a higher $T_{\text{on,MPE}}$. The proof of our simple argument requires further theoretical and experimental investigations.

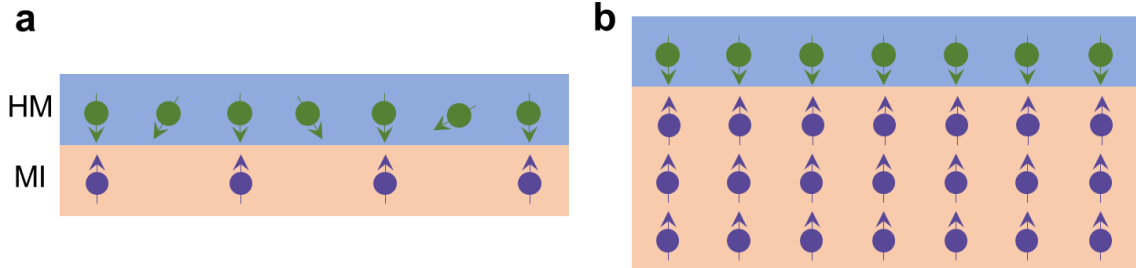


Figure 5-7 Schematic of exchange coupling at finite temperature in the HM/MI bilayer. Purple arrows represent the atomic magnetic moments in the MI, whose density represents the saturation magnetization. The surface HM atoms (green arrows) interact with the surface magnetization of MI. When the MI is much thinner like in case (a) than the bulk case (b), the T_{MI} is strongly suppressed and thus at a finite temperature (around the half of the MI Curie temperature), the saturation magnetization is much smaller in (a) than (b). Smaller saturation magnetization leads to weaker exchange interaction and thus lower $T_{\text{on,MPE}}$. Reprinted with permission from [155], Copyright (2019) American Physical Society

While the $T_{\text{on,MPE}}$ is always observed when the MPE presents, the AHE sign change does not always occur in the W/TmIG. In the low-temperature regime where the MPE is strongest, we expect an AHE sign change temperature (T_1) only if the MPE-AHE fully dominates over the SH-AHE. This sign change does not always happen in the W/TmIG as shown in Figure 5-8. In the Pt/TmIG, we observe a T_1 in all the samples examined. However, there is no clear relation between T_1 and TmIG thickness in either the Pt/TmIG or W/TmIG. There are two possible explanations the lack of a T_1 in some W/TmIG. Firstly, it is possible that the T_1 occurs below 10 K, the lowest measured temperature, or that the coercive field is too large. Alternatively, we note that a T_1 requires that the MPE-AHE dominates over the SH-AHE. According to the theory [161], the MPE-

AHE is very sensitive to the Fermi level position of the HM. For our 5 nm-thick W thin films, the resistivity varies from 140 to 170 $\mu\Omega\cdot\text{cm}$ despite the use of same sputtering procedures and conditions. This variation in W may explain the absence of T_1 in some W/TmIG. Further investigations are required to clarify this point.

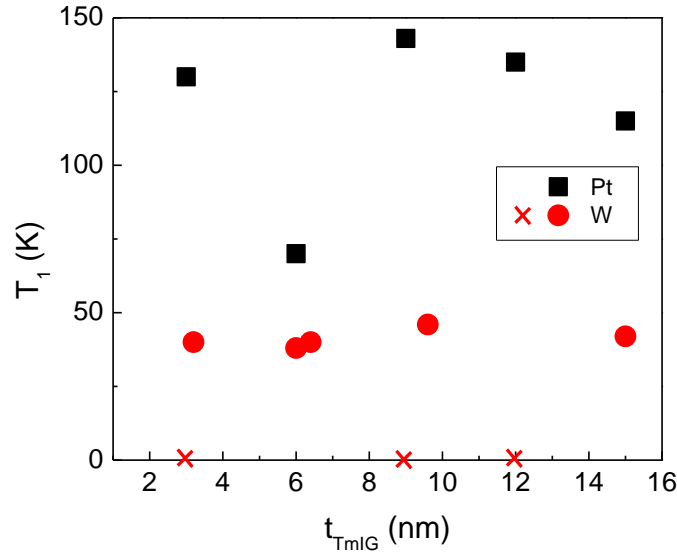


Figure 5-8 The low temperature AHE sign change temperature (T_1) due to the MPE in the Pt/TmIG and W/TmIG with different TmIG thicknesses. The label \times on the x -axis indicates that the T_1 is not clearly observed. Reprinted with permission from [155], Copyright (2019) American Physical Society

5.1.3 Magnetization compensation temperature

Having addressed the various AHE contributions, we note that in rare-earth transition metal alloys an AHE sign change has been observed across the T_M since the spin polarization at the Fermi level is flipped across the T_M . Simultaneously, the B_C diverges at T_M since a zero-magnetization material is highly insensitive to an applied field. In contrast, the AHE response across T_M in HM/FMI bilayer remains unclear since the Fermi level is in the bandgap of the FMI and no mobile carriers

from the FMI contribute to the AHE. We explore this exchange coupling-induced AHE across the T_M using W/TmIG. While in previous studies both bulk and thin-film TmIGs do not show a T_M above 5 K [162, 163], some films in the present study exhibit a T_M above 10 K. The presence and variability of T_M is most likely due to cation off-stoichiometry, which is challenging to precisely control and may stabilize or boost the T_M significantly even with small variation during growth. We experimentally identify this T_M by investigating the B_C of out-of-plane hysteresis loops (Figure 5-9a). We observe a divergent B_C around 75 K in a W/TmIG(6 nm) sample (Figure 5-9b), the same temperature at which the AHE sign reverses, suggesting that the interfacial exchange coupling follows one sublattice rather than the net magnetization. We suspect that the exchange coupling effect follows the Fe sublattices since Fe d -orbitals are highly delocalized relative to Tm f -orbitals. Highlighting the complex balance between all these effects, we note that two AHE sign changes occur in the same W/TmIG(6 nm) sample. As described above the AHE sign abruptly changes from negative to positive at 75 K, while the AHE sign gradually switches from positive to negative again near 45 K (Figure 5-9b). At 75 K, we observe a divergent B_C which identifies this transition as T_M , while the sign change at 45 K is accompanied by a relatively constant B_C . Further, removing the sign change associated with T_M (Figure 5-9b inset) by mirroring the AHE resistance below 75 K about the x -axis yield results in excellent agreement with those in Figure 5-1e. Thus, we associate the sign change at 45 K with competition between MPE-AHE and SH-AHE.

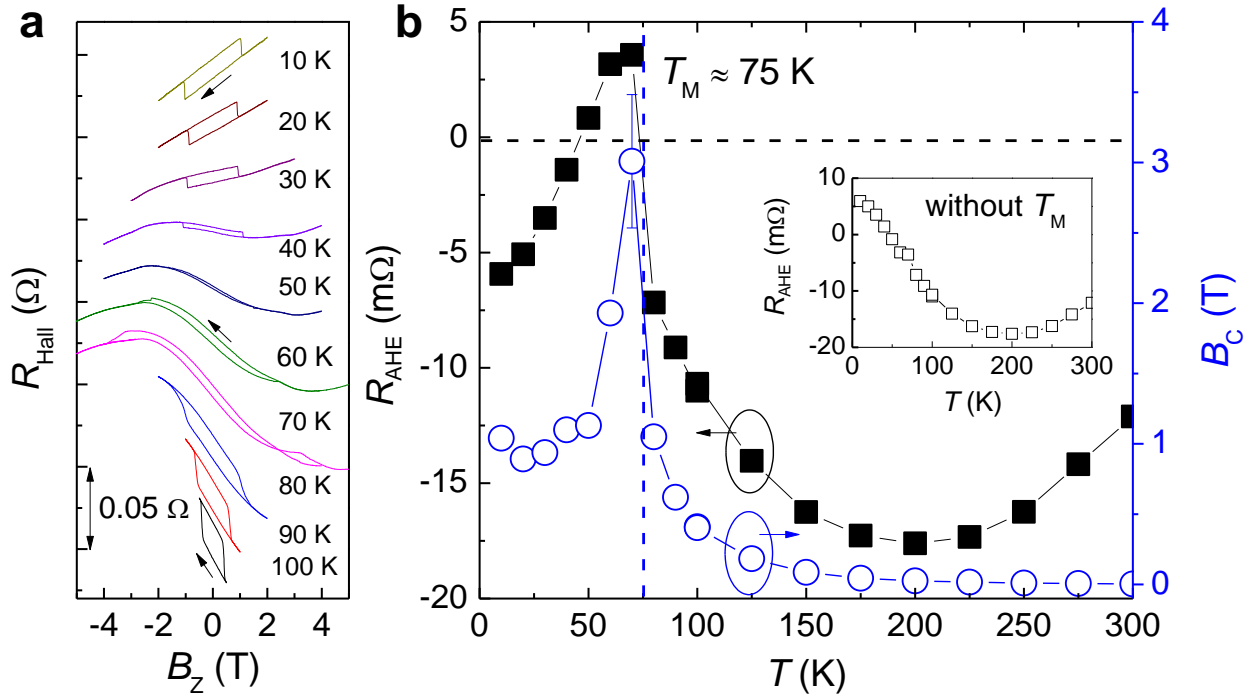


Figure 5-9 Emergence of the AHE sign change at the magnetization compensation temperature (T_M) in a W(5 nm)/TmIG(6 nm) bilayer. (a) Hall resistance vs. out-of-plane magnetic field for different temperatures. The arrow indicates the field sweeping direction. (b) AHE resistance and coercive field of out-of-plane hysteresis loops as a function of temperature. The vertical blue dashed line indicates the T_M . Inset is the inferred data for the case without a T_M . Reprinted with permission from [155], Copyright (2019) American Physical Society

We observe similar T_M -induced AHE sign changes and divergent B_c in Pt/TmIG(6 nm), where the T_M is 75 K (see Figure 5-4 and Figure 5-5). Note that the Pt/TmIG(6 nm) and W/TmIG(6 nm) Hall bar devices are fabricated at different locations on the same TmIG thin film, so that the identical T_M values strongly suggest that the T_M -induced AHE is insensitive to the choice of HM.

To further validate our argument that across the T_M , the induced AHE in the HM layer changes sign, we probed the AHE in Pt/TbIG and W/TbIG. Pt/TbIG and W/TbIG are prepared on different GGG substrates and both show a perpendicular magnetic anisotropy. The T_M are 290 K and 355 K

for Pt/TbIG and W/TbIG (Figure 5-10), respectively, which are much higher than the bulk value (250 K). As expected, the AHE changes sign and the B_C is divergent near the T_M in these two bilayers as well.

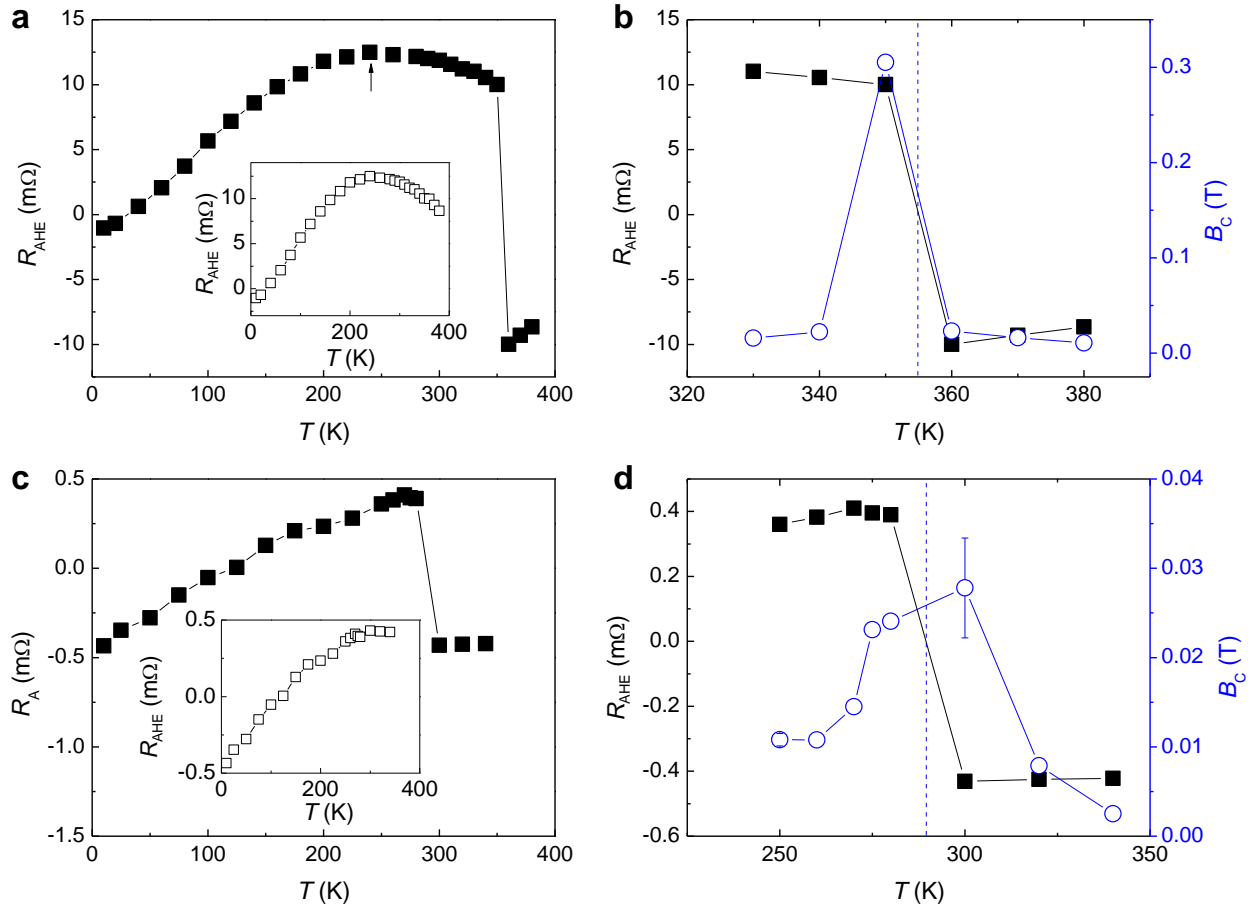


Figure 5-10 AHE resistance as function of temperature in W/TbIG and Pt/TbIG. (a) AHE resistance as a function of temperature in the W(5 nm)/TbIG(6 nm). Inset is the inferred data for the case without a T_M . (b) AHE resistance and coercive field of out-of-plane hysteresis loops near the T_M in the W(5 nm)/TbIG(6 nm). The vertical blue dashed line indicates the T_M . (c) AHE resistance as a function of temperature in the Pt(5 nm)/TbIG(6 nm). Inset is the inferred data for the case without a T_M . (d) AHE resistance and coercive field of out-of-plane hysteresis loops near the T_M in the Pt(5 nm)/TbIG(6 nm). The vertical blue dashed line indicates the T_M . Reprinted with permission from [155], Copyright (2019) American Physical Society

I want to mention that we observe a nonmonotonic change of the R_{AHE} slope below 100 K in W(5 nm)/TmIG(3.2 nm) (Figure 5-2b), which is suggestive of a T_{M} . This is also indicated in the temperature dependence of B_{C} in Figure 5-3b, where the slope of the curve is nonmonotonic.

5.1.4 Discussions

In summary, both direct measurements of the magnetization, decomposing the magnetic signal as a function of element and depth within the film, reveal good agreement with the transport data and interpretations discussed above. Both XMCD (Session 5.3) and PNR (Session 5.4) favor the interpretation that the MPE favors antiparallel exchange coupling between the W and the Fe in the W/TmIG. Experimentally, we determine a positive MPE-AHE sign when the TmIG magnetization is pointing along the $+z$ direction. To make a consistent comparison for different HMs, we define AHE sign in a magnetized HM when the HM magnetization is pointing along the $+z$ direction. Since the measured MPE-AHE is positive and W and TmIG magnetizations are antiparallel, the magnetized W has a negative AHE sign. We now summarize the AHE sign associated with various magnetized HMs in Table 5-1 [151, 161]. With the information from the AHE, we can extract the exchange coupling configuration in arbitrary HM/magnetic insulator (MI) bilayers. For instance, Zhou *et al.* [151] and Amamou *et al.* [164] observed the AHE signs due to MPE are negative and positive for the Pd/YIG and Pt/CoFe₂O₄ (CoFe₂O₄ is a MI), respectively, so that we can predict parallel exchange coupling for both Pd/YIG and Pt/CoFe₂O₄ by using Table 5-1. We also summarize results of the exchange coupling configurations in HM/magnet bilayers in Table 5-2 [149, 151, 164-167], where all magnetic materials contain Fe elements. We can see that the exchange coupling configurations in HM/Fe bilayers are the same as in HM/MI bilayers, strongly

suggesting that the exchange coupling is dominated by the HM-Fe exchange interaction. As discussed in [149, 166, 167], the exchange coupling configuration between two transition metals can typically be described using the Bethe-Slater curve, which describes the exchange coupling energy as a function of the ratio of the interatomic distance to the radius of the incompletely filled d shells. The ratio decreases when moving from the more to the less filled shells and leads to a sign change in exchange energy from positive (ferromagnetic) to negative (antiferromagnetic). The Pt and Pd have more-than-half-filled d shells, and thus a ferromagnetic exchange coupling, while W has less-than-half-filled d shells and thus an antiferromagnetic exchange coupling. The consistency of this picture is surprising considering the complexity of the oxide/metal interface. Note that future studies are encouraged to expand Table 5-1 and Table 5-2.

In two recent publications [168, 169], the AHE temperature dependence in the Pt/TbIG were reported. We plot these data in Figure 5-11. Figure 5-11a reveals a T_M around 230 K and a $T_{on,MPE}$ around 140 K. Figure 5-11b reveals a T_M around 355 K and a $T_{on,MPE}$ higher than 350 K. We show that their data can be interpreted using our temperature-dependent AHE model, although the details and parameters may vary somewhat.

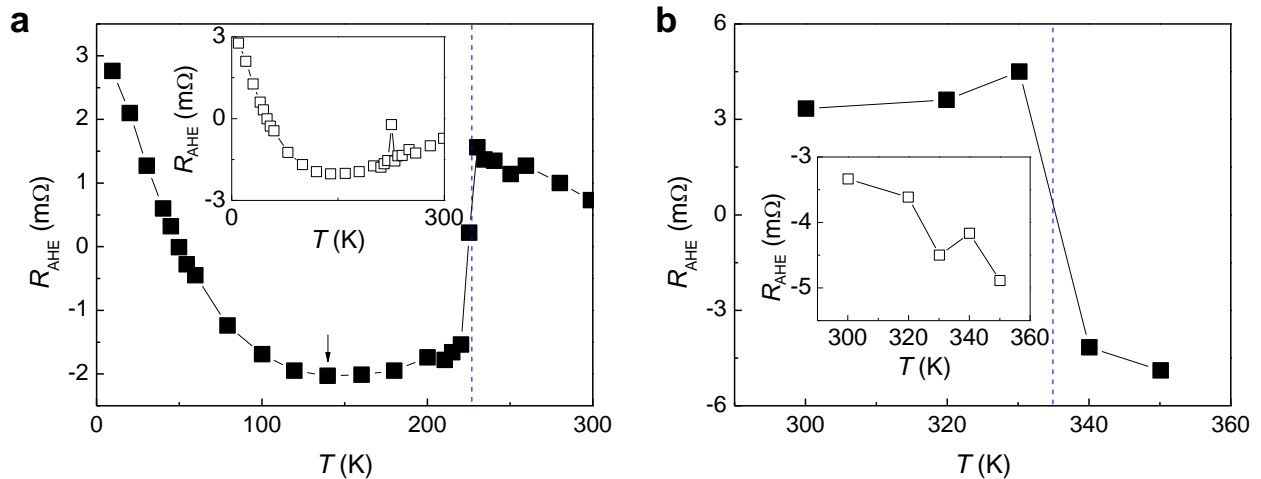


Figure 5-11 Temperature dependence of AHE in the Pt(5nm)/TbIG(30nm) [168] and the Pt(4nm)/TbIG(10nm) [169]

Table 5-1 Sign of AHE in various magnetized heavy metals. Adapted with permission from [155], Copyright (2019) American Physical Society

Heavy metal element	Pt	Pd	W
Sign of AHE	Positive (this work and [151, 161])	Negative[151, 161]	Negative (this work)

Table 5-2 Exchange coupling configuration in various heavy metal/magnet bilayers. Adapted with permission from [155], Copyright (2019) American Physical Society

Type of magnet	Magnetic metal			Magnetic insulator		
	Pt/ Fe [149, 166]	Pd/ Fe [166, 167]	W/ Fe [149, 166]	Pt/ Y ₃ Fe ₅ O ₁₂ [165], CoFe ₂ O ₄ [164], Tm ₃ Fe ₅ O ₁₂ [*] , Tb ₃ Fe ₅ O ₁₂ [*])	Pd/ Y ₃ Fe ₅ O ₁₂ [151]	W/ (Tm ₃ Fe ₅ O ₁₂ [*] , Tb ₃ Fe ₅ O ₁₂ [*])
Exchange coupling configuration	FM	FM	AFM	(FM, FM ^{**} , FM ^{**} , FM ^{**})	FM [*]	(AFM, AFM ^{**})

* This work

** Predicted using the experimental AHE sign and Table 5-1

5.2 Spin Hall magnetoresistance effect

5.2.1 SMR in heavy metal/magnetic insulator

In heavy metal/magnetic insulator bilayers, SMR theory has been discussed in ref. [127],

$$\frac{\rho_{\text{SMR}}}{\rho} = \frac{2\theta_{\text{SH}}^2 \lambda^2}{d} \frac{\text{Re}G_{\uparrow\downarrow} \tanh^2 \frac{d}{2\lambda}}{\frac{1}{\rho} + 2\lambda \text{Re}G_{\uparrow\downarrow} \coth \frac{d}{\lambda}}$$

First, we assume a spin Hall effect picture for the W/TmIG. According to SMR theory [127], the

spin mixing conductance ($G_{\uparrow\downarrow} = G_r + iG_i$) can be estimated by using $\frac{\rho_{\text{SMR}}}{\rho} = \frac{2\theta_{\text{SH}}^2 \lambda^2}{d} \text{Re} \frac{G_{\uparrow\downarrow} \tanh^2 \frac{d}{2\lambda}}{\frac{1}{\rho} + 2\lambda G_{\uparrow\downarrow} \coth \frac{d}{\lambda}}$

and $\frac{\rho_{\text{SMR-AH}}}{\rho} = -\frac{2\theta_{\text{SH}}^2 \lambda^2}{d} \text{Im} \frac{G_{\uparrow\downarrow} \tanh^2 \frac{d}{2\lambda}}{\frac{1}{\rho} + 2\lambda G_{\uparrow\downarrow} \coth \frac{d}{\lambda}}$, where θ_{SH} is the spin Hall angle, d is the W thickness, ρ

is the resistivity $155 \pm 15 \mu\Omega \cdot \text{cm}$ and λ is the spin diffusion length of W layer, respectively. The

magnitude of SMR is determined as shown in Figure 5-12. If we assume the θ_{SH} is 0.3 [26] and

the λ is 2.1 nm [72], we get $G_r \approx 2 \times 10^{12} \Omega^{-1} \text{m}^{-2}$ and $G_i \approx 1 \times 10^{12} \Omega^{-1} \text{m}^{-2}$.

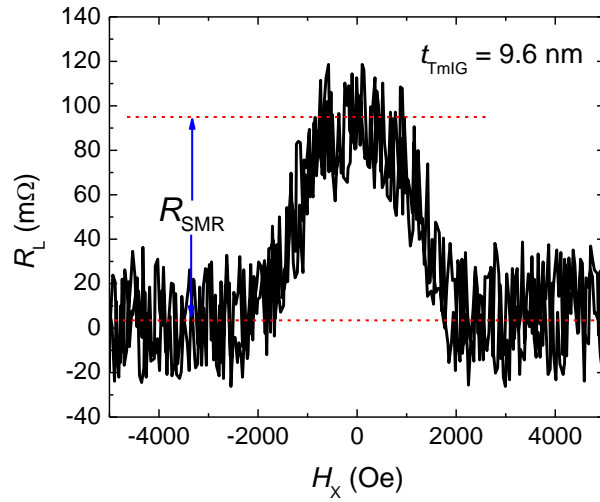


Figure 5-12 Longitudinal resistance as a function of an external magnetic field along the $\pm x$ direction for the W (5 nm)/TmIG (9.6 nm), where SMR is observed as the resistance is minimized when magnetization is along the $\pm x$ direction. Reprinted with permission from [119], Copyright (2018) Springer Nature

5.2.2 SMR in heavy metal/ferromagnetic metal

In heavy metal/ferromagnetic metal bilayers, SMR theory may include additional longitudinal spin current absorption [146],

$$\frac{\rho_{\text{SMR}}}{\rho} = \frac{\theta_{\text{SH}}^2 \lambda \tanh^2 \frac{d}{2\lambda}}{d(1+\xi)} \left[\frac{2\lambda \rho \text{Re}G_{\uparrow\downarrow}}{1+2\lambda \rho \text{Re}G_{\uparrow\downarrow} \coth \frac{d}{\lambda}} - \frac{g_F}{1+g_F \coth \frac{d}{\lambda}} \right],$$

where $g_F = \frac{(1-P^2)\lambda\rho}{\rho_F \lambda_F \coth \frac{t_F}{\lambda_F}}$ and $\xi = \frac{\rho t_F}{\rho_F d}$. If we include additional light metal layer like Cu, the only

difference is the $\xi = \frac{\rho t_F}{\rho_F d} + \frac{\rho t_{\text{Cu}}}{\rho_{\text{Cu}} d}$. In Figure 5-13, we show a typical CoFeB thickness dependent

SMR in W/CoFeB bilayers.

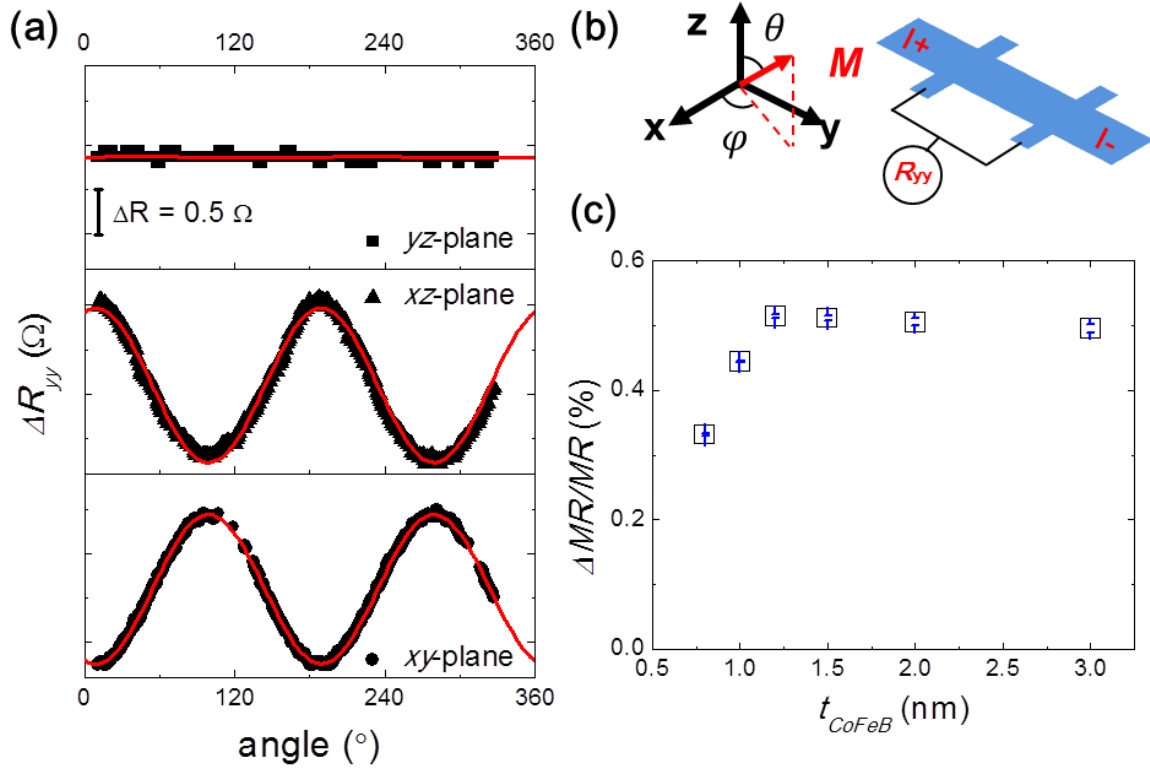


Figure 5-13 SMR in W/CoFeB. (a) Longitudinal resistance (R_{yy}) as a function of the angle of magnetization for 1.2 nm as-grown CoFeB film. The magnetization rotates in the xy ($\theta = 90^\circ$), xz

($\phi = 0^\circ$) and yz ($\phi = 90^\circ$) planes. (b) The schematic diagram of the coordinates and measurement. The magnetization is rotated by rotating an external magnetic field of 2T, which is larger than the saturation fields for all the different thickness samples. (c) The CoFeB thickness dependence of the spin Hall magnetoresistance. Reprinted with permission from [64], Copyright (2016) AIP Publishing

5.3 X-ray magnetic circular dichroism

In order to confirm the validity of our analysis and demonstrate the usefulness of the AHE as a probe of both the HM and FMI, we examined the MPE and interfacial coupling using direct magnetization probes with elemental sensitivity and depth resolution. We employed XMCD, which uses circularly polarized photons and inherent spin-orbit coupling effects in electron energy level transitions to probe spin-dependent orbital occupancy and extract element-specific magnetic information from the W/TmIG. By tuning the incident X-ray energy to the resonant absorption edge of a given element and taking the absorption difference between left and right circularly polarized light, we may isolate the magnetization contribution of that element specifically. For XMCD measurements, we collected both total electron yield and luminescence yield data on $\text{Nd}_3\text{Ga}_5\text{O}_{12}(111)/\text{TmIG}(10\text{ nm})/\text{W}(5\text{ nm})/\text{Pt}(2\text{ nm})$ films. XAS spectra and XMCD were taken at beamline 4.0.2 of the advanced light source at a range of temperatures from 320 K to 8 K in applied fields of ± 400 mT. Measurements were performed at the Fe $L^{3,2}$, Tm M^5 , and W N^3 edges in the total electron yield and luminescence yield configurations at alternating applied fields and photon helicities.

X-ray absorption spectra (XAS) and XMCD taken at Fe L_3 edge and Tm M_5 edge are shown in Figure 5-14a, b and Figure 5-14c, d, respectively. The XMCD spectra reveal both Fe and Tm have a nonzero magnetization at all the investigated temperatures, but the magnetism of Tm exhibits a

much stronger temperature dependence, nearly disappearing by 320 K (see Appendix G). This shows that Fe/W exchange coupling likely dominates over Tm/W, as expected. The XMCD spectra also show that the Fe and Tm have the opposite sign, indicating the two elements are anti-ferromagnetically coupled, consistent with previous studies [162] and as expected in most rare-earth iron garnets [131].

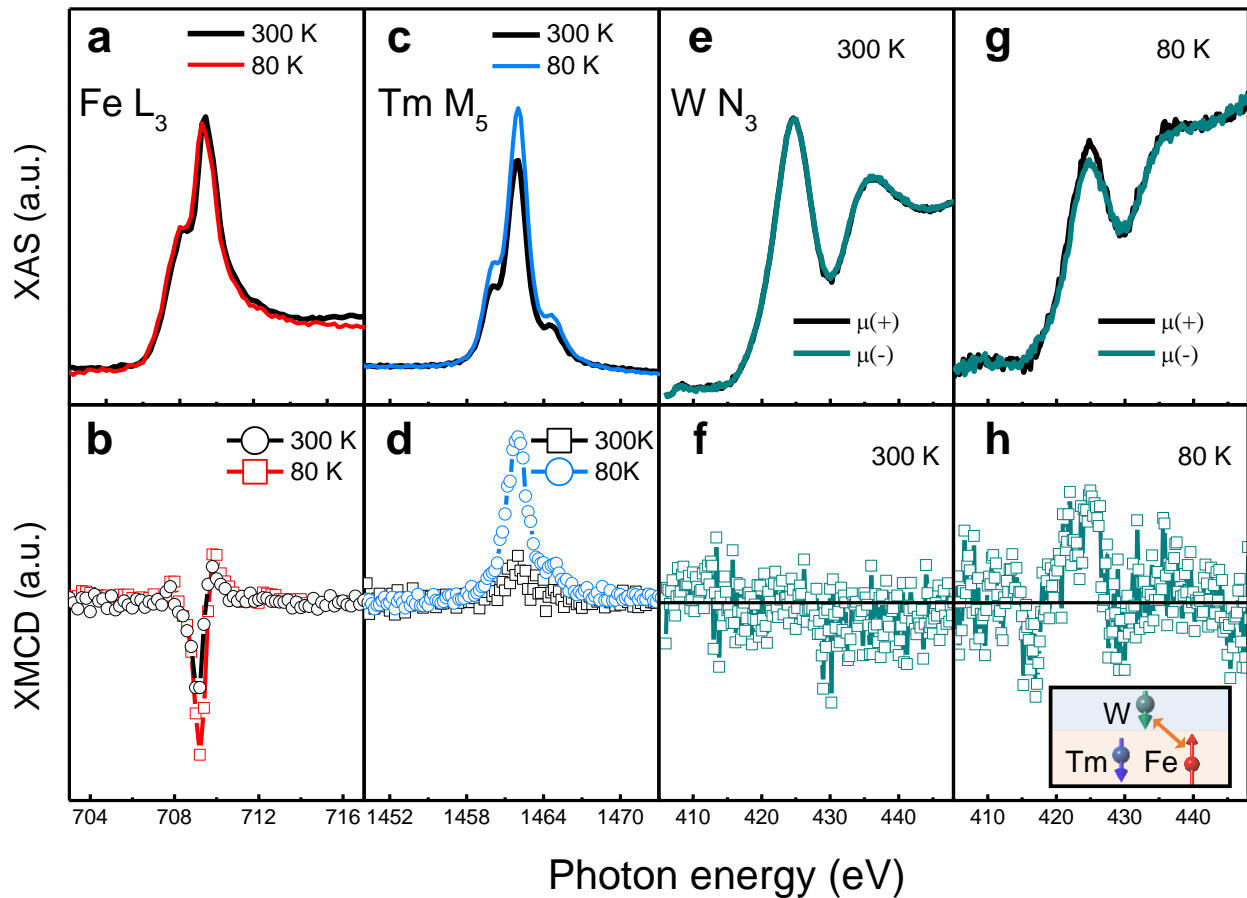


Figure 5-14 Capturing the exchange interactions in the W(5 nm)/TmIG(10 nm) by X-ray techniques. (a) XAS and (b) XMCD spectra taken at Fe L₃ edge at 80 K and 300 K. (c) XAS and (d) XMCD spectra taken on Tm M₅ edge at 80 K and 300 K. XAS taken on W N₃ edge at 300 K (e) and 80 K (g) with two opposite x-ray helicities, μ(+) and μ(-). XMCD at W N₃ edge taken at 300 K (f) and 80 K (h). Inset in (h) illustrates relative spin alignments of the Fe, Tm, and induced W moment at 80 K based on the sign of XMCD. Reprinted with permission from [155], Copyright (2019) American Physical Society

XAS and XMCD measurements at W N_3 edge taken at 300 K and 80 K are shown in Figure 5-14e, f and Figure 5-14g, h, respectively. At 300 K, there is clearly no XMCD observed in the W, indicating an exceedingly weak MPE at higher temperatures. This indicates that the AHE above room temperature is due to the SHE. In contrast, a small but still distinguishable XMCD at the W N_3 edge appears at 80 K. We argue that the MPE-induced magnetic moment in the W is antiferromagnetically exchange-coupled to the Fe instead of the Tm (see inset in Figure 5-14h) since Fe d -orbitals are relatively delocalized and Tm f -orbitals are more localized and previous studies have shown this antiferromagnetic exchange coupling in W/Fe systems [149, 166].

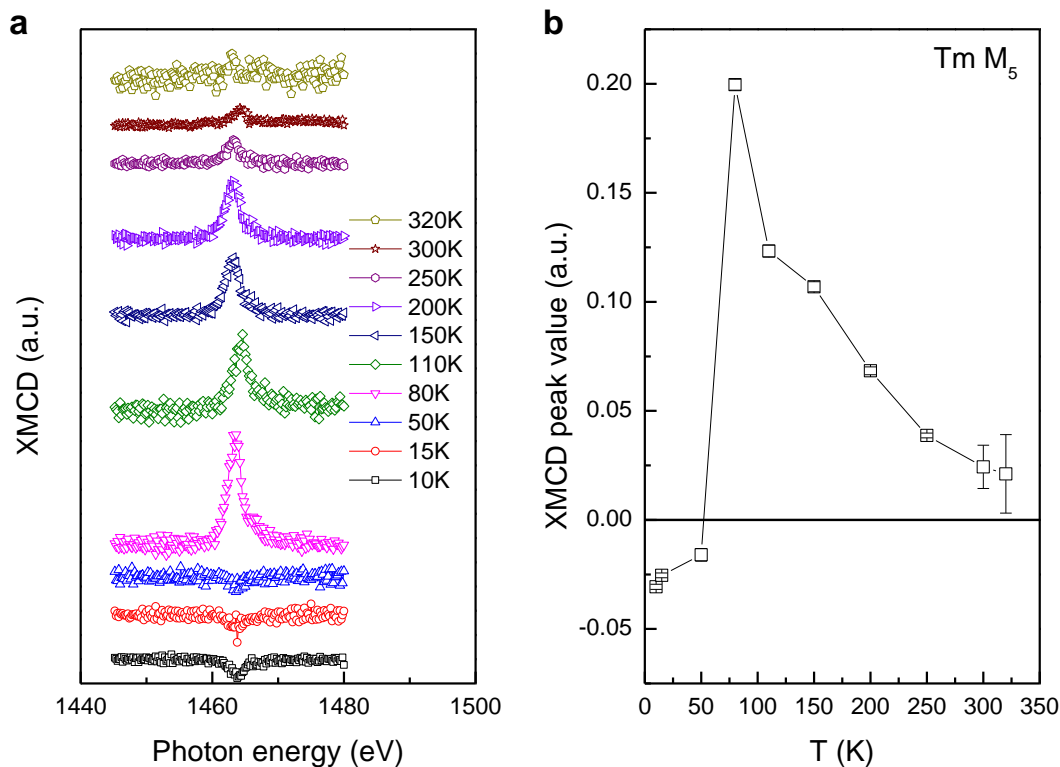


Figure 5-15 XMCD across the T_M . (a) XMCD signals at different temperature. (b) $T_M M_5$ XMCD peak value as a function of temperature. Reprinted with permission from [155], Copyright (2019) American Physical Society

Although the extremely large B_C near a T_M necessitated measurements to be taken on a minor loop, we note that the Tm XMCD sign reverses through the suspected T_M in one measured sample. Total electron yield and luminescence yield XMCD was taken for both the Fe L- and Tm M-edges through a suspected T_M . Unfortunately, the highest available field in the end station used was 400 mT, so that the magnetization could not be switched completely due to the divergence of the coercivity near the T_M . In this case, the Fe XMCD signal was too weak to clearly resolve. However, the Tm XMCD remained measurable and its temperature dependence is plotted in Figure 5-15. Even measurements along a minor magnetization hysteresis loop provide significant insight, and in this case the XMCD on the Tm edge is reversed below the suspected T_M , confirming our interpretation of T_M in some of our TmIG thin films.

5.4 Polarized neutron reflectometry

To confirm the existence of a MPE in the W with antiparallel coupling, we utilize PNR to extract the magnetic and structural depth profile in a W/TmIG bilayer. For PNR measurements, we use $\text{Nd}_3\text{Ga}_5\text{O}_{12}(111)/\text{TmIG}(10\text{ nm})/\text{W}(5\text{ nm})/\text{AlO}_x(3\text{ nm})$. PNR measurements were performed after field cooling to 200 K and 80 K in an applied magnetic field of 700 mT using the PBR instrument at the NIST Center for Neutron Research.

Measurements were performed in the specular reflection geometry, with the direction of wave vector transfer perpendicular to the film surface. The neutron propagation direction was perpendicular to both the sample surface and the applied field direction. In any case, the perpendicular anisotropy of TmIG ensures that moments which do not align fully along the in-

plane field will instead cant along the growth axis and consequently will not produce spin-flip scattering. We therefore consider only the non-spin-flip scattering cross sections and in all cases the incident and scattered neutrons were polarized either spin-up or spin-down with respect to the applied magnetic field. Scattering length density (SLD) is a measure of the potential experienced by the neutron as a function of depth within the sample. Specifically, if we define the potential energy of a neutron traveling in a given medium as V , then the nuclear SLD (associated with scattering from nuclei) is linearly related to the potential by

$$V = \frac{2\pi\hbar^2}{m} SLD_{Nuclear}$$

While the magnetic SLD is simply an adjustment which depends on the magnetization of the media and the direction of the neutron spin. Specifically,

$$SLD_{Magnetic} = \mp \frac{m}{2\pi\hbar^2} \mu B$$

Where the sign depends on the neutron spin direction, B is the magnetic field, and μ is the neutron magnetic moment. The nuclear and magnetic SLDs are directly proportional to the nuclear scattering potential and the film magnetization respectively, so that fitting the data allows the structural and magnetic depth profiles to be deduced. The reflected intensity was measured as a function of the momentum transfer vector Q and modeled using the NIST Refl1D software package [170].

The best fits to the reflectivities and the resulting nuclear and magnetic scattering length density (SLD) profiles are shown in Figure 5-16a and its inset. Here, the nuclear and magnetic SLDs are directly proportional to the nuclear scattering potential and the film magnetization respectively, so that fitting the data allows the structural and magnetic depth profiles to be deduced. The corresponding spin asymmetry and fit are shown in Figure 5-16b. The PNR excludes the possibility

of a MPE which couples ferromagnetically to the net Fe moment of the TmIG, instead favoring an antiparallel magnetization of $53(23)$ emu/cm³ (1 emu/cm³= 1 kA/m) at the interface at 200 K.

To quantify the in-plane magnetization component when we subject the sample to a 700 mT in-plane external field in PNR experiments, we determine the B_K at different temperatures for a reference sample W(5 nm)/TmIG(10 nm) using hard-axis (in-plane) Hall hysteresis loops (Figure 5-17). The determined B_K 's are 470 mT and 2.8 T at 200 K and 80 K, respectively.

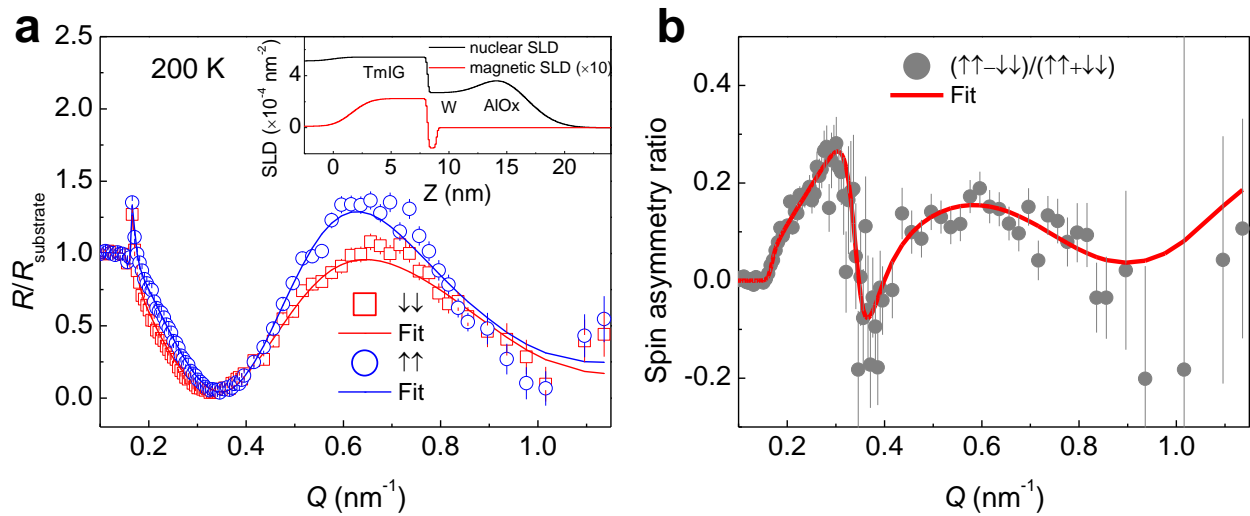


Figure 5-16 Capturing the spin textures in the W(5 nm)/TmIG(10 nm) by neutron techniques at 200 K. (a) Polarized neutron reflectivities (with a 700 mT in-plane field) for the spin-polarized $R^{\uparrow\uparrow}$ and $R^{\downarrow\downarrow}$ channels. Inset shows the corresponding models with structural and magnetic scattering length densities (SLDs) used to obtain the best fits. (b) The spin asymmetry ratio $(R^{\uparrow\uparrow} - R^{\downarrow\downarrow}) / (R^{\uparrow\uparrow} + R^{\downarrow\downarrow})$ between the $R^{\uparrow\uparrow}$ and $R^{\downarrow\downarrow}$ channels. The error bars are ± 1 s.d. Reprinted with permission from [155], Copyright (2019) American Physical Society

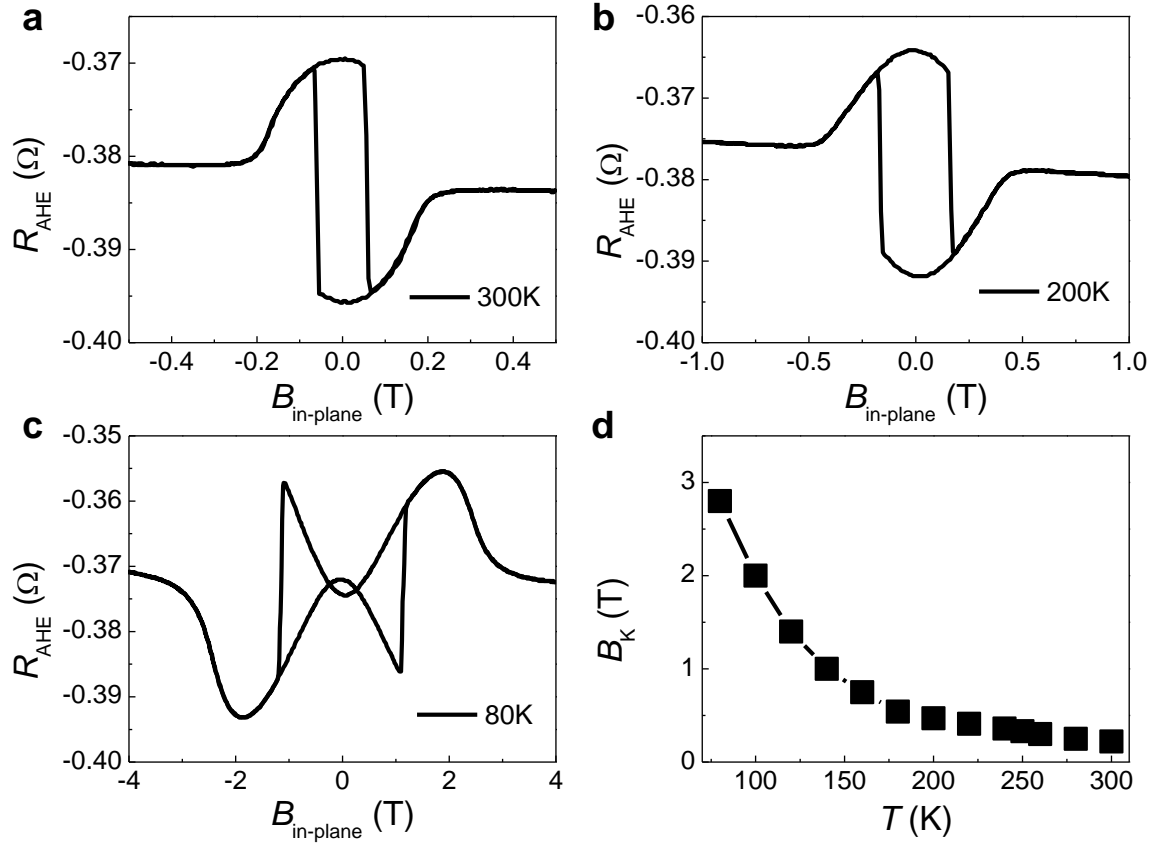


Figure 5-17 Temperature dependence of in-plane Hall hysteresis loops at 300 K (a), 200 K (b) and 80 K (c). (d) Temperature dependence of B_K . Reprinted with permission from [155], Copyright (2019) American Physical Society

Similar results are obtained at 80 K. However, due to the huge perpendicular magnetic anisotropy effective field ($B_K \approx 2.8 \text{ T}$), the in-plane magnetization is very small. As shown in Figure 5-18, we indeed observe that the measured magnetic moment is smaller and correspondingly, the measurement uncertainty is significantly larger than the case at 200 K. Nevertheless, qualitatively, the results are similar to those at 200 K, suggesting an antiparallel coupling between W and TmIG.

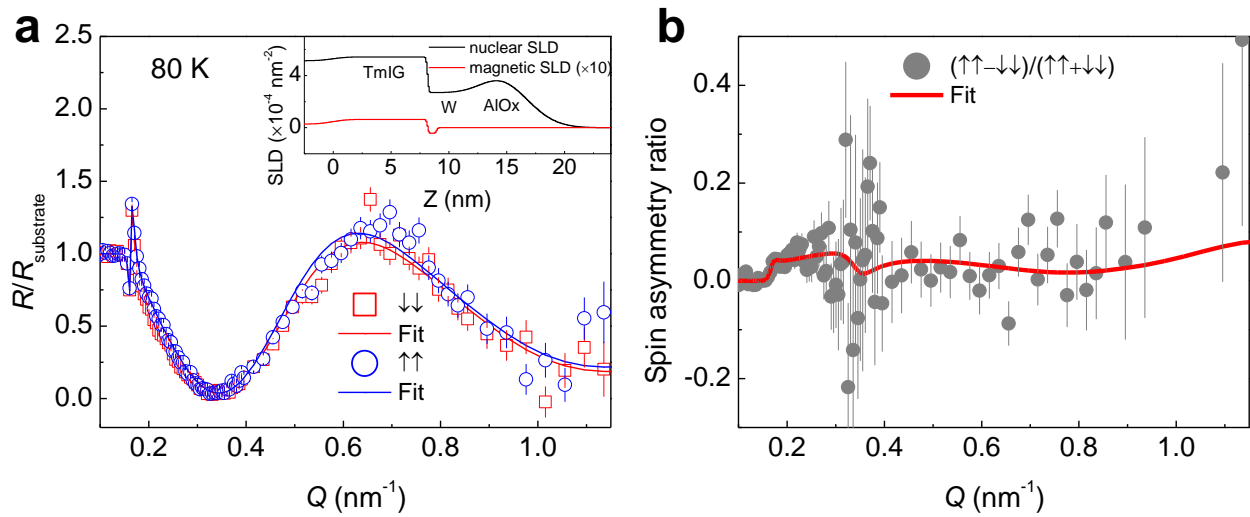


Figure 5-18 Capturing the spin textures in the W(5 nm)/TmIG(10 nm) by neutron techniques at 80 K. (a) Polarized neutron reflectivities (with a 700 mT in-plane field) for the spin-polarized $R^{\uparrow\uparrow}$ and $R^{\downarrow\downarrow}$ channels. Inset shows the corresponding models with structural and magnetic scattering length densities used to obtain the best fits. (b) The spin asymmetry ratio $(R^{\uparrow\uparrow} - R^{\downarrow\downarrow}) / (R^{\uparrow\uparrow} + R^{\downarrow\downarrow})$ between the $R^{\uparrow\uparrow}$ and $R^{\downarrow\downarrow}$ channels. The error bars are ± 1 s.d. Reprinted with permission from [155], Copyright (2019) American Physical Society

Chapter 6 Skyrmions

Non-volatile memory and computing technology rely on efficient read and write of ultra-tiny information carriers that do not wear out. Magnetic skyrmions are emerging as a potential carrier since they are topologically robust nanoscale spin textures that can be manipulated with ultralow current density[171, 172]. To date, most of skyrmions are reported in metallic films[39, 40, 173-178], which suffer from additional Ohmic loss and thus high energy dissipation. Therefore, skyrmions in magnetic insulators are of technological importance for low-power information processing applications due to their low damping and the absence of Ohmic loss. Moreover, they attract fundamental interest in studying various magnon-skyrmion interactions[179]. Skyrmions have been observed in one insulating material Cu_2OSeO_3 at cryogenic temperatures, where they are stabilized by bulk Dzyaloshinskii-Moriya interaction[180]. In this Session, we report the signature of magnetic skyrmions, topological Hall effect (THE), that survive above room temperature in magnetic insulator/heavy metal heterostructures, i.e., thulium iron garnet/platinum. In-plane bias field and magnetic insulator thickness dependence suggest that the magnetic skyrmions are stabilized by the interfacial Dzyaloshinskii-Moriya interaction. Through tuning the magnetic anisotropy via varying temperature, we obtain skyrmions in a large window of external magnetic field and enhanced stability of skyrmions in the easy-plane anisotropy regime. Our results will help create a new platform for insulating skyrmion-based room temperature low dissipation spintronic applications.

In Session 6.1, we further introduce the history of skyrmions and motivations for high-temperature insulating skyrmions. In Session 6.2 and 6.3, we discuss the condition for the existence of skyrmions by using analytical calculations and numerical micromagnetic simulations, respectively.

In Session 6.4, we report the observation of THE in a high-temperature MI-based heterostructures. In Session 6.5, I discuss progress toward direct imaging of skyrmions in MIs.

6.1 Motivation for high-temperature insulating skyrmions

More than four decades ago, movable magnetic bubbles in garnets and ferrites had excited huge interest for “magnetic bubble memory” applications [181]. However, two critical shortcomings precluded the commercialization of these bubble devices. First, the size of these bubbles was around 0.1 – 10 micrometers, which was too large for practical applications. Second, the manipulation of these bubbles required an on-chip magnetic field generator, which added significant complexity of circuit design and cost to the devices, making scaling difficult. The recently discovered skyrmions in B20 compounds and transition metal/ heavy metal thin films may easily overcome these two disadvantages and thus again ignite the interest of using skyrmions as information carriers [39, 40, 171, 173-178, 180]. First, the size of skyrmions has been scaled down to sub-100 nanometers in material systems that have appreciable Dzyaloshinskii-Moriya interaction (DMI) due to inversion symmetry breaking either in bulk or at the interface [40]. Second, skyrmions can be moved by using low threshold electric current and by electric field [172, 176, 182], which makes the scaling of skyrmion-based devices much more convenient compared with the case of using external magnetic field. Furthermore, for memory applications, the writing of skyrmions using spin-polarized current has been demonstrated at room temperature [39, 175], and the electrical detection (reading) of skyrmions can be achieved with the topological Hall effect (THE); THE is resulted from the Berry phase acquired by the spin-polarized carriers going through a skyrmion texture [183, 184].

Magnetic insulators that host skyrmions are particularly attractive since they have very low damping and allow long-distance information transmission free of Joule heating [109]. Moreover, various exotic phenomena based on magnon-skyrmion interactions [179], like magnon quantum Hall [185], long-range magnon transport [186], and magnon driven skyrmion motion [187], have been predicted in insulating skyrmion systems. To date, however, the only B20 magnetic insulator (Cu_2OSeO_3) that has been reported to host bulk DMI-stabilized skyrmions has a Curie temperature ($T_C \sim 60$ K) [180]. In this insulating skyrmion system, magnetic excitations [188] and thermally-driven skyrmion motion [189, 190] have been observed. The choice of magnetic insulators is limited due to the strict requirement of the crystal structure with inversion symmetry breaking, which is essential to generate strong DMI. The commonly studied high-temperature magnetic insulators, like garnets and ferrites, are centrosymmetric and thus magnetic bubbles lack a preferred chirality due to the absence of DMI [191].

6.2 Theoretical phase diagram

We calculate the stability of skyrmion phase by minimizing the free energy following refs. [192, 193]. The energy functional is written as

$$F = A \sum_{i=x,y,z} \left(\frac{\partial m}{\partial x_i} \right)^2 - K m_z^2 - D \left(m_x \frac{\partial m_z}{\partial y} + m_z \frac{\partial m_y}{\partial x} - m_z \frac{\partial m_x}{\partial y} - m_y \frac{\partial m_z}{\partial x} \right) - B_E \cdot m, \quad (6-1)$$

where the four items on the right side are the exchange, the anisotropy (with $K > 0$ for PMA), the DMI (with DMI vector lying in the film plane) and the Zeeman energy, respectively. The direction and magnitude of B_E are given by the direction of the external field and $B_E = M_S B_Z$, respectively. The link between atomic spin model and micromagnetic field energy model is discussed in Appendix B. We determine if a skyrmion phase presents for a certain combination of A , K , D , and

B_z by comparing the energies of skyrmion phase, ferromagnetic phase and spin spiral phase. During the numerical minimization of the energy functional for spin spiral phase and skyrmion phase, the periodic boundary condition with a periodicity $2R^*$ is applied (Figure 6-1a), where the R^* is also determined variationally. For the spiral phase, $2R^*$ is the length of one period of the spin spiral. For the skyrmion phase, $2R^*$ is the distance between two neighboring skyrmions in a perfect hexagonal lattice. For more details about calculation, see ref. [192].

The skyrmion phase diagram we obtained is presented in Figure 6-1b, which is consistent with previous calculation in ref. [192]. One important conclusion is that only when $|K| < 1.25 D^2/A$, a skyrmion phase can be stabilized, which is consistent with the simple theory $K \leq \frac{\pi^2 D^2}{16 A}$ in the PMA regime. From the variational minimization of the energy functional, the half of inter-skyrmion distance R^* is found to be ranged from 63 nm to 200 nm under different external fields. We then calculate the skyrmion density by using $\frac{1}{2\sqrt{3}R^{*2}}$. The calculated skyrmion density diagram as shown in Figure 6-1b is qualitatively consistent with the experimental observed THE phase diagram as shown in Figure 6-2, which agrees with the theory that the topological charge density is proportional to the skyrmion density.

The ordinary Hall coefficient (ρ_0) for the 3.2 nm-thick TmIG is $-4.64 \times 10^{-12} \Omega \cdot \text{cm}/\text{mT}$. We could estimate skyrmion density ρ_{sk} through $\rho_{THE} = \frac{\rho_0 P h}{e} \rho_{sk}$, which has been successfully used to predict single band B20 crystals that host skyrmion lattice [183]. Using a spin polarization $P = 0.1$, ρ_{THE} spans from 0 to 4.6 n $\Omega \cdot \text{cm}$ and thus ρ_{sk} spans from 0 to 4800 μm^{-2} . This is much larger than the estimated skyrmion density from magnetic parameters, which spans from 0 to 70 μm^{-2} . This suggests that single band model may not be precise for the complex magnetic multilayer thin films. There are two reasons. First, there could be other complex chiral spin textures, like worm-like

structures [194], that host many quantum fluxes for a single magnetic object. Second, the ordinary Hall coefficient is an overall effect raising from the complex band structures of polycrystalline Pt films. The conduction electrons that interact with the skyrmion or other chiral textures may not follow this overall ordinary Hall coefficient. The difference of measured and estimated topological Hall effect is the latest topic that attracts extensive discussions now, including experimental works [194-197] and theoretical investigations [198, 199].

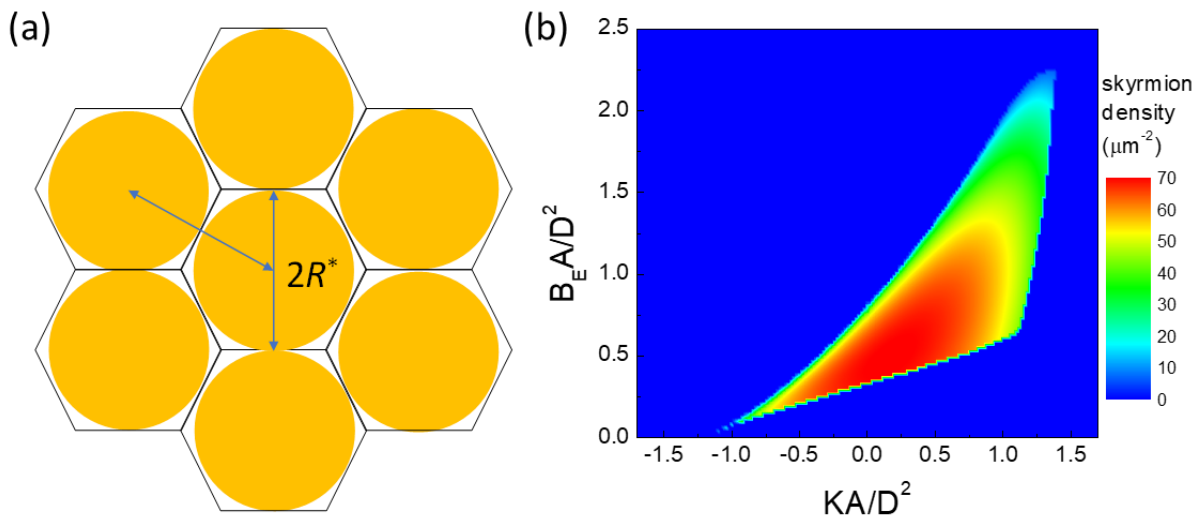


Figure 6-1 Analytical model and results for skyrmion lattice. (a) Schematic of a hexagonal skyrmion lattice. The area of a unit cell is given by $2\sqrt{3}R^{*2}$, where R^* is the half of inter-skyrmion distance. (b) Theoretical skyrmion density diagram as a function of the normalized anisotropy energy (KA/D^2) and the Zeeman energy (B_EA/D^2).

6.3 Numerical micromagnetic simulation

We perform the full micromagnetic simulation using mumax³ [41] to include the dipolar effect. For each simulation, *i.e.* a certain combination of K_U , A , D , and B_z , we start from random magnetization and then do energy relaxation to obtain the most stable magnetic configuration that corresponds to the minimum energy. The full micromagnetic simulation with the magnetostatic

energy produces a larger skyrmion phase diagram as shown in Figure 6-2 compared with the theoretical calculation without the magnetostatic energy (Figure 6-1b). We have checked that with different starting random magnetization configurations, similar results to the Figure 6-2 are obtained. This enhanced stability could be related to the dipolar effect. The simple idea is following. In the perpendicular magnetic anisotropy (PMA) regime, if the domain wall energy ($\sigma = \sqrt{AK} - \pi D$) is smaller than the reduction of magnetostatic energy by creating a domain wall, the magnetostatic energy will favor multi-domain state, which helps stabilize skyrmions [200]. Here, A is the exchange stiffness, K is the PMA energy, and D is the DMI. In our case, qualitatively, near the skyrmion phase, K is small and thus σ is relatively small. Thus, the magnetostatic energy will favor multi-domain and these bubble domains will be chiral due to the presence of DMI. Therefore, the skyrmion phase can be larger in the presence of the magnetostatic energy.

Typical results of micromagnetic are shown in Figure 6-3a and Figure 6-3b. We can determine the skyrmion size and inter-skyrmion distance by tracing the magnetization profile of individual skyrmions. The skyrmion magnetic profiles along the radial direction at two different external fields are shown in Figure 6-3c and Figure 6-3d. We see that as the external field increases from 10 mT to 70 mT, the skyrmion radius R shrinks from ~ 40 nm to ~ 8 nm. Correspondingly, the half of inter-skyrmion distance R^* reduces from ~ 100 nm to ~ 40 nm.

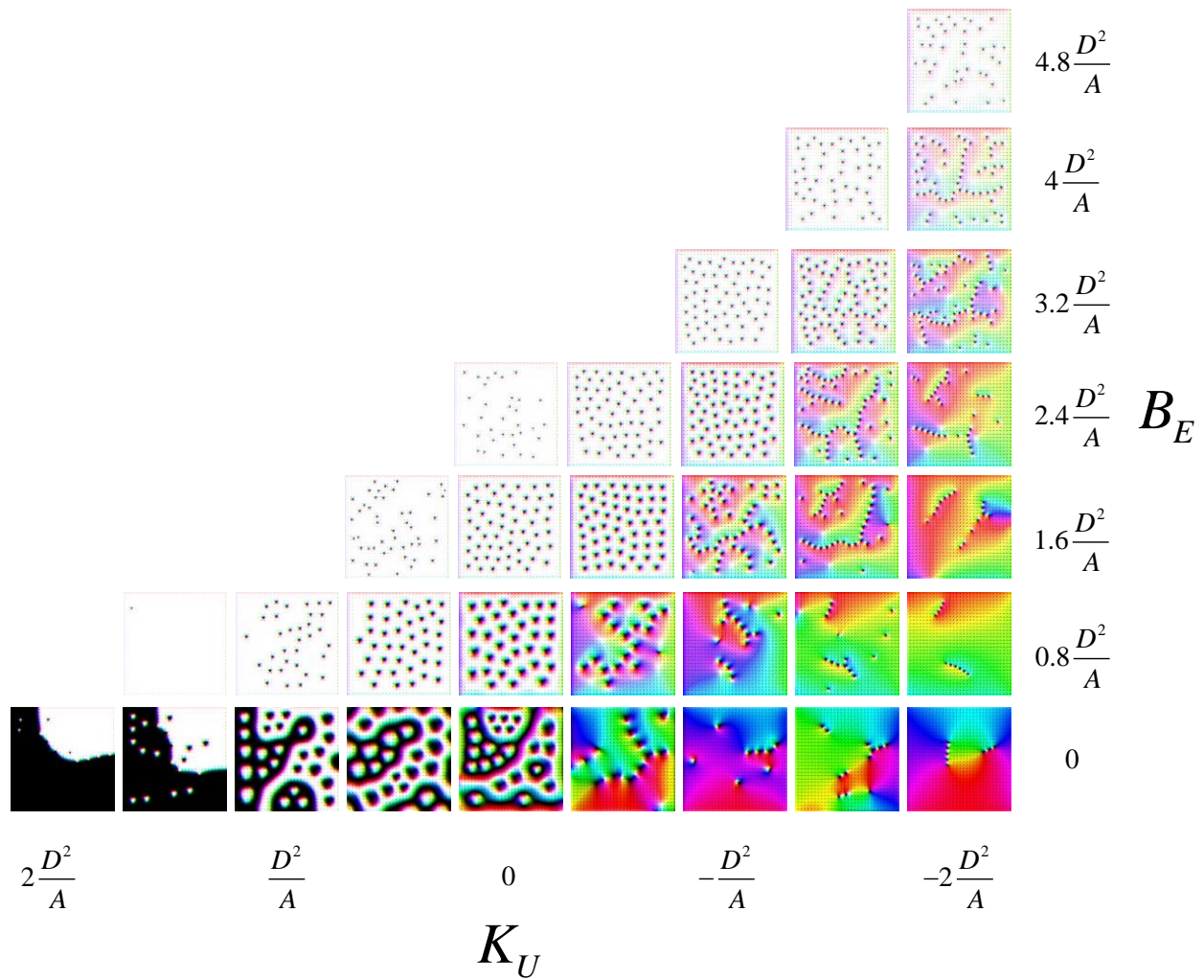


Figure 6-2 Skyrmion phase diagram from full micromagnetic simulations, which reveals a larger skyrmion window compared with that from analytical calculations (Figure 6-1b) when the dipolar effect is included. Simulation parameters: $D = 50 \mu\text{J}/\text{m}^2$, $M_S = 50 \text{ kA}/\text{m}$ and $A = 0.8 \text{ pJ}/\text{m}$.

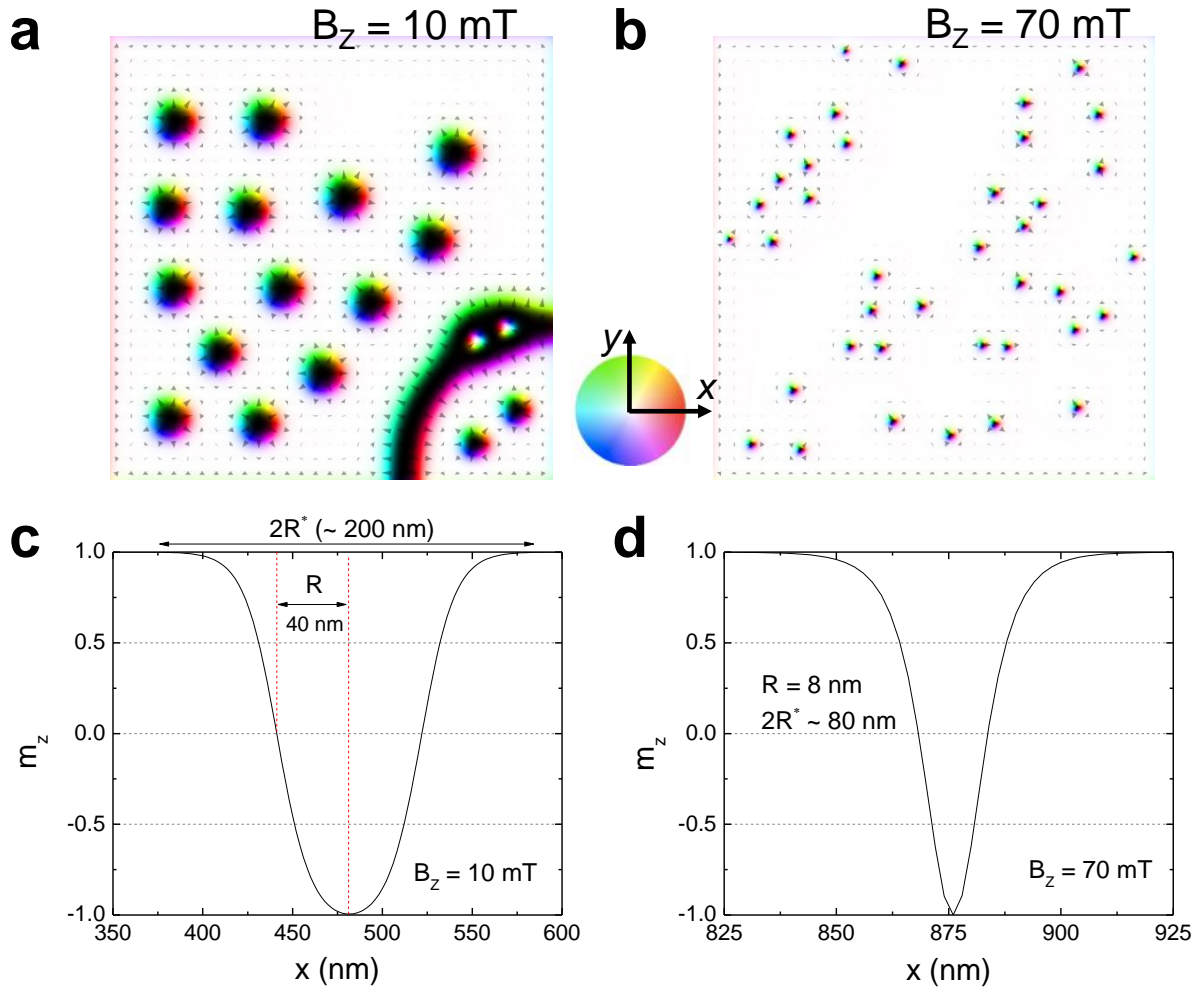


Figure 6-3 Field dependence of skyrmion configurations. Snapshots of magnetization map ($1\mu\text{m} \times 1\mu\text{m}$) for different out-of-plane external field, 10 mT (a) and 70 mT (b). Spin texture of skyrmions under different external fields along the $+z$ direction, 10 mT (c) and 70 mT (d). Simulation parameters: $K_U = 3 \text{ kJ/m}^3$, $D = 50 \mu\text{J/m}^2$, $M_S = 50 \text{ kA/m}$ and $A = 0.8 \text{ pJ/m}$.

6.4 Topological Hall effect

Here, we demonstrate the electrical detection of above-room-temperature magnetic skyrmions using a pronounced THE in a bilayer heterostructure composed of a magnetic insulator thulium iron garnet ($\text{Tm}_3\text{Fe}_5\text{O}_{12}$, TmIG) thin film in contact with a Pt film (Figure 6-4a). The T_C for bulk TmIG is $\sim 560 \text{ K}$ [181]. The skyrmions are stabilized by the interfacial DMI, which is the result

of strong spin-orbit coupling and inversion symmetry breaking at the TmIG/Pt interface. The THE is enabled by the exchange coupling between the skyrmions in TmIG and the finite spin polarization in the bottom of Pt layer. By varying the temperature, the magnetic anisotropy of TmIG can be tuned from easy axis anisotropy (out-of-film-plane) to easy plane anisotropy (in-the-film-plane), which allows for investigating the stability of skyrmions in both cases. Our experimentally observed skyrmion phase diagram established from the THE is consistent with the ones obtained by using analytical calculations and micromagnetic simulations. We discover an enhanced stability of skyrmions against the external field when the magnetic anisotropy is transitioned from the easy axis to the easy plane. At last, we show that the skyrmion phase diagram becomes smaller and eventually diminishes as the TmIG thickness increases, which is consistent with the interfacial DMI picture.

6.4.1 Materials and methods

Deposition of high-quality ferrimagnetic insulator TmIG with PMA on substituted gadolinium gallium garnet (SGGG) substrate with pulse laser deposition has been demonstrated in previous work[117]. Here we choose $\text{Nd}_3\text{Ga}_5\text{O}_{12}$ (NGG) as the substrate, which has a very close lattice constant to SGGG. TmIG films are grown at a low temperature of about 200 °C and an oxygen pressure of 0.3 mTorr, and post annealed at 850°C for 200s with sufficient oxygen gas flow. TmIG thickness is determined using a pre-calibrated growth rate. Strong PMA is confirmed by perpendicular magnetization measurement with vibrating sample magnetometer. Our atomic force microscope image indicates a high-quality atomic flat surface with a root-mean-square roughness ~ 0.14 nm. After careful characterizations, NGG/TmIG thin films are transferred to a high-vacuum magnetron sputtering chamber. We perform a light Ar plasma cleaning of the TmIG surface first

and then a thin layer of Pt is deposited at room temperature. The Ar plasma cleaning is not necessary for achieving the THE.

The whole TmIG/Pt films are patterned into Hall bar structures with a channel width of 20 μm by using standard photo-lithography and dry etching. Then, contact metals Cr(10 nm)/Au(100 nm) are deposited using e-beam evaporation. The electrical measurement is performed using lock-in technique in a physical property measurement system.

6.4.2 Observation of THE

The robust perpendicular magnetic anisotropy (PMA) is obtained at room temperature through the strain-induced magneto-elastic effect as a result of the lattice mismatch between TmIG and $\text{Nd}_3\text{Ga}_5\text{O}_{12}$ [117]. Then, a thin 4 nm-thick Pt layer is sputtered on the TmIG at room temperature. The exchange coupling between TmIG and Pt makes the conducting electrons spin polarized, resulting in the anomalous Hall effect (AHE) and spin Hall magnetoresistance (SMR) at and above room temperature in a patterned Hall bar device [117, 127, 153]. Assuming a smooth spin texture, we have a generic expression for antisymmetric Hall resistivity (ρ_{xy}) obtained on symmetry grounds (see Appendix C)

$$\rho_{xy} = \rho_o B_z + \rho_A m_z + \frac{\rho_T}{4\pi} \iint d^2r m \cdot \left(\frac{\partial m}{\partial x} \times \frac{\partial m}{\partial y} \right), \quad (6-2)$$

where ρ_o is ordinary Hall effect (OHE) coefficient, ρ_A is the saturation AHE resistivity, m_z is the average z -component of magnetization unit vector in the Hall contact area and the third term is the topological Hall effect (THE) contribution (ρ_{THE}). In the THE term, ρ_T is the THE coefficient and the integral counts how many times $m(r) = m(x, y)$ wraps a unit sphere, which is the skyrmion number in real space.

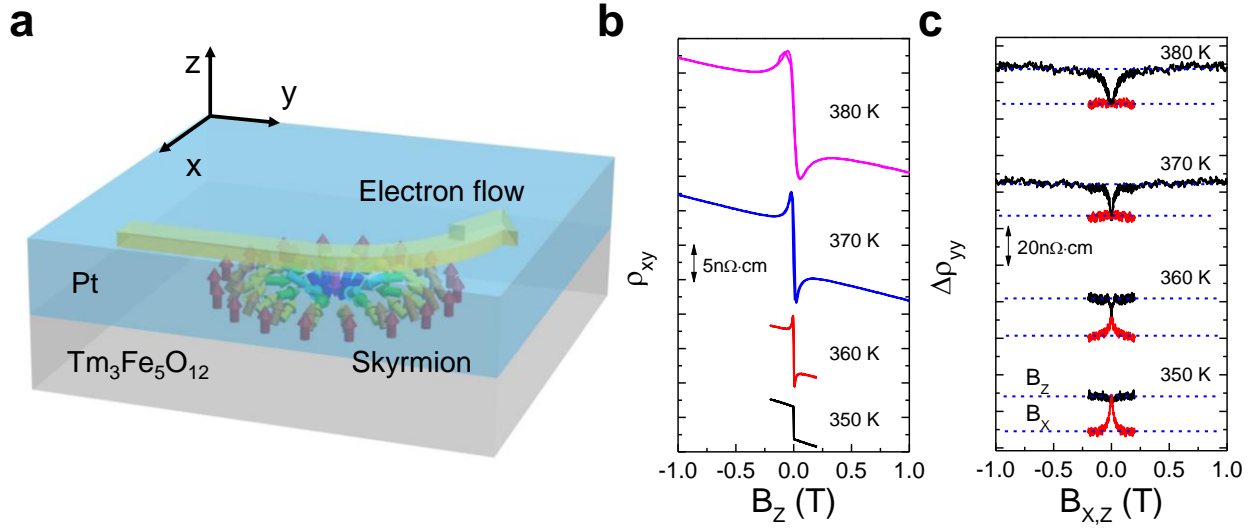


Figure 6-4 Illustration of topological Hall effect in the TmIG/Pt and transport properties of the TmIG(3.2 nm)/Pt (4 nm) bilayer. **a**, Schematic of the topological Hall effect in the TmIG/Pt. The current at the TmIG/Pt interface goes through the emergent electromagnetic field generated by the skyrmion in the TmIG and gives rise to the transverse Hall current. **b**, Hall resistivity as a function of the out-of-plane magnetic field at different temperatures. Above 350 K, topological Hall effect is observed as peaks and dips happen at low fields. **c**, Longitudinal resistivity as a function of both the out-of-plane (black, along the $\pm z$ direction) and in-plane (red, along the $\pm x$ direction) magnetic fields at different temperatures, from which we determine the out-of-plane magnetization component of TmIG as a function of external field using the theory of spin Hall magnetoresistance (see Session 6.4.3). The data are offset for clarity.

We observe a typical sharp hysteresis loop of ρ_{xy} as a function of out-of-plane external field (B_z) for the TmIG (3.2 nm)/Pt(4 nm) bilayer at 350 K (Figure 6-4b), where the step function at low fields is due to the AHE and the linear background with a negative slope at large fields arises from the OHE. Above 350 K, unusual ρ_{xy} dips at low positive fields and peaks at low negative fields emerge and gradually disappear at large fields as shown in Figure 6-4b. We identify the overshoot in these out-of-plane hysteresis loops as the THE due to the presence of magnetic skyrmions [201,

202]. Moving spin-polarized electrons (as evidenced by AHE and SMR) can pick up the skyrmion-induced Berry phase by adjusting their spins to the local spin direction of the skyrmion texture, which gives rise to the THE. To obtain the AHE contribution in ρ_{xy} , we determine the m_z as a function of B_z by tracking the change of longitudinal resistance $\Delta\rho_{yy}$ (Figure 6-4c) since $\Delta\rho_{yy} \propto m_z^2$ according to the theory of SMR [127] (See Session 6.4.3 for details).

We plot the measured ρ_{xy} and the simulated contributions from the OHE and AHE together in Figure 6-5a for $T = 360$ K, where we observe an apparent difference between these two plots. By subtracting the contributions from the OHE and AHE, we determine the magnitude of the ρ_{THE} (Figure 6-5a).

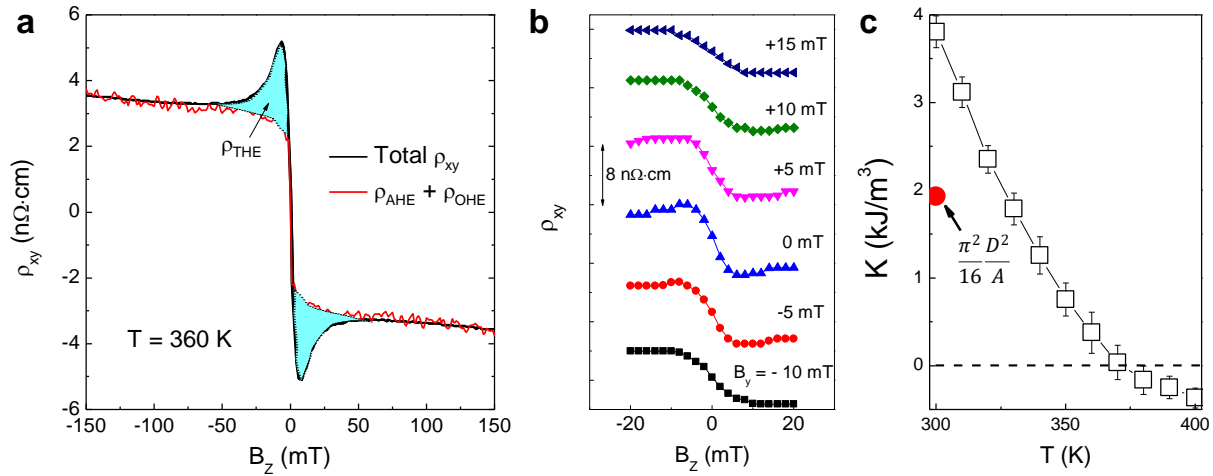


Figure 6-5 Observation of topological Hall effect (THE) in the TmIG(3.2 nm)/Pt (4 nm) bilayer. **a**, Hall resistivity (black curve) as a function of an out-of-plane magnetic field at $T = 360$ K. The red curve is the contribution of the anomalous Hall effect and the ordinary Hall effect. The shaded light blue region is the contribution of THE. **b**, Out-of-plane Hall hysteresis loops in the presence of different in-plane external fields. **c**, Anisotropy energy K (black square symbols and curve) as a function of T . The red symbol is $\frac{\pi^2 D^2}{16 A}$, where D is interfacial DMI energy and A is the exchange stiffness. The anisotropy transitions from perpendicular magnetic anisotropy to easy-plane

anisotropy near 370 K. **d**, Skyrmion phase diagram from the THE as a function of temperature T and external field B_z . The color bar indicates the value of measured THE resistivity. Interpolation between experimentally measured data points is applied. **e**, Theoretical skyrmion density diagram as a function of the normalized anisotropy energy (KA/D^2) and the Zeeman energy ($B_{\text{E}}A/D^2$).

To host magnetic skyrmions in the TmIG, there must be a sizable interfacial DMI energy (D) at the interface between the TmIG and the Pt for stabilizing magnetic chiral structures. Experimentally, Pt/ferromagnetic metal bilayers have been reported to show a very strong interfacial DMI, $D \sim 1\text{-}2 \text{ mJ/m}^2$, which supports sub-100 nm skyrmions at room temperature [176, 177]. In theory, we also expect to have a sizeable interfacial DMI at the TmIG/Pt interface due to a strong coupling between Pt and Fe atoms as evidenced by the AHE and SMR. We estimate the magnitude of D in our TmIG/Pt bilayer by employing a domain wall motion technique described in ref. [75]. The determined D is $\sim 51 \text{ } \mu\text{J/m}^2$ at room temperature (see Session 6.4.4). While the absolute value of D at room temperature for our TmIG/Pt is smaller than the case in Pt/ferromagnetic metal bilayers, the ratio of D over exchange stiffness (A) is comparable since A is estimated to be $\sim 0.84 \text{ pJ/m}$ (see Session 6.4.4). To highlight the importance of interfacial DMI, we apply in-plane external field to overcome the DMI effective field and eliminate the magnetic chiral structures. Experimentally, we observe that when the applied in-plane field increases, the overshoot in the out-of-plane hysteresis loops becomes less obvious (Figure 6-5b), which suggests reduced THE.

The appropriate anisotropy energy (K) of TmIG is achieved by varying the temperature to satisfy the requirement for the presence of skyrmions. Theory shows that K should be $\leq \frac{\pi^2 D^2}{16 A}$ to form a skyrmion lattice [193, 195], which suggests that skyrmions can only be stabilized in a weak anisotropy regime. For our TmIG/Pt, the K can be continuously tuned from positive (PMA) to

negative (easy plane anisotropy) by changing the temperature, which passes the zero-anisotropy energy. This tunability is critical for the formation of skyrmions in a window of temperature. The increase of temperature reduces K , most likely due to the reduced magneto-elastic coefficient that contributes to the PMA [162]. To illustrate the importance of the tunable K , we plot the temperature dependence of K as shown in Figure 6-5c. K is initially much larger than $\frac{\pi^2 D^2}{16 A}$ at $T = 300$ K. As temperature increases, the K decreases then eventually becomes negative. By varying the temperature, we obtain a skyrmion phase diagram from the THE as a function of temperature and external field (Figure 6-6). We can see that the THE emerges when the K is close to zero. With the sizable D and appropriate K , we conclude that the presence of magnetic skyrmions is the driving force for the observation of THE in the TmIG/Pt.

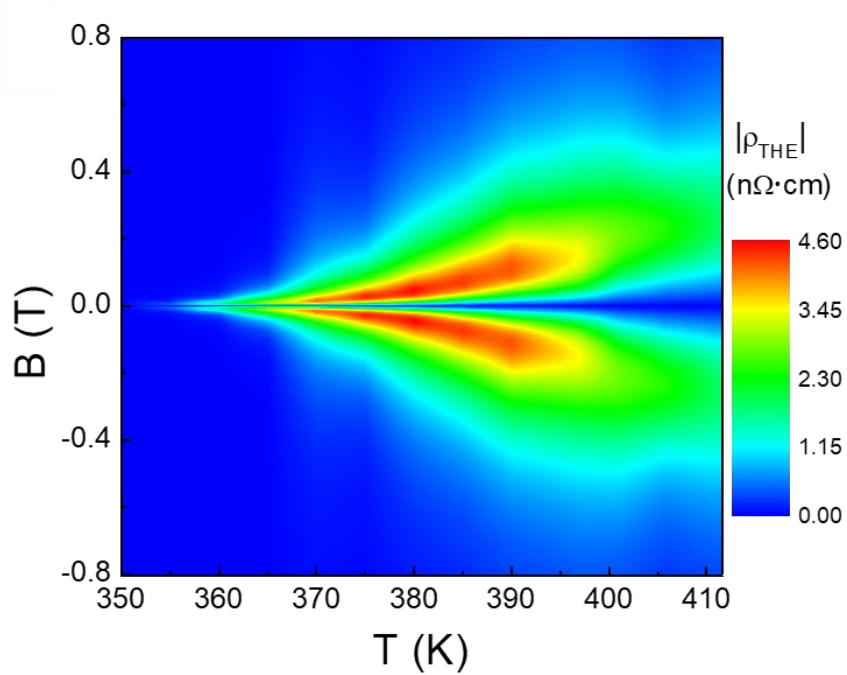


Figure 6-6 Skyrmion phase diagram from the THE as a function of temperature T and external field B_z in the TmIG(3.2 nm)/Pt (4 nm) bilayer. The color bar indicates the value of measured THE resistivity. Interpolation between experimentally measured data points is applied.

We now focus on the external field dependence of THE. We anticipate a spin spiral phase (or a balanced number of skyrmions with topological charge +1 and -1) near zero field and a ferromagnetic phase at large fields, in which the THE is minimized [183]. We estimate the stability of a skyrmion lattice by employing a free energy minimization method, in which we consider exchange, anisotropy, DMI, and Zeeman energy [192, 193]. Here, we assume a perfect hexagonal skyrmion lattice for simplicity of calculation. Since the ρ_{THE} is proportional to the skyrmion density, we compute a skyrmion density diagram as a function of normalized K and Zeeman energy (Figure 6-1b), where $B_E = M_S B_Z$. Full micromagnetic simulations reveal an even larger skyrmion window of K and B_Z when the magnetostatic energy is included (Figure 6-2). In agreement with the calculated skyrmion density in Figure 6-1b, the ρ_{THE} at a given temperature first increases and then decreases with the external field (Figure 6-6). Also, below 370 K, the ρ_{THE} at a given field increases as temperature increases (Figure 6-6) due to the reduced PMA (Figure 6-5c), which agrees with Figure 6-1b and is consistent with the very recent observation in Ir/Fe/Co/Pt multilayers [195]. Furthermore, we observe a larger external field window in a higher temperature for stable skyrmions in Figure 6-6, when the K transitions from PMA ($K > 0$) to easy plane anisotropy ($K < 0$) near 370 K (Figure 6-5c). Thanks to the great tunability of K in the TmIG/Pt bilayer through varying temperature, the stability of skyrmions against external field is enhanced and the ρ_{THE} is increased in the easy plane anisotropy regime. Our observations are consistent with the calculations (Figure 6-1b) and the prediction by Banerjee *et al.* [192]. Therefore, the temperature and external field dependences of THE agree with the theoretical expectations, confirming the existence of magnetic skyrmions in TmIG/Pt.

6.4.3 Self-calibrated determination of topological Hall effect

The signatures of topological Hall effect (THE), which are overshoots (peaks and dips at small fields) in the out-of-plane Hall resistivity hysteresis loops, have been clearly observed in multiple TmIG(3.2 nm)/Pt(4 nm) Hall bar devices (number of measured devices ≥ 5). We show the temperature dependence of out-of-plane Hall hysteresis loops for three devices D1, D2, and D3 in Figure 6-7a, Figure 6-7b, and Figure 6-7c, respectively. The data of Figure 6-4b, Figure 6-4c and Figure 6-5a are from device D1. The data of Figure 6-6 are from device D2. These devices show quantitatively consistent results and THE emerge above 350 K in all devices. To extract the THE contribution, we need to subtract the anomalous Hall effect (AHE) and ordinary Hall effect (OHE) contributions from the measured (total) Hall resistivity ρ_{xy} . A typical method to determine the AHE contribution is using a separately measured magnetization versus out-of-plane external field (M_Z - B_Z) loop on a large-size thin film sample [183, 201, 202]. We develop a self-calibrated technique to measure the M_Z - B_Z loop for a single (micro-size) Hall bar device by tracing the longitudinal resistivity as a function of B_Z . Before doing this, we emphasize that the observed THE remains significant no matter what kind of AHE contribution is subtracted since the features of overshoots are very clear in the hysteresis loops (see Figure 6-5a and Figure 6-8c-d).

The M_Z - B_Z loop of a Hall bar device is obtained from the external field dependence of longitudinal resistivity (Figure 6-4c). In the studied temperature range (≥ 300 K), we have $\rho_{x,sat} < \rho_{y,sat} = \rho_{z,sat}$, where $\rho_{i,sat}$ ($i = x, y, z$) is the longitudinal resistivity when the magnetization is saturated along the i direction. The relation is consistent with the theory of spin Hall magnetoresistance [127]. When the external field is swept along a specific direction, the change of longitudinal resistance can be written as $\Delta\rho_{yy} = \rho_{SMR}(1 - m_x^2)$, where $\rho_{SMR} (> 0)$ is the magnitude of spin

Hall magnetoresistance. From 300 K to 350 K, the $\Delta\rho_{yy}$ of TmIG/Pt shows a peak at zero field while sweeping external field along the $\pm x$ direction (see 350 K curve in Figure 6-4c). This is because, at large fields, the magnetization is pulled along the $\pm x$ direction, whereas at zero field, the magnetization is out-of-plane due to the PMA. When the temperature is raised to 360 K, the PMA becomes weaker as evidenced by the increased saturation field in the out-of-plane direction. As the temperature continues to increase, the PMA disappears as it is harder to saturate the magnetization in the out-of-plane direction compared with the in-plane direction, which is reflected by a dip of $\Delta\rho_{yy}$ at zero field while sweeping external field along the $\pm z$ direction (see 380 K curve in Figure 6-4c). By using $\Delta\rho_{yy} = \rho_{SMR}(1 - m_x^2) = \rho_{SMR}m_z^2$, we determine the M_z - B_z loops for the TmIG (3.2 nm)/Pt (4 nm) device D1 (see Figure 6-8a). Therefore, from 350 K to 380 K, the magnetic anisotropy of TmIG changes from the easy axis anisotropy (PMA) to the easy plane anisotropy.

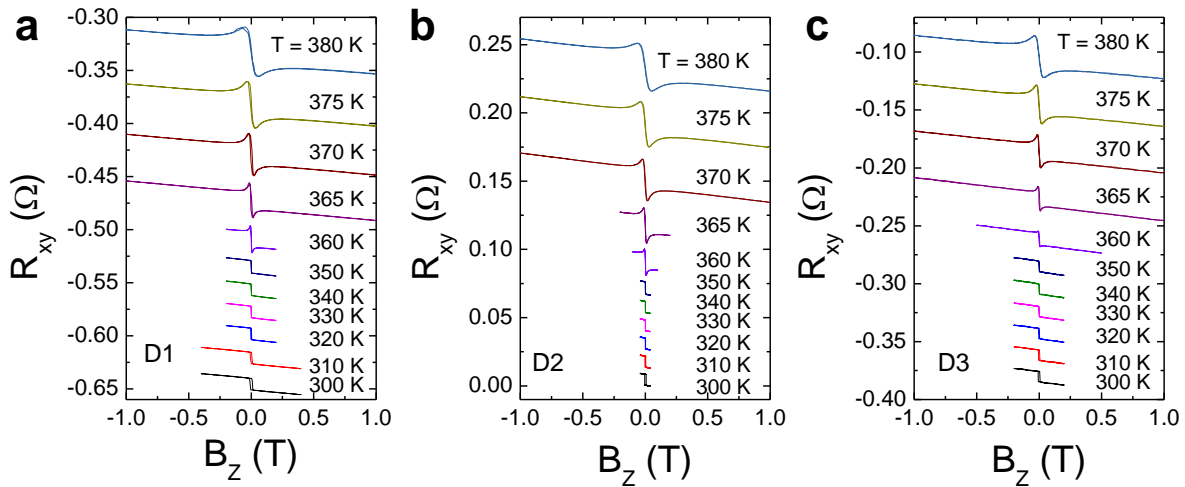


Figure 6-7 Hall resistance as a function of out-of-plane magnetic field for three different TmIG(3.2 nm)/Pt(4 nm) Hall bar devices, D1 (a), D2 (b) and D3 (c).

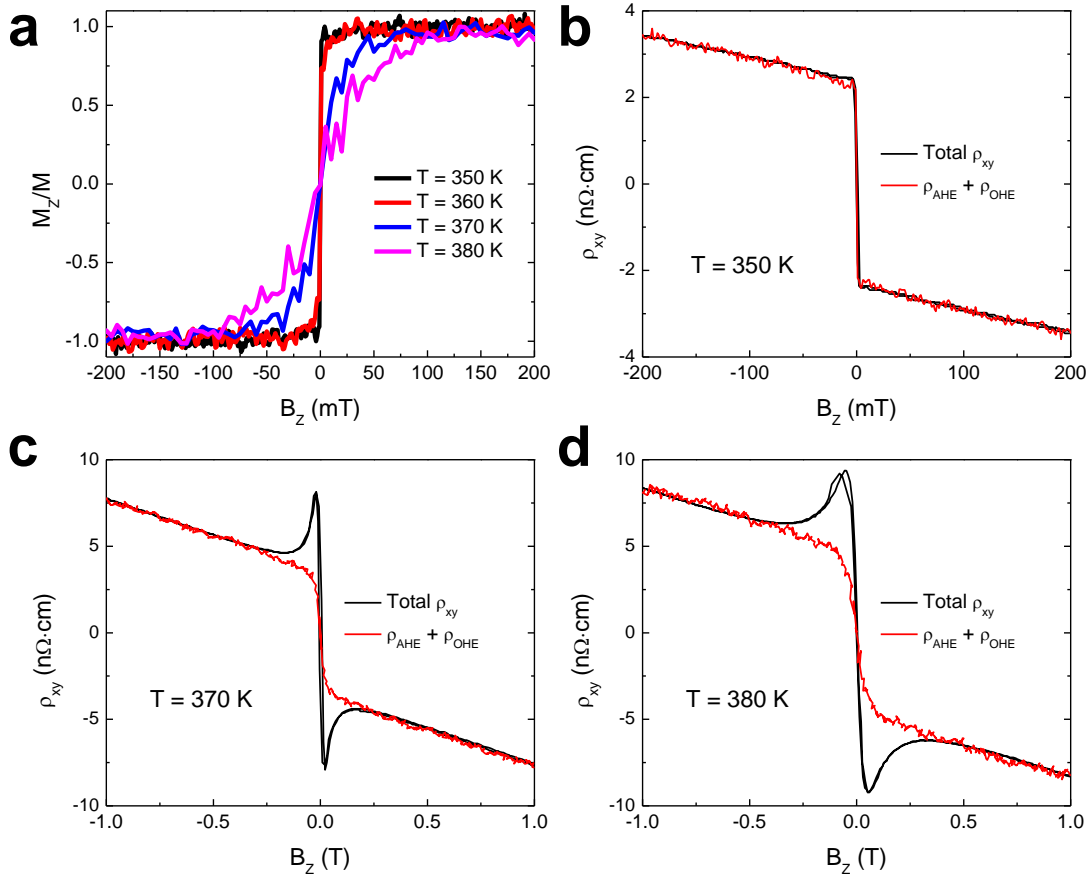


Figure 6-8 Self-consistent determination of THE for the TmIG(3.2 nm)/Pt (4 nm) device D1. **a**, Normalized M_z as a function of B_z inferred from measurements of longitudinal resistance as a function of B_z (see Fig. 1c). (**b-d**) Measured ρ_{xy} (black curve) and simulated contributions from the ordinary Hall and anomalous Hall effects (red curve) for the TmIG(3.2 nm)/Pt(4 nm) Device 1 at $T = 350$ K (**b**), 370 K (**c**) and 380 K (**d**).

We plot the measured ρ_{xy} and simulated contributions from the OHE and AHE together for TmIG (3.2 nm)/Pt (4 nm) device D1 in Figure 6-5a at $T = 360$ K and Figure 6-8b-d at $T = 350$ K, 370 K and 380 K, respectively. By subtracting off the simulated contributions from the OHE and AHE, we determine the magnitude of the THE (ρ_{THE}) at different temperatures. Note that the method we

use to determine the THE is self-calibrated in the sense that the ρ_{THE} is determined from the measured total ρ_{xy} by subtracting the magnitude of OHE and AHE, which are simulated from the measured $\Delta\rho_{yy}$. Therefore, we do not need to know the exact value of m_z in a micro-size Hall bar device from separately measured M_Z - B_Z loops using a large film. Nevertheless, we have confirmed the consistency between simulated and measured M_Z - B_Z loops at different temperatures using a TmIG(4 nm)/Pt(4 nm) bilayer.

6.4.4 Determination of DMI energy at room temperature

The DMI effective field (H_{DMI}) is determined by the asymmetric domain expansion in the presence of current-induced spin-orbit torque [75]. The principles are illustrated in Figure 6-9a-b and has been well explained in Session 2.4 and ref. [75]. This technique does not assume the metallic nature of the ferromagnetic layer since its analysis only depends on how the spin texture of the magnetic layer responds to the external field and electric current. We have shown that that the electric current can generate a sizable SOT and lead to magnetization switching in both Pt/Tm₃Fe₅O₁₂ (see Session 4.4.2) and W/Tm₃Fe₅O₁₂ [119] just like magnetic metallic systems like Pt/Co and W/CoFeB. Figure 6-9c shows the out-of-plane Hall resistance hysteresis as a function of current when $H_y = + 500$ Oe is applied. Figure 6-9d summarizes the shift per unit current as a function of in-plane external field, in which we determine the H_{DMI} and the damping-like spin-orbit torque effective field. After we determine H_{DMI} , we calculate DMI energy D using $D = \mu_0 M_S \Delta |H_{DMI}|$, where μ_0 is the vacuum permeability, M_S is the saturation magnetization, and Δ is the domain wall width. The domain wall width is given by $\Delta = \sqrt{\frac{A}{K}}$, where A is the exchange stiffness and K is the anisotropy (PMA) energy. From Figure 6-9d, we obtain an effective DMI

field (H_{DMI}) of $H_{DMI} \sim 475$ Oe and a DMI energy of $D \sim 51 \mu\text{J}/\text{m}^2$ at room temperature; here we use saturation magnetization (M_S) 73 kA/m for TmIG (Figure 6-11b).

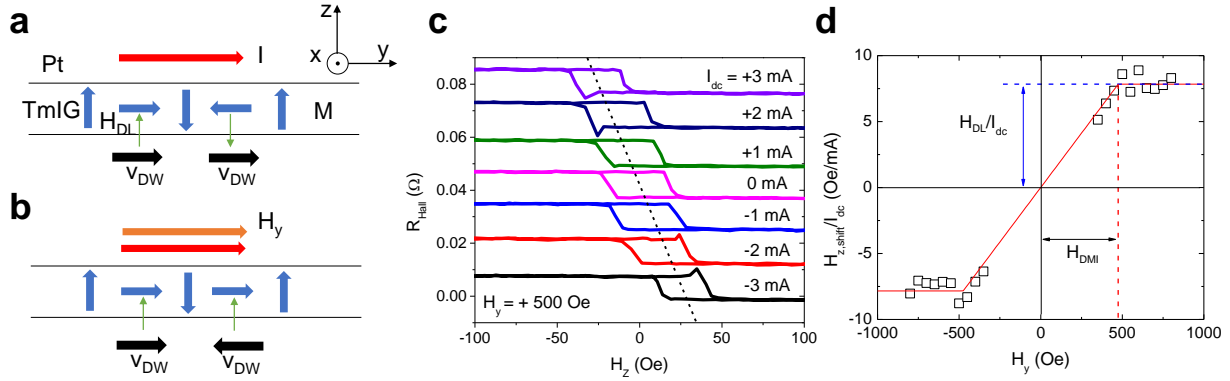


Figure 6-9 Current-induced asymmetric domain expansion and out-of-plane field hysteresis loop shift. **a**, In the absence of the external field and the presence of DMI (assuming right-handed chirality), the magnetization direction in the domain wall is always pointing from up to down. Due to the current-induced damping-like spin-orbit torque (effective field, H_{DL}), the velocities of both up to down and down to up domain walls are along the same direction and there is no domain expansion. Therefore, the presence of current will not favor one particular magnetization direction and thus there is no shift of out-of-plane hysteresis loop. **b**, When the external field along the $+y$ direction is able to overcome the DMI effective field (H_{DMI}) and pull the magnetization in all domain walls along the $+y$ direction, the velocities of up to down and down to domain walls in the presence of current along the $+y$ direction are opposite and there is an up domain expansion. Therefore, the current along the $+y$ direction will favor up magnetization and thus shifts the out-of-plane hysteresis towards the negative field. **c**, The out-of-plane Hall resistance hysteresis as a function of lateral current when $H_y = +500$ Oe is applied. **d**, The shift of out-of-plane Hall hysteresis loop as a function of in-plane external magnetic field, from which the DMI effective field (H_{DMI}) is determined by the saturation field of damping-like spin-orbit field (H_{DL}/I_{dc}). Measurements are done at 300 K.

Here, we discuss how we estimate the value of A and the effect of A on the D and emergence of magnetic skyrmions. The magnitude of A is of order $|J|\langle S \rangle^2/a$, where J is the exchange constant, a is the lattice parameter and $\langle S \rangle$ may be interpreted crudely as a thermal average over subnetwork spin or M_S in our case [181]. In ultrathin TmIG films, $|J|$ is smaller compared with the bulk value, as evidenced by the lower Curie temperature ($T_C \sim |J|$), which is ~ 450 K estimated from Figure 6-11b. M_S (~ 73 kA/m) of a 4 nm-thick TmIG at room temperature is also reduced compared with the bulk value (~ 110 kA/m) [131]. For bulk YIG at room temperature, $A \sim 4.15$ pA/m with $M_S \sim 145$ kA/m and $T_C \sim 560$ K [181]. We estimate the A for our TmIG(4 nm) is ~ 0.84 pA/m at room temperature from $A(\text{TmIG}) = A(\text{YIG}) \cdot J_{\text{TmIG}}/J_{\text{YIG}} \cdot (M_{S,\text{TmIG}}/M_{S,\text{YIG}})^2$. While the value of A has a direct impact on the value of D since $D = \mu_0 M_S \sqrt{\frac{A}{K}} |H_{DMI}|$, the absolute value of A does not affect the boundary condition for emergence of magnetic skyrmions, $\frac{\pi^2 D^2}{16 A}$, which is only related to measured M_S and H_{DMI} .

To understand the origin of the interfacial DMI, we made a control sample W(5nm)/TmIG(3.2nm) and measured its Hall effect in the presence of out-of-plane external fields (Figure 6-11). There is no clear topological Hall effect (THE) being observed during the transition temperature window for magnetic anisotropy from perpendicular magnetic anisotropy to easy-plane anisotropy. While we cannot fully exclude the presence of DMI at the TmIG/NGG interface, our results about the Pt/TmIG and W/TmIG strongly suggest that the Pt/TmIG is critical for the presence of the DMI and thus THE.

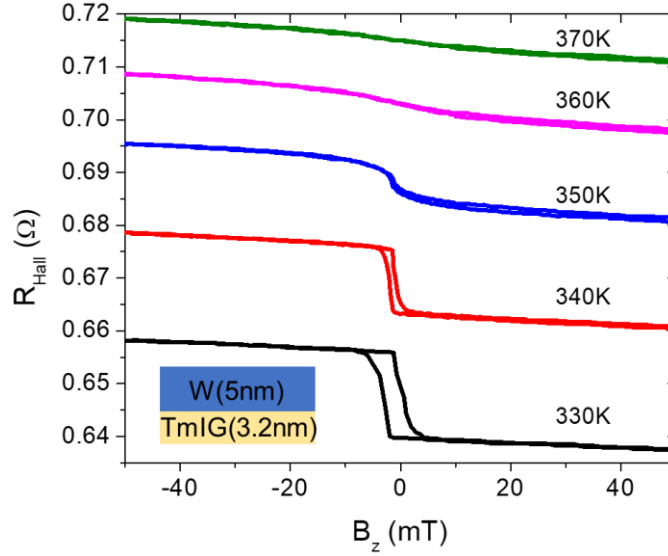


Figure 6-10 Temperature-dependent out-of-plane hysteresis loops in the W(5nm)/TmIG(3.2nm)/NGG(substrate).

6.4.5 Temperature dependence of saturation magnetization and anisotropy energy

Here, we estimate the temperature dependence of M_S and K .

We measure the magnetic moment of a TmIG(4 nm)/Pt(4 nm) film ($5 \text{ mm} \times 5 \text{ mm}$) using SQUID at different temperatures. Figure 6-11a shows the temperature dependence of the magnetic moment, indicating that the temperature of magnetic anisotropy transition from the easy axis to the easy plane is around 390 K, which is consistent with the transport measurement. The temperature dependence of M_S is shown in Figure 6-11b.

The magnitude of K is determined using $K = K_U - 2\pi M_S^2 = \mu_0 M_S H_K$, where K_U is the uniaxial anisotropy due to strain (magnetoelastic) effect and H_K is the effective anisotropy field. The values of H_K at different temperatures are experimentally determined by measuring the saturation field of

hard-axis hysteresis loops (Figure 6-12). The obtained values of H_K for different TmIG thickness are presented in Figure 6-14.

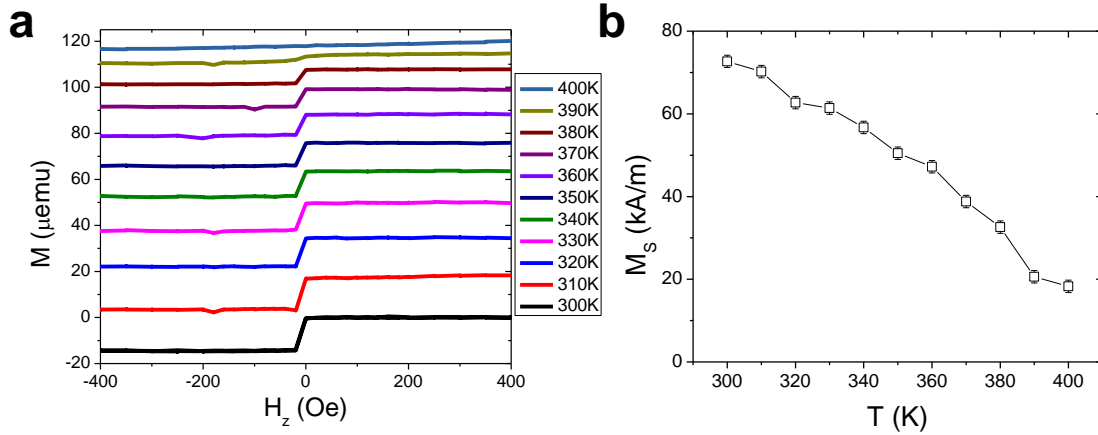


Figure 6-11 Temperature-dependent magnetization for a TmIG. **a**, M as a function of H_z at different temperatures measured by SQUID for a TmIG(4 nm)/Pt(4 nm) bilayer film with area $5 \text{ mm} \times 5 \text{ mm}$. All the curves are offset for clarity. **b**, M_s as a function of temperature for a reference TmIG(4 nm)/Pt(4 nm) thin film.

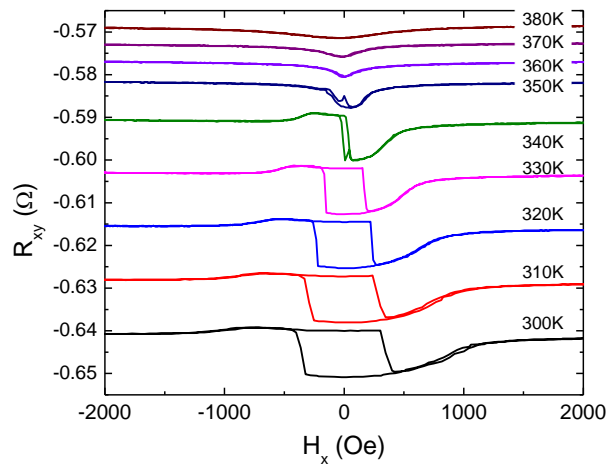


Figure 6-12 In-plane Hall resistance hysteresis loops at different temperatures for TmIG(3.2 nm)/Pt(4 nm) device D1. We determine the H_K from the saturation field of the hard-axis hysteresis loops, i.e., in-plane hysteresis loops for PMA case.

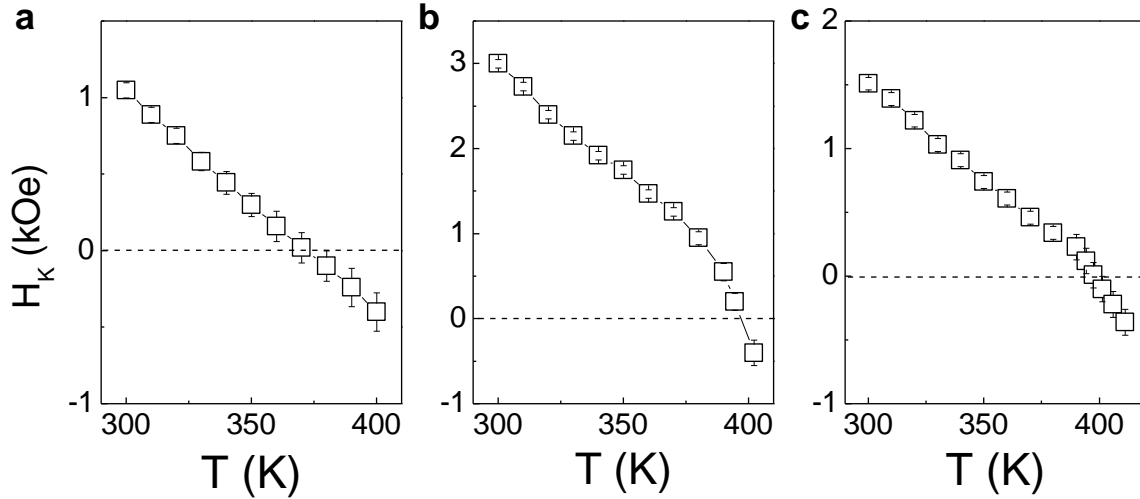


Figure 6-13 Temperature dependent magnetic anisotropy effective field for different TmIG thickness. **a**, 3.2 nm. **b**, 4 nm. **c**, 6 nm.

6.4.6 MI thickness dependence

We now investigate the TmIG thickness (t_{TmIG}) dependent THE in TmIG/Pt(4 nm) bilayers to clarify the importance of the interfacial DMI. Since the magnitude of interfacial DMI is inversely proportional to the ferromagnetic layer thickness [203], we do not expect the presence of magnetic skyrmions in the thick TmIG limit. In the extremely thin TmIG, the ferromagnetism disappears. Experimentally, the results of skyrmion phase diagram from THE from the $t_{\text{TmIG}} = 3.2$ nm, 4 nm and 6 nm are shown in Figure 6-14a-c, respectively. The detailed phase diagrams are shown in Figure 6-6, Figure 6-15, and Figure 6-16, respectively. We have two major findings. First, for all TmIG thicknesses, the THE only emerges when the magnetic anisotropy is in the transition from PMA to easy-plane anisotropy or close to zero. This is consistent with the theory as we discussed above. Second, near the magnetic anisotropy transition temperature, the temperature-field window of the THE becomes smaller as the t_{TmIG} increases, and eventually disappears for the $t_{\text{TmIG}} = 6.4$

nm (Figure 6-17). This shows that even when the K is meeting the condition of skyrmion formation, the skyrmion cannot exist in thicker films. The absence of the THE in thicker TmIG films suggests that the DMI is negligible in these films, which is consistent with the interfacial DMI from the Pt/TmIG interface.

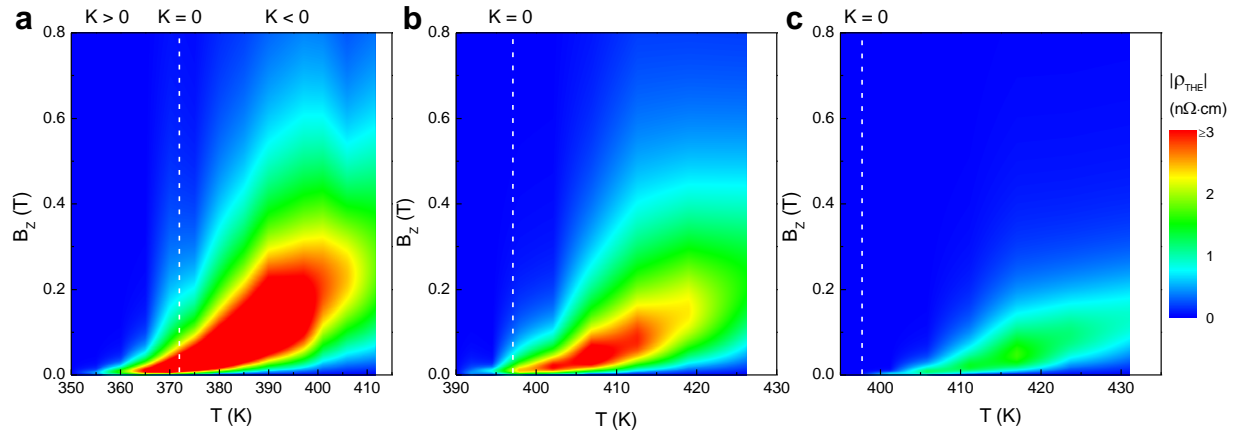


Figure 6-14 Experimentally obtained evolution of skyrmion phase diagram as a function of TmIG thickness (t_{TmIG}) in TmIG/Pt (4 nm) bilayers. **a**, $t_{\text{TmIG}} = 3.2$ nm. **b**, $t_{\text{TmIG}} = 4$ nm. **c**, $t_{\text{TmIG}} = 6$ nm. Note that the highest THE resistivity drops as the t_{TmIG} increases, which are $4.58 \text{ n}\Omega\cdot\text{cm}$, $3.44 \text{ n}\Omega\cdot\text{cm}$, $1.66 \text{ n}\Omega\cdot\text{cm}$ for the 3.2 nm, 4 nm and 6 nm, respectively (see Fig. 2d and Supplementary Information S7). The dashed white line indicates the temperature, at which the magnetic anisotropy transitions from PMA to in-plane anisotropy (see Supplementary Fig. S7). We set the highest value of the plotted THE resistivity to $3 \text{ n}\Omega\cdot\text{cm}$ to show a good color contrast (see color bar). Interpolation between experimentally measured data points is applied.

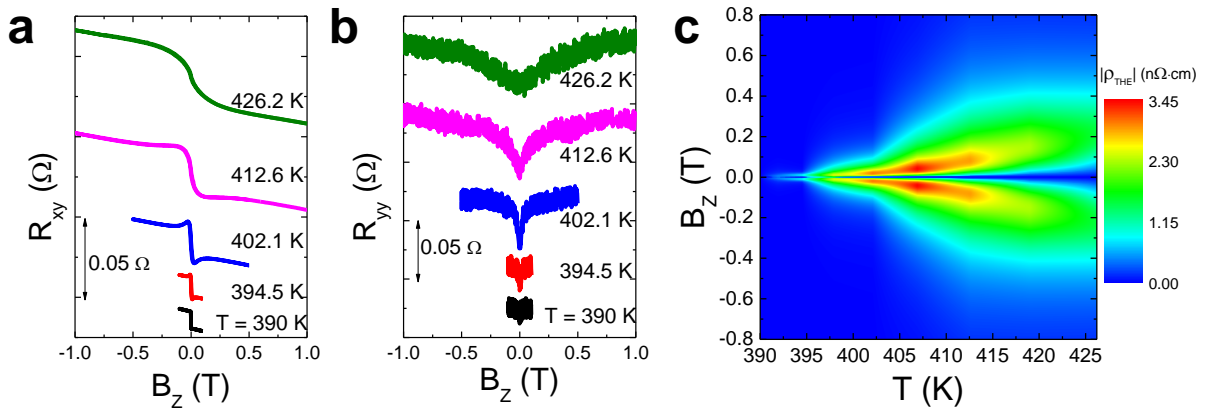


Figure 6-15 Skymion phase diagram from the THE in the TmIG (4 nm)/Pt (4 nm) bilayer. **a**, Out-of-plane Hall hysteresis loops at different temperatures. **b**, Longitudinal resistance as a function of the out-of-plane external field at different temperatures. **c**, Skymion phase diagram from the THE resistivity. Note that the scale of color bar is different from Fig. 3b. Interpolation between experimentally measured data points is applied.

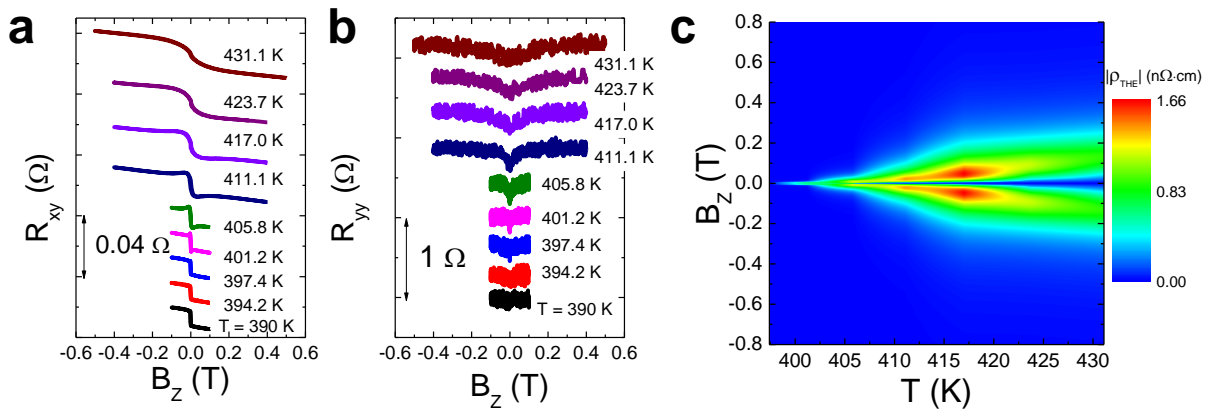


Figure 6-16 Skymion phase diagram from the THE in the TmIG (6 nm)/Pt (4 nm) bilayer. **a**, Out-of-plane Hall hysteresis loops at different temperatures. **b**, Longitudinal resistance as a function of the out-of-plane external field at different temperatures. **c**, Skymion phase diagram from the THE resistivity. Note that the scale of color bar is different from Fig. 3c. Interpolation between experimentally measured data points is applied.

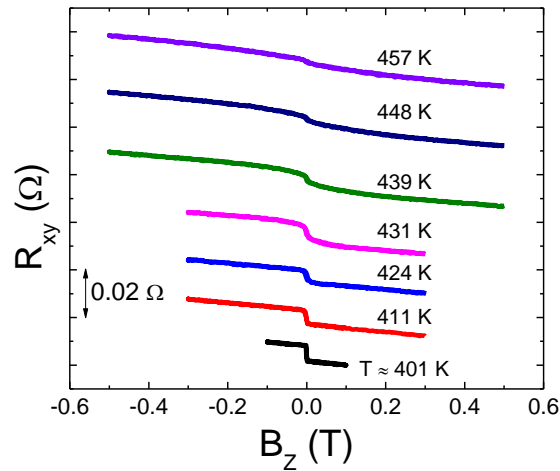


Figure 6-17 Out-of-plane Hall hysteresis loops at different temperatures in the TmIG (6.4 nm)/Pt (4 nm) bilayer.

To extend the range of measurement temperature beyond 390 K, we apply a.c. current to heat up the device and thus raise the device temperature equivalently. We estimate the temperature increase due to Joule heating by using the temperature-resistance curve (Figure 6-18a). In experiments, we measure the a.c. current dependent Hall bar device longitudinal resistance and thus use the temperature coefficient to calibrate the device temperature (Figure 6-18b).

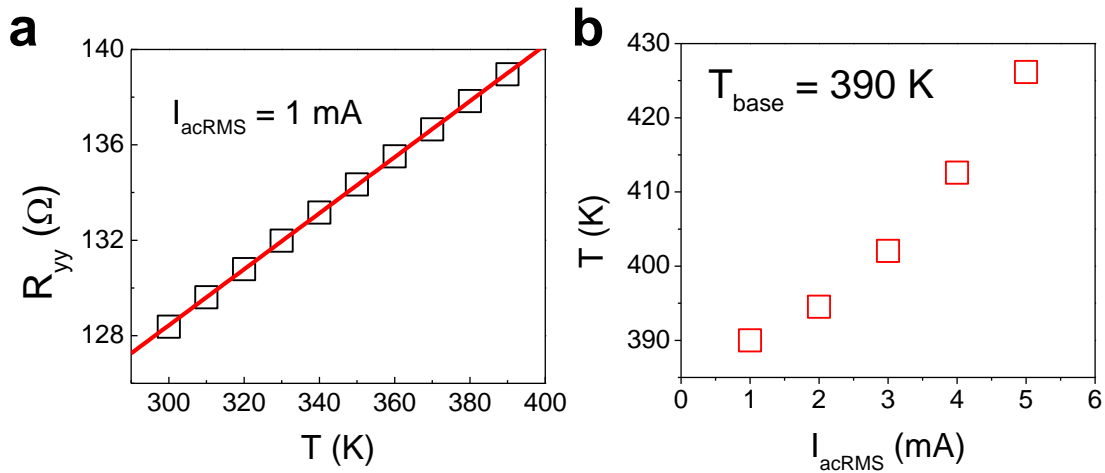


Figure 6-18 Temperature increase due to current-induced Joule heating. **a**, Longitudinal resistance as a function of temperature for the TmIG(4 nm)/Pt (4 nm) bilayer Hall bar device. **b**, Current dependence of temperature increase for the same device.

6.4.7 Origins of THE

We comment on the possibilities of other topological origins of ρ_{THE} and skyrmion density inferred from the observed ρ_{THE} . First, our ρ_{THE} is unlikely due to the emergent magnetic field associated with avoided band crossings in the reciprocal space [204, 205] that requires crystalline structure since the TmIG is an insulator with no itinerant electrons and Pt is a normal metal with no topological characteristics. Furthermore, our Pt is at best polycrystalline due to the nature of sputtering process, which can average out the effects of the emergent magnetic fields. Second, the noncollinear spin texture at the atomic scale, which was shown to be able to induce AHE in frustrated magnets [206], cannot be used to explain our ρ_{THE} since the TmIG is not a frustrated magnet. Thus, the ρ_{THE} must be due to presence of magnetic skyrmions and related localized chiral spin textures that carry nonzero topological charge. Experimentally, we achieved maximum ρ_{THE} around 4.6 n Ω ·cm for the 3.2 nm-thick TmIG. This corresponds to a maximum skyrmion density (ρ_{sk}) around 4800 μm^{-2} if we use $\rho_{\text{THE}} = \frac{\rho_0 P h}{e} \rho_{sk}$ [183]. Here, $\rho_0 = -4.64 \times 10^{-12} \Omega \cdot \text{cm}/\text{mT}$, $\frac{h}{e}$ is the quantum flux and we assume $P = 0.1$. This is much larger than the estimated maximum skyrmion density (Fig. 2e), which is around 70 μm^{-2} . This discrepancy has also been reported in metallic magnetic multilayers [195-197] and could be due to multi-band transport, distorted spin texture and nonadiabatic effect [194]. Nevertheless, this discrepancy suggests that single band model may not be precise for the complex magnetic multilayer thin films. We present two possible

reasons here. First, there could be other complex chiral spin textures, like worm-like structures [194], that host many quantum fluxes for a single magnetic object. Second, the ordinary Hall coefficient is an overall effect arising from the complex band structures of polycrystalline Pt films. The conduction electrons that interact with the skyrmion or other chiral textures may not follow this overall ordinary Hall coefficient. The difference of measured and estimated topological Hall effect is the latest topic that attracts extensive discussions now, including experimental works [194-197] and theoretical investigations [198, 199].

In addition to the electrical THE detection of skyrmions, the current-induced spin-orbit torques in the magnetic insulator/heavy metal bilayer could provide an efficient way to manipulate the skyrmion in the magnetic insulator. We have shown that the strong spin-orbit torque generated by the current in Pt can efficiently switch the magnetization of TmIG at room temperature (Figure 4-12). Therefore, we believe that the discovery of skyrmions in a simple magnetic insulator/heavy metal bilayer heterostructure like TmIG/Pt encourages and promises enormous future efforts for realizing low-power skyrmion-based applications at room temperature beyond studying fundamental problems such as magnon-skyrmion interaction in magnetic insulators. There are also many open questions remaining. For example, formulation for the proximity-induced THE, current-driven skyrmion dynamics, direct imaging of a skyrmion, and behaviors of the magnon-skyrmion interaction in the magnetic insulator/heavy metal bilayer system require further investigation.

6.5 Spin texture imaging techniques

To directly confirm the existence of particle-like skyrmions, we need to use magnetization imaging techniques with spatial resolution. The various techniques have been introduced in ref. [207].

Previously, our group have extensively used wide-field MOKE for imaging skyrmion and its dynamics [175, 208]. However, the spatial resolution is limited to a number 0.1 – 1 μm since the polarized light is visible light (wave length 380-740 nm). To have a better resolution, we have utilized nitrogen vacancy (NV) center in diamond to sense the skyrmion texture [209] with the help from UCSB Ania C. Bleszynski Jayich's group. To image the skyrmion in magnetic insulators, we have tried the Lorentz transmission electron microscopy (LTEM) with the help from KAUST Xixiang Zhang's group. To have a PMA, TmIG has to be grown on a crystalline substrate like NGG or SGGG. To study this heterostructure using LTEM, one needs to thin the film down to sub-100 nm. It is technically challenging and has not be solved yet. Meanwhile, I have collaborated with Rajesh Vilas Chopdekar from Advanced Light Source to use XMCD-photoemission electron microscopy (PEEM) to image the Pt/TmIG/NGG heterostructure. The advantage of this technique is that it does not require to process the sample and has reasonably good resolution (down to 10 nm).

We have prepared two samples, Pt(2nm)/TmIG(\sim 20nm) and Pt(2nm)/TmIG(\sim 2nm). The Pt thickness is smaller in the XMCD-PEEM measurements than in the transport measurements since the penetration depth of X-ray is limited. First, we confirmed the antiferromagnetic coupling between Fe and Tm (Figure 6-19).

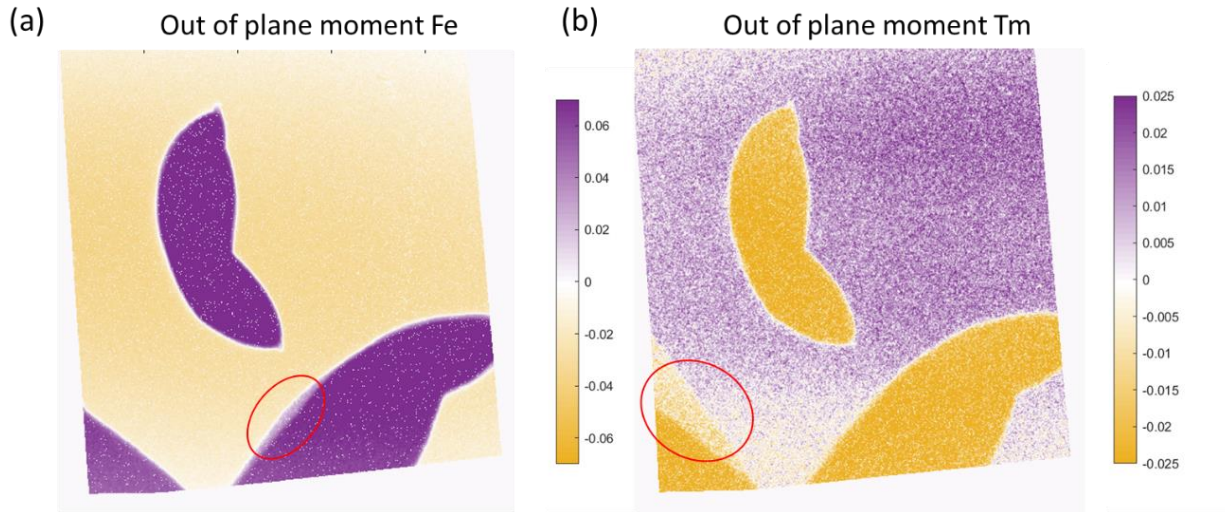


Figure 6-19 XMCD-PEED data for Pt(2nm)/TmIG(~20nm) at room temperature. The field of view is 20 μm .

The detailed spin texture analysis shows a rich chirality (Figure 6-20), which suggests a weak DMI in the bulk TmIG. This is consistent with previous reports on Sc-doped BaM [191], where random chirality has been shown. To show the effect of interfacial DMI, we studied thinner TmIG films. Unfortunately, the TmIG thickness was not optimized. We do not have a TmIG that is thinner enough to show the effect of interfacial DMI while keeps a finite magnetization at room temperature. The Pt(2nm)/TmIG(~2nm) does not have magnetization at room temperature. We cooled down the sample to 150 K and studied the XMCD-PEEM. We identified a circular bubble domain (Figure 6-21). Unfortunately, the detailed spin texture analysis requires sample tilting, which can be done at room temperature. Thus, the chirality of this bubble domain remains unknown. We are working on prepare TmIG with right thickness and design pattern to confine the skyrmion texture.

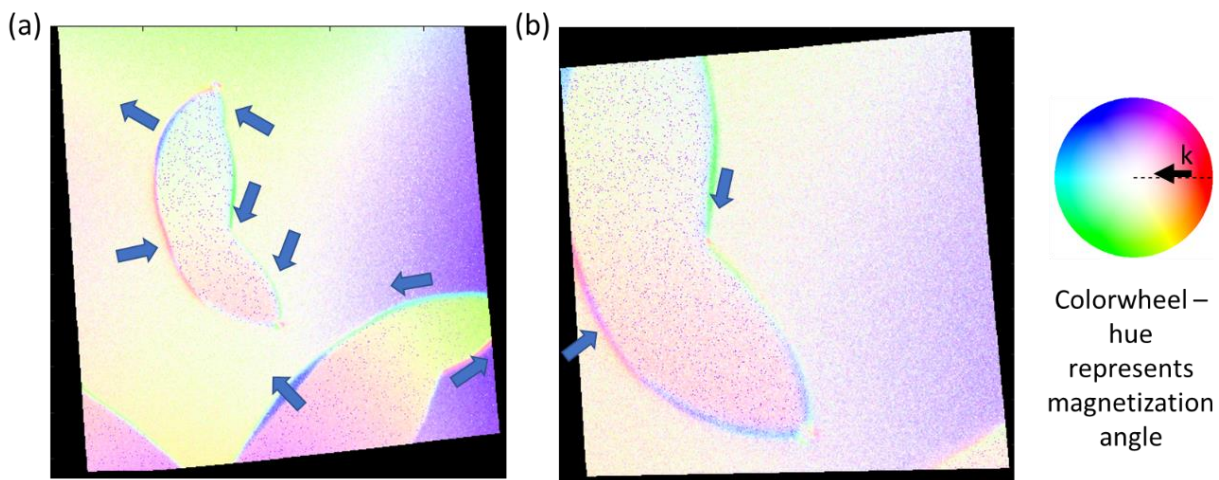


Figure 6-20 Detailed magnetization analysis of XMCD-PEED data for Pt(2nm)/TmIG(~20nm) at room temperature. The field of view is 20 μm and 10 μm for the left and right images, respectively.

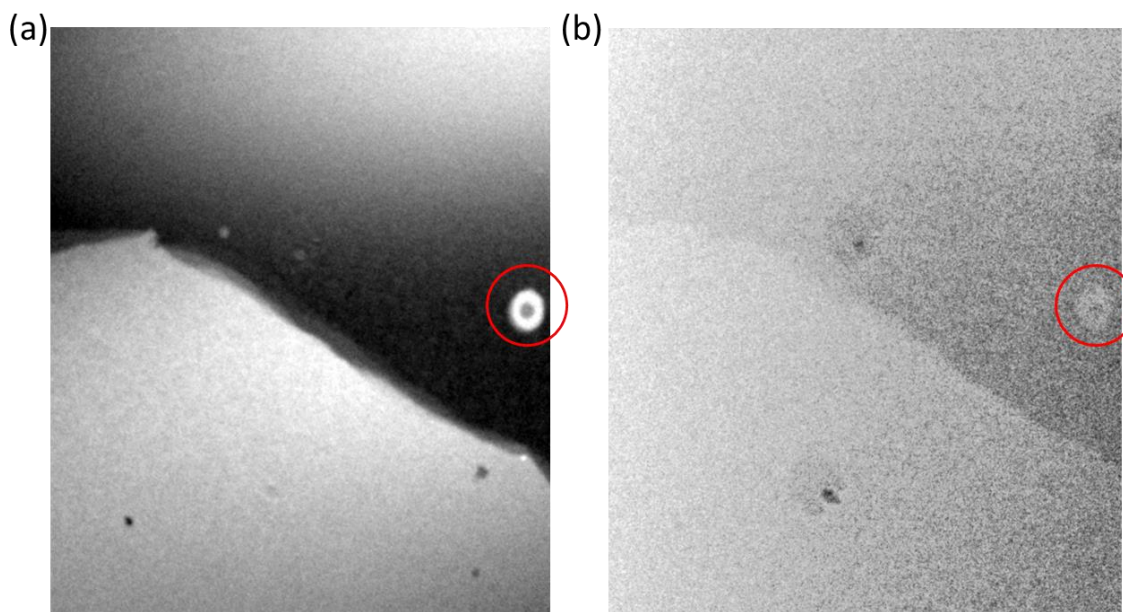


Figure 6-21 XMCD-PEED data for Pt(2nm)/TmIG(~2nm) at 150K. The field of view is 20 μm .

Chapter 7 Device modeling and applications

So far, I have discussed about device physics and characterizations. In this chapter, I will present some discussions on device modeling and applications, which are critical to connect devices to real applications.

7.1 SOT-MRAM design

Here, we discuss the modeling of single SOT-MRAM unit cell, especially for the purpose of single device energy performance optimization and scaling performance study.

7.1.1 SOT-MRAM with different channel materials

Figure 7-1 shows a schematic of a SOT-MRAM unit cell. For simplicity, we assume a square MTJ shape ($A_{\text{MTJ}} = R^2$), which is valid for the PMA case. Figure 7-2 and Figure 7-3 show the write energy (E_{write}) and write voltage (V_{write}) as a function of $\rho_{\text{HM, TI}}$, where we have two assumptions. First, we assume that switching time is 3 ns and $J_{\text{sw}} = 10^6$ MA/m² for $R = 10$ nm, $\Delta = 40$, and $\zeta_{\text{DL}} = 0.1$. Second, we assume that the SOT generation is dominated by the intrinsic mechanism [4], which means the $\zeta_{\text{DL}} = \rho_{\text{HM, TI}} \cdot \sigma_{\text{SH}}$, where σ_{SH} is the intrinsic spin Hall conductivity. The parameters used for Figure 7-2 and Figure 7-3 are shown in Table 1. We observe that the E_{write} is lowest for Bi₂Se₃ thanks to its large ζ_{DL} . Meanwhile, the V_{write} is well below 0.3 V, which is feasible for practical applications. Figure 7-4 shows that the E_{write} increases as the MTJ size scales down following $E_{\text{write}} \propto R^2$.

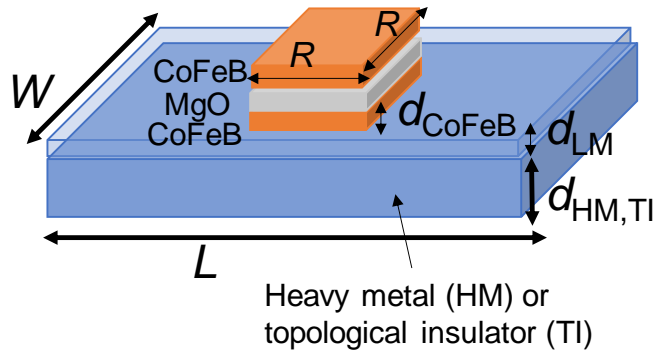


Figure 7-1 Schematic of a single SOT-MRAM bit. For calculations in this work, we use $W = 2R$, $L = 3R$, $\rho_{\text{CoFeB}} = 170 \mu\Omega \cdot \text{cm}$, $d_{\text{CoFeB}} = 1 \text{ nm}$, and $d_{\text{HM, TI}} = 6 \text{ nm}$. Reprinted with permission from [35], Copyright (2018) IEEE

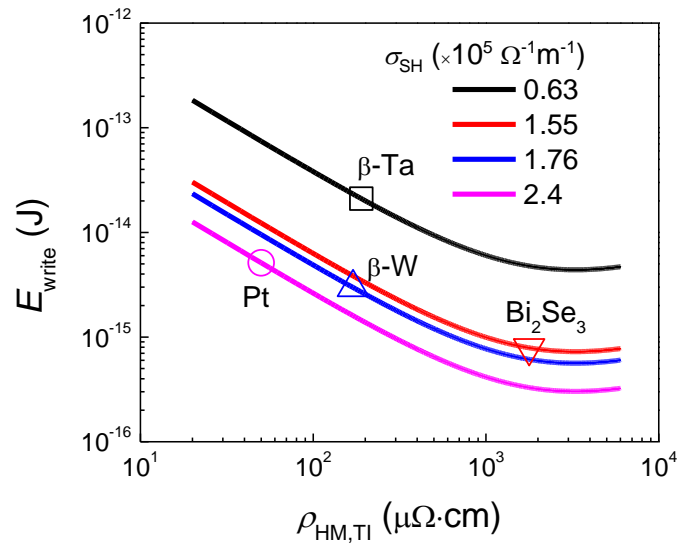


Figure 7-2 Write energy as a function of channel material resistivity for different σ_{SH} ($R = 10 \text{ nm}$). Reprinted with permission from [35], Copyright (2018) IEEE

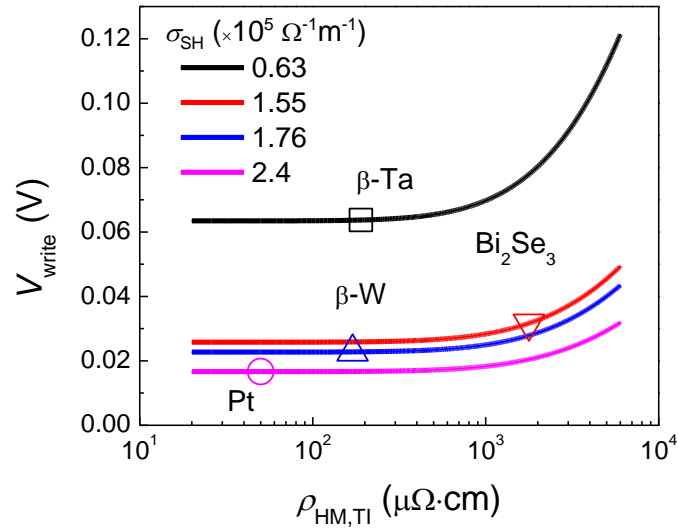


Figure 7-3 Write voltage as a function of channel material resistivity for different σ_{SH} ($R = 10 \text{ nm}$). Reprinted with permission from [35], Copyright (2018) IEEE

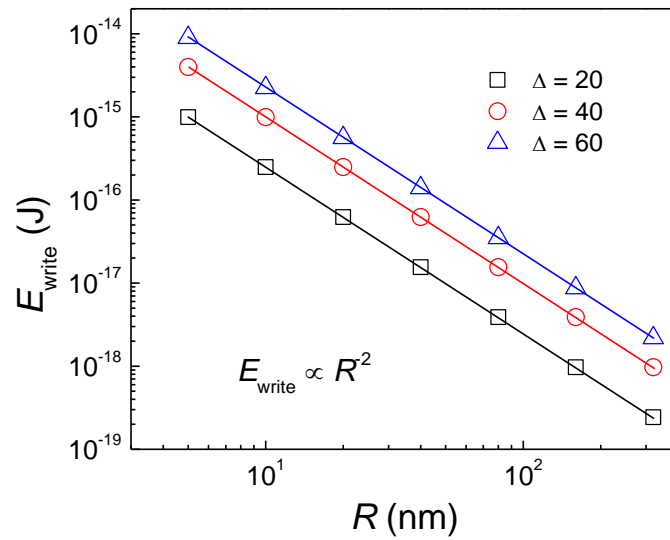


Figure 7-4 Write energy as a function of MTJ radius for different Δ ($\rho_{\text{TI}} = 10^3 \mu\Omega\cdot\text{cm}$, $\sigma_{\text{SH}} = 1.55 \times 10^5 \Omega^{-1}\cdot\text{m}^{-1}$). Reprinted with permission from [35], Copyright (2018) IEEE

7.1.2 Light metal spacer insertion for PMA and lower write energy

CoFeB is a widely used free layer due to its high TMR ratio in CoFeB/MgO/CoFeB MTJ. However, TI/CoFeB/MgO does not exhibit PMA. By inserting a light metal (LM) spacer between TI and CoFeB, interfacial PMA can be achieved. Note that the LM is for keeping the spin current and thus the large ζ_{DL} in TIs. Furthermore, Figure 7-5 shows that by appropriately choosing the spacer thickness and ρ_{LM} , reduction of the E_{write} is achieved.

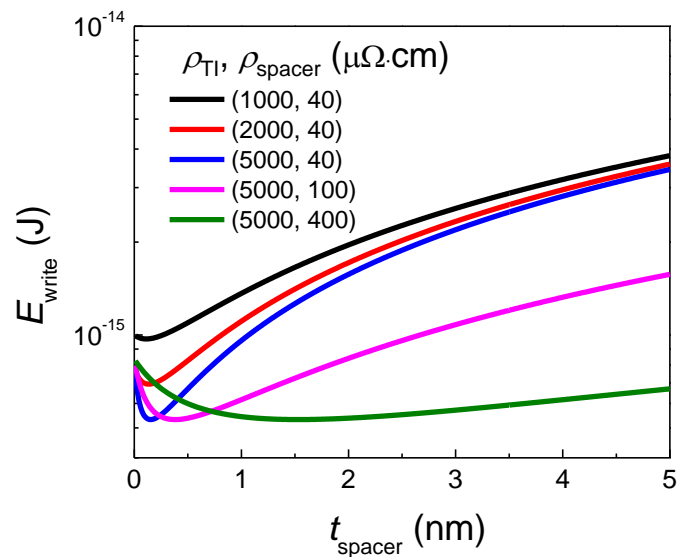


Figure 7-5 Write energy as a function of spacer thickness for different TI and spacer material resistivities ($R = 10$ nm, $\sigma_{SH} = 1.55 \times 10^5 \Omega^{-1} \cdot m^{-1}$). Reprinted with permission from [35], Copyright (2018) IEEE

7.2 MRAM scaling: comparison of current- and voltage- approach

In this dissertation, we have been extensively focused on the current-based MRAM. There is an alternative way of using voltage-based MRAM, which is referred as magnetoelectric RAM (MeRAM) [210]. The scaling analysis of voltage-controlled MeRAM as compared with the current-driven STT-MRAM is described as follows: a critical parameter which determines the

scaling behavior for nonvolatile MRAM is the ratio of switching voltage (or current) over the thermal stability factor, which should ideally be minimized. For perpendicular MeRAM, this is given by

$$\frac{V_C}{\Delta} = \frac{kT d_t}{A \zeta}, \quad (7-1)$$

where Δ is the thermal stability factor, A is the MEJ area, d_t is the thickness of the dielectric barrier and ζ is the voltage controlled magnetic anisotropy (VCMA) coefficient. Here, a MEJ, referred as a magnetoelectric junction (in order to emphasize the VCMA), is a MTJ used for MeRAM (*i.e.*, which has a thicker dielectric layer as compared with the one used for STT-MRAM). The thermal stability factor is given by $\Delta = \frac{(S(0) - M_s^2 t_f / 2\mu_0) A}{kT}$, where $S(0) \equiv S(V = 0)$ as the interfacial anisotropy. This interfacial anisotropy can be controlled by voltage, namely $S(V) = S(0) - \zeta V / d_t$.

It is noted that the scaling of conventional magnetic memories to smaller bit areas requires increasing $S(0)$ and/or reducing M_s to maintain a constant thermal stability (hence nonvolatile retention time) of the bits. However, Eq. (7-1) shows that this does not necessarily lead to an increase of the switching voltage V_C (which depends mostly on ζ) in MeRAM. It is interesting to compare this to the corresponding scaling parameter for perpendicular STT-MRAM, which is given by [211-213]

$$\frac{I_C}{\Delta} = \frac{4e\alpha k_B T}{\hbar \eta}, \quad (7-2)$$

where I_C is the switching current, e is the electron charge, α is the Gilbert damping constant, and η is the spin-transfer efficiency. It can be seen that in Eq. (7-2), the ratio of switching current over thermal stability for STT-MRAM is largely set by fundamental constants or by parameters with a

limited tuning range. Hence, scaling with a constant- Δ rule (by increasing magnetic anisotropy field and/or M_S) will lead to a constant switching current (rather than constant switching voltage) across technology nodes.

The above-mentioned scenario presents a fundamental problem for the scaling of current-controlled STT-MRAM, as the transistor widths needed to drive this constant switching current will not significantly shrink with successive technology nodes, hence hitting a current-drive-limited barrier on transistor width (and thus the cell area). By contrast, MeRAM is a voltage-driven memory, and thus has very small leakage current. This feature allows for the use of minimum-sized transistors at each technology node, and hence enables MeRAM to exhibit a distinct density advantage. Figure 7-6 shows the projected unit cell size (for scaled technology node) required for a 1-transistor/1-MEJ MeRAM cell as compared with that of a 1-transistor/1-MTJ STT-MRAM cell for three different values of STT-MRAM switching current densities. Estimates on the CMOS operating voltage and current drive capability are obtained from Refs. [214, 215]. It is seen that, as the memory unit cell scales down, the unit cell area (in unit of F^2) will increase dramatically for STT-MRAM. Even that lowering the switching current density (resulted from a reduced α/η ratio) and improving the drive capability of transistors may further improve the scaling of STT-MRAM, the minimum unit cell area of STT-MRAM ($6 F^2$) is still larger than that of MeRAM ($4 F^2$). Here 1 diode – 1 MEJ and the unipolar write scheme are used.

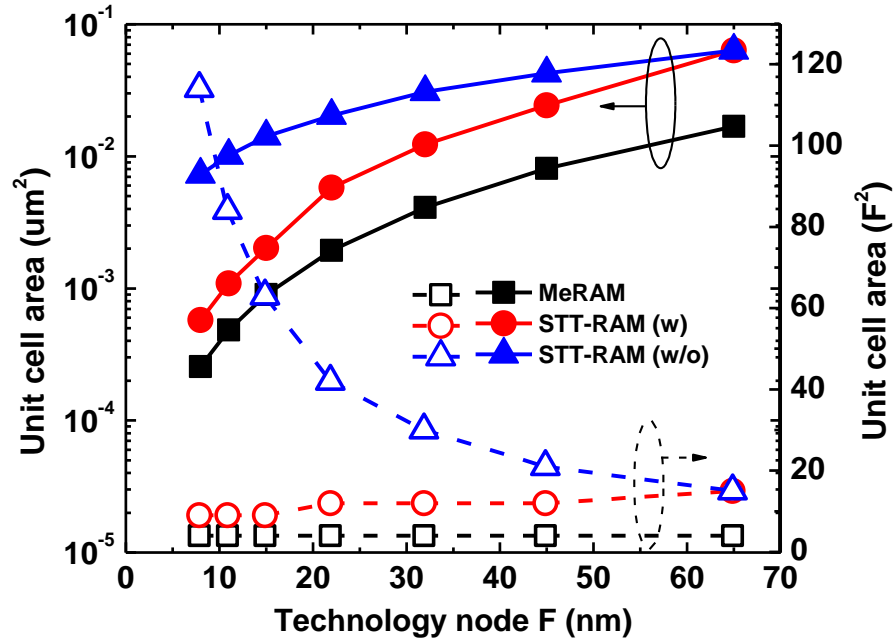


Figure 7-6 Estimated unit cell size (left vertical axis) and scaled feature sizes (right vertical axis) for MeRAM and STT-MRAM for each technology node. STT-MRAM (w) stands for STT-MRAM with the improvement of the α/η ratio (0.0918 to 0.0105 for 65 nm to 8 nm) and the current drive capability of the supporting transistor (1100 $\mu\text{A}/\mu\text{m}$ to 2000 $\mu\text{A}/\mu\text{m}$ for 65 nm to 8 nm); while STT-MRAM (w/o) represents STT-MRAM without these innovations (*i.e.*, just using $\alpha/\eta = 0.0918$ and a drive capability of 1100 $\mu\text{A}/\mu\text{m}$ across all technology nodes). Reprinted with permission from [210], Copyright (2016) IEEE

More importantly, in addition to memory cell size, the energy efficiency advantage (in terms of switching energy per bit) of MeRAM (over STT-MRAM) becomes more pronounced as the bit dimensions are further scaled-down. This is because for STT-MRAM bits to retain an approximately constant write energy $E_w = RI_c^2 t_w$ (assuming a constant write time t_w across all technology nodes), the MTJ's resistance-area product (RA) needs to be reduced sufficiently (*i.e.* the MgO barrier can be made thin enough) to prevent both the resistance R and the write voltage

RA from increasing (The reduction of RA with scaled STT-MRAM dimensions is also demanded to maintain the compatibility with CMOS read and write circuits). Consequently, the required thinner MgO barrier thickness based on the STT-MRAM scaling rule (with constant E_w) may eventually lead to reliability issues (similar to dielectric layer challenge for MOSFET scaling).

On the contrary, in the case of MeRAM, the voltage-controlled switching mechanism does not impose such a constraint (*i.e.*, reduce the MgO thickness for smaller RA) with scaled MeRAM cell.

Hence, given the following relation

$$E_{MeRAM} = IV_C t_w + \frac{1}{2} CV_C^2 = \frac{V_C^2 t_w}{RA(d_t)} \cdot A + \frac{1}{2} \frac{\epsilon_t V_C^2}{d_t} \cdot A, \quad (7-3)$$

where $C = \epsilon_t \cdot A / d_t$ is the capacitance of the MEJ, it is seen that the writing energy E_{MeRAM} decreases as the technology node advances owing to the increased resistance of MEJ and reduced C for a smaller bit area A (now RA is constant). In principle, due to the high resistance of voltage-switched MEJs, one may in general need to consider the parasitic capacitance C in the calculations of switching energy; yet we need to point out that for current practical MeRAM device with relatively smaller MEJ resistance ($< 200 \text{ K}\Omega$), the energy dissipation is still dominated by the resistance R [216]. Accordingly, the energy scaling (*i.e.*, projected write energy per bit for a write time of 1 ns) comparisons between MeRAM and STT-MRAM are illustrated in Figure 7-7. It shows that MeRAM has a significant improvement of energy efficiency for the present technology node (30 nm), and such energy advantage gap becomes more distinct for smaller nodes. These projections indicate that MeRAM, other than STT-MRAM, would be able to address memory applications where energy efficiency and/or density are major concerns (*i.e.*, embedded SRAM Cache and DRAM in mobile applications).

To assess MeRAM for on-chip embedded applications, we need to further draw a comparison between MeRAM and SRAM. It is known that one SRAM unit consists of six transistors, and the write energy per bit is given by kCV^2 , where k is the activity factor, C is the total capacitance (we consider the unit cell size of a SRAM is 140 F^2 and the effective oxide thickness is 1 nm), and V is the write voltage [217, 218]. From the 45 nm to the 8 nm technology node, the activity factor increases from ~ 0.01 to ~ 1 , because the leakage energy increases significantly as the voltage is scaled down, and the write voltage is reduced from 1 V to 0.7 V [217, 219]. Accordingly, the energy consumptions per write for SRAM are estimated to be around 0.1 fJ and 0.15 fJ for the 45 nm and 8 nm technology nodes, respectively [218]. In contrast, MeRAM is expected to consume a lower write energy ($< 0.1 \text{ fJ}$ in Figure 7-7) than SRAM for technology nodes smaller than 8 nm ; if we further take into account the nonvolatile nature of MeRAM (which greatly reduces the static leakage current) as well as its superior density advantage (*i.e.*, 4 F^2 of MeRAM versus 140 F^2 of SRAM for the 8 nm node), it can be concluded that MeRAM may be much more efficient than SRAM for advanced technology nodes.

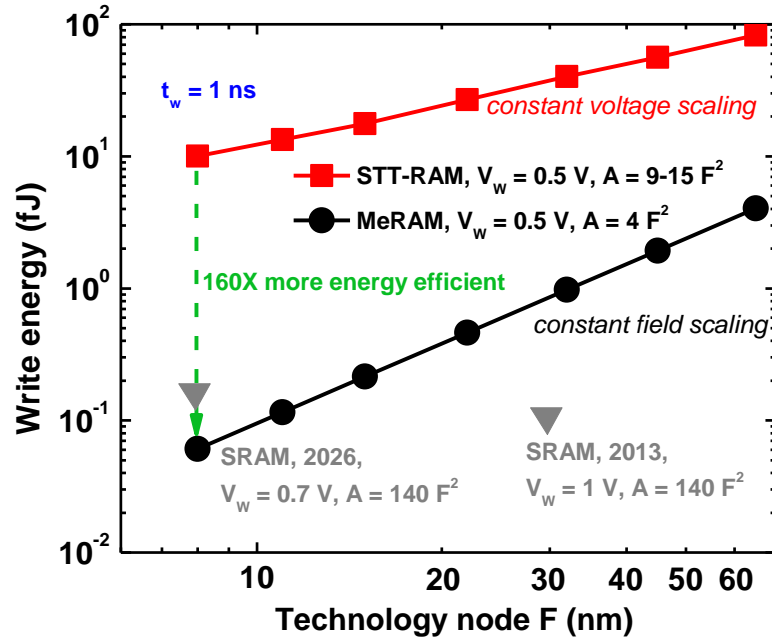


Figure 7-7 Write energy for MeRAM and STT-MRAM at each technology node for embedded applications. The SRAM data are taken from ITRS (2013) [218]. The write time is assumed to be $t_w = 1$ ns. The values of V_w and A give the corresponding write voltage and unit cell area related to the technology node, respectively. Here, we set the MgO thickness to around 1.3 nm ($RA \sim 206 \Omega \cdot \mu\text{m}^2$). In this case, the ratio of leakage to dynamic energy is around 146 for each technology node; we assume that leakage energy still dominates, which is the typical case in practical experiments [216, 220, 221]. Reprinted with permission from [210], Copyright (2016) IEEE

Under the single-domain approximation, the scaling rules for circuit performances of MeRAM, STT-MRAM, and SRAM are summarized in Table 7-1. It is clearly seen that in terms of energy consumption, MeRAM scales much faster ($1/K^2$), as compared with $1/K$ and K in STT-MRAM and SRAM, respectively. This is because the scaling behavior of MeRAM is close to a constant field scaling, as discussed in Eq. (7-3) and Figure 7-7, while for STT-MRAM, the necessity to reduce the tunnel barrier thickness for maintaining a critical switching current results in a constant

voltage scaling. Meanwhile, the power density of MeRAM remains almost constant across all technology nodes, which is very crucial for practical applications. It should be noted, however, that the scaling characteristics given in both Figure 7-6 and Figure 7-7 are only based on single 1-transistor/1-MEJ cell without the knowledge of the entire memory array size. Hence, to obtain an accurate assessment of the energy consumption and array density of any particular MeRAM array needs further investigations.

Table 7-1 Scaling rules for circuit performance, where $K > 1$ and the single-domain approximation is used. In the table: * for keeping constant voltage and RA such that the ratio of damping factor over spin transfer efficiency has to be scaled. Adapted with permission from [210], Copyright (2016) IEEE

Parameters	MeRAM (constant voltage)	STT-MRAM (constant voltage)	CMOS based SRAM (constant voltage*)
Device dimension, length and width of PMTJ (for CMOS, include gate dielectric barrier t_{ox})	$1/K$ (Scaling)	$1/K$ (Scaling)	$1/K$ (Scaling)
Resistance-area product of PMTJ, RA	1 (Assumption)	$1/K^*$ (Assumption)	
Voltage, V	1 (Assumption)	1	1 (Assumption)
Current, I	$1/K^2$	$1/K$ (Assumption)	K
Area, A	$1/K^2$	$1/K^2$	$1/K^2$
Power, P	$1/K^2$	$1/K$	K
Power density, P_A	1	K	K^3
VCMA coefficient ζ	K^2		
Saturation magnetization M_s	1	1	
Interfacial anisotropy $S(0)$	K^2	K^2	
Damping factor / Spin transfer efficiency α/η		$1/K^*$	
Doping concentration, N_D (N_A)			K^2 (Assumption)

Finally, the unipolar write scheme of MeRAM also confers an indirect advantage in terms of the read-out process. In particular, given that the free layer switching in MeRAM is only sensitive to

the voltage of one polarity, the voltage of the opposite polarity can be used for a disturbance-free readout. In other words, the device can be read out using a voltage level similar to that used for writing, but with the opposite polarity (unlike STT-MRAM, which requires a much smaller read voltage to prevent read disturbance), hence allowing for a fast readout despite the increased resistance of the device.

The successful realization of these potential advantages will require additional development of improved MeRAM bits. In particular, it is important to increase the VCMA effect (*i.e.* increase ζ) through materials optimization in scaled nodes, while maintaining a high TMR for readout. With these challenges resolved, it is expected that MeRAM can then be a candidate for energy-efficient, dense, and fast nonvolatile memory with better scalability than previous types of MRAM.

7.3 Memristors with MRAM

To implement artificial neural network (Figure 7-8), we want to have memristors. This is because if we use traditional computer, the major energy consumption is on the matrix calculation and weight update. With memristors, first, the resistance can be electrically tuned in a nonvolatile fashion. Second, the matrix multiplication can be naturally implemented using Kirchhoff circuit laws. I will investigate how to use MRAM to achieve analog magnetic states.

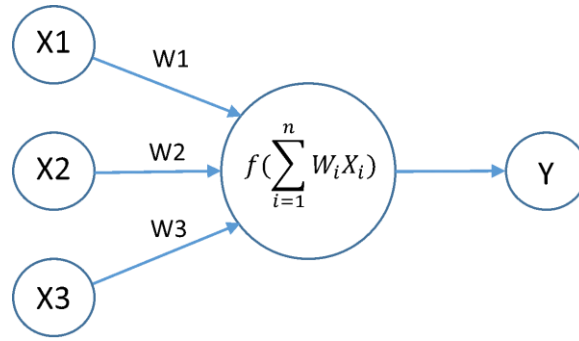


Figure 7-8 Simple neural network.

Interestingly, we observe memristor-like switching behavior in TI/Mo/CoFeB samples (Figure 7-9). This could be due to the multi-domain state formation during the switching in this trilayer [222]. This effect could be potentially utilized for neuromorphic computing.

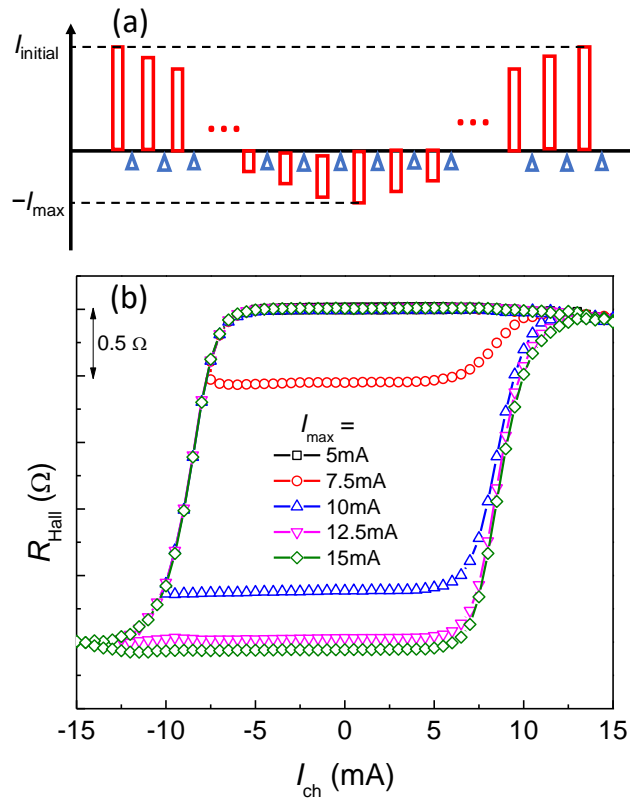


Figure 7-9 Multi-stable resistance state in TI/Mo/CoFeB. (a) Red (write) pulse is 5 ms (1 s interval) and blue (read) pulse is 0.5 s (b) Memristor-like switching behavior in the $(\text{BiSb})_2\text{Te}_3(6\text{nm})/\text{Mo}(2\text{nm})/\text{CoFeB}(0.93\text{nm})$ sample at 200 K. Reprinted with permission from [210], Copyright (2018) IEEE

Brain has other important features, including neuron potential oscillation and coupling [223]. People try to mimic these important features and implement related neuromorphic functions using spintronic devices [224-226]. MTJs can exhibit oscillatory behavior upon applying enough large d.c. current, which is a spin-torque nano oscillator. The oscillating voltage is tuned by the current magnitude. This feature has been used to achieve spoken-digit recognition with reservoir computing [226]. For MTJs with super-paramagnet, the MTJ resistance can fluctuate at a spiking rate, which can be tuned by a d.c. bias current. With this tunable spiking rate, MTJs could provide a tuning curve for population coding in neuroscience [224]. Neighboring MTJ-based spin torque nano oscillators can achieve frequency coupling, which has been used for pattern classification [225]. In future, more functionalities of MTJs and other spintronic devices can be potentially utilized for neuromorphic applications.

7.4 Microwave applications

Besides nonvolatile memory-based applications, the MTJ can also be used for other applications. Here, I discuss one possibility of using nonlinear MTJ resistance response to current for microwave applications. This part is adapted from the published manuscript [227].

A magnetic tunnel junction (MTJ) consists of one tunnel oxide sandwiched between two magnetic layers: a free layer, whose magnetization is easy to manipulate, and a layer with fixed

magnetization (Figure 7-10a). The relative magnetization orientation, i.e., the angle θ between the magnetization directions of these two layers determines the tunnel resistance (Figure 7-10b): if their magnetization is parallel, the MTJ is in a low resistance state; if they are antiparallel, the MTJ has a high resistance. This change in resistance determines the tunnel magnetoresistance (TMR) ratio. The discovery of electric current-driven spin-transfer torques (STTs) enabled efficient manipulation of the free layer's magnetization without the need for an external magnetic field. This inspired various spintronic applications beyond magnetic random-access memories [77], including microwave generators and detectors. Writing in *Nature Nanotechnology*, Minori Goto *et al.* now demonstrate a MTJ-based spintronic microwave amplifier [228], which was originally proposed in 1997 [229].

MTJ-based microwave applications rely on the nonlinear dependence of the MTJ resistance on the relative magnetization angle. When the magnetization of the free layer precesses around the equilibrium position, the MTJ resistance also oscillates (Figure 7-10b). For a microwave generator [230] (Figure 7-10c), a d.c. current is injected into the MTJ. The induced STT produces an auto-oscillation of the magnetization and thus an alternating MTJ resistance. Then, the output voltage (V_{out}) is the product of the d.c. current and the time-dependent MTJ resistance, resulting in a microwave signal. Similarly, a microwave signal can be detected [231] if its frequency matches the MTJ resonance frequency (Figure 7-10d). The oscillating input current and the varying MTJ resistance are rectified to produce a d.c. output voltage, which reaches a maximum when the resonance condition is met.

Beside microwave generation and detection, an efficient microwave amplifier (Figure 7-10e) is needed for functional spintronic microwave devices. For amplification, in addition to the input microwave a.c. current, a d.c. bias current is applied. The a.c. current yields a magnetization

precession and, thus, a MTJ resistance oscillation. Then, the output microwave voltage is the product of the d.c. current and the oscillating MTJ resistance. The efficiency of an amplifier is determined by the gain, the ratio of output voltage over input voltage, which should be larger than one. Simply increasing the d.c. current is not feasible because a large d.c. current will cause magnetization auto-oscillation, which makes the MTJ become a microwave generator, but not a stable microwave amplifier. Hence, the key to achieve microwave amplification is to have a high TMR ratio and a large magnetization precession angle.

Increasing the STT yields an enhanced magnetization precession angle. Yet, this strategy couldn't push gains close to one in conventional two-terminal MTJ device so far [232]. Alternatively, the voltage-controlled magnetic anisotropy (VCMA) effect [233] has been shown to enable magnetization precession and switching similar to STTs [210]. To realize a large VCMA effect and thus a large magnetization precession angle, Minori Goto *et al.* utilize the Joule heat in the free FeB layer of a CoFeB/MgO/FeB MTJ. In general, at the nanoscale heat dissipates fast due to the large surface-to-volume ratio. Yet, high thermal resistance was discovered at the MgO/CoFeB interface recently [234]. By utilizing a double MgO structure, the researchers confine the current-induced Joule heat in the free FeB layer between two MgO insulating layers (Figure 7-10f). This heat reduces the magnetic anisotropy of the free layer and produces a quadratic dependence of the magnetic anisotropy on the applied voltage. The researchers also verify that this effective VCMA effect is much larger than the traditional STTs or the linear VCMA effect. The VCMA effect excites a large magnetization precession angle and bears microwave amplification with a gain larger than one.

To obtain a technologically useful amplifier, there are still many challenges to overcome. For example, a fully functional spintronic microwave amplifier requires placing the device in a

microwave circuit with a circulator to separate the input from the output signals. Furthermore, the efficiency of the device and the maximum power output need to be improved. This could potentially be achieved in a three-terminal device, where higher gains are expected ⁶. Finally, because the microwave amplification is heat-driven, this could cause undesirable side effects, such as reduced fidelity, which have to be considered carefully.

From a broader perspective, this heat-assisted microwave amplification reminds us that it can be beneficial to utilize, sometimes unavoidable, the heat in integrated circuits. Earlier examples include the heat-assisted magnetic recording and the phase-change memory, in which the focused heat allows effective information recording. The key here is to control the heat flow and employ its effects instead of fighting them.

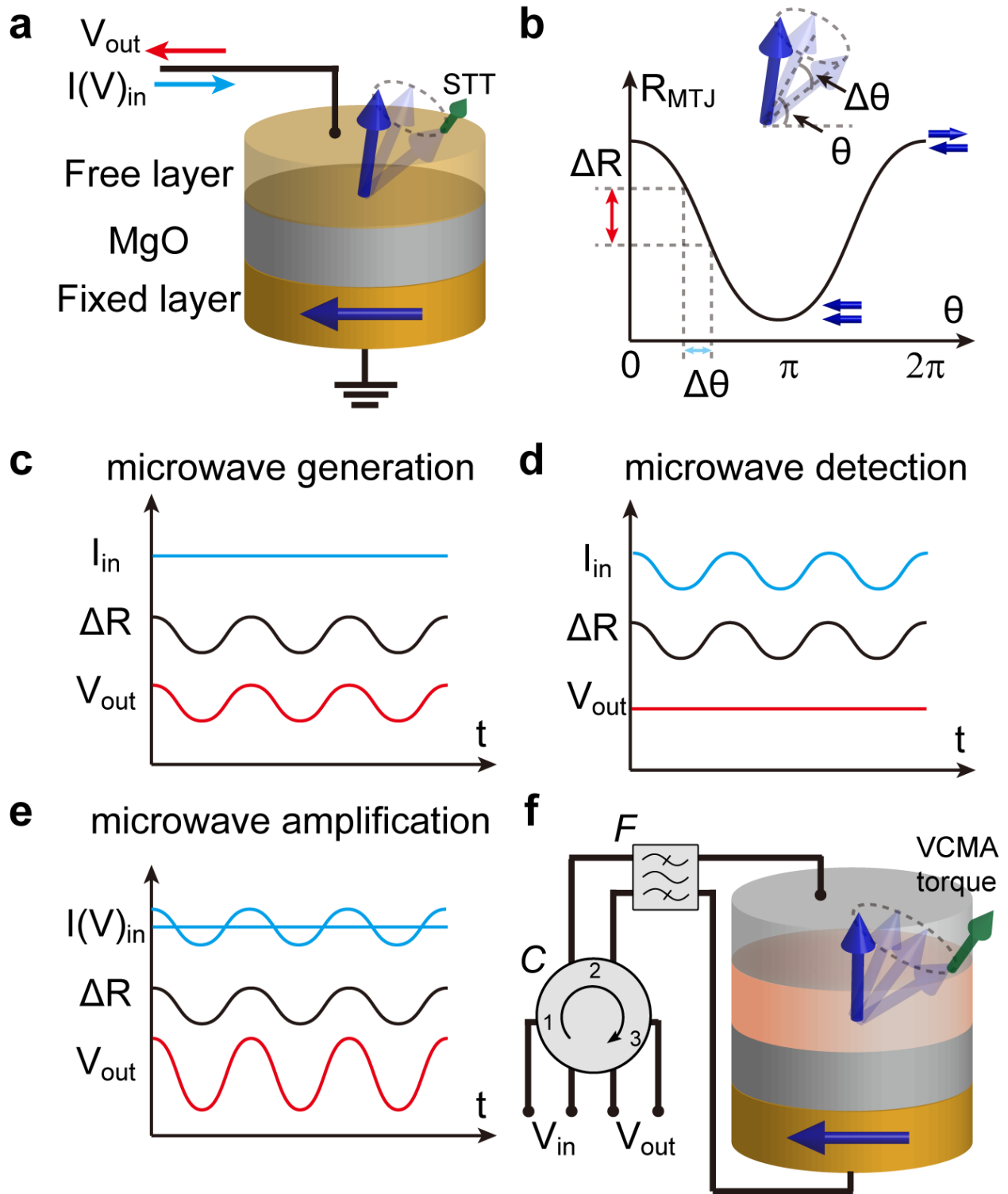


Figure 7-10 Three types of existing microwave applications based on magnetic tunnel junctions (MTJs). (a) A typical MTJ includes an MgO tunnel barrier sandwiched between a free and fixed layer. The magnetization (blue arrow) of the free layer can be manipulated by the input signal

through spin transfer torque (STT). (b) The MTJ resistance R_{MTJ} as a function of the relative angle θ between the magnetization of the free and fixed layer. An oscillation in the relative angle causes an oscillating MTJ resistance ΔR . (c) Spintronic microwave generator. The d.c. input current I_{in} leads to sustained free layer magnetization precession and thus an MTJ resistance oscillation. The product of d.c. input current and a.c. MTJ resistance produces an a.c. (microwave) output voltage V_{out} . (d) Spintronic microwave detector. When the frequencies of I_{in} and the MTJ resonance frequency match, a rectified d.c. V_{out} is generated. (e) Spintronic microwave amplifier. In traditional MTJs, an a.c. I_{in} excites a magnetization precession through STT and causes an MTJ resistance oscillation. The product of the oscillating resistance and the d.c. I_{in} produces an a.c. V_{out} . The ratio of a.c. V_{out} over input a.c. voltage V_{in} is defined as microwave amplification gain. (f) Embedding the MTJ in a microwave circuit. In a double MgO structure, the heat is confined in the free layer. The heat causes the temperature to rise and thus a reduction of the anisotropy energy, which effectively amplifies the voltage-controlled magnetic anisotropy (VCMA) torque and leads to a large precession angle. The bandpass filter F chooses the microwave frequency and the circulator C separates the input from the output signals. Reprinted with permission from [227]

Chapter 8 Outlook

In this dissertation, I have extensively the spin-orbit torque generated from different materials, including traditional heavy metals, 2D TMDs, and topological insulators. Finding the right material with the highest possible SOT efficiency is critical for improving the SOT-MRAM efficiency. We have shown that with careful examination, different SOT techniques should provide a similar SOT efficiency value. We demonstrate the possibility for generating SOTs from monolayer TMDs, which may be beneficial for future compatible spintronic devices. The large SOT efficiency from TIs in an integrated TI/Mo/CoFeB/MgO suggests that the TI may be potentially utilized in future SOT-MRAM. In the future, more functional quantum materials, especially those low-dimensional materials with broken symmetries, could be utilized for generating SOTs. For example, 1T' phase WTe₂ could be an outstanding candidate due to strong spin-orbit coupling and broken rotational symmetry. Another important category could be ferromagnet and antiferromagnet, which have magnetization in the bulk and at the interface that naturally break the symmetry.

I have also studied various magnetic material systems, including ferromagnetic metals and ferrimagnetic insulators. The current-induced switching of nearly compensated ferrimagnet has been achieved, which may be critical for future ultrafast and low-power spintronic applications. However, so far, the switching current pulse of the compensated ferrimagnet still has a current pulse width at the order of millisecond. Further ultrafast switching experiment on this system is required. Nowadays, 2D layered magnetic materials have emerged as an interesting subject since they have exhibited many exotic phenomena, such as giant spin-filter TMR ratio in graphene/few-layer CrI₃/graphene tunnel junctions [18, 19]. Also, the itinerant ferromagnetic metal Fe₃GeTe₂

could have a room-temperature ferromagnetism under the electrostatic gate voltage [235]. Recent review article has listed four major research directions of 2D magnetic materials [236].

One major contribution of this dissertation is the discovery of the signatures of skyrmions in magnetic insulator thin films. However, the skyrmion dynamics in the magnetic insulator thin films remains unexplored, which requires a direct imaging technique. Since magnetic insulator skyrmion systems still need a crystalline structure, at this moment magnetic metal skyrmion systems may still be better in terms of integration to the silicon technology. We have also investigated many metallic skyrmion systems and their device implications using MOKE imaging technique [39, 178, 209]. The significant challenge is how to readily study sub-100 nm skyrmion in these metallic systems. Investigating skyrmion-based MTJ structure is very important.

In the previous chapter, I have discussed the device applications of these spintronic devices and mentioned the potential future directions. Here, I want to emphasize the fundamental challenges for spintronic devices.

1. How can we reduce the write energy down to fundamental limit?

This is critical for the overall energy efficiency. If we are using current-based MRAM, what is the ultimate charge-to-spin conversion efficiency? If we are using voltage-based MRAM, how can we achieve VMCA coefficient like 1000 fJ/Vm? (This is one of the 1000 challenge provided by my advisor in last year's International Electron Device Meeting [237].)

2. What is the fundamental limit of magnetoresistance ratio? And how can we improve it to the limit?

Nowadays, the commonly available MTJs only have TMR around 200%, which is 2. This is very low compared with other nonvolatile systems, including PCM and RRAM. Improving this value to 1000% is very helpful for increasing the read margin and thus read speed. (This is the other one of the 1000 challenge proposed by my advisor in last year's International Electron Device Meeting [237].)

These two could be the most critical issues to be resolved before the MRAM gets everywhere in our daily lives.

Chapter 9 Appendix

A. Materials characterization of monolayer TMD/CoFeB

Section 1. Details of the chemical vapor deposition of MoS₂ and WSe₂

Growth of MoS₂ full film: Molybdenum trioxide (MoO₃) powders were weighed of 0.3g and placed in a sapphire boat located in the center of furnace. The sulfur powders were then placed at the upstream side of furnace and keep the temperature of 160 °C. The furnace environment was kept at a pressure of 45 Torr with a carrier gas of argon (70 sccm). The furnace was heated up to 755 °C as a process temperature and kept for 15 minutes and then cooled down to room temperature naturally.

Growth of WSe₂ full film: The WO₃ powders (0.3 g) were put in a quartz boat and placed in the heating zone center of the furnace. The Se powders were prepared in a separate quartz boat at the upper stream side of the furnace. The sapphire substrates for growing WSe₂ were put at the downstream side, next to WO₃ powders quartz boat. The gas flow was brought by an Ar/H₂ flowing gas (Ar = 90 sccm, H₂ = 9 sccm), and the chamber pressure was controlled at 4 Torr. The center heating zone was heated to 925°C at a ramping rate 28°C/min, and the temperature of Se boat was maintained at 290°C by heating tape during the reaction. Note that the temperature of the sapphire substrates was at about 850°C when the center heating zone reaches 925°C. After reaching 925°C, the heating zone was kept for 15 minutes for reaction and the furnace was then naturally cooled down to room temperature.

Note that our monolayer films are continuous over mm scale, but they may not be single crystalline.

Section 2. Deposition details and Raman characterization after deposition

To minimize damage to the monolayers, we used off-angle magnetron sputtering to deposit 3 nm of CoFeB onto the monolayers. The CoFeB deposition rates were kept at 0.03 nm/s and were performed in an ambient argon pressure of 3 mTorr. We then deposited a protective 1.5 nm of Ta layer and used 120 seconds of oxygen plasma to oxidize it into around 3 nm of TaO_x layer. The TaO_x is insulating (resistivity is larger than 10³ Ω·cm).

After the deposition of CoFeB and TaO_x capping layer, we use Raman spectroscopy to confirm the existence of well-defined monolayers. When we deposit CoFeB by grazing-angle sputtering onto a single-layer of WSe₂ on sapphire, the Raman signatures of the WSe₂ are preserved as shown in Figure 9-1.

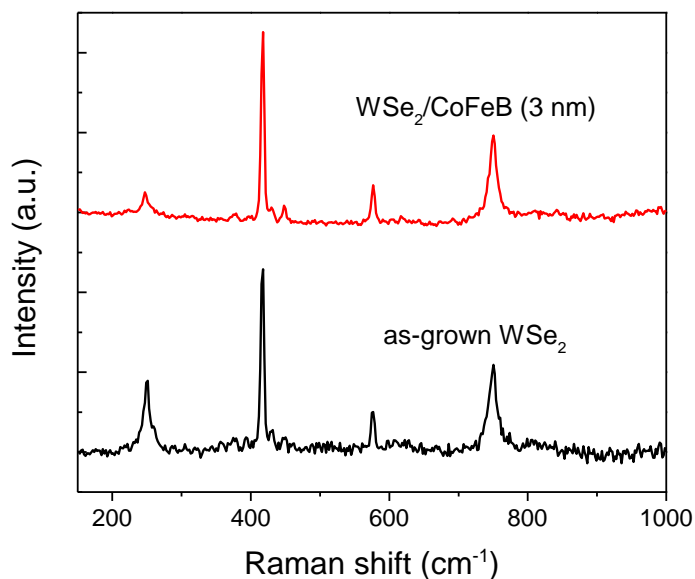


Figure 9-1 Raman spectra of CVD-grown single-layer WSe₂ before (black) and after (red) the deposition of the CoFeB layer by grazing-angle sputtering. Reprinted with permission from [55], Copyright (2016) American Chemical Society

B. Atomic model (discrete) to micromagnetic field model (continuum)

The Dzyaloshinskii–Moriya interaction (DMI) energy (Hamiltonian) between two neighboring atomic spins can be written as

$$\mathcal{H}_{DMI,atomic} = -\vec{D}_0 \cdot (\vec{S}_1 \times \vec{S}_2), \quad (\text{B-1})$$

where \vec{D}_0 is the DMI vector and the units of $\mathcal{H}_{DMI,atomic}$ and D_0 are J. For bulk DMI, the \vec{D}_0 is along the \hat{r}_{ij} direction [192], where i and j are atomic spin labels. Eq. (B-1) describes the atomistic spins and energy. In normal magnetic systems, the difference between the neighboring two atomic spins are very small. In the continuum limit, the spatial spin directions can be treated as a field $\vec{m}(\vec{r})$, which describes the average spin directions (magnetization) at location \vec{r} . Normally, the magnetic texture $\vec{m}(\vec{r})$ is smooth and the derivative of $\vec{m}(\vec{r})$ is very small at a scale that is much larger than the atomic distance. In micromagnetic model, bulk DMI is written as

$$E_{DMI,eff} = -D_{in}\vec{m} \cdot (\nabla \times \vec{m}), \quad (\text{B-2})$$

where the units of $E_{DMI,eff}$ and D_{in} are J/m^3 and J/m^2 , respectively.

Now we show that Eqs. (B-1) and (B-2) are equivalent with a constant conversion factor. First, we can use Eq. (B-2) to calculate the total energy of a system:

$$E_{total} = \int E_{DMI,eff} dx dy dz$$

$$- \int D_{in} [m_x(\partial_y m_z - \partial_z m_y) + m_y(\partial_z m_x - \partial_x m_z) + m_z(\partial_x m_y - \partial_y m_x)] dx dy dz. \quad (\text{B-3})$$

Then, we use Eq. (B-1) to calculate the total energy of a system under the assumption of smooth magnetic texture. To simplify the calculation, we assume a cubic spin lattice with spacing d (Figure 9-2a). Then

$$\begin{aligned}
E_{total} &= \sum_{all\ i} \sum_{all\ j} \sum_{all\ k} \mathcal{H}_{DMI,atomic}(i, i + 1; j, j + 1; k, k + 1) \\
&= -\frac{1}{d^3} \int [\vec{D}_0 \cdot (\vec{S}_{i,j,k} \times \vec{S}_{i+1,j,k}) + \vec{D}_0 \cdot (\vec{S}_{i,j,k} \times \vec{S}_{i,j+1,k}) + \vec{D}_0 \cdot (\vec{S}_{i,j,k} \times \vec{S}_{i,j,k+1})] dx dy dz \cong \\
&\quad -\frac{D_0}{d^3} \int [\hat{x} \cdot (\vec{m}(\vec{r}) \times \vec{m}(\vec{r} + d\hat{x})) + \hat{y} \cdot (\vec{m}(\vec{r}) \times \vec{m}(\vec{r} + d\hat{y})) + \hat{z} \cdot (\vec{m}(\vec{r}) \times \vec{m}(\vec{r} + \\
&\quad d\hat{z}))] dx dy dz \cong \\
&\quad -\frac{D_0}{d^3} \int \left[\hat{x} \cdot \left(\vec{m}(\vec{r}) \times \left(\vec{m}(\vec{r}) + \frac{\partial \vec{m}(\vec{r})}{\partial x} d \right) \right) + \hat{y} \cdot \left(\vec{m}(\vec{r}) \times \left(\vec{m}(\vec{r}) + \frac{\partial \vec{m}(\vec{r})}{\partial z} d \right) \right) + \hat{z} \cdot \right. \\
&\quad \left. \left(\vec{m}(\vec{r}) \times \left(\vec{m}(\vec{r}) + \frac{\partial \vec{m}(\vec{r})}{\partial z} d \right) \right) \right] dx dy dz = \\
&\quad -\frac{D_0}{d^2} \int \left[\hat{x} \cdot \left(\vec{m} \times \frac{\partial \vec{m}}{\partial x} \right) + \hat{y} \cdot \left(\vec{m} \times \frac{\partial \vec{m}}{\partial z} \right) + \hat{z} \cdot \left(\vec{m} \times \frac{\partial \vec{m}}{\partial z} \right) \right] dx dy dz = \\
&\quad -\frac{D_0}{d^2} \int [m_x(\partial_y m_z - \partial_z m_y) + m_y(\partial_z m_x - \partial_x m_z) + m_z(\partial_x m_y - \partial_y m_z)] dx dy dz. \quad (B-4)
\end{aligned}$$

This is the end of the proof. We also see that the units of D_0 and D_{in} are consistent.

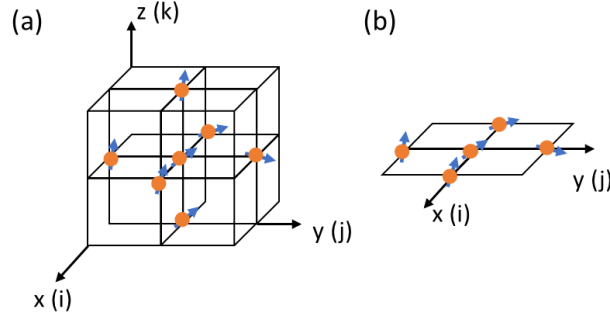


Figure 9-2 Simple 3D and 2D spin lattice. (a) Simple 3D cubic spin lattice. (b) Simple 2D square spin lattice.

For interfacial DMI, the \vec{D}_0 is along the $\hat{z} \times \hat{r}_{ij}$ direction [192]. In the continuum limit, the interfacial DMI is also written as

$$E_{DMI,eff} = -D_{in}[m_z \cdot (\nabla \cdot \vec{m}) - (\vec{m} \cdot \nabla)m_z], \quad (B-5)$$

where the units of $E_{DMI,eff}$ and D_{in} are J/m^2 and J/m , respectively.

To show Eqs. (B-1) and (B-5) are consistent, we first use Eq. (B-5) to calculate the total energy of a system:

$$E_{total} = \int E_{DMI,eff} dx dy = \\ - \int D_{in} [(m_z \partial_x m_x - m_x \partial_x m_z) - (m_y \partial_y m_z - m_z \partial_y m_y)] dx dy. \quad (B-6)$$

Then, we use Eq. (B-1) to calculate the total energy of a system under the assumption of smooth magnetic texture. To simplify the calculation, we assume a square spin lattice with spacing d (Figure 9-2b). Then

$$E_{total} = \sum_{all i} \sum_{all j} \mathcal{H}_{DMI,atomic}(i, i+1; j, j+1) \\ = -\frac{1}{d^2} \int [\vec{D}_0 \cdot (\vec{S}_{i,j} \times \vec{S}_{i+1,j}) + \vec{D}_0 \cdot (\vec{S}_{i,j} \times \vec{S}_{i,j+1})] dx dy \cong \\ -\frac{D_0}{d^2} \int [(\hat{z} \times \hat{x}) \cdot (\vec{m}(\vec{r}) \times \vec{m}(\vec{r} + d\hat{x})) + (\hat{z} \times \hat{y}) \cdot (\vec{m}(\vec{r}) \times \vec{m}(\vec{r} + d\hat{y}))] dx dy \cong \\ -\frac{D_0}{d^2} \int \left[\hat{y} \cdot \left(\vec{m}(\vec{r}) \times \left(\vec{m}(\vec{r}) + \frac{\partial \vec{m}(\vec{r})}{\partial x} d \right) \right) - \hat{x} \cdot \left(\vec{m}(\vec{r}) \times \left(\vec{m}(\vec{r}) + \frac{\partial \vec{m}(\vec{r})}{\partial z} d \right) \right) \right] dx dy = \\ -\frac{D_0}{d} \int \left[\hat{y} \cdot \left(\vec{m} \times \frac{\partial \vec{m}}{\partial x} \right) - \hat{x} \cdot \left(\vec{m} \times \frac{\partial \vec{m}}{\partial z} \right) \right] dx dy dz = \\ -\frac{D_0}{d} \int [m_x (\partial_y m_z - \partial_z m_y) + m_y (\partial_z m_x - \partial_x m_z) + m_z (\partial_x m_y - \partial_y m_z)] dx dy dz. \quad (B-7)$$

This is the end of the proof. Again, we see that the units of D_0 and D_{in} are consistent.

To calculate stable magnetic texture in a 2D magnet with uniaxial magnetic anisotropy (K_u) or perpendicular magnetic anisotropy (PMA), we need to consider all the energy terms as follows:

$$\mathcal{H} = \sum_{all i} \sum_{all j} \mathcal{H}_{DMI,atomic}(i, i + 1; j, j + 1) - J \sum_{all i} \sum_{all j} (\vec{S}_{i,j} \cdot \vec{S}_{i+1,j} + \vec{S}_{i,j} \cdot \vec{S}_{i,j+1}) - K_0 \sum_{all i} \sum_{all j} (\vec{S}_{i,j} \cdot \hat{z})^2 - g\mu_B \sum_{all i} \sum_{all j} \vec{S}_{i,j} \cdot \vec{B}_{ext}, \quad (\text{B-8})$$

where J is the exchange energy strength between neighboring atomic spins, K_0 is the atomic PMA energy, g is Landé-g factor, μ_B is the Bohr magneton, and \vec{B}_{ext} is the external magnetic field. On the right side of Eq. (B-8), from left to right, they are DMI energy, exchange energy, PMA energy and Zeeman energy. In the continuum limit, the energy functional is written as

$$E_{eff} = E_{DMI,eff} - A \frac{(\nabla \vec{m})^2}{2} - K_u \frac{(\vec{m} \cdot \hat{z})^2}{2} - \vec{m} \cdot \vec{B}_{ext}, \quad (\text{B-9})$$

where A is the exchange stiffness. For bulk DMI and interfacial DMI, the expressions of $E_{DMI,eff}$ are given by Eqs. (B-2) and (B-5), respectively.

C. Symmetry analysis of proximity-induced resistance effect

The form of the resistivity tensor,

$$\hat{\rho}[m, \partial m] = \begin{pmatrix} \rho_{xx} & \rho_{xy} \\ \rho_{yx} & \rho_{yy} \end{pmatrix}, \quad (\text{C-1})$$

where m is the unit vector along the magnetization, is dictated by the symmetry of the system.

Ultimately, we are interested in the off-diagonal component, ρ_{xy} and ρ_{yx} , to describe the Hall resistance. In particular, we would like to derive the antisymmetric non-dissipative part $\rho_{xy} - \rho_{yx}$.

For the subsequent analysis, it is sometimes convenient to separate the magnetization $m \equiv (m^{\parallel}, m_z)$ into the in-plane variable m^{\parallel} and the out-of-plane variable m_z .

For our systems, first, the resistivity tensor is assumed to be covariant under simultaneous spin and spatial rotations about the z axis:

$$\hat{\rho}[\mathcal{R}m, (\mathcal{R}\partial)(\mathcal{R}m)] = \mathcal{R}\hat{\rho}[m, \partial m]\mathcal{R}^T, \quad (\text{C-2})$$

where $\mathcal{R} = \cos \theta \hat{I} + \sin \theta \hat{\varepsilon}$ is an arbitrary rotation matrix in the xy plane, \hat{I} is the 2×2 identity matrix (in the xy space) and $\hat{\varepsilon}$ is the antisymmetric matrix (also in the xy space), $\varepsilon_{xy} = 1 = -\varepsilon_{yx}$.

Secondly, the reflection symmetry with respect to the yz plane requires

$$\hat{\rho}[\mathcal{M}_s m, (\mathcal{M}_0 \partial)(\mathcal{M}_s m)] = \mathcal{M}_0 \hat{\rho}[m, \partial m] \mathcal{M}_0^T, \quad (\text{C-3})$$

where $\mathcal{M}_s = \text{diag}(1, -1, -1)$ and $\mathcal{M}_0 = \text{diag}(-1, 1)$ are the representations of the reflection operator for spin and orbital, respectively. Thirdly, assuming linear response, it should satisfy Onsager's reciprocal relation,

$$\rho_{xy}[m] = \rho_{yx}[-m]. \quad (\text{C-4})$$

If we demand the three-dimensional spin-rotational symmetry independent of spatial orientation of the sample, i.e., by neglecting spin-orbit coupling, the first condition becomes more strict:

$$\hat{\rho}[\mathcal{R}m] = \hat{\rho}[m], \quad \mathcal{R}\hat{\rho}\mathcal{R}^T = \hat{\rho}, \quad (\text{C-5})$$

where \mathcal{R} is arbitrary three-dimensional rotation matrix. In this case, all the components of the resistivity tensor should be scalar with respect to spin rotations.

Below, we will obtain the contributions to the resistivity tensor as a series expansion in the gradient of m :

$$\hat{\rho}[m, \partial m] = \rho^0 + \rho^1 + \rho^2 + O((\partial m)^3), \quad (\text{C-6})$$

where the superscript represents the order in the gradient of m . For the first two terms, we allow spin-orbit coupling by demanding the conditions [Eqs. (C-2, C-3, C-4)]. For the third term, we demand the full spin-rotational symmetry [Eq. (C-5)], the mirror symmetry [Eq. (C-3)], and the Onsager's reciprocity [Eq. (C-4)]. In each term, we consider the minimal even and odd number of occurrences of the magnetization. Specifically, for ρ^0 and ρ^1 , we consider the terms that include the magnetization up to two times, and, for ρ^2 , we consider the terms that include the magnetization up to three times.

By demanding the rotational symmetry [Eq. (C-2) or Eq. (C-5)], the reflection symmetry with respect to the yz plane [Eq. (C-4)] and Onsager's reciprocal relation [Eq. (C-3)], we found the terms in the resistivity tensor (Eq. (C-1)) up to second order in the spatial gradient of the magnetization (by assuming spatially smooth magnetic textures) and the spin-orbit coupling effects (i.e., the total number of magnetization indices that are either uncontracted or contracted with the spatial indices). The zeroth order terms in the gradient are

$$\hat{I} = \begin{pmatrix} 1 & 0 \\ 0 & 1 \end{pmatrix}, \quad m_z^2 \hat{I} = \begin{pmatrix} m_z^2 & 0 \\ 0 & m_z^2 \end{pmatrix}, \quad m_z \hat{\varepsilon} = \begin{pmatrix} 0 & m_z \\ -m_z & 0 \end{pmatrix}, \quad m^\parallel (m^\parallel)^T = \begin{pmatrix} m_x^2 & m_x m_y \\ m_x m_y & m_y^2 \end{pmatrix}.$$

The first term describes the longitudinal resistivity in the absence of the magnetization. The second and last terms can describe anisotropic and spin Hall magnetoresistance. The third term describes anomalous Hall effects. (It also captures ordinary Hall effect symmetry wise.) The first order terms in the gradient are

$$[m_z(\nabla \cdot \mathbf{m}) - (\mathbf{m} \cdot \nabla)m_z] \hat{I}, \quad \nabla \cdot (m_z \mathbf{m}) \hat{I}, \quad \hat{\mathbf{z}} \cdot (\nabla \times \mathbf{m}) \hat{I}, \quad m_z(\partial_i m_j^\parallel + \partial_j m_i^\parallel), \quad (\partial_i m_z) m_j^\parallel + (\partial_j m_z) m_i^\parallel,$$

where the last two lines represent matrix elements ρ_{ij} . Note that the first term is proportional to the interfacial Dzyaloshinskii-Moriya interaction. The second order terms in the gradient are

$$\left((\partial_x m)^2 + (\partial_y m)^2 \right) \hat{I}, \quad \mathbf{m} \cdot (\partial_x \mathbf{m} \times \partial_y \mathbf{m}) \hat{\varepsilon}.$$

The second term is proportional to the skyrmion charge density.

We are interested in the antisymmetric non-dissipative (Hall) part, $\rho_{xy} - \rho_{yx}$. The general expression for this part is given by

$$A \begin{pmatrix} 0 & m_z \\ -m_z & 0 \end{pmatrix} + B \begin{pmatrix} 0 & \mathbf{m} \cdot (\partial_x \mathbf{m} \times \partial_y \mathbf{m}) \\ -\mathbf{m} \cdot (\partial_x \mathbf{m} \times \partial_y \mathbf{m}) & 0 \end{pmatrix}. \quad (\text{C-7})$$

Here, A and B can be arbitrary numbers. The first term represents anomalous Hall effects. The second term represents the topological Hall effect, which is proportional to the skyrmion charge density. The Eq. (C-7) with ordinary Hall effect is the Eq. (6-2) in the main text.

Below, we show details of deriving the zeroth order ρ^0 , first order ρ^1 and second order ρ^2 of $\hat{\rho}[m, \partial m]$.

In the index notation, Eq. (C-2) is given by

$$\rho_{ij}[\mathcal{R}m, (\mathcal{R}\partial)(\mathcal{R}m)] = R_{ik}R_{jl}\rho_{kl}[m, \partial m],$$

where R_{ij} represents the matrix element of \mathcal{R} .

Also, Eq. (C-3) can be written as

$$\rho_{xx}[(m_x, -m_y, m_z), -\partial_x(m_x, -m_y, m_z), \partial_y(m_x, -m_y, m_z)] = \rho_{xx}[m, \partial m],$$

$$\rho_{yy}[(m_x, -m_y, m_z), -\partial_x(m_x, -m_y, m_z), \partial_y(m_x, -m_y, m_z)] = \rho_{yy}[m, \partial m],$$

$$\rho_{xy}[(m_x, -m_y, m_z), -\partial_x(m_x, -m_y, m_z), \partial_y(m_x, -m_y, m_z)] = -\rho_{xy}[m, \partial m],$$

$$\rho_{yx}[(m_x, -m_y, m_z), -\partial_x(m_x, -m_y, m_z), \partial_y(m_x, -m_y, m_z)] = -\rho_{yx}[m, \partial m].$$

The zeroth order term ρ^0 can be expanded as follows:

$$\rho_{ij}^0 = A_{ij} + B_{ij}m_z + C_{ij}m_z^2 + D_{ijk}m_k^{\parallel} + E_{ijk}m_k^{\parallel}m_z + F_{ijkl}m_k^{\parallel}m_l^{\parallel} + O(m^3),$$

up to second order in the magnetization. The rotational symmetry requirements [Eq. (C-2)] are then given by

$$A_{ij} = R_{ia}R_{jb}A_{ab}, B_{ij} = R_{ia}R_{jb}B_{ab}, C_{ij} = R_{ia}R_{jb}C_{ab}, D_{ijk} = R_{ia}R_{jb}R_{kc}D_{abc}, E_{ijk} = R_{ia}R_{jb}R_{kc}E_{abc}, F_{ijkl} = R_{ia}R_{jb}R_{kc}R_{ld}F_{abcd}.$$

Since R can be an arbitrary rotation matrix, these tensors must be isotropic tensors. In two dimensions, there is no isotropic tensor of odd rank. Therefore, $D_{ijk} = 0$ and $E_{ijk} = 0$. There are two linearly independent isotropic tensors of rank 2:

$$\delta_{ij}, \varepsilon_{ij}.$$

With these tensors and Onsager's reciprocity, the possible terms in $\hat{\rho}$ from A_{ij} , $B_{ij}m_z$ and $C_{ij}m_z^2$ are the following:

$$\hat{I}, m_z \hat{I}, m_z^2 \hat{I}, m_z \hat{\varepsilon}.$$

Here, the second term $m_z \hat{I}$ is forbidden by the reflection symmetry. The last term can describe anomalous Hall effects. For F_{ijkl} , there are six linearly independent isotropic tensors of rank 4 [238]:

$$\delta_{ij}\delta_{kl}, \delta_{ik}\delta_{jl}, \delta_{il}\delta_{jk}, \delta_{ij}\varepsilon_{kl}, \delta_{ik}\varepsilon_{jl}, \delta_{il}\varepsilon_{jk}.$$

With these tensors and Onsager's reciprocity, the possible terms in $\hat{\rho}$ from $F_{ijkl}m_k^{\parallel}m_l^{\parallel}$ are the following:

$$(m^{\parallel})^2 \hat{I}, m^{\parallel}(m^{\parallel})^T = \begin{pmatrix} m_x^2 & m_x m_y \\ m_x m_y & m_y^2 \end{pmatrix}.$$

The first term can be captured by $m_z^2 \hat{I}$, which has already been derived above. To sum up, we have found the following contributions to the zeroth order term (in the gradient of m):

$$\hat{I}, m_z^2 \hat{I}, m_z \hat{\varepsilon}, m^{\parallel}(m^{\parallel})^T.$$

Note that the traces of the second and the last terms are m_z^2 and $m_x^2 + m_y^2$, which are linearly dependent.

The first order term ρ^1 in the gradient of m can be expanded as follows:

$$\begin{aligned} \rho_{ij}^1 &= A_{ijk}(\partial_k m_z) + B_{ijk}m_z(\partial_k m_z) + C_{ijkl}(\partial_k m_l^{\parallel}) + D_{ijkl}m_z(\partial_k m_l^{\parallel}) + E_{ijkl}m_k^{\parallel}(\partial_l m_z) \\ &+ F_{ijklm}m_k^{\parallel}(\partial_l m_m^{\parallel}) + O(m^3) \end{aligned}$$

up to second order in the magnetization. By removing tensors of odd rank, we can reduce the above expression to

$$\rho_{ij}^1 = C_{ijkl}(\partial_k m_l^{\parallel}) + D_{ijkl}m_z(\partial_k m_l^{\parallel}) + E_{ijkl}m_k^{\parallel}(\partial_l m_z).$$

For C_{ijkl} with isotropic tensors of rank 4, Onsager's reciprocity, and the reflection symmetry, we have only one possible term:

$$\hat{\mathbf{z}} \cdot (\nabla \times \mathbf{m}) \hat{I}.$$

For D_{ijkl} , with isotropic tensors of rank 4, Onsager's reciprocity, and the reflection symmetry, we have the following possible terms:

$$m_z(\nabla \cdot \mathbf{m}) \hat{I}, \quad m_z(\partial_i m_j^{\parallel} + \partial_j m_i^{\parallel}),$$

Note that the traces of the two terms are identical.

The possible terms from E_{ijkl} can be obtained from the results for D_{ijkl} :

$$(\mathbf{m} \cdot \nabla) m_z \hat{I}, \quad (\partial_i m_z) m_j^{\parallel} + (\partial_j m_z) m_i^{\parallel}.$$

Note that the interfacial DMI is a combination of the traces of these terms, $m_z(\nabla \cdot \mathbf{m}) - (\mathbf{m} \cdot \nabla) m_z$.

For the second order terms in the gradient expansion, ∂m , we will demand the full spin-only rotational symmetry Eq. (C-5). Then, the allowed linearly independent scalars (with respect to three-dimensional spin rotations) are

$$(\partial_x m)^2 + (\partial_y m)^2, \quad (\partial_x m)^2 - (\partial_y m)^2, \quad \mathbf{m} \cdot (\partial_x m \times \partial_y m).$$

Then, the possible terms in the resistivity tensor are

$$\begin{aligned} & \left((\partial_x m)^2 + (\partial_y m)^2 \right) \hat{I}, \left((\partial_x m)^2 + (\partial_y m)^2 \right) \hat{\varepsilon}, \left((\partial_x m)^2 - (\partial_y m)^2 \right) \hat{I}, \\ & \left((\partial_x m)^2 - (\partial_y m)^2 \right) \hat{\varepsilon}, m \cdot (\partial_x m \times \partial_y m) \hat{I}, m \cdot (\partial_x m \times \partial_y m) \hat{\varepsilon}. \end{aligned}$$

The second term is forbidden by the reflection symmetry. The third term is forbidden by the spatial rotational symmetry. The fourth term is forbidden by the reflection symmetry. The fifth term is forbidden by the reflection symmetry. Therefore, the only allowed terms are

$$\left((\partial_x m)^2 + (\partial_y m)^2 \right) \hat{I}, m \cdot (\partial_x m \times \partial_y m) \hat{\varepsilon}.$$

Recently, a noncollinear magnetoresistance (NCMR) effect has been proposed [239, 240] and experimentally realized [240]. This effect shows a change of MR when the neighboring magnetizations change from collinear to noncollinear. First, in our TmIG/Pt system, the SMR dominates. As shown in Fig. 1c, in the single domain (collinear magnetization configuration under the large field), the MR changes when the magnetization direction changes. This change is consistent with the spin Hall magnetoresistance (SMR) picture, where the magnetization collinear with the spin polarization (along the $\pm x$ direction) in the presence of charge current (along the $\pm y$ direction) gives rise to the lowest MR.

Second, the above symmetry analysis shows that the asymmetric Hall resistivity observed in the experiment can be only due to the resistivity contribution that is proportional to the m to the odd orders. The NCMR is an even function of the m sine it only depends on the noncollinearity of two neighboring magnetizations. Thus, for skyrmions with topological charge +1 and -1, the NCMR is the same. Thus, the observed asymmetric Hall resistivity cannot be due to the NCMR.

D. Symmetry analysis of current-induced spin-orbit torques

We analyze the torques acting on an in-plane magnetization as an example. The important references for this part are refs. [42, 52, 73].

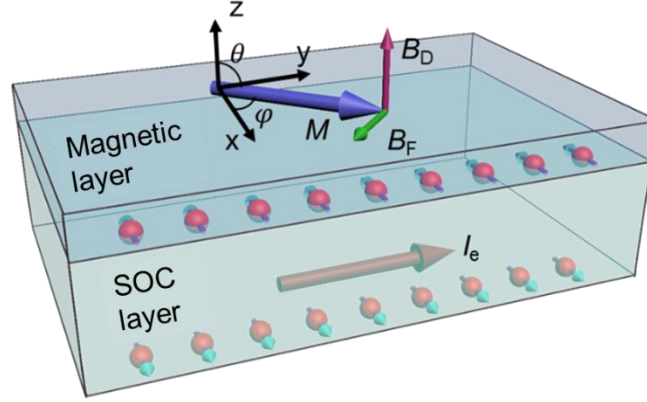


Figure 9-3 Schematic of a nonmagnetic spin-orbit coupled (SOC) layer/magnetic layer bilayer for symmetry analysis of current-induced SOTs. assume the current is flowing along the y direction, the angle between magnetization and x direction is azimuthal angle φ and angle between magnetization and z direction is polar angle θ . We assume that the mirror symmetry is broken for the yz plane for the analysis

The general torques can be expressed as $\vec{\tau}_{\parallel}(\hat{m}, E) = \tau_{\parallel}(\varphi, E)\hat{m} \times \hat{z}$ and $\vec{\tau}_{\perp}(\hat{m}, E) = \tau_{\perp}(\varphi, E)\hat{z}$, where E is the applied electric field (along the y direction, see Figure 9-3). The torque coefficients $\tau_{\parallel}(\varphi, E)$ and $\tau_{\perp}(\varphi, E)$ can be expressed as

$$\tau_{\parallel}(\varphi, E) = E(S_0 + S_1 \cos \varphi + S_2 \sin \varphi + S_3 \cos 2\varphi + S_4 \sin 2\varphi + S_5 \cos 3\varphi + S_6 \sin 3\varphi + \dots)$$

(D1-1)

$$\tau_{\perp}(\varphi, E) = E(A_0 + A_1 \cos \varphi + A_2 \sin \varphi + A_3 \cos 2\varphi + A_4 \sin 2\varphi + A_5 \cos 3\varphi + A_6 \sin 3\varphi + \dots)$$

(D1-2)

The mirror symmetry operation \mathcal{M}_{xz} flips the electric field E and x-component of M since E is a vector and M is a pseudovector. So, this is equivalent to transformations $E \rightarrow -E$ and $\varphi \rightarrow \pi - \varphi$.

The torques are also pseudovectors which need to follow certain transformation rules. To obtain the transformation rule, we rewrite the torque coefficients to be $\tau_{\parallel}(\varphi, E) = \vec{\tau}_{\parallel} \cdot (\hat{m} \times \hat{z})$ and $\tau_{\perp}(\varphi, E) = \vec{\tau}_{\perp} \cdot \hat{z}$.

The $\vec{\tau}_{\parallel} \cdot (\hat{m} \times \hat{z})$ is a pseudovector since $\vec{\tau}_{\parallel}$ is a pseudovector and $\hat{m} \times \hat{z}$ is a vector. Here, the cross product of a pseudovector \hat{m} and a vector \hat{z} is a vector. Under the mirror symmetry operation \mathcal{M}_{xz} , $\vec{\tau}_{\parallel} \cdot (\hat{m} \times \hat{z}) \rightarrow -\vec{\tau}_{\parallel} \cdot (\hat{m} \times \hat{z})$. Therefore, we need to make sure that $\tau_{\parallel}(\pi - \varphi, -E) = -\vec{\tau}_{\parallel} \cdot (\hat{m} \times \hat{z}) = -\tau_{\parallel}(\varphi, E)$.

The $\vec{\tau}_{\perp} \cdot \hat{z}$ is a pseudovector since $\vec{\tau}_{\perp}$ is a pseudovector and \hat{z} is a vector. Under the mirror symmetry operation \mathcal{M}_{xz} , $\vec{\tau}_{\perp} \cdot \hat{z} \rightarrow -\vec{\tau}_{\perp} \cdot \hat{z}$. Therefore, we need to make sure that $\tau_{\perp}(\pi - \varphi, -E) = -\vec{\tau}_{\perp} \cdot \hat{z} = -\tau_{\perp}(\varphi, E)$.

Furthermore, we assume a linear response of the spin-orbit torque to the current. Therefore, $\tau_{\parallel}(\pi - \varphi, -E) = -\tau_{\parallel}(\pi - \varphi, E) = -\tau_{\parallel}(\varphi, E) \Rightarrow \tau_{\parallel}(\pi - \varphi, E) = \tau_{\parallel}(\varphi, E)$. Similarly, $\tau_{\perp}(\pi - \varphi, E) = \tau_{\perp}(\varphi, E)$. After we force these two symmetry requirements on the Eq. D1, we obtain

$$\tau_{\parallel}(\varphi, E) = E(S_0 + S_2 \sin \varphi + S_4 \cos 2\varphi + S_6 \sin 3\varphi + \dots) \quad (\text{D2-1})$$

$$\tau_{\perp}(\varphi, E) = E(A_0 + A_2 \sin \varphi + A_4 \cos 2\varphi + A_6 \sin 3\varphi + \dots) \quad (\text{D2-2})$$

The S_2 and A_2 are normal damping-like and field-like spin-orbit torques. The S_0 and A_0 are the additional spin-orbit torques due to the mirror symmetry breaking with respect to the yz plane.

If we apply current along the x direction, the mirror symmetry operation \mathcal{M}_{xz} keeps the electric field E and flips the x-component of M . So, this is equivalent to transformations $E \rightarrow E$ and $\varphi \rightarrow$

$\pi - \varphi$. Following the similar argument as the current along the y direction case, we need to satisfy $\tau_{\parallel}(\pi - \varphi, E) = -\tau_{\parallel}(\varphi, E)$ and $\tau_{\perp}(\pi - \varphi, E) = -\tau_{\perp}(\varphi, E)$. After we force these two symmetry requirements on the Eq. D1, we obtain

$$\tau_{\parallel}(\varphi, E) = E(S_1 \cos \varphi + S_4 \sin 2\varphi + S_5 \cos 3\varphi + \dots) \quad (\text{D3-1})$$

$$\tau_{\perp}(\varphi, E) = E(A_1 \cos \varphi + A_4 \sin 2\varphi + A_5 \cos 3\varphi + \dots) \quad (\text{D3-2})$$

If we force mirror symmetry operation \mathcal{M}_{yz} on spin-orbit torques, we need to satisfy additional symmetry requirements. Let's say we still apply current along the y direction. The mirror symmetry operation \mathcal{M}_{yz} keeps the electric field E and flips the y-component of M . So, this is equivalent to transformations $E \rightarrow E$ and $\varphi \rightarrow -\varphi$. Again, we need to satisfy $\tau_{\parallel}(-\varphi, E) = -\tau_{\parallel}(\varphi, E)$ and $\tau_{\perp}(-\varphi, E) = -\tau_{\perp}(\varphi, E)$. After we force these two symmetry requirements on the Eq. D2, we obtain

$$\tau_{\parallel}(\varphi, E) = E(S_2 \sin \varphi + S_6 \sin 3\varphi + \dots) \quad (\text{D4-1})$$

$$\tau_{\perp}(\varphi, E) = E(A_2 \sin \varphi + A_6 \sin 3\varphi + \dots) \quad (\text{D4-2})$$

So, we are only left with traditional damping-like and field-like spin-orbit torques. In this circumstance, there is no switching in the absence of external field. We need to apply external field along y direction or z direction. This field can be potentially provided by the exchange bias from an antiferromagnet or a tilted magnetic anisotropy (towards y direction). Recently, people have been studying spin-orbit torques from ferromagnets. In principle, spin-orbit torque from a ferromagnet with magnetization pointing towards the y or z directions could induce zero-field switching (current along the y direction) since the yz plane mirror symmetry is broken.

At last, we want to show that if there is no inversion symmetry breaking in the magnetic multilayers, the spin-orbit torque cannot exist. Again, let's say we still apply current along the y direction. The mirror symmetry operation \mathcal{M}_{xy} keeps the electric field E and flips the M . So, this is equivalent to transformations $E \rightarrow E$ and $\varphi \rightarrow \pi + \varphi$. Under the \mathcal{M}_{xy} , the torques need to satisfy $\vec{\tau}_{\parallel} \cdot (\hat{m} \times \hat{z}) \rightarrow \vec{\tau}_{\parallel} \cdot (\hat{m} \times \hat{z})$ and $\vec{\tau}_{\perp} \cdot \hat{z} \rightarrow \vec{\tau}_{\perp} \cdot \hat{z}$. Therefore, $\tau_{\parallel}(\pi + \varphi, E) = \tau_{\parallel}(\varphi, E)$ and $\tau_{\perp}(\pi + \varphi, E) = \tau_{\perp}(\varphi, E)$. After we force these two symmetry requirements on the Eq. D4, we obtain $\tau_{\parallel}(\varphi, E) = 0$ and $\tau_{\perp}(\varphi, E) = 0$.

Similarly, we can analyze the rotational symmetry. Note that both pseudovectors and vectors follow the same transformation rules under a proper rotation. Pseudovectors gain an additional sign flip under an improper rotation, including reflection with respect to a mirror plane and inversion with respect to a point.

E. Pulsed laser deposition

Pulsed laser deposition (PLD) utilizes a high-power pulsed laser to strike a target material in the high vacuum or in the presence of a background gas. For example, when we deposit magnetic garnet, including YIG, TmIG, and TbIG, we have oxygen as the background gas to fully oxygenate the deposited film. The details of the PLD system are introduced in Figure 9-4 and Figure 9-5.

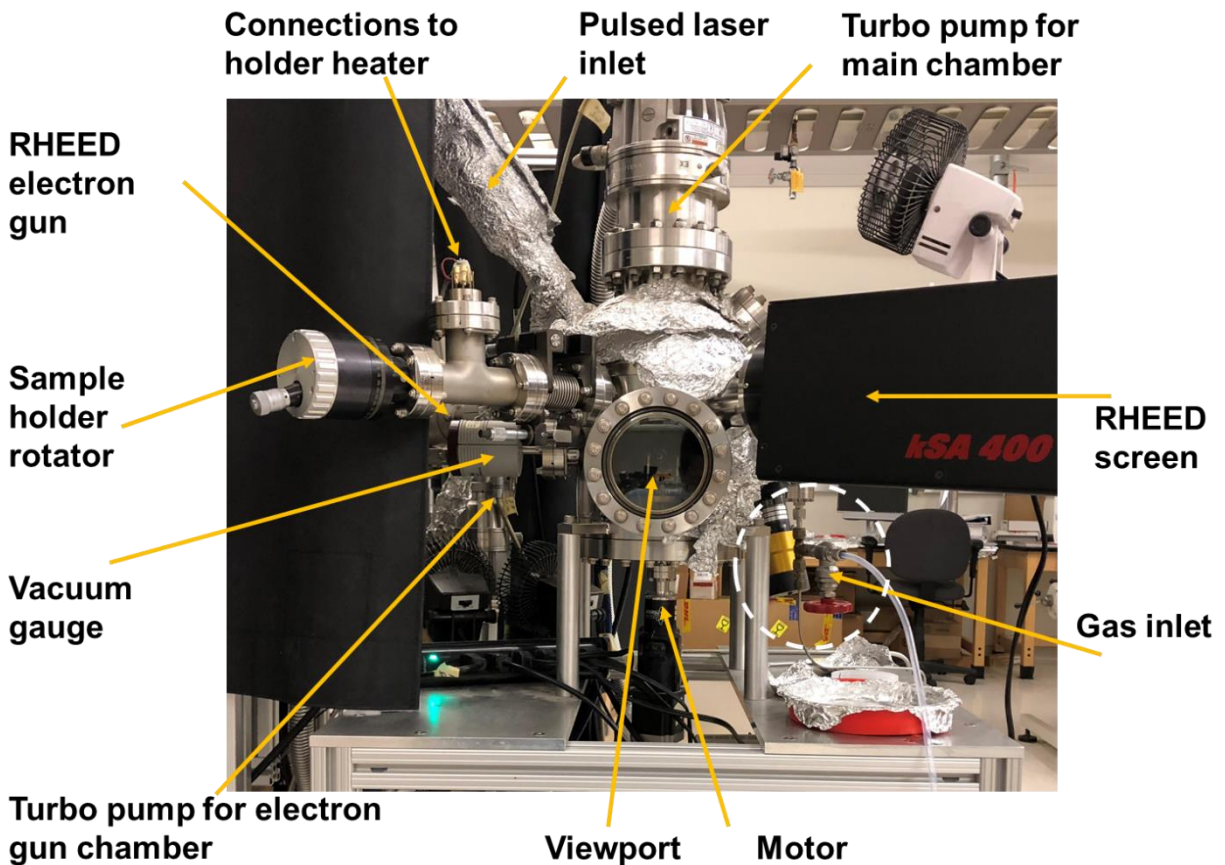


Figure 9-4 Picture of a PLD chamber. The chamber oxygen/ozone pressure is controlled by the gas inlet. The growth quality can be monitored using RHEED. Credit: Jing Shi' lab at UC Riverside

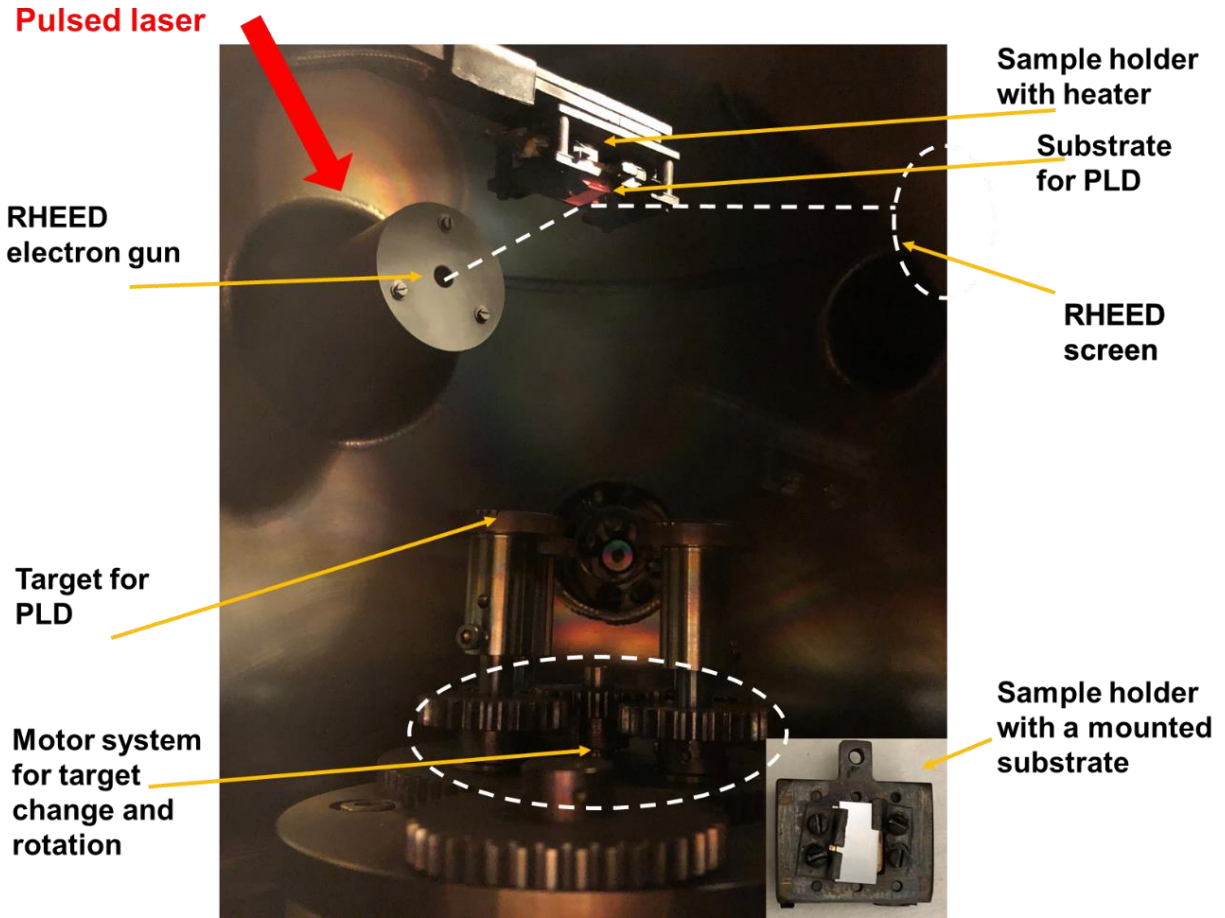


Figure 9-5 Inside a PLD chamber. The growth temperature is controlled by a heater underneath the sample holder. To avoid constant strike on the same point, the target is rotated using a motor system. Credit: Jing Shi' lab at UC Riverside

We can monitor the sample quality by using reflection high-energy electron diffraction (RHEED). We show RHEED pattern of a NiO grown on TmIG/NGG(111). As shown in Figure 9-6a, the pattern is very sharp for TmIG, which indicates a high quality. As the time goes on, the pattern becomes more and more blurred Figure 9-6b-d, which indicates that the NiO is polycrystalline.

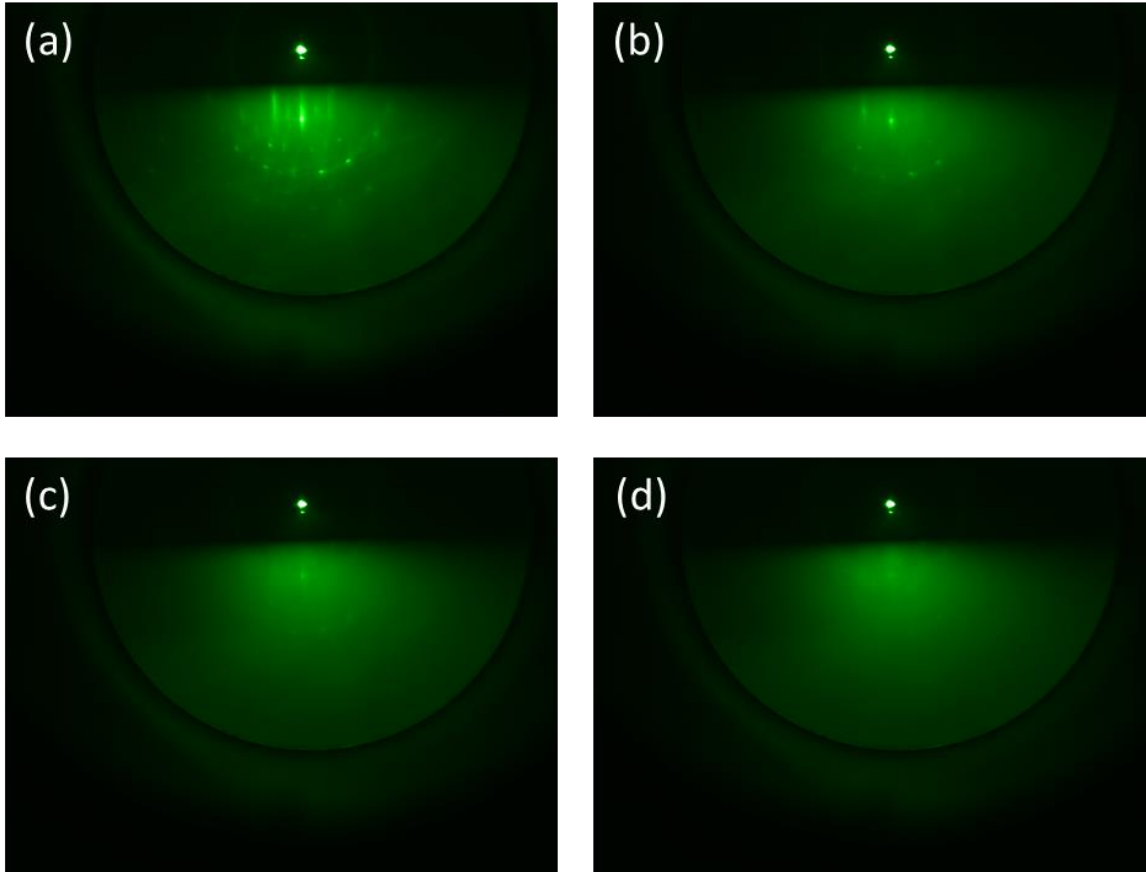


Figure 9-6 RHEED pattern of NiO growth on TmIG(111)/NGG(111). From left top to right bottom, the RHEED images are taken at (a) 0 min (before growth), (b) 1 min, (c) 2 min, and (d) 3min

References

- [1] S. A. Wolf, D. D. Awschalom, R. A. Buhrman, J. M. Daughton, S. von Molnar, M. L. Roukes, A. Y. Chtchelkanova, and D. M. Treger, "Spintronics: a spin-based electronics vision for the future," *Science*, vol. 294, no. 5546, pp. 1488-95, Nov 16, 2001.
- [2] T. D. Ladd, F. Jelezko, R. Laflamme, Y. Nakamura, C. Monroe, and J. L. O'Brien, "Quantum computers," *Nature*, vol. 464, no. 7285, pp. 45-53, Mar 4, 2010.
- [3] C. L. Kane, and E. J. Mele, "Quantum spin Hall effect in graphene," *Phys Rev Lett*, vol. 95, no. 22, pp. 226801, Nov 25, 2005.
- [4] B. A. Bernevig, T. L. Hughes, and S. C. Zhang, "Quantum spin Hall effect and topological phase transition in HgTe quantum wells," *Science*, vol. 314, no. 5806, pp. 1757-61, Dec 15, 2006.
- [5] M. Konig, S. Wiedmann, C. Brune, A. Roth, H. Buhmann, L. W. Molenkamp, X. L. Qi, and S. C. Zhang, "Quantum spin hall insulator state in HgTe quantum wells," *Science*, vol. 318, no. 5851, pp. 766-70, Nov 2, 2007.
- [6] X. Kou, S. T. Guo, Y. Fan, L. Pan, M. Lang, Y. Jiang, Q. Shao, T. Nie, K. Murata, J. Tang, Y. Wang, L. He, T. K. Lee, W. L. Lee, and K. L. Wang, "Scale-invariant quantum anomalous Hall effect in magnetic topological insulators beyond the two-dimensional limit," *Phys Rev Lett*, vol. 113, no. 13, pp. 137201, Sep 26, 2014.
- [7] C. Z. Chang, J. Zhang, X. Feng, J. Shen, Z. Zhang, M. Guo, K. Li, Y. Ou, P. Wei, L. L. Wang, Z. Q. Ji, Y. Feng, S. Ji, X. Chen, J. Jia, X. Dai, Z. Fang, S. C. Zhang, K. He, Y. Wang, L. Lu, X. C. Ma, and Q. K. Xue, "Experimental observation of the quantum anomalous Hall effect in a magnetic topological insulator," *Science*, vol. 340, no. 6129, pp. 167-70, Apr 12, 2013.
- [8] D. D. Awschalom, L. C. Bassett, A. S. Dzurak, E. L. Hu, and J. R. Petta, "Quantum spintronics: engineering and manipulating atom-like spins in semiconductors," *Science*, vol. 339, no. 6124, pp. 1174-9, Mar 8, 2013.
- [9] G. Binasch, P. Grünberg, F. Saurenbach, and W. Zinn, "Enhanced magnetoresistance in layered magnetic structures with antiferromagnetic interlayer exchange," *Physical Review B*, vol. 39, no. 7, pp. 4828-4830, 1989.

- [10] M. N. Baibich, J. M. Broto, A. Fert, F. N. Van Dau, F. Petroff, P. Etienne, G. Creuzet, A. Friederich, and J. Chazelas, “Giant Magnetoresistance of (001)Fe/(001)Cr Magnetic Superlattices,” *Physical Review Letters*, vol. 61, no. 21, pp. 2472-2475, 1988.
- [11] S. S. Parkin, C. Kaiser, A. Panchula, P. M. Rice, B. Hughes, M. Samant, and S. H. Yang, “Giant tunnelling magnetoresistance at room temperature with MgO (100) tunnel barriers,” *Nat Mater*, vol. 3, no. 12, pp. 862-7, Dec, 2004.
- [12] S. Yuasa, T. Nagahama, A. Fukushima, Y. Suzuki, and K. Ando, “Giant room-temperature magnetoresistance in single-crystal Fe/MgO/Fe magnetic tunnel junctions,” *Nat Mater*, vol. 3, no. 12, pp. 868-71, Dec, 2004.
- [13] H. S. Wong, and S. Salahuddin, “Memory leads the way to better computing,” *Nat Nanotechnol*, vol. 10, no. 3, pp. 191-4, Mar, 2015.
- [14] Q. Shao, “Spin-orbit torques in topological insulators,” University of California, Los Angeles, ProQuest Dissertations Publishing, 2015.
- [15] C. Kittel, *Introduction to Solid State Physics*, 7th ed.: John Wiley & Sons, Inc., 1996.
- [16] V. Baltz, A. Manchon, M. Tsoi, T. Moriyama, T. Ono, and Y. Tserkovnyak, “Antiferromagnetic spintronics,” *Reviews of Modern Physics*, vol. 90, no. 1, 2018.
- [17] S. Ikeda, J. Hayakawa, Y. Ashizawa, Y. M. Lee, K. Miura, H. Hasegawa, M. Tsunoda, F. Matsukura, and H. Ohno, “Tunnel magnetoresistance of 604% at 300K by suppression of Ta diffusion in CoFeB/MgO/CoFeB pseudo-spin-valves annealed at high temperature,” *Applied Physics Letters*, vol. 93, no. 8, pp. 082508, 2008.
- [18] D. R. Klein, D. MacNeill, J. L. Lado, D. Soriano, E. Navarro-Moratalla, K. Watanabe, T. Taniguchi, S. Manni, P. Canfield, J. Fernandez-Rossier, and P. Jarillo-Herrero, “Probing magnetism in 2D van der Waals crystalline insulators via electron tunneling,” *Science*, vol. 360, no. 6394, pp. 1218-1222, Jun 15, 2018.
- [19] T. Song, X. Cai, M. W. Tu, X. Zhang, B. Huang, N. P. Wilson, K. L. Seyler, L. Zhu, T. Taniguchi, K. Watanabe, M. A. McGuire, D. H. Cobden, D. Xiao, W. Yao, and X. Xu, “Giant tunneling magnetoresistance in spin-filter van der Waals heterostructures,” *Science*, vol. 360, no. 6394, pp. 1214-1218, Jun 15, 2018.
- [20] Y. Fan, P. Upadhyaya, X. Kou, M. Lang, S. Takei, Z. Wang, J. Tang, L. He, L. T. Chang, M. Montazeri, G. Yu, W. Jiang, T. Nie, R. N. Schwartz, Y. Tserkovnyak, and K. L.

- Wang, “Magnetization switching through giant spin-orbit torque in a magnetically doped topological insulator heterostructure,” *Nat Mater*, vol. 13, no. 7, pp. 699-704, Jul, 2014.
- [21] A. R. Mellnik, J. S. Lee, A. Richardella, J. L. Grab, P. J. Mintun, M. H. Fischer, A. Vaezi, A. Manchon, E. A. Kim, N. Samarth, and D. C. Ralph, “Spin-transfer torque generated by a topological insulator,” *Nature*, vol. 511, no. 7510, pp. 449-51, Jul 24, 2014.
- [22] M. Z. Hasan, and C. L. Kane, “Colloquium: Topological insulators,” *Reviews of Modern Physics*, vol. 82, no. 4, pp. 3045-3067, 2010.
- [23] X.-L. Qi, and S.-C. Zhang, “Topological insulators and superconductors,” *Reviews of Modern Physics*, vol. 83, no. 4, pp. 1057-1110, 2011.
- [24] Y. L. Chen, J. G. Analytis, J. H. Chu, Z. K. Liu, S. K. Mo, X. L. Qi, H. J. Zhang, D. H. Lu, X. Dai, Z. Fang, S. C. Zhang, I. R. Fisher, Z. Hussain, and Z. X. Shen, “Experimental realization of a three-dimensional topological insulator, Bi₂Te₃,” *Science*, vol. 325, no. 5937, pp. 178-81, Jul 10, 2009.
- [25] Y. Fan, X. Kou, P. Upadhyaya, Q. Shao, L. Pan, M. Lang, X. Che, J. Tang, M. Montazeri, K. Murata, L. T. Chang, M. Akyol, G. Yu, T. Nie, K. L. Wong, J. Liu, Y. Wang, Y. Tserkovnyak, and K. L. Wang, “Electric-field control of spin-orbit torque in a magnetically doped topological insulator,” *Nat Nanotechnol*, vol. 11, no. 4, pp. 352-9, Apr, 2016.
- [26] C.-F. Pai, L. Liu, Y. Li, H. W. Tseng, D. C. Ralph, and R. A. Buhrman, “Spin transfer torque devices utilizing the giant spin Hall effect of tungsten,” *Applied Physics Letters*, vol. 101, no. 12, pp. 122404, 2012.
- [27] M. Dc, R. Grassi, J. Y. Chen, M. Jamali, D. Reifsnyder Hickey, D. Zhang, Z. Zhao, H. Li, P. Quarterman, Y. Lv, M. Li, A. Manchon, K. A. Mkhoyan, T. Low, and J. P. Wang, “Room-temperature high spin-orbit torque due to quantum confinement in sputtered Bi_xSe_(1-x) films,” *Nat Mater*, Jul 30, 2018.
- [28] N. H. D. Khang, Y. Ueda, and P. N. Hai, “A conductive topological insulator with large spin Hall effect for ultralow power spin-orbit torque switching,” *Nat Mater*, vol. 17, no. 9, pp. 808-813, Sep, 2018.
- [29] K. Kondou, R. Yoshimi, A. Tsukazaki, Y. Fukuma, J. Matsuno, K. S. Takahashi, M. Kawasaki, Y. Tokura, and Y. Otani, “Fermi-level-dependent charge-to-spin current

- conversion by Dirac surface states of topological insulators,” *Nature Physics*, vol. 12, no. 11, pp. 1027-1031, 2016.
- [30] J. Han, A. Richardella, S. A. Siddiqui, J. Finley, N. Samarth, and L. Liu, “Room-Temperature Spin-Orbit Torque Switching Induced by a Topological Insulator,” *Phys Rev Lett*, vol. 119, no. 7, pp. 077702, Aug 18, 2017.
- [31] L. Liu, T. Moriyama, D. C. Ralph, and R. A. Buhrman, “Spin-torque ferromagnetic resonance induced by the spin Hall effect,” *Phys Rev Lett*, vol. 106, no. 3, pp. 036601, Jan 21, 2011.
- [32] Y. Wang, P. Deorani, K. Banerjee, N. Koirala, M. Brahlek, S. Oh, and H. Yang, “Topological Surface States Originated Spin-Orbit Torques in Bi(2)Se(3),” *Phys Rev Lett*, vol. 114, no. 25, pp. 257202, Jun 26, 2015.
- [33] L. Liu, C. F. Pai, Y. Li, H. W. Tseng, D. C. Ralph, and R. A. Buhrman, “Spin-torque switching with the giant spin Hall effect of tantalum,” *Science*, vol. 336, no. 6081, pp. 555-8, May 4, 2012.
- [34] Q. M. Shao, G. Q. Yu, L. Pan, X. Y. Che, Y. Fan, K. Murata, Q. L. He, T. X. Nie, X. F. Kou, and K. L. Wang, "Large Room Temperature Charge-to-Spin Conversion Efficiency in Topological Insulator/CoFeB bilayers." pp. 1-2.
- [35] Q. Shao, H. Wu, Q. Pan, P. Zhang, L. Pan, K. Wong, X. Che, and K. L. Wang, "Room Temperature Highly Efficient Topological Insulator/Mo/CoFeB Spin-Orbit Torque Memory with Perpendicular Magnetic Anisotropy." pp. 36.3.1-36.3.4.
- [36] L. Pan, and D. B. Bogy, “Heat-assisted magnetic recording,” *Nature Photonics*, vol. 3, no. 4, pp. 189-190, 2009.
- [37] S. S. Parkin, M. Hayashi, and L. Thomas, “Magnetic domain-wall racetrack memory,” *Science*, vol. 320, no. 5873, pp. 190-4, Apr 11, 2008.
- [38] S. Parkin, and S. H. Yang, “Memory on the racetrack,” *Nat Nanotechnol*, vol. 10, no. 3, pp. 195-8, Mar, 2015.
- [39] G. Yu, P. Upadhyaya, Q. Shao, H. Wu, G. Yin, X. Li, C. He, W. Jiang, X. Han, P. K. Amiri, and K. L. Wang, “Room-Temperature Skyrmion Shift Device for Memory Application,” *Nano Lett*, vol. 17, no. 1, pp. 261-268, Jan 11, 2017.
- [40] A. Fert, V. Cros, and J. Sampaio, “Skyrmions on the track,” *Nat Nanotechnol*, vol. 8, no. 3, pp. 152-6, Mar, 2013.

- [41] A. Vansteenkiste, J. Leliaert, M. Dvornik, M. Helsen, F. Garcia-Sanchez, and B. Van Waeyenberge, “The design and verification of MuMax3,” *AIP Advances*, vol. 4, no. 10, pp. 107133, 2014.
- [42] D. MacNeill, G. M. Stiehl, M. H. D. Guimaraes, R. A. Buhrman, J. Park, and D. C. Ralph, “Control of spin–orbit torques through crystal symmetry in WTe₂/ferromagnet bilayers,” *Nature Physics*, 2016.
- [43] L. Fu, “Hexagonal warping effects in the surface states of the topological insulator Bi₂Te₃,” *Phys Rev Lett*, vol. 103, no. 26, pp. 266801, Dec 31, 2009.
- [44] P. He, S. S. L. Zhang, D. Zhu, Y. Liu, Y. Wang, J. Yu, G. Vignale, and H. Yang, “Bilinear magnetoelectric resistance as a probe of three-dimensional spin texture in topological surface states,” *Nature Physics*, vol. 14, no. 5, pp. 495-499, 2018.
- [45] T. Ideue, K. Hamamoto, S. Koshikawa, M. Ezawa, S. Shimizu, Y. Kaneko, Y. Tokura, N. Nagaosa, and Y. Iwasa, “Bulk rectification effect in a polar semiconductor,” *Nature Physics*, 2017.
- [46] C. O. Avci, K. Garello, A. Ghosh, M. Gabureac, S. F. Alvarado, and P. Gambardella, “Unidirectional spin Hall magnetoresistance in ferromagnet/normal metal bilayers,” *Nature Physics*, vol. 11, no. 7, pp. 570-575, 2015.
- [47] Y. Fan, Q. Shao, L. Pan, X. Che, Q. He, G. Yin, C. Zheng, G. Yu, T. Nie, M. R. Masir, A. H. MacDonald, and K. L. Wang, “Unidirectional Magneto-Resistance in Modulation-Doped Magnetic Topological Insulators,” *Nano Lett*, vol. 19, no. 2, pp. 692-698, Feb 13, 2019.
- [48] K. Yasuda, A. Tsukazaki, R. Yoshimi, K. S. Takahashi, M. Kawasaki, and Y. Tokura, “Large Unidirectional Magnetoresistance in a Magnetic Topological Insulator,” *Physical Review Letters*, vol. 117, no. 12, 2016.
- [49] U. H. Pi, K. Won Kim, J. Y. Bae, S. C. Lee, Y. J. Cho, K. S. Kim, and S. Seo, “Tilting of the spin orientation induced by Rashba effect in ferromagnetic metal layer,” *Applied Physics Letters*, vol. 97, no. 16, pp. 162507, 2010.
- [50] C. O. Avci, A. Quindeau, C. F. Pai, M. Mann, L. Caretta, A. S. Tang, M. C. Onbasli, C. A. Ross, and G. S. Beach, “Current-induced switching in a magnetic insulator,” *Nat Mater*, vol. 16, no. 3, pp. 309-314, Mar, 2017.

- [51] J. Kim, J. Sinha, M. Hayashi, M. Yamanouchi, S. Fukami, T. Suzuki, S. Mitani, and H. Ohno, "Layer thickness dependence of the current-induced effective field vector in Ta|CoFeB|MgO," *Nat Mater*, vol. 12, no. 3, pp. 240-5, Mar, 2013.
- [52] K. Garello, I. M. Miron, C. O. Avci, F. Freimuth, Y. Mokrousov, S. Blugel, S. Auffret, O. Boulle, G. Gaudin, and P. Gambardella, "Symmetry and magnitude of spin-orbit torques in ferromagnetic heterostructures," *Nat Nanotechnol*, vol. 8, no. 8, pp. 587-93, Aug, 2013.
- [53] C. O. Avci, K. Garello, M. Gabureac, A. Ghosh, A. Fuhrer, S. F. Alvarado, and P. Gambardella, "Interplay of spin-orbit torque and thermoelectric effects in ferromagnet/normal-metal bilayers," *Physical Review B*, vol. 90, no. 22, pp. 224427, 2014.
- [54] M. Hayashi, J. Kim, M. Yamanouchi, and H. Ohno, "Quantitative characterization of the spin-orbit torque using harmonic Hall voltage measurements," *Physical Review B*, vol. 89, no. 14, 2014.
- [55] Q. Shao, G. Yu, Y. W. Lan, Y. Shi, M. Y. Li, C. Zheng, X. Zhu, L. J. Li, P. K. Amiri, and K. L. Wang, "Strong Rashba-Edelstein Effect-Induced Spin-Orbit Torques in Monolayer Transition Metal Dichalcogenide/Ferromagnet Bilayers," *Nano Lett*, vol. 16, no. 12, pp. 7514-7520, Dec 14, 2016.
- [56] J. Li, G. Yu, C. Tang, Y. Liu, Z. Shi, Y. Liu, A. Navabi, M. Aldosary, Q. Shao, K. L. Wang, R. Lake, and J. Shi, "Deficiency of the bulk spin Hall effect model for spin-orbit torques in magnetic-insulator/heavy-metal heterostructures," *Physical Review B*, vol. 95, no. 24, pp. 241305(R), 2017.
- [57] X. Fan, H. Celik, J. Wu, C. Ni, K. J. Lee, V. O. Lorenz, and J. Q. Xiao, "Quantifying interface and bulk contributions to spin-orbit torque in magnetic bilayers," *Nat Commun*, vol. 5, pp. 3042, 2014.
- [58] M. Montazeri, P. Upadhyaya, M. C. Onbasli, G. Yu, K. L. Wong, M. Lang, Y. Fan, X. Li, P. Khalili Amiri, R. N. Schwartz, C. A. Ross, and K. L. Wang, "Magneto-optical investigation of spin-orbit torques in metallic and insulating magnetic heterostructures," *Nat Commun*, vol. 6, pp. 8958, Dec 8, 2015.
- [59] H. Kubota, A. Fukushima, K. Yakushiji, T. Nagahama, S. Yuasa, K. Ando, H. Maehara, Y. Nagamine, K. Tsunekawa, D. D. Djayaprawira, N. Watanabe, and Y. Suzuki,

- “Quantitative measurement of voltage dependence of spin-transfer torque in MgO-based magnetic tunnel junctions,” *Nature Physics*, vol. 4, no. 1, pp. 37-41, 2007.
- [60] J. C. SANKEY, “Measurement of the spin-transfer-torque vector in magnetic tunnel junctions,” *Nature Physics*, 2008.
- [61] L. Q. Liu, T. Moriyama, D. C. Ralph, and R. A. Buhrman, “Spin-Torque Ferromagnetic Resonance Induced by the Spin Hall Effect,” *Physical Review Letters*, vol. 106, pp. 036601, Jan 20, 2011.
- [62] T. X. Nan, S. Emori, C. T. Boone, X. J. Wang, T. M. Oxholm, J. G. Jones, B. M. Howe, G. J. Brown, and N. X. Sun, “Comparison of spin-orbit torques and spin pumping across NiFe/Pt and NiFe/Cu/Pt interfaces,” *Physical Review B*, vol. 91, pp. 214416, Jun 11, 2015.
- [63] C. F. Pai, L. Q. Liu, Y. Li, H. W. Tseng, D. C. Ralph, and R. A. Buhrman, “Spin transfer torque devices utilizing the giant spin Hall effect of tungsten,” *Applied Physics Letters*, vol. 101, pp. 122404, Sep 17, 2012.
- [64] C. He, A. Navabi, Q. Shao, G. Yu, D. Wu, W. Zhu, C. Zheng, X. Li, Q. L. He, S. A. Razavi, K. L. Wong, Z. Zhang, P. K. Amiri, and K. L. Wang, “Spin-torque ferromagnetic resonance measurements utilizing spin Hall magnetoresistance in W/Co₄₀Fe₄₀B₂₀/MgO structures,” *Applied Physics Letters*, vol. 109, no. 20, pp. 202404, 2016.
- [65] X. Y. Liu, W. Z. Zhang, M. J. Carter, and G. Xiao, “Ferromagnetic resonance and damping properties of CoFeB thin films as free layers in MgO-based magnetic tunnel junctions,” *Journal of Applied Physics*, vol. 110, pp. 033910, Aug 1, 2011.
- [66] G. Malinowski, K. C. Kuiper, R. Lavrijsen, H. J. M. Swagten, and B. Koopmans, “Magnetization dynamics and Gilbert damping in ultrathin Co₄₈Fe₃₂B₂₀ films with out-of-plane anisotropy,” *Applied Physics Letters*, vol. 94, pp. 102501, Mar 9, 2009.
- [67] Y. Tserkovnyak, A. Brataas, and G. E. W. Bauer, “Enhanced Gilbert damping in thin ferromagnetic films,” *Physical Review Letters*, vol. 88, no. 11, Mar 18, 2002.
- [68] P. Deorani, and H. Yang, “Role of spin mixing conductance in spin pumping: Enhancement of spin pumping efficiency in Ta/Cu/Py structures,” *Applied Physics Letters*, vol. 103, no. 23, Dec 2, 2013.
- [69] S. Iihama, S. Mizukami, H. Naganuma, M. Oogane, Y. Ando, and T. Miyazaki, “Gilbert damping constants of Ta/CoFeB/MgO(Ta) thin films measured by optical detection of

- precessional magnetization dynamics,” *Physical Review B*, vol. 89, pp. 174416, May 13, 2014.
- [70] I. Barsukov, Y. Fu, A. M. Goncalves, M. Spasova, M. Farle, L. C. Sampaio, R. E. Arias, and I. N. Krivorotov, “Field-dependent perpendicular magnetic anisotropy in CoFeB thin films,” *Applied Physics Letters*, vol. 105, pp. 152403, Oct 13, 2014.
- [71] K. Kondou, H. Sukegawa, S. Kasai, S. Mitani, Y. Niimi, and Y. Otani, “Influence of inverse spin Hall effect in spin-torque ferromagnetic resonance measurements,” *Applied Physics Express*, vol. 9, no. 2, pp. 023002, 2016.
- [72] H. L. Wang, C. H. Du, Y. Pu, R. Adur, P. C. Hammel, and F. Y. Yang, “Scaling of spin Hall angle in 3d, 4d, and 5d metals from Y3Fe5O12/metal spin pumping,” *Phys Rev Lett*, vol. 112, no. 19, pp. 197201, May 16, 2014.
- [73] G. Yu, P. Upadhyaya, Y. Fan, J. G. Alzate, W. Jiang, K. L. Wong, S. Takei, S. A. Bender, L. T. Chang, Y. Jiang, M. Lang, J. Tang, Y. Wang, Y. Tserkovnyak, P. K. Amiri, and K. L. Wang, “Switching of perpendicular magnetization by spin-orbit torques in the absence of external magnetic fields,” *Nat Nanotechnol*, vol. 9, no. 7, pp. 548-54, Jul, 2014.
- [74] S. Emori, E. Martinez, K.-J. Lee, H.-W. Lee, U. Bauer, S.-M. Ahn, P. Agrawal, D. C. Bono, and G. S. D. Beach, “Spin Hall torque magnetometry of Dzyaloshinskii domain walls,” *Physical Review B*, vol. 90, no. 18, 2014.
- [75] C.-F. Pai, M. Mann, A. J. Tan, and G. S. D. Beach, “Determination of spin torque efficiencies in heterostructures with perpendicular magnetic anisotropy,” *Physical Review B*, vol. 93, no. 14, pp. 144409, Apr 8, 2016.
- [76] K. L. Wang, J. G. Alzate, and P. K. Amiri, “Low-power non-volatile spintronic memory: STT-RAM and beyond,” *Journal Of Physics D-Applied Physics*, vol. 46, no. 7, pp. 074003, Feb 20, 2013.
- [77] N. Locatelli, V. Cros, and J. Grollier, “Spin-torque building blocks,” *Nat Mater*, vol. 13, no. 1, pp. 11-20, Jan, 2014.
- [78] I. M. Miron, K. Garello, G. Gaudin, P. J. Zermatten, M. V. Costache, S. Auffret, S. Bandiera, B. Rodmacq, A. Schuhl, and P. Gambardella, “Perpendicular switching of a single ferromagnetic layer induced by in-plane current injection,” *Nature*, vol. 476, no. 7359, pp. 189-93, Aug 11, 2011.

- [79] S. Emori, U. Bauer, S. M. Ahn, E. Martinez, and G. S. Beach, “Current-driven dynamics of chiral ferromagnetic domain walls,” *Nat Mater*, vol. 12, no. 7, pp. 611-6, Jul, 2013.
- [80] G. Yu, P. Upadhyaya, K. L. Wong, W. Jiang, J. G. Alzate, J. Tang, P. K. Amiri, and K. L. Wang, “Magnetization switching through spin-Hall-effect-induced chiral domain wall propagation,” *Physical Review B*, vol. 89, no. 10, pp. 104421, 2014.
- [81] H. Kurebayashi, J. Sinova, D. Fang, A. C. Irvine, T. D. Skinner, J. Wunderlich, V. Novak, R. P. Campion, B. L. Gallagher, E. K. Vehstedt, L. P. Zarbo, K. Vyborny, A. J. Ferguson, and T. Jungwirth, “An antidamping spin-orbit torque originating from the Berry curvature,” *Nat Nanotechnol*, vol. 9, no. 3, pp. 211-7, Mar, 2014.
- [82] A. Chernyshov, M. Overby, X. Liu, J. K. Furdyna, Y. Lyanda-Geller, and L. P. Rokhinson, “Evidence for reversible control of magnetization in a ferromagnetic material by means of spin-orbit magnetic field,” *Nature Physics*, vol. 5, no. 9, pp. 656-659, 2009.
- [83] W. Han, “Perspectives for spintronics in 2D materials,” *APL Materials*, vol. 4, no. 3, pp. 032401, 2016.
- [84] D. Pesin, and A. H. MacDonald, “Spintronics and pseudospintronics in graphene and topological insulators,” *Nat Mater*, vol. 11, no. 5, pp. 409-16, May, 2012.
- [85] J. Balakrishnan, G. Kok Wai Koon, M. Jaiswal, A. H. Castro Neto, and B. Özyilmaz, “Colossal enhancement of spin-orbit coupling in weakly hydrogenated graphene,” *Nature Physics*, vol. 9, no. 5, pp. 284-287, 2013.
- [86] J. Balakrishnan, G. K. Koon, A. Avsar, Y. Ho, J. H. Lee, M. Jaiswal, S. J. Baeck, J. H. Ahn, A. Ferreira, M. A. Cazalilla, A. H. Castro Neto, and B. Ozyilmaz, “Giant spin Hall effect in graphene grown by chemical vapour deposition,” *Nat Commun*, vol. 5, pp. 4748, 2014.
- [87] A. A. Taskin, S. Sasaki, K. Segawa, and Y. Ando, “Manifestation of topological protection in transport properties of epitaxial Bi₂Se₃ thin films,” *Phys Rev Lett*, vol. 109, no. 6, pp. 066803, Aug 10, 2012.
- [88] A. Manchon, H. C. Koo, J. Nitta, S. M. Frolov, and R. A. Duine, “New perspectives for Rashba spin-orbit coupling,” *Nat Mater*, vol. 14, no. 9, pp. 871-82, Sep, 2015.
- [89] X. Xu, W. Yao, D. Xiao, and T. F. Heinz, “Spin and pseudospins in layered transition metal dichalcogenides,” *Nature Physics*, vol. 10, no. 5, pp. 343-350, 2014.

- [90] D. Xiao, G. B. Liu, W. Feng, X. Xu, and W. Yao, “Coupled spin and valley physics in monolayers of MoS₂ and other group-VI dichalcogenides,” *Phys Rev Lett*, vol. 108, no. 19, pp. 196802, May 11, 2012.
- [91] W. Feng, Y. Yao, W. Zhu, J. Zhou, W. Yao, and D. Xiao, “Intrinsic spin Hall effect in monolayers of group-VI dichalcogenides: A first-principles study,” *Physical Review B*, vol. 86, no. 16, 2012.
- [92] W. Zhang, J. Sklenar, B. Hsu, W. Jiang, M. B. Jungfleisch, J. Xiao, F. Y. Fradin, Y. Liu, J. E. Pearson, J. B. Ketterson, Z. Yang, and A. Hoffmann, “Research Update: Spin transfer torques in permalloy on monolayer MoS₂,” *APL Materials*, vol. 4, no. 3, pp. 032302, 2016.
- [93] J. K. Huang, J. Pu, C. L. Hsu, M. H. Chiu, Z. Y. Juang, Y. H. Chang, W. H. Chang, Y. Iwasa, T. Takenobu, and L. J. Li, “Large-area synthesis of highly crystalline WSe₂ monolayers and device applications,” *ACS Nano*, vol. 8, no. 1, pp. 923-30, Jan 28, 2014.
- [94] M. Y. Li, Y. Shi, C. C. Cheng, L. S. Lu, Y. C. Lin, H. L. Tang, M. L. Tsai, C. W. Chu, K. H. Wei, J. H. He, W. H. Chang, K. Suenaga, and L. J. Li, “NANO-ELECTRONICS. Epitaxial growth of a monolayer WSe₂-MoS₂ lateral p-n junction with an atomically sharp interface,” *Science*, vol. 349, no. 6247, pp. 524-8, Jul 31, 2015.
- [95] X. Fan, J. Wu, Y. Chen, M. J. Jerry, H. Zhang, and J. Q. Xiao, “Observation of the nonlocal spin-orbital effective field,” *Nat Commun*, vol. 4, pp. 1799, 2013.
- [96] J. C. Sanchez, L. Vila, G. Desfonds, S. Gambarelli, J. P. Attane, J. M. De Teresa, C. Magen, and A. Fert, “Spin-to-charge conversion using Rashba coupling at the interface between non-magnetic materials,” *Nat Commun*, vol. 4, pp. 2944, 2013.
- [97] K. Lee, W. S. Yun, and J. D. Lee, “Giant Rashba-type splitting in molybdenum-driven bands of MoS₂/Bi(111) heterostructure,” *Physical Review B*, vol. 91, no. 12, 2015.
- [98] A. Kalitsov, S. A. Nikolaev, J. Velez, M. Chshiev, and O. Mryasov, “Intrinsic spin orbit torque in a single domain nanomagnet,” *arXiv:1604.07885 [cond-mat.mes-hall]*, 2016.
- [99] S. Shimizu, K. S. Takahashi, T. Hatano, M. Kawasaki, Y. Tokura, and Y. Iwasa, “Electrically tunable anomalous Hall effect in Pt thin films,” *Phys Rev Lett*, vol. 111, no. 21, pp. 216803, Nov 22, 2013.
- [100] K. F. Mak, K. He, J. Shan, and T. F. Heinz, “Control of valley polarization in monolayer MoS₂ by optical helicity,” *Nat Nanotechnol*, vol. 7, no. 8, pp. 494-8, Aug, 2012.

- [101] C. Cheng, J.-C. R. Sánchez, M. Collet, V. Ivanovskaya, B. Dlubak, P. Seneor, A. Fert, H. Kim, G. H. Han, Y. H. Lee, H. Yang, and A. Anane, “Direct observation of spin-to-charge conversion in MoS₂ monolayer with spin pumping,” *arXiv:1510.03451 [cond-mat.mes-hall]*, 2015.
- [102] M. H. Nguyen, D. C. Ralph, and R. A. Buhrman, “Spin Torque Study of the Spin Hall Conductivity and Spin Diffusion Length in Platinum Thin Films with Varying Resistivity,” *Phys Rev Lett*, vol. 116, no. 12, pp. 126601, Mar 25, 2016.
- [103] A. Nomura, T. Tashiro, H. Nakayama, and K. Ando, “Temperature dependence of inverse Rashba-Edelstein effect at metallic interface,” *Applied Physics Letters*, vol. 106, no. 21, pp. 212403, 2015.
- [104] K. S. Novoselov, A. Mishchenko, A. Carvalho, and A. H. Castro Neto, “2D materials and van der Waals heterostructures,” *Science*, vol. 353, no. 6298, pp. aac9439-aac9439, 2016.
- [105] J. Finley, and L. Liu, “Spin-Orbit-Torque Efficiency in Compensated Ferrimagnetic Cobalt-Terbium Alloys,” *Physical Review Applied*, vol. 6, no. 5, 2016.
- [106] M. Liu, J. Zhang, C. Z. Chang, Z. Zhang, X. Feng, K. Li, K. He, L. L. Wang, X. Chen, X. Dai, Z. Fang, Q. K. Xue, X. Ma, and Y. Wang, “Crossover between weak antilocalization and weak localization in a magnetically doped topological insulator,” *Phys Rev Lett*, vol. 108, no. 3, pp. 036805, Jan 20, 2012.
- [107] D. Wu, G. Yu, Q. Shao, X. Li, H. Wu, K. L. Wong, Z. Zhang, X. Han, P. Khalili Amiri, and K. L. Wang, “In-plane current-driven spin-orbit torque switching in perpendicularly magnetized films with enhanced thermal tolerance,” *Applied Physics Letters*, vol. 108, no. 21, pp. 212406, 2016.
- [108] M.-Z. Wu, and A. Hoffmann, *Recent advances in magnetic insulators—from spintronics to microwave applications*: Academic Press, 2013.
- [109] Y. Kajiwara, K. Harii, S. Takahashi, J. Ohe, K. Uchida, M. Mizuguchi, H. Umezawa, H. Kawai, K. Ando, K. Takanashi, S. Maekawa, and E. Saitoh, “Transmission of electrical signals by spin-wave interconversion in a magnetic insulator,” *Nature*, vol. 464, no. 7286, pp. 262-6, Mar 11, 2010.
- [110] L. J. Cornelissen, J. Liu, R. A. Duine, J. B. Youssef, and B. J. van Wees, “Long-distance transport of magnon spin information in a magnetic insulator at room temperature,” *Nature Physics*, vol. 11, no. 12, pp. 1022-1026, 2015.

- [111] J. Tang, Q. Shao, P. Upadhyaya, P. K. Amiri, and K. L. Wang, “Electric Control of Magnetic Devices for Spintronic Computing,” pp. 53-112, 2015.
- [112] A. Khitun, M. Bao, and K. L. Wang, “Magnonic logic circuits,” *Journal of Physics D: Applied Physics*, vol. 43, no. 26, pp. 264005, 2010.
- [113] K. J. Kim, S. K. Kim, Y. Hirata, S. H. Oh, T. Tono, D. H. Kim, T. Okuno, W. S. Ham, S. Kim, G. Go, Y. Tserkovnyak, A. Tsukamoto, T. Moriyama, K. J. Lee, and T. Ono, “Fast domain wall motion in the vicinity of the angular momentum compensation temperature of ferrimagnets,” *Nat Mater*, vol. 16, no. 12, pp. 1187-1192, Dec, 2017.
- [114] C. D. Stanciu, A. V. Kimel, F. Hansteen, A. Tsukamoto, A. Itoh, A. Kirilyuk, and T. Rasing, “Ultrafast spin dynamics across compensation points in ferrimagnetic GdFeCo: The role of angular momentum compensation,” *Physical Review B*, vol. 73, no. 22, 2006.
- [115] P. Li, T. Liu, H. Chang, A. Kalitsov, W. Zhang, G. Csaba, W. Li, D. Richardson, A. DeMann, G. Rimal, H. Dey, J. S. Jiang, W. Porod, S. B. Field, J. Tang, M. C. Marconi, A. Hoffmann, O. Mryasov, and M. Wu, “Spin-orbit torque-assisted switching in magnetic insulator thin films with perpendicular magnetic anisotropy,” *Nat Commun*, vol. 7, pp. 12688, Sep 01, 2016.
- [116] S. Iida, “Magnetostriction Constants of Rare Earth Iron Garnets,” *Journal of the Physical Society of Japan*, vol. 22, no. 5, pp. 1201-1209, 1967.
- [117] C. Tang, P. Sellappan, Y. Liu, Y. Xu, J. E. Garay, and J. Shi, “Anomalous Hall hysteresis in Tm₃Fe₅O₁₂/Pt with strain-induced perpendicular magnetic anisotropy,” *Physical Review B*, vol. 94, no. 14, pp. 140403(R), 2016.
- [118] C. Tang, C. Z. Chang, G. Zhao, Y. Liu, Z. Jiang, C. X. Liu, M. R. McCartney, D. J. Smith, T. Chen, J. S. Moodera, and J. Shi, “Above 400-K robust perpendicular ferromagnetic phase in a topological insulator,” *Sci Adv*, vol. 3, no. 6, pp. e1700307, Jun, 2017.
- [119] Q. Shao, C. Tang, G. Yu, A. Navabi, H. Wu, C. He, J. Li, P. Upadhyaya, P. Zhang, S. A. Razavi, Q. L. He, Y. Liu, P. Yang, S. K. Kim, C. Zheng, Y. Liu, L. Pan, R. K. Lake, X. Han, Y. Tserkovnyak, J. Shi, and K. L. Wang, “Role of dimensional crossover on spin-orbit torque efficiency in magnetic insulator thin films,” *Nat Commun*, vol. 9, no. 1, pp. 3612, Sep 6, 2018.

- [120] Qiming Shao, Alexander Grutter, Yawen Liu, Guoqiang Yu, Chao-Yao Yang, Dustin A. Gilbert, Elke Arenholz, Padraic Shafer, Xiaoyu Che, Chi Tang, Mohammed Aldosary, Aryan Navabi, Qing Lin He, Brian J. Kirby, Jing Shi, and K. L. Wang, “Exploring interfacial exchange coupling and sublattice effect in heavy metal/ferrimagnetic insulator heterostructures using Hall measurements, x-ray magnetic circular dichroism, and neutron reflectometry,” *Physical Review B*, vol. 00, pp. 004400, 2019.
- [121] V. H. Ortiz, M. Aldosary, J. Li, Y. Xu, M. I. Lohmann, P. Sellappan, Y. Kodera, J. E. Garay, and J. Shi, “Systematic control of strain-induced perpendicular magnetic anisotropy in epitaxial europium and terbium iron garnet thin films,” *APL Materials*, vol. 6, no. 12, pp. 121113, 2018.
- [122] G. E. Bauer, E. Saitoh, and B. J. van Wees, “Spin caloritronics,” *Nat Mater*, vol. 11, no. 5, pp. 391-9, May, 2012.
- [123] K. Uchida, S. Takahashi, K. Harii, J. Ieda, W. Koshibae, K. Ando, S. Maekawa, and E. Saitoh, “Observation of the spin Seebeck effect,” *Nature*, vol. 455, no. 7214, pp. 778-81, Oct 09, 2008.
- [124] X. Qiu, K. Narayanapillai, Y. Wu, P. Deorani, D. H. Yang, W. S. Noh, J. H. Park, K. J. Lee, H. W. Lee, and H. Yang, “Spin-orbit-torque engineering via oxygen manipulation,” *Nat Nanotechnol*, vol. 10, no. 4, pp. 333-8, May, 2015.
- [125] L. Liu, O. J. Lee, T. J. Gudmundsen, D. C. Ralph, and R. A. Buhrman, “Current-induced switching of perpendicularly magnetized magnetic layers using spin torque from the spin Hall effect,” *Phys Rev Lett*, vol. 109, no. 9, pp. 096602, Aug 31, 2012.
- [126] H. Nakayama, M. Althammer, Y. T. Chen, K. Uchida, Y. Kajiwara, D. Kikuchi, T. Ohtani, S. Geprags, M. Opel, S. Takahashi, R. Gross, G. E. Bauer, S. T. Goennenwein, and E. Saitoh, “Spin Hall magnetoresistance induced by a nonequilibrium proximity effect,” *Phys Rev Lett*, vol. 110, no. 20, pp. 206601, May 17, 2013.
- [127] Y.-T. Chen, S. Takahashi, H. Nakayama, M. Althammer, S. T. B. Goennenwein, E. Saitoh, and G. E. W. Bauer, “Theory of spin Hall magnetoresistance,” *Physical Review B*, vol. 87, no. 14, pp. 144411, 2013.
- [128] C. Hahn, G. de Loubens, O. Klein, M. Viret, V. V. Naletov, and J. Ben Youssef, “Comparative measurements of inverse spin Hall effects and magnetoresistance in YIG/Pt and YIG/Ta,” *Physical Review B*, vol. 87, no. 17, pp. 174417, 2013.

- [129] W. Zhang, W. Han, X. Jiang, S.-H. Yang, and S. S. P. Parkin, “Role of transparency of platinum–ferromagnet interfaces in determining the intrinsic magnitude of the spin Hall effect,” *Nature Physics*, vol. 11, no. 6, pp. 496-502, 2015.
- [130] C.-F. Pai, Y. Ou, L. H. Vilela-Leão, D. C. Ralph, and R. A. Buhrman, “Dependence of the efficiency of spin Hall torque on the transparency of Pt/ferromagnetic layer interfaces,” *Physical Review B*, vol. 92, no. 6, pp. 064426, 2015.
- [131] A. Paoletti, *Physics of Magnetic Garnets*: North-Holland Publishing Company, 1978.
- [132] R. Zhang, and R. F. Willis, “Thickness-dependent Curie temperatures of ultrathin magnetic films: effect of the range of spin-spin interactions,” *Phys Rev Lett*, vol. 86, no. 12, pp. 2665-8, Mar 19, 2001.
- [133] F. Huang, M. T. Kief, G. J. Mankey, and R. F. Willis, “Magnetism in the few-monolayers limit: A surface magneto-optic Kerr-effect study of the magnetic behavior of ultrathin films of Co, Ni, and Co-Ni alloys on Cu(100) and Cu(111),” *Physical Review B*, vol. 49, no. 6, pp. 3962-3971, 1994.
- [134] C. A. F. Vaz, J. A. C. Bland, and G. Lauhoff, “Magnetism in ultrathin film structures,” *Reports on Progress in Physics*, vol. 71, no. 5, pp. 056501, 2008.
- [135] Y. Li, and K. Baberschke, “Dimensional crossover in ultrathin Ni(111) films on W(110),” *Phys Rev Lett*, vol. 68, no. 8, pp. 1208-1211, Feb 24, 1992.
- [136] K.-i. Uchida, H. Adachi, T. Ota, H. Nakayama, S. Maekawa, and E. Saitoh, “Observation of longitudinal spin-Seebeck effect in magnetic insulators,” *Applied Physics Letters*, vol. 97, no. 17, pp. 172505, 2010.
- [137] A. Ghosh, S. Auffret, U. Ebels, and W. E. Bailey, “Penetration depth of transverse spin current in ultrathin ferromagnets,” *Phys Rev Lett*, vol. 109, no. 12, pp. 127202, Sep 21, 2012.
- [138] X. Qiu, W. Legrand, P. He, Y. Wu, J. Yu, R. Ramaswamy, A. Manchon, and H. Yang, “Enhanced Spin-Orbit Torque via Modulation of Spin Current Absorption,” *Phys Rev Lett*, vol. 117, no. 21, pp. 217206, Nov 18, 2016.
- [139] Y. Ou, C.-F. Pai, S. Shi, D. C. Ralph, and R. A. Buhrman, “Origin of fieldlike spin-orbit torques in heavy metal/ferromagnet/oxide thin film heterostructures,” *Physical Review B*, vol. 94, no. 14, pp. 140414(R), 2016.

- [140] S. A. Bender, and Y. Tserkovnyak, “Interfacial spin and heat transfer between metals and magnetic insulators,” *Physical Review B*, vol. 91, no. 14, pp. 140402(R), 2015.
- [141] Y. Ohnuma, H. Adachi, E. Saitoh, and S. Maekawa, “Enhanced dc spin pumping into a fluctuating ferromagnet near TC,” *Physical Review B*, vol. 89, no. 17, pp. 174417, 2014.
- [142] X. Jia, K. Liu, K. Xia, and G. E. W. Bauer, “Spin transfer torque on magnetic insulators,” *EPL (Europhysics Letters)*, vol. 96, no. 1, pp. 17005, 2011.
- [143] M. Farle, “Ferromagnetic resonance of ultrathin metallic layers,” *Reports on Progress in Physics*, vol. 61, no. 7, pp. 755-826, 1998.
- [144] C. Du, H. Wang, F. Yang, and P. C. Hammel, “Enhancement of Pure Spin Currents in Spin Pumping Y₃Fe₅O₁₂/Cu/Metal Trilayers through Spin Conductance Matching,” *Physical Review Applied*, vol. 1, no. 4, pp. 044004, 2014.
- [145] M. B. Jungfleisch, V. Lauer, R. Neb, A. V. Chumak, and B. Hillebrands, “Improvement of the yttrium iron garnet/platinum interface for spin pumping-based applications,” *Applied Physics Letters*, vol. 103, no. 2, pp. 022411, 2013.
- [146] J. Kim, P. Sheng, S. Takahashi, S. Mitani, and M. Hayashi, “Spin Hall Magnetoresistance in Metallic Bilayers,” *Phys Rev Lett*, vol. 116, no. 9, pp. 097201, Mar 04, 2016.
- [147] O. J. Lee, L. Q. Liu, C. F. Pai, Y. Li, H. W. Tseng, P. G. Gowtham, J. P. Park, D. C. Ralph, and R. A. Buhrman, “Central role of domain wall depinning for perpendicular magnetization switching driven by spin torque from the spin Hall effect,” *Physical Review B*, vol. 89, no. 2, pp. 024418, 2014.
- [148] B. D. Josephson, “Possible new effects in superconductive tunnelling,” *Physics Letters*, vol. 1, no. 7, pp. 251-253, 1962.
- [149] F. Wilhelm, P. Pouloupoulos, H. Wende, A. Scherz, K. Baberschke, M. Angelakeris, N. K. Flevaris, and A. Rogalev, “Systematics of the induced magnetic moments in 5d layers and the violation of the third Hund's rule,” *Phys Rev Lett*, vol. 87, no. 20, pp. 207202, Nov 12, 2001.
- [150] S. Meyer, R. Schlitz, S. Geprägs, M. Opel, H. Huebl, R. Gross, and S. T. B. Goennenwein, “Anomalous Hall effect in YIG|Pt bilayers,” *Applied Physics Letters*, vol. 106, no. 13, pp. 132402, 2015.

- [151] X. Zhou, L. Ma, Z. Shi, G. Y. Guo, J. Hu, R. Q. Wu, and S. M. Zhou, “Tuning magnetotransport in PdPt/Y₃Fe₅O₁₂: Effects of magnetic proximity and spin-orbit coupling,” *Applied Physics Letters*, vol. 105, no. 1, pp. 012408, 2014.
- [152] X. Zhou, L. Ma, Z. Shi, W. J. Fan, J.-G. Zheng, R. F. L. Evans, and S. M. Zhou, “Magnetotransport in metal/insulating-ferromagnet heterostructures: Spin Hall magnetoresistance or magnetic proximity effect,” *Physical Review B*, vol. 92, no. 6, 2015.
- [153] S. Y. Huang, X. Fan, D. Qu, Y. P. Chen, W. G. Wang, J. Wu, T. Y. Chen, J. Q. Xiao, and C. L. Chien, “Transport Magnetic Proximity Effects in Platinum,” *Physical Review Letters*, vol. 109, no. 10, 2012.
- [154] T. Lin, C. Tang, H. M. Alyahyaei, and J. Shi, “Experimental investigation of the nature of the magnetoresistance effects in Pd-YIG hybrid structures,” *Phys Rev Lett*, vol. 113, no. 3, pp. 037203, Jul 18, 2014.
- [155] Q. Shao, A. Grutter, Y. Liu, G. Yu, C.-Y. Yang, D. A. Gilbert, E. Arenholz, P. Shafer, X. Che, C. Tang, M. Aldosary, A. Navabi, Q. L. He, B. J. Kirby, J. Shi, and K. L. Wang, “Exploring interfacial exchange coupling and sublattice effect in heavy metal/ferrimagnetic insulator heterostructures using Hall measurements, x-ray magnetic circular dichroism, and neutron reflectometry,” *Physical Review B*, vol. 99, no. 10, 2019.
- [156] S. Geprags, A. Kehlberger, F. Della Coletta, Z. Qiu, E. J. Guo, T. Schulz, C. Mix, S. Meyer, A. Kamra, M. Althammer, H. Huebl, G. Jakob, Y. Ohnuma, H. Adachi, J. Barker, S. Maekawa, G. E. Bauer, E. Saitoh, R. Gross, S. T. Goennenwein, and M. Klaui, “Origin of the spin Seebeck effect in compensated ferrimagnets,” *Nat Commun*, vol. 7, pp. 10452, Feb 04, 2016.
- [157] K. Ganzhorn, J. Barker, R. Schlitz, B. A. Piot, K. Ollefs, F. Guillou, F. Wilhelm, A. Rogalev, M. Opel, M. Althammer, S. Geprägs, H. Huebl, R. Gross, G. E. W. Bauer, and S. T. B. Goennenwein, “Spin Hall magnetoresistance in a canted ferrimagnet,” *Physical Review B*, vol. 94, no. 9, 2016.
- [158] Z. Wang, C. Tang, R. Sachs, Y. Barlas, and J. Shi, “Proximity-induced ferromagnetism in graphene revealed by the anomalous Hall effect,” *Phys Rev Lett*, vol. 114, no. 1, pp. 016603, Jan 9, 2015.

- [159] K.-i. Uchida, T. Kikkawa, A. Miura, J. Shiomi, and E. Saitoh, “Quantitative Temperature Dependence of Longitudinal Spin Seebeck Effect at High Temperatures,” *Physical Review X*, vol. 4, no. 4, 2014.
- [160] W. Zhang, M. B. Jungfleisch, W. Jiang, Y. Liu, J. E. Pearson, S. G. E. t. Velthuis, A. Hoffmann, F. Freimuth, and Y. Mokrousov, “Reduced spin-Hall effects from magnetic proximity,” *Physical Review B*, vol. 91, no. 11, 2015.
- [161] G. Y. Guo, Q. Niu, and N. Nagaosa, “Anomalous Nernst and Hall effects in magnetized platinum and palladium,” *Physical Review B*, vol. 89, no. 21, Jun 9, 2014.
- [162] A. Quindeau, C. O. Avci, W. Liu, C. Sun, M. Mann, A. S. Tang, M. C. Onbasli, D. Bono, P. M. Voyles, Y. Xu, J. Robinson, G. S. D. Beach, and C. A. Ross, “Tm₃Fe₅O₁₂/Pt Heterostructures with Perpendicular Magnetic Anisotropy for Spintronic Applications,” *Advanced Electronic Materials*, vol. 3, no. 1, pp. 1600376, 2017.
- [163] S. Geller, J. P. Remeika, R. C. Sherwood, H. J. Williams, and G. P. Espinosa, “Magnetic Study of the Heavier Rare-Earth Iron Garnets,” *Physical Review*, vol. 137, no. 3A, pp. A1034-A1038, 1965.
- [164] W. Amamou, I. V. Pinchuk, A. H. Trout, R. E. A. Williams, N. Antolin, A. Goad, D. J. O'Hara, A. S. Ahmed, W. Windl, D. W. McComb, and R. K. Kawakami, “Magnetic proximity effect in Pt/CoFe₂O₄ bilayers,” *Physical Review Materials*, vol. 2, no. 1, Jan 12, 2018.
- [165] Y. M. Lu, Y. Choi, C. M. Ortega, X. M. Cheng, J. W. Cai, S. Y. Huang, L. Sun, and C. L. Chien, “Pt magnetic polarization on Y₃Fe₅O₁₂ and magnetotransport characteristics,” *Phys Rev Lett*, vol. 110, no. 14, pp. 147207, Apr 05, 2013.
- [166] R. Tyer, G. van der Laan, W. M. Temmerman, Z. Szotek, and H. Ebert, “Systematic theoretical study of the spin and orbital magnetic moments of 4d and 5d interfaces with Fe films,” *Physical Review B*, vol. 67, no. 10, 2003.
- [167] J. Vogel, A. Fontaine, V. Cros, F. Petroff, J.-P. Kappler, G. Krill, A. Rogalev, and J. Goulon, “Structure and magnetism of Pd in Pd/Fe multilayers studied by x-ray magnetic circular dichroism at the Pd L_{2,3} edges,” *Physical Review B*, vol. 55, no. 6, pp. 3663-3669, 1997.

- [168] Y. K. Liu, H. F. Wong, K. K. Lam, K. H. Chan, C. L. Mak, and C. W. Leung, “Anomalous Hall effect in Pt/Tb₃Fe₅O₁₂ heterostructure: Effect of compensation point,” *Journal of Magnetism and Magnetic Materials*, vol. 468, pp. 235-240, 2018.
- [169] E. R. Rosenberg, L. Beran, C. O. Avci, C. Zeledon, B. Song, C. Gonzalez-Fuentes, J. Mendil, P. Gambardella, M. Veis, C. Garcia, G. S. D. Beach, and C. A. Ross, “Magnetism and spin transport in rare-earth-rich epitaxial terbium and europium iron garnet films,” *Physical Review Materials*, vol. 2, no. 9, 2018.
- [170] B. J. Kirby, P. A. Kienzle, B. B. Maranville, N. F. Berk, J. Krycka, F. Heinrich, and C. F. Majkrzak, “Phase-sensitive specular neutron reflectometry for imaging the nanometer scale composition depth profile of thin-film materials,” *Current Opinion in Colloid & Interface Science*, vol. 17, no. 1, pp. 44-53, 2012.
- [171] S. Muhlbauer, B. Binz, F. Jonietz, C. Pfleiderer, A. Rosch, A. Neubauer, R. Georgii, and P. Boni, “Skyrmion lattice in a chiral magnet,” *Science*, vol. 323, no. 5916, pp. 915-9, Feb 13, 2009.
- [172] F. Jonietz, S. Muhlbauer, C. Pfleiderer, A. Neubauer, W. Munzer, A. Bauer, T. Adams, R. Georgii, P. Boni, R. A. Duine, K. Everschor, M. Garst, and A. Rosch, “Spin transfer torques in MnSi at ultralow current densities,” *Science*, vol. 330, no. 6011, pp. 1648-51, Dec 17, 2010.
- [173] S. Heinze, K. von Bergmann, M. Menzel, J. Brede, A. Kubetzka, R. Wiesendanger, G. Bihlmayer, and S. Blügel, “Spontaneous atomic-scale magnetic skyrmion lattice in two dimensions,” *Nature Physics*, vol. 7, no. 9, pp. 713-718, 2011.
- [174] N. Nagaosa, and Y. Tokura, “Topological properties and dynamics of magnetic skyrmions,” *Nat Nanotechnol*, vol. 8, no. 12, pp. 899-911, Dec, 2013.
- [175] W. Jiang, P. Upadhyaya, W. Zhang, G. Yu, M. B. Jungfleisch, F. Y. Fradin, J. E. Pearson, Y. Tserkovnyak, K. L. Wang, O. Heinonen, S. G. te Velthuis, and A. Hoffmann, “Magnetism. Blowing magnetic skyrmion bubbles,” *Science*, vol. 349, no. 6245, pp. 283-6, Jul 17, 2015.
- [176] S. Woo, K. Litzius, B. Krüger, M.-Y. Im, L. Caretta, K. Richter, M. Mann, A. Krone, R. M. Reeve, M. Weigand, P. Agrawal, I. Lemesh, M.-A. Mawass, P. Fischer, M. Kläui, and G. S. D. Beach, “Observation of room-temperature magnetic skyrmions and their current-driven dynamics in ultrathin metallic ferromagnets,” *Nature Materials*, 2016.

- [177] C. Moreau-Luchaire, S. C. Mouta, N. Reyren, J. Sampaio, C. A. Vaz, N. Van Horne, K. Bouzehouane, K. Garcia, C. Deranlot, P. Warnicke, P. Wohlhuter, J. M. George, M. Weigand, J. Raabe, V. Cros, and A. Fert, “Additive interfacial chiral interaction in multilayers for stabilization of small individual skyrmions at room temperature,” *Nat Nanotechnol*, Jan 18, 2016.
- [178] G. Yu, P. Upadhyaya, X. Li, W. Li, S. K. Kim, Y. Fan, K. L. Wong, Y. Tserkovnyak, P. K. Amiri, and K. L. Wang, “Room-Temperature Creation and Spin-Orbit Torque Manipulation of Skyrmions in Thin Films with Engineered Asymmetry,” *Nano Lett*, vol. 16, no. 3, pp. 1981-8, Mar 9, 2016.
- [179] C. Schütte, and M. Garst, “Magnon-skyrmion scattering in chiral magnets,” *Physical Review B*, vol. 90, no. 9, 2014.
- [180] S. Seki, X. Z. Yu, S. Ishiwata, and Y. Tokura, “Observation of skyrmions in a multiferroic material,” *Science*, vol. 336, no. 6078, pp. 198-201, Apr 13, 2012.
- [181] A. P. Malozemoff, and J. C. Slonczewski, *Magnetic Domain Walls in Bubble Materials*: Academic Press, 1979.
- [182] P. Upadhyaya, G. Yu, P. K. Amiri, and K. L. Wang, “Electric-field guiding of magnetic skyrmions,” *Physical Review B*, vol. 92, no. 13, 2015.
- [183] A. Neubauer, C. Pfleiderer, B. Binz, A. Rosch, R. Ritz, P. G. Niklowitz, and P. Boni, “Topological Hall effect in the A phase of MnSi,” *Phys Rev Lett*, vol. 102, no. 18, pp. 186602, May 08, 2009.
- [184] J. Zang, M. Mostovoy, J. H. Han, and N. Nagaosa, “Dynamics of Skyrmion crystals in metallic thin films,” *Phys Rev Lett*, vol. 107, no. 13, pp. 136804, Sep 23, 2011.
- [185] K. Nakata, J. Klinovaja, and D. Loss, “Magnonic quantum Hall effect and Wiedemann-Franz law,” *Physical Review B*, vol. 95, no. 12, 2017.
- [186] H. Ochoa, S. K. Kim, and Y. Tserkovnyak, “Topological spin-transfer drag driven by skyrmion diffusion,” *Physical Review B*, vol. 94, no. 2, 2016.
- [187] L. Kong, and J. Zang, “Dynamics of an insulating Skyrmion under a temperature gradient,” *Phys Rev Lett*, vol. 111, no. 6, pp. 067203, Aug 09, 2013.
- [188] Y. Onose, Y. Okamura, S. Seki, S. Ishiwata, and Y. Tokura, “Observation of magnetic excitations of Skyrmion crystal in a helimagnetic insulator Cu₂OSeO₃,” *Phys Rev Lett*, vol. 109, no. 3, pp. 037603, Jul 20, 2012.

- [189] M. Mochizuki, X. Z. Yu, S. Seki, N. Kanazawa, W. Koshibae, J. Zang, M. Mostovoy, Y. Tokura, and N. Nagaosa, “Thermally driven ratchet motion of a skyrmion microcrystal and topological magnon Hall effect,” *Nat Mater*, vol. 13, no. 3, pp. 241-6, Mar, 2014.
- [190] S. Pollath, J. Wild, L. Heinen, T. N. G. Meier, M. Kronseder, L. Tutsch, A. Bauer, H. Berger, C. Pfliederer, J. Zweck, A. Rosch, and C. H. Back, “Dynamical Defects in Rotating Magnetic Skyrmion Lattices,” *Phys Rev Lett*, vol. 118, no. 20, pp. 207205, May 19, 2017.
- [191] X. Yu, M. Mostovoy, Y. Tokunaga, W. Zhang, K. Kimoto, Y. Matsui, Y. Kaneko, N. Nagaosa, and Y. Tokura, “Magnetic stripes and skyrmions with helicity reversals,” *Proc Natl Acad Sci U S A*, vol. 109, no. 23, pp. 8856-60, Jun 05, 2012.
- [192] S. Banerjee, J. Rowland, O. Erten, and M. Randeria, “Enhanced Stability of Skyrmions in Two-Dimensional Chiral Magnets with Rashba Spin-Orbit Coupling,” *Physical Review X*, vol. 4, no. 3, 2014.
- [193] A. Bogdanov, and A. Hubert, “Thermodynamically stable magnetic vortex states in magnetic crystals,” *Journal of Magnetism and Magnetic Materials*, vol. 138, no. 3, pp. 255-269, 1994.
- [194] M. Raju, A. Yagil, Anjan Soumyanarayanan, Anthony K. C. Tan, A. Almoalem, O. M. Auslaender, and C. Panagopoulos, “Chiral magnetic textures in Ir/Fe/Co/Pt multilayers: Evolution and topological Hall signature,” *arXiv:1708.04084 [cond-mat.mes-hall]*, 2017.
- [195] A. Soumyanarayanan, M. Raju, A. L. Gonzalez Oyarce, A. K. C. Tan, M.-Y. Im, A. P. Petrović, P. Ho, K. H. Khoo, M. Tran, C. K. Gan, F. Ernult, and C. Panagopoulos, “Tunable room-temperature magnetic skyrmions in Ir/Fe/Co/Pt multilayers,” *Nature Materials*, 2017.
- [196] D. Maccariello, W. Legrand, N. Reyren, K. Garcia, K. Bouzehouane, S. Collin, V. Cros, and A. Fert, “Electrical detection of single magnetic skyrmions in metallic multilayers at room temperature,” *Nat Nanotechnol*, vol. 13, no. 3, pp. 233-237, Mar, 2018.
- [197] K. Zeissler, S. Finizio, K. Shahbazi, J. Massey, F. A. Ma'Mari, D. M. Bracher, A. Kleibert, M. C. Rosamond, E. H. Linfield, T. A. Moore, J. Raabe, G. Burnell, and C. H. Marrows, “Discrete Hall resistivity contribution from Neel skyrmions in multilayer nanodiscs,” *Nat Nanotechnol*, vol. 13, no. 12, pp. 1161-1166, Dec, 2018.

- [198] K. S. Denisov, I. V. Rozhansky, N. S. Averkiev, and E. Lähderanta, “General theory of the topological Hall effect in systems with chiral spin textures,” *Physical Review B*, vol. 98, no. 19, 2018.
- [199] P. B. Ndiaye, C. A. Akosa, and A. Manchon, “Topological Hall and spin Hall effects in disordered skyrmionic textures,” *Physical Review B*, vol. 95, no. 6, 2017.
- [200] O. Boulle, J. Vogel, H. Yang, S. Pizzini, D. de Souza Chaves, A. Locatelli, T. O. Mendes, A. Sala, L. D. Buda-Prejbeanu, O. Klein, M. Belmeguenai, Y. Roussigne, A. Stashkevich, S. M. Cherif, L. Aballe, M. Foerster, M. Chshiev, S. Auffret, I. M. Miron, and G. Gaudin, “Room-temperature chiral magnetic skyrmions in ultrathin magnetic nanostructures,” *Nat Nanotechnol*, vol. 11, no. 5, pp. 449-54, May, 2016.
- [201] K. Yasuda, R. Wakatsuki, T. Morimoto, R. Yoshimi, A. Tsukazaki, K. S. Takahashi, M. Ezawa, M. Kawasaki, N. Nagaosa, and Y. Tokura, “Geometric Hall effects in topological insulator heterostructures,” *Nature Physics*, 2016.
- [202] J. Matsuno, N. Ogawa, K. Yasuda, F. Kagawa, W. Koshihara, N. Nagaosa, Y. Tokura, and M. Kawasaki, “Interface-driven topological Hall effect in SrRuO₃-SrIrO₃ bilayer,” *Sci Adv*, vol. 2, no. 7, pp. e1600304, Jul, 2016.
- [203] J. Cho, N. H. Kim, S. Lee, J. S. Kim, R. Lavrijsen, A. Solignac, Y. Yin, D. S. Han, N. J. van Hoof, H. J. Swagten, B. Koopmans, and C. Y. You, “Thickness dependence of the interfacial Dzyaloshinskii-Moriya interaction in inversion symmetry broken systems,” *Nat Commun*, vol. 6, pp. 7635, Jul 08, 2015.
- [204] T. Suzuki, R. Chisnell, A. Devarakonda, Y.-T. Liu, W. Feng, D. Xiao, J. W. Lynn, and J. G. Checkelsky, “Large anomalous Hall effect in a half-Heusler antiferromagnet,” *Nature Physics*, vol. 12, pp. 1119-1123, 2016.
- [205] K. S. Takahashi, H. Ishizuka, T. Murata, Q. Y. Wang, Y. Tokura, N. Nagaosa, and M. Kawasaki, “Anomalous Hall effect derived from multiple Weyl nodes in high-mobility EuTiO₃ films,” *Sci Adv*, vol. 4, no. 7, pp. eaar7880, Jul, 2018.
- [206] Y. Taguchi, Y. Oohara, H. Yoshizawa, N. Nagaosa, and Y. Tokura, “Spin chirality, Berry phase, and anomalous Hall effect in a frustrated ferromagnet,” *Science*, vol. 291, no. 5513, pp. 2573-6, Mar 30, 2001.
- [207] W. Jiang, G. Chen, K. Liu, J. Zang, S. G. E. te Velthuis, and A. Hoffmann, “Skyrmions in magnetic multilayers,” *Physics Reports*, vol. 704, pp. 1-49, 2017.

- [208] W. Jiang, X. Zhang, G. Yu, W. Zhang, X. Wang, M. Benjamin Jungfleisch, John E. Pearson, X. Cheng, O. Heinonen, K. L. Wang, Y. Zhou, A. Hoffmann, and Suzanne G. E. te Velthuis, "Direct observation of the skyrmion Hall effect," *Nature Physics*, vol. 13, no. 2, pp. 162-169, 2016.
- [209] G. Yu, A. Jenkins, X. Ma, S. A. Razavi, C. He, G. Yin, Q. Shao, Q. L. He, H. Wu, W. Li, W. Jiang, X. Han, X. Li, A. C. Bleszynski Jayich, P. K. Amiri, and K. L. Wang, "Room-Temperature Skyrmions in an Antiferromagnet-Based Heterostructure," *Nano Lett*, vol. 18, no. 2, pp. 980-986, Feb 14, 2018.
- [210] K. L. Wang, X. Kou, P. Upadhyaya, Y. Fan, Q. Shao, G. Yu, and P. K. Amiri, "Electric-Field Control of Spin-Orbit Interaction for Low-Power Spintronics," *Proceedings of the IEEE*, vol. 104, no. 10, pp. 1974-2008, 2016.
- [211] J. Z. Sun, "Spin-current interaction with a monodomain magnetic body: A model study," *Physical Review B*, vol. 62, no. 1, pp. 570-578, Jul 1, 2000.
- [212] J. A. Katine, and E. E. Fullerton, "Device implications of spin-transfer torques," *Journal of Magnetism and Magnetic Materials*, vol. 320, no. 7, pp. 1217-1226, Apr, 2008.
- [213] S. Ikeda, K. Miura, H. Yamamoto, K. Mizunuma, H. D. Gan, M. Endo, S. Kanai, J. Hayakawa, F. Matsukura, and H. Ohno, "A perpendicular-anisotropy CoFeB-MgO magnetic tunnel junction," *Nature Materials*, vol. 9, no. 9, pp. 721-724, Sep, 2010.
- [214] A. Sellai, A. Mesli, M. Petit, V. L. Thanh, D. Taylor, and M. Henini, "Barrier height and interface characteristics of Au/Mn 5 Ge 3 /Ge (1 1 1) Schottky contacts for spin injection," *Semicond. Sci. Technol.*, vol. 27, no. 3, pp. 035014, 2012.
- [215] W. Zhao, and Y. Cao, "Predictive technology model for nano-CMOS design exploration," *J. Emerg. Technol. Comput. Syst.*, vol. 3, no. 1, pp. 1, 2007.
- [216] J. G. Alzate, P. Khalili Amiri, P. Upadhyaya, S. S. Cherepov, J. Zhu, M. Lewis, R. Dorrance, J. A. Katine, J. Langer, K. Galatsis, D. Markovic, I. Krivorotov, and K. L. Wang, "Voltage-Induced Switching of Nanoscale Magnetic Tunnel Junctions," *IEDM Tech Digest*, pp. 29.5. 1-29.5. 4, 2012.
- [217] A. M. Ionescu, and H. Riel, "Tunnel field-effect transistors as energy-efficient electronic switches," *Nature*, vol. 479, no. 7373, pp. 329-37, Nov 17, 2011.
- [218] "International technology Roadmap for Semiconductors," 2013.

- [219] E. Pop, “Energy dissipation and transport in nanoscale devices,” *Nano Research*, vol. 3, no. 3, pp. 147-169, 2010.
- [220] Y. Shiota, T. Nozaki, F. Bonell, S. Murakami, T. Shinjo, and Y. Suzuki, “Induction of coherent magnetization switching in a few atomic layers of FeCo using voltage pulses,” *Nature Materials*, vol. 11, no. 1, pp. 39-43, Jan, 2012.
- [221] S. Kanai, M. Yamanouchi, S. Ikeda, Y. Nakatani, F. Matsukura, and H. Ohno, “Electric field-induced magnetization reversal in a perpendicular-anisotropy CoFeB-MgO magnetic tunnel junction,” *Applied Physics Letters*, vol. 101, no. 12, pp. 122403, 2012.
- [222] S. Fukami, C. Zhang, S. DuttaGupta, A. Kurenkov, and H. Ohno, “Magnetization switching by spin-orbit torque in an antiferromagnet-ferromagnet bilayer system,” *Nat Mater*, vol. 15, no. 5, pp. 535-41, May, 2016.
- [223] J. Grollier, D. Querlioz, and M. D. Stiles, “Spintronic nanodevices for bioinspired computing,” *Proceedings of the IEEE*, vol. 104, no. 10, pp. 2024-2039, 2016.
- [224] A. Mizrahi, T. Hirtzlin, A. Fukushima, H. Kubota, S. Yuasa, J. Grollier, and D. Querlioz, “Neural-like computing with populations of superparamagnetic basis functions,” *Nat Commun*, vol. 9, no. 1, pp. 1533, Apr 18, 2018.
- [225] M. Romera, P. Talatchian, S. Tsunegi, F. Abreu Araujo, V. Cros, P. Bortolotti, J. Trastoy, K. Yakushiji, A. Fukushima, H. Kubota, S. Yuasa, M. Ernoult, D. Vodenicarevic, T. Hirtzlin, N. Locatelli, D. Querlioz, and J. Grollier, “Vowel recognition with four coupled spin-torque nano-oscillators,” *Nature*, vol. 563, no. 7730, pp. 230-234, Nov, 2018.
- [226] J. Torrejon, M. Riou, F. A. Araujo, S. Tsunegi, G. Khalsa, D. Querlioz, P. Bortolotti, V. Cros, K. Yakushiji, A. Fukushima, H. Kubota, S. Yuasa, M. D. Stiles, and J. Grollier, “Neuromorphic computing with nanoscale spintronic oscillators,” *Nature*, vol. 547, no. 7664, pp. 428-431, Jul 26, 2017.
- [227] Q. Shao, and K. L. Wang, “Heat-assisted microwave amplifier,” *Nat Nanotechnol*, vol. 14, no. 1, pp. 9-11, Jan, 2019.
- [228] M. Goto, Y. Wakatake, U. K. Oji, S. Miwa, N. Strelkov, B. Dieny, H. Kubota, K. Yakushiji, A. Fukushima, S. Yuasa, and Y. Suzuki, “Microwave amplification in a magnetic tunnel junction induced by heat-to-spin conversion at the nanoscale,” *Nat Nanotechnol*, vol. 14, no. 1, pp. 40-43, Jan, 2019.
- [229] Slonczewski, *Electronic device using magnetic components*, US US5695864A, 1997.

- [230] S. I. Kiselev, J. C. Sankey, I. N. Krivorotov, N. C. Emley, R. J. Schoelkopf, R. A. Buhrman, and D. C. Ralph, "Microwave oscillations of a nanomagnet driven by a spin-polarized current," *Nature*, vol. 425, no. 6956, pp. 380-3, Sep 25, 2003.
- [231] A. A. Tulapurkar, Y. Suzuki, A. Fukushima, H. Kubota, H. Maehara, K. Tsunekawa, D. D. Djayaprawira, N. Watanabe, and S. Yuasa, "Spin-torque diode effect in magnetic tunnel junctions," *Nature*, vol. 438, no. 7066, pp. 339-42, Nov 17, 2005.
- [232] L. Xue, C. Wang, Y.-T. Cui, J. A. Katine, R. A. Buhrman, and D. C. Ralph, "Conditions for microwave amplification due to spin-torque dynamics in magnetic tunnel junctions," *Applied Physics Letters*, vol. 99, no. 2, pp. 022505, 2011.
- [233] T. Maruyama, Y. Shiota, T. Nozaki, K. Ohta, N. Toda, M. Mizuguchi, A. A. Tulapurkar, T. Shinjo, M. Shiraishi, S. Mizukami, Y. Ando, and Y. Suzuki, "Large voltage-induced magnetic anisotropy change in a few atomic layers of iron," *Nat Nanotechnol*, vol. 4, no. 3, pp. 158-61, Mar, 2009.
- [234] T. Böhnert, R. Dutra, R. L. Sommer, E. Paz, S. Serrano-Guisan, R. Ferreira, and P. P. Freitas, "Influence of the thermal interface resistance on the thermovoltage of a magnetic tunnel junction," *Physical Review B*, vol. 95, no. 10, 2017.
- [235] Y. Deng, Y. Yu, Y. Song, J. Zhang, N. Z. Wang, Z. Sun, Y. Yi, Y. Z. Wu, S. Wu, J. Zhu, J. Wang, X. H. Chen, and Y. Zhang, "Gate-tunable room-temperature ferromagnetism in two-dimensional Fe₃GeTe₂," *Nature*, vol. 563, no. 7729, pp. 94-99, Nov, 2018.
- [236] K. S. Burch, D. Mandrus, and J. G. Park, "Magnetism in two-dimensional van der Waals materials," *Nature*, vol. 563, no. 7729, pp. 47-52, Nov, 2018.
- [237] K. L. Wang, H. Wu, S. A. Razavi, and Q. Shao, "Spintronic devices for low energy dissipation." pp. 36.2.1-36.2.4.
- [238] M. A. Rashid, F. Ahmad, and N. Amir, "Linear Invariants of a Cartesian Tensor Under SO(2), SO(3) and SO(4)," *International Journal of Theoretical Physics*, vol. 50, no. 2, pp. 479-487, 2010.
- [239] D. M. Crum, M. Bouhassoune, J. Bouaziz, B. Schweflinghaus, S. Blugel, and S. Lounis, "Perpendicular reading of single confined magnetic skyrmions," *Nat Commun*, vol. 6, pp. 8541, Oct 16, 2015.
- [240] C. Hanneken, F. Otte, A. Kubetzka, B. Dupe, N. Romming, K. von Bergmann, R. Wiesendanger, and S. Heinze, "Electrical detection of magnetic skyrmions by tunnelling

non-collinear magnetoresistance,” *Nat Nanotechnol*, vol. 10, no. 12, pp. 1039-42, Dec, 2015.

- [241] J. F. DiTusa, S. B. Zhang, K. Yamaura, Y. Xiong, J. C. Prestigiacomo, B. W. Fulfer, P. W. Adams, M. I. Brickson, D. A. Browne, C. Capan, Z. Fisk, and Julia Y. Chan, “Magnetic, thermodynamic, and electrical transport properties of the noncentrosymmetric B20 germanides MnGe and CoGe,” *Phys Rev B* 90, 144404 (2014)